

Dissertation  
submitted to the  
Combined Faculty of the Natural Sciences and Mathematics  
of Heidelberg University, Germany  
for the degree of  
Doctor of Natural Sciences

Put forward by  
Arthur Eugen Bolz  
born in: Filderstadt

Oral examination: November 27, 2019



# Measurement of Differential $\rho^0$ Photoproduction

## Cross-Sections at HERA

Referees: Prof. Dr. André Schöning  
Prof. Dr. Ulrich Uwer



## Abstract

Exclusive photoproduction of  $\rho^0$  vector mesons is studied with the H1 detector at HERA. A sample of over 900 000  $\pi^+\pi^-$  photoproduction events was collected in the years 2006-2007 using the H1 Fast Track Trigger. It corresponds to an integrated luminosity of  $1.3 \text{ pb}^{-1}$ . The dataset is used to study single-, double-, and triple-differential  $\pi^+\pi^-$  photoproduction cross-sections as a function of the invariant mass of the pions  $m_{\pi\pi}$ , the photon-proton collision energy  $W_{\gamma p}$ , and the squared momentum transfer at the proton vertex  $t$ . The phasespace is restricted to  $0.5 \text{ GeV} < m_{\pi\pi} < 2.2 \text{ GeV}$ ,  $20 \text{ GeV} < W_{\gamma p} < 80 \text{ GeV}$ ,  $-t < 1.5 \text{ GeV}^2$ , and a photon virtuality  $Q^2 < 0.1 \text{ GeV}^2$ . Reactions in which the scattered proton stays intact are statistically separated from those where it dissociates to a low-mass hadronic system in the range  $m_p < m_Y < 10 \text{ GeV}$ .

The  $m_{\pi\pi}$  distributions are parametrized by a Söding model to extract the  $\rho^0$  contribution to  $\pi^+\pi^-$  production. Single- and double-differential  $\rho^0$  cross-sections are measured as a function of  $W_{\gamma p}$  and  $t$ . The observed kinematic cross-section dependencies are parametrized using fits and are compared to expectations from phenomenological models as well as results from previous measurements. From the double-differential  $\rho^0$  cross-section, the effective intercept and slope of the leading Regge trajectory in the measurement phasespace are extracted:

$$\begin{aligned}\alpha(t=0) &= 1.0659 \pm 0.0033 \text{ (stat.) } \begin{matrix} +0.0099 \\ -0.0059 \end{matrix} \text{ (syst.)} \\ \alpha'(t=0) &= 0.243 \pm 0.050 \text{ (stat.) } \begin{matrix} +0.030 \\ -0.042 \end{matrix} \text{ (syst.) GeV}^{-2}.\end{aligned}$$

## Kurzfassung

Exklusive Photoproduktion von  $\rho^0$  Vektormesonen wird mit dem H1 Detektor am HERA Beschleuniger studiert. Ein Datensatz von über 900 000  $\pi^+\pi^-$  Photoproduktionsereignissen wurde in den Jahren 2006-2007 unter Verwendung des H1 Fast Track Triggers aufgezeichnet. Er entspricht einer integrierten Luminosität von  $1.3 \text{ pb}^{-1}$ . Der Datensatz wird verwendet um einfach, doppelt und dreifach differenzielle  $\pi^+\pi^-$  Photoproduktionswirkungsquerschnitte als Funktion der invarianten Masse der beiden Pionen  $m_{\pi\pi}$ , der Photon-Proton Kollisionsenergie  $W_{\gamma p}$  und des quadratischen Impulsübertrags am Protonvertex  $t$  zu studieren. Der Phasenraum ist auf  $0.5 \text{ GeV} < m_{\pi\pi} < 2.2 \text{ GeV}$ ,  $20 \text{ GeV} < W_{\gamma p} < 80 \text{ GeV}$ ,  $-t < 1.5 \text{ GeV}^2$ , sowie eine Photonvirtualität  $Q^2 < 0.1 \text{ GeV}^2$  beschränkt. Ereignisse, in denen das gestreute Proton erhalten bleibt, werden statistisch von solchen getrennt, in denen es in ein hadronisches System niedriger Masse im Bereich  $m_p < m_Y < 10 \text{ GeV}$  dissoziiert.

Die  $m_{\pi\pi}$  Verteilungen werden durch ein Söding-Modell parametrisiert, um den  $\rho^0$  Beitrag zur  $\pi^+\pi^-$  Produktion zu extrahieren. Einfach und doppelt differenzielle  $\rho^0$  Wirkungsquerschnitte werden als Funktion von  $W_{\gamma p}$  und  $t$  gemessen. Die beobachteten kinematischen Abhängigkeiten der Wirkungsquerschnitte werden mittels Fits parametrisiert und mit Erwartungen aus phänomenologischen Modellen sowie Ergebnissen früherer Messungen verglichen. Aus dem doppelt differenziellen  $\rho^0$  Wirkungsquerschnitt werden der effektive Achsenabschnitt und die Steigung der führenden Regge-Trajektorie im Phasenraum der Messung extrahiert:

$$\begin{aligned}\alpha(t=0) &= 1.0659 \pm 0.0033 \text{ (stat.) } \begin{matrix} +0.0099 \\ -0.0059 \end{matrix} \text{ (syst.)} \\ \alpha'(t=0) &= 0.243 \pm 0.050 \text{ (stat.) } \begin{matrix} +0.030 \\ -0.042 \end{matrix} \text{ (syst.) GeV}^{-2}.\end{aligned}$$



# Contents

<b>1</b>	<b>Introduction</b>	<b>1</b>
<b>2</b>	<b>Theory</b>	<b>3</b>
2.1	The Standard Model of Particle Physics . . . . .	3
2.1.1	Phenomenology of the Strong Force . . . . .	4
2.2	Diffractive Scattering of Hadrons . . . . .	5
2.2.1	Phenomenology of Soft Diffraction . . . . .	6
2.2.2	Regge Theory . . . . .	8
2.2.3	The Pomeron . . . . .	13
2.2.4	Diffractive Dissociation . . . . .	16
2.3	Photoproduction . . . . .	18
2.3.1	$\pi^+\pi^-$ Photoproduction . . . . .	19
2.4	Diffractive Electron-Proton Scattering . . . . .	20
<b>3</b>	<b>HERA and the H1-Detector</b>	<b>23</b>
3.1	The HERA Collider . . . . .	23
3.2	The H1 Detector at HERA . . . . .	24
3.2.1	The H1 Central Tracking Detector . . . . .	26
3.2.2	The H1 Calorimetry System . . . . .	29
3.2.3	H1 Forward Instrumentation . . . . .	30
3.3	The H1 Trigger System . . . . .	31
3.3.1	The Fast Track Trigger . . . . .	32
3.3.2	The CIP Trigger . . . . .	35
3.4	Luminosity Measurement . . . . .	36
<b>4</b>	<b><math>\pi^+\pi^-</math> Photoproduction Data Sample</b>	<b>37</b>
4.1	H1 Dataset and Trigger . . . . .	37
4.2	Event Variables Reconstruction . . . . .	39
4.3	Event Selection . . . . .	41
4.3.1	Base Selection . . . . .	41
4.3.2	Signal Region Selection . . . . .	42
4.3.3	Background Control Regions . . . . .	48
4.4	Proton-Dissociation Tagging . . . . .	52
4.4.1	Forward Detectors For Tagging . . . . .	53
4.4.2	Application of Tagging Information . . . . .	56
<b>5</b>	<b>Simulation of <math>\pi^+\pi^-</math> Production</b>	<b>61</b>
5.1	The DiffVM Generator . . . . .	61
5.2	The H1 Detector Simulation . . . . .	63
5.3	Modeling the $\pi^+\pi^-$ Photoproduction Dataset . . . . .	64
5.4	DiffVM Sample Tuning . . . . .	66
5.4.1	Signal $\rho^0$ MC Tuning . . . . .	66
5.4.2	Background Sample Tuning . . . . .	70
5.4.3	Detector Level Corrections . . . . .	70
5.5	Systematic Uncertainties . . . . .	71

<b>6</b>	<b>Trigger Simulation Correction</b>	<b>77</b>
6.1	DIS $\pi^+\pi^-$ Data Set . . . . .	77
6.2	s14 Subtrigger Performance . . . . .	81
6.2.1	FTT Performance . . . . .	82
6.2.2	Performance of Other Trigger Elements . . . . .	86
6.3	Trigger Correction Factors . . . . .	87
6.3.1	FTT && CIP Correction . . . . .	88
6.3.2	FTi2 Veto Correction . . . . .	91
6.3.3	Applying Trigger Correction Factors . . . . .	94
<b>7</b>	<b><math>\rho^0 \rightarrow \pi^+\pi^-</math> Cross-Section Measurement</b>	<b>95</b>
7.1	Detector Effects . . . . .	95
7.1.1	Detector Acceptance and Efficiency . . . . .	95
7.1.2	Detector Resolution and Migrations . . . . .	97
7.1.3	Visible and Fiducial Phasespace . . . . .	98
7.2	Unfolding $\pi^+\pi^-$ Cross-Sections . . . . .	101
7.2.1	Regularized Template Fit . . . . .	101
7.2.2	Background Subtraction . . . . .	102
7.2.3	Response Matrix Definition . . . . .	102
7.2.4	Regularization . . . . .	106
7.2.5	Uncertainty Propagation . . . . .	108
7.2.6	Unfolding Procedure Overview . . . . .	110
7.2.7	$\pi^+\pi^-$ Cross-Section Definition . . . . .	110
7.3	$\rho^0$ Cross-Section Definition . . . . .	111
7.3.1	Söding Model . . . . .	111
7.3.2	Ross-Stodolsky Model . . . . .	113
7.3.3	Cross-Section Extraction . . . . .	113
7.4	Cross-Section Fits and $\chi^2$ Definition . . . . .	114
7.4.1	Propagation of Uncertainties Through Fits . . . . .	114
<b>8</b>	<b>Results</b>	<b>117</b>
8.1	$\pi^+\pi^-$ Photoproduction Cross-Sections . . . . .	117
8.1.1	Fiducial $\pi^+\pi^-$ Cross-Section . . . . .	118
8.1.2	Söding Fit and Extraction of the $\rho^0$ Cross-Sections . . . . .	120
8.2	$\rho^0$ Photoproduction Cross-Sections . . . . .	124
8.2.1	Energy Dependence of the $\rho^0$ Cross-Sections . . . . .	124
8.2.2	$t$ Dependence of the $\rho^0$ Cross-Sections . . . . .	128
8.2.3	Double-Differential $\rho^0$ Cross-Sections . . . . .	133
<b>9</b>	<b>Conclusion</b>	<b>139</b>
<b>Appendices</b>		
<b>A</b>	<b>Further <math>\pi^+\pi^-</math> Cross-Section Studies</b>	<b>141</b>
A.1	Interpreting the Extended Mass Range . . . . .	141
A.2	Model Comparison . . . . .	144
<b>B</b>	<b>Event Selection Cuts</b>	<b>147</b>
<b>C</b>	<b>Derivations</b>	<b>149</b>
C.1	Reconstructing $W_{\gamma p}$ from the $\pi^+\pi^-$ System . . . . .	149
C.2	Reconstructing $t$ from the $\pi^+\pi^-$ System . . . . .	149
C.3	Splitting The Total Covariance Matrix . . . . .	150
<b>D</b>	<b>Mass Fit Plots For <math>\rho^0</math> Extraction</b>	<b>151</b>
D.1	Fit $\sigma(\gamma p \rightarrow \pi^+\pi^-Y)(W_{\gamma p}; m_{\pi\pi})$ (Section 8.2.1) . . . . .	151

D.2	Fit $d^2\sigma(\gamma p \rightarrow \pi^+\pi^-Y)/dm_{\pi\pi}dt(t; m_{\pi\pi})$ (Section 8.2.2) . . . . .	153
D.3	Fit $d^2\sigma(\gamma p \rightarrow \pi^+\pi^-Y)/dm_{\pi\pi}dt(W_{\gamma p}, t; m_{\pi\pi})$ (Section 8.2.3) . . . . .	155
<b>E</b>	<b>Unfolding Factors</b> . . . . .	<b>159</b>
E.1	1D $\pi^+\pi^-$ Distributions . . . . .	159
E.2	2D $\pi^+\pi^-$ Distributions . . . . .	161
E.2.1	$t \otimes m_{\pi\pi}$ . . . . .	161
E.2.2	$m_{\pi\pi} \otimes W_{\gamma p}$ . . . . .	163
E.3	3D $\pi^+\pi^-$ Distributions . . . . .	165
E.3.1	$m_{\pi\pi} \otimes W_{\gamma p} \otimes t$ . . . . .	165
<b>F</b>	<b>Cross-Section and Related Tables</b> . . . . .	<b>167</b>
F.1	$\pi^+\pi^-$ Cross-Sections . . . . .	167
F.1.1	$d\sigma(\gamma p \rightarrow \pi^+\pi^-Y)/dm_{\pi\pi}(m_{\pi\pi})$ . . . . .	167
F.1.2	$\sigma(\gamma p \rightarrow \pi^+\pi^-Y)(W_{\gamma p})$ . . . . .	168
F.1.3	$d\sigma(\gamma p \rightarrow \pi^+\pi^-Y)/dt(t)$ . . . . .	169
F.1.4	$d\sigma(\gamma p \rightarrow \pi^+\pi^-Y)/dm_{\pi\pi}(m_{\pi\pi}, W_{\gamma p})$ . . . . .	170
F.1.5	$d^2\sigma(\gamma p \rightarrow \pi^+\pi^-Y)/dm_{\pi\pi}dt(m_{\pi\pi}, t)$ . . . . .	174
F.1.6	$d^2\sigma(\gamma p \rightarrow \pi^+\pi^-Y)/dm_{\pi\pi}dt(m_{\pi\pi}, W_{\gamma p}, t)$ . . . . .	180
F.2	$\rho^0$ Cross-Sections . . . . .	192
F.2.1	$\sigma(\gamma p \rightarrow \rho^0Y)(W_{\gamma p})$ . . . . .	192
F.2.2	$d\sigma(\gamma p \rightarrow \rho^0Y)/dt(t)$ . . . . .	192
F.2.3	$d\sigma(\gamma p \rightarrow \rho^0Y)/dt(W_{\gamma p}, t)$ . . . . .	193
F.3	Misc. Parameter Tables . . . . .	194
<b>G</b>	<b>Data Samples</b> . . . . .	<b>195</b>
	<b>Bibliography</b> . . . . .	<b>195</b>



# 1 INTRODUCTION

In this thesis *exclusive diffractive production* of  $\rho^0$  mesons is studied in electron-proton collisions at the HERA collider. That is the scattering process  $ep \rightarrow e\rho^0 Y$ , in which the final state systems  $\rho^0$  and  $Y$  are well separated spatially in the center-of-mass frame. A diagram of the process is given in Figure 1.1. As depicted, the  $\rho^0$  meson decays almost exclusively in the  $\pi^+\pi^-$  channel at  $BR(\rho^0 \rightarrow \pi^+\pi^-) \simeq 100\%$  [1]. Concerning the system  $Y$ , two scenarios are considered: *elastic scattering*, where  $Y = p$  is the elastically scattered proton, and *diffractive proton-dissociation*, where the incoming proton scatters inelastically and dissociates into a system of multiple particles with small invariant mass.

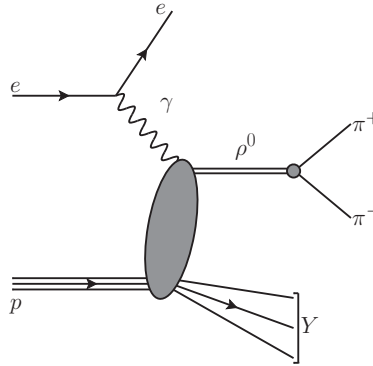


**Figure 1.1:** Diagram for  $\rho^0$  electroproduction in the  $\pi^+\pi^-$  decay channel.

Exclusive production of vector mesons, of which the  $\rho^0$  meson is the lightest, is a phenomenon of the *strong interaction*. It is a special case of soft hadron-hadron scattering. As such, it satisfies all characteristics of these kinds of interactions. Namely:

- a steep, exponentially falling momentum transfer distribution (*forward scattering*),
- a slowly increasing cross-section (elastic and total) with the scattering energy, and
- shrinkage of the forward peak with the scattering energy.

In general, the strong interaction is described by the theory of *quantum chromodynamics* (QCD). Complex QCD observables can only be evaluated perturbatively, which requires the presence of a hard energy scale. Given the small momentum transfer in soft hadron-hadron scattering, such a scale is typically missing. As a consequence, perturbative QCD is not applicable. Instead, other theoretical models have to be employed to describe it. In this thesis, scattering cross-sections are studied in the context of *Regge theory*, which is one of the oldest and most fundamental of those. In particular, it describes the energy dependence of the cross-section and the shrinkage of the forward peak as the consequence of the coherent exchange of resonance families, which are characterized by so-called *Regge trajectories*. In the high-energy regime that is studied in this thesis, the exchange of the *Pomeron trajectory* plays the dominant role.

Exclusive vector meson production offers a unique environment to study soft hadron scattering. For once, it allows measuring interactions at continuous scattering energies at a single experimental setup. In particular, in the context of Regge theory, this allows studying Regge trajectories in a single measurement. Furthermore, in vector meson electroproduction a typical energy scale of the process  $\mu = m_{\text{VM}}^2 + Q^2$  is given by the mass of the vector meson  $m_{\text{VM}}$  and the squared momentum transfer at the electron vertex  $Q^2$ . Thus, measurements of

---

vector meson production for a range of mesons of different mass and in various  $Q^2$  regimes allow investigating the transition of the strong interaction from the non-perturbative (small  $\mu$ ) into the perturbative QCD regime (large  $\mu$ ). Vector meson production has been studied extensively at HERA for  $\rho^0$  [2–17],  $\omega$  [18, 19],  $\phi$  [2, 3, 15, 16, 20–23],  $J/\psi$  [7, 15–17, 24–35],  $\psi(2S)$  [36, 37], and  $\Upsilon$  [29, 38–40] mesons and in various  $Q^2$  regimes. Further measurements have also been performed at various fixed-target experiments and other colliders, such as the Large Hadron Collider (LHC) at CERN.

This analysis focusses on the production of  $\rho^0$  mesons in the *photoproduction* regime with  $Q^2 \simeq 0 \text{ GeV}^2$ , i.e., in interactions with quasi-real photons. In particular, multi-dimensional differential cross-sections are measured as a function of scattering energy and the momentum transfer at the proton vertex. They allow extracting properties the leading Regge trajectory directly. The measurement is based on a large dataset of  $\pi^+\pi^-$  photoproduction events collected with the H1 detector at the HERA collider. With roughly 900 000 selected  $\pi^+\pi^-$  events, the dataset is the largest available at H1 and thus offers higher statistical precision than any previous measurement.

One of the main challenges of measuring vector meson photoproduction at HERA is that the final state kinematics can only be partially reconstructed. One consequence is a reduced resolution of measured kinematic variables and the experimental indistinguishability of elastic and proton-dissociative events. Building on previous H1 analyses [41–43], an improved unfolding approach is devised for this thesis to fully take into account and correct these resolution effects and to statistically separate elastic from proton-dissociative scattering events. While the chosen unfolding approach relies on the simulation of  $\rho^0$  photoproduction in H1, it is set up in a way that significantly reduces the dependence on the underlying Monte Carlo models. Doing so is vital because for vector meson photoproduction only phenomenological models which parametrize previous measurements are available at H1. The unfolding approach then allows measuring elastic and proton-dissociative differential cross-sections as functions of well defined kinematic variables and in a well defined fiducial phase space. When measuring  $\rho^0$  photoproduction, an additional challenge comes from irreducible background contributions to the  $\pi^+\pi^-$  final state. Following the approaches taken by past  $\rho^0$  analyses, first  $\pi^+\pi^-$  cross-sections are measured. Subsequently, the  $\rho^0$  contribution is extracted by fitting a Söding model to the measured invariant  $\pi^+\pi^-$  mass distributions.

The document is structured as follows: An introduction into the theoretical concepts relevant for the understanding of  $\rho^0$  meson photoproduction is given in Chapter 2. A focus is put on Regge theory to describe soft hadronic scattering cross-sections. The experimental setup, i.e., the HERA collider and H1 detector, is described in Chapter 3. The  $\pi^+\pi^-$  photoproduction dataset used for the present cross-section measurement is described in Chapter 4. The chapter covers the underlying H1 dataset, event selection and reconstruction, composition of the data and contamination by background processes, and the tagging of proton-dissociative events. The simulation of  $\pi^+\pi^-$  photoproduction and other relevant processes in the H1 detector is described in Chapter 5. The modeling does not perfectly reproduce the reality, and systematic uncertainties are derived to cover potential discrepancies. In particular, the simulation of the H1 trigger system is flawed, which requires the introduction of ad-hoc trigger correction factors. They are derived in a dedicated trigger study that is documented in Chapter 6. The methods applied for the cross-section measurement are explained in Chapter 7. A focus is put on unfolding measured detector level  $\pi^+\pi^-$  distributions, calculating differential  $\pi^+\pi^-$  cross-sections, and extracting the  $\rho^0$  contribution to these. Results, i.e., elastic and proton-dissociative differential  $\pi^+\pi^-$  and  $\rho^0$  cross-sections are then presented in Chapter 8. They are interpreted using models in the context of diffractive scattering and Regge theory. The analysis and main results are summarized in Chapter 9.

## 2 THEORY

Our modern understanding of the natural world sees it built from a set of fundamental elementary particles. They interact with one another via four fundamental forces: the *gravitational*, *electromagnetic*, *strong*, and *weak force*. Mathematical theories are employed to describe the particles and their interactions; the most successful and fundamental of which is the *standard model of particle physics* (SM). Around the SM, a multitude of other models exists to describe particular, isolated phenomena.

Particle physics analyses benefit from a close interplay between theory and experiment. Only experimental observations can provide the input upon which theories can be built. In turn, the theories provide a structured understanding of observed phenomena. They can also help to design reasonable experiments and define relevant observables. For the analysis performed in this thesis, theoretical concepts are used to build Monte Carlo event generators that aim to model and reproduce experimental observations (Chapter 5). Moreover, a simulation of the experimental setup is used to correct the measured data for detector effects (Chapter 7). The measured cross-sections are then interpreted in the context of Regge theory (Chapter 8).

Theoretical concepts that are relevant for understanding the present measurement are thus briefly introduced in the following sections. In Section 2.1, basic ideas of the SM are outlined with a focus on the strong force. In Section 2.2, diffractive scattering of hadrons, a phenomenon of the strong force is discussed. The photoproduction of vector mesons is introduced as a particular case of diffractive scattering in Section 2.3. It can be studied in electron-proton scattering as is explained in Section 2.4.

### 2.1 The Standard Model of Particle Physics

The standard model of particle physics is a set of mathematical concepts that describe fundamental particles and their interactions via the electromagnetic, strong, and weak force. In the following basic features are summarized. For a detailed introduction, it is referred to the literature, e.g., the introductory books by Griffiths [44] or Peskin and Schroeder [45].

The SM is formulated as a collection of relativistic quantum field theories, in which quantized gauge fields mediate the interactions. The fundamental matter particles are twelve fermions of spin  $1/2$  which come in 3 generations. Each generation consists of a *lepton* and *quark doublet*. The lepton doublets consist of a neutral particle, the neutrino, that couples only to the weak force and an electromagnetically charged particle that couples to both the weak and electromagnetic force. Quarks couple to all three forces. The coupling of the fermions to the gauge fields is determined by a set of quantum numbers: the electric charge, weak isospin, and strong color.

The electromagnetic and weak force are described in a unified gauge theory with a  $U(1) \times SU(2)$  symmetry group [46–48]. The symmetry is spontaneously broken by the Higgs-mechanism [49–51]. After symmetry breaking, the fundamental gauge bosons mix to form the massive  $W^\pm$  and  $Z^0$  bosons that mediate the weak interaction, as well as the massless photon for the electromagnetic interaction. The weak force only couples to left-handed particles. The coupling of the  $W^\pm$  bosons to quarks is special in that it does not couple directly to the mass eigenstates but rather to mixtures thereof, which then form weak eigenstates. The mixing of mass into weak eigenstates is described by the CKM matrix formalism [52, 53]. All fermions except for the three neutrinos obtain a mass from a Yukawa coupling to the Higgs

field. Neutrinos obtain tiny masses only because of mixing between the three generations, as described by the PMNS formalism [54–57].

The field theory describing the strong interaction is *Quantum Chromodynamics* (QCD) [58, 59], a non-abelian gauge theory with symmetry group  $SU(3)$ . The structure of the gauge group predicts eight massless exchange bosons, the gluons. Among the fermions, only the quarks couple to gluons. However, the gluons themselves carry two color charges each which give rise to self-coupling.

There are several phenomena the standard model does not describe. Most importantly, while it obeys the rules of special relativity, it does not include the rules and metric of general relativity. Hence, it is not capable of describing gravitational effects. On the level of individual particles, these are so small compared to the other forces that they are virtually negligible. The SM also fails to describe other phenomena such as the observation of dark matter. Nor can it explain the asymmetry between the matter and antimatter content in the universe. Moreover, for many phenomena that are in principle governed by the particles and interactions included in the SM, numerical predictions can not be made. Relevant for this thesis are in particular phenomena of the strong interaction that can not be calculated in QCD.

### 2.1.1 Phenomenology of the Strong Force

The strong force exhibits two very distinct and opposing features. For short-distance interactions with large momentum transfer, it becomes very weak, resulting in *asymptotic freedom* of quarks [60, 61]. Asymptotic freedom first revealed itself experimentally in deep inelastic electron-proton scattering where the measured cross-section can be described in terms of an interaction between the electron and seemingly free partons within the proton [62, 63]. At large distances, on the other hand, the strong force becomes increasingly strong, resulting in the *confinement* of quarks [64]. A consequence of confinement is that quarks can not be freely observed, but only within colorless bound states, called hadrons<sup>1</sup>.

The great success of QCD as the fundamental description of the strong interaction can be attributed to the fact that it can describe both phenomena as a consequence of the self-interaction of gluons. QCD is most successfully evaluated *perturbatively*, i.e., observables are expanded in a series in powers of the strong coupling strength  $\alpha_s$ . Among the higher-order contributions are those with internal quark and gluon loops. Upon numerical evaluation, they result in ultra-violet divergences that would also cause a divergence of the expansion series. QCD is a *renormalizable* theory which means that for every order of the series the divergences can be absorbed into the strong coupling constant, whose (finite) value then can not be predicted by the theory anymore but has to be experimentally measured. Renormalization depends on the typical energy scale of a studied process, which results in a scale dependence of the effective strong coupling constant. Combining perturbative QCD with measurements, the scale dependence of  $\alpha_s$  can be determined. Example measurements are shown in Figure 2.1. For large scales, i.e., short-distance interactions, indeed  $\alpha_s$  becomes small and the interactions increasingly weak whereas for small scales, i.e., long-distance interactions,  $\alpha_s$  diverges.

For small scale processes, such as the hadronization of quarks,  $\alpha_s$  becomes so large that the perturbative series converges only slowly or not at all. Although they are thought to be fundamentally described by QCD, these processes can then not be numerically evaluated<sup>2</sup>.

Due to the self-interaction of gluons and confinement, free gluons can not be exchanged over large distances. However, QCD still gives rise to long-distance phenomena. Historically, the strong force was discovered as the nuclear binding force between protons and neutrons. However, as first predicted by Yukawa [65], the force is then not mediated by gluons but

---

<sup>1</sup>An exception is the top quark which due to its short lifetime decays before it can hadronize.

<sup>2</sup>An alternative way to evaluate QCD are lattice calculations. Thus far they can only be performed for very simple observables.

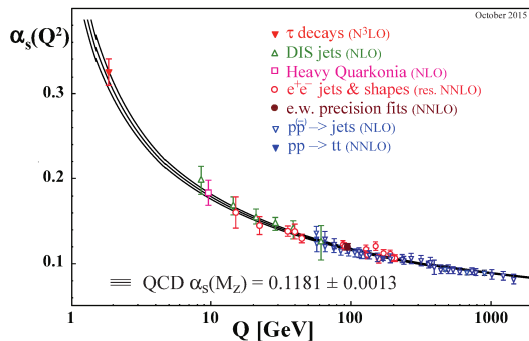


**Figure 2.1:** Measurements of  $\alpha_s$  as a function of the energy scale  $Q$ . The order of perturbative QCD employed in the extraction of  $\alpha_s$  is indicated in brackets. Figure from the PDG [1].

pions. A similar phenomenon is found in high-energy diffractive scattering processes. These typically happen at low momentum transfer such that (free) gluons can again not be the force mediators; nor can perturbative QCD be employed to calculate diffractive scattering processes.

## 2.2 Diffractive Scattering of Hadrons

Elastic and inelastic hadronic scattering cross-sections are dominated by *soft interactions*. For these, there is no large momentum transfer or mass present that would give rise to a hard scale at which  $\alpha_s \ll 1$ . Consequently, these processes can not be calculated in perturbative QCD and alternative models are needed to describe them. For reference, in Table 2.1 the total and elastic  $pp$  cross-section at a center-of-mass scattering energy of  $\sqrt{s} = 13 \text{ TeV}$ <sup>3</sup> is compared to dominant perturbative processes; even inclusive jet production with the highest cross-section lies several orders of magnitude below the total and the elastic cross-section.

cross-section	measured value
$\sigma_{pp}(\text{total})$	$\sim 110 \text{ mb}$
$\sigma_{pp}(\text{elastic})$	$\sim 30 \text{ mb}$
$\sigma_{pp}(\text{incl. jet } R = 0.4,  y  < 3)$	$\sim 1.9 \mu\text{b}$
$\sigma_{pp}(W)$	$\sim 190 \text{ nb}$
$\sigma_{pp}(t\bar{t})$	$\sim 800 \text{ pb}$

**Table 2.1:**  $pp$  scattering cross-sections for selected processes at  $\sqrt{s} = 13 \text{ TeV}$ . The large gap between typical perturbative processes and the total cross-section is filled by soft interactions, a significant contribution to which comes from elastic scattering. Numbers measured by the ATLAS Collaboration [66].

Due to the phenomenology of soft interactions and qualitative parallels to Fraunhofer diffraction of classical light waves, they are often referred to as *diffractive* interactions. Detailed introductions to diffractive hadron scattering are given by Alberi and Goggi [67], or Predazzi [68], for example. An extensive overview of current experimental results and their interpretation is given by Pancheri and Srivastava [69]. Here, only basic concepts that are relevant for this thesis are summarized, broadly following the arguments given in the references.

<sup>3</sup>Throughout the text natural units are used with  $c = \hbar = 1$ .

### 2.2.1 Phenomenology of Soft Diffraction

The phenomenology of diffractive interactions is studied by considering  $2 \rightarrow 2$  scattering of hadrons as an example. A generic diagram depicting the scattering of initial state particles  $a$  and  $b$  into final state particles  $c$  and  $d$  is given in Figure 2.2.

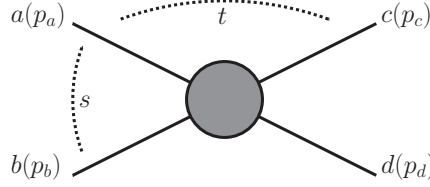


**Figure 2.2:**  $2 \rightarrow 2$  scattering diagram.

Three Lorentz-invariant variables, the Mandelstam [70] variables, can be calculated from the four-momenta  $p$  of the scattering particles:

$$s = (p_a + p_b)^2, \quad (2.1)$$

$$t = (p_a - p_c)^2, \quad (2.2)$$

$$u = (p_a - p_d)^2. \quad (2.3)$$

Only two of them are independent because

$$\sum_{i=a,b,c,d} m_i^2 = s + t + u, \quad (2.4)$$

where the sum runs over the masses  $m_i$  of the scattering particles. In the following, the *center-of-mass scattering energy*  $s$  and the *momentum transfer*  $t$  between particles  $a$  and  $c$  will be used. In particular,  $t$  is related to the *scattering angle* between  $a$  and  $c$  in the center-of-mass frame. If all masses of the participating particles are equal to  $m$ , the relation is simply

$$\cos \theta = \frac{\vec{p}_a \cdot \vec{p}_c}{|\vec{p}_a| |\vec{p}_c|} = 1 + \frac{2t}{s - 4m^2}. \quad (2.5)$$

Under the equal mass assumption, the physical ranges for the Mandelstam variable values are  $s > 4m^2$ ,  $t < 0$ , and  $u < 0$ ; which is still approximately true in the general mass case.

Mathematically, the scattering can be described in terms of a *scattering amplitude*  $A_{ab \rightarrow cd}$ . The squared amplitude gives the probability that final state  $c(p_c) d(p_d)$  is reached from an initial state  $a(p_a) b(p_b)$  with given momentum configurations. Instead of scattering amplitudes, scattering processes are typically described in terms of *scattering cross-sections*  $\sigma_{ab \rightarrow cd}$  in an experimental context. These describe event rates and thus can be measured. The *differential cross-section*  $d\sigma/d\Omega$  is defined as:

$$\frac{d\sigma}{d\Omega} = \frac{\text{“rate of scattered particles into the solid angle } d\Omega\text{”}}{\text{“flux of incoming particles”} \cdot d\Omega}. \quad (2.6)$$

In the high-energy limit, where particle masses  $m \ll s$  can be neglected with respect to the scattering energy, the  $2 \rightarrow 2$  scattering cross-section is related to the scattering amplitude via

$$\frac{d\sigma}{d\Omega} = \frac{1}{16\pi^2 s} |A_{ab \rightarrow cd}(\Omega)|^2, \quad (2.7)$$

where the pre-factor describes the flux of incoming particles.

### Differential Diffractive Cross-Sections

The total and elastic  $pp$  scattering cross-sections are shown as a function of the center-of-mass energy  $s$  in Figure 2.3. Both are driven by soft diffractive interactions and exhibit the same qualitative behavior to be expected for all diffractive processes. At first, the cross-sections fall off with some power of  $s$  at low energies before they start to rise slowly with increasing  $s$ . Noticeably, the elastic cross-section changes more steeply with  $s$  than the total cross-section.

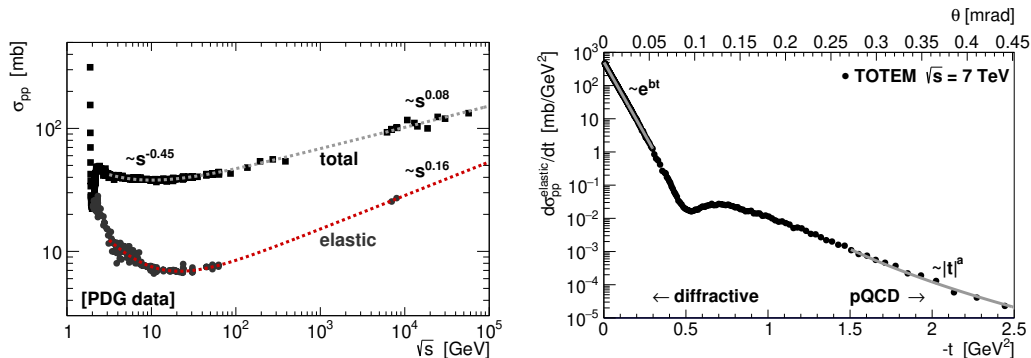


**Figure 2.3:** Total and elastic  $pp$  cross-section as a function of the center-of-mass energy  $\sqrt{s}$  (left) and differential elastic cross-section  $d\sigma_{pp}/dt$  as a function of momentum transfer  $t$  at  $\sqrt{s} = 7$  TeV (right). Data from [1] and [71, 72].

A further characteristic of hadronic scattering is the generally small momentum transfer  $t$ , i.e., particles are predominantly scattered under small angles. As an example, the differential elastic  $pp$  cross-section  $d\sigma/dt$  as a function of  $t$  and the scattering angle  $\theta$  between the in- and the out-going proton is also shown in Figure 2.3. The cross-section falls off exponentially at small  $|t|$  and then transitions into a softer power-law dependence at larger  $|t|$ , where perturbative QCD again becomes applicable.

### Parallels to Optical Diffraction of Light Waves

The Fraunhofer limit studies scattering of a light wave off a target under the *small wavelength* and *large distance* condition, i.e., the wavelength  $\lambda$  is much smaller than the size of the target  $R$ ,  $R/\lambda \gg 1$ , and the intensity pattern of the scattered wave is observed at a distance  $D$  far away from the target,  $R/D \ll 1$ . The combined Fraunhofer requirement is  $R^2/(\lambda D) \ll 1$ . Let  $I_0 e^{ik \cdot r}$  be an incoming plane wave with amplitude  $I_0$  and wave vector  $k$ . The wavelength is then given by  $\lambda = \frac{2\pi}{|k|}$ . In the Fraunhofer limit, the amplitude of the scattered wave  $I(r)$  can be written as [67]:

$$I(r) = \frac{I_0}{k} e^{ik \cdot r} + \frac{i I_0}{2\pi r} e^{ik \cdot r} \int f(\vec{b}) e^{-i\vec{b} \cdot \vec{q}} d^2\vec{b}, \quad (2.8)$$

i.e., as the undisturbed wave plus additional contributions from the scattering of the incoming wave off the target. The function  $f(\vec{b})$  is the profile function describing the absorption by the two-dimensional target at position  $\vec{b}$ , and  $q = k - k'$  the momentum transfer between in- and outgoing waves. The scattering amplitude  $A$  corresponds to the second part of Equation (2.8). It is given by the Fourier transform of the profile function  $f(\vec{b})$ . For a fully absorbing black disc of radius  $R$  with  $f(\vec{b}) = 1$  for  $|\vec{b}| < R$  and  $f(\vec{b}) = 0$  otherwise, the scattering amplitude is

$$A(r) \propto \frac{J_1(|\vec{q}|R)}{|\vec{q}|R}, \quad (2.9)$$

with  $J_1$  being a Bessel function of the first kind. For a Gaussian profile, the amplitude follows an exponential function; compare Figure 2.4.

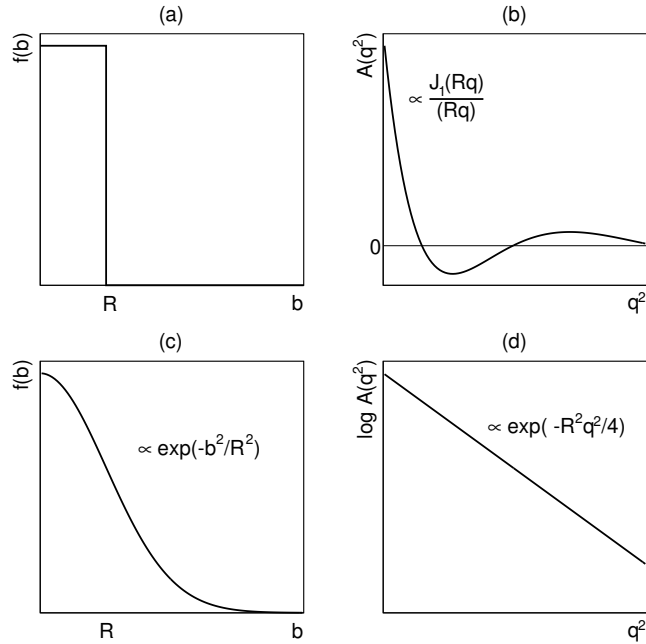


**Figure 2.4:** Profile functions for a circular disc with radius  $R$  (a) and a Gaussian function with width  $R$  (c). The corresponding scattering amplitudes  $A$  are shown in (b) and (d), respectively.

In the context of the *particle-wave-duality* [73] these considerations also apply to high-energy particle scattering. The *de Broglie wavelength* of a particle with momentum  $\vec{p}$  is

$$\lambda_{dB} = \frac{2\pi}{|\vec{p}|}. \quad (2.10)$$

The typical size of a hadron is  $R \sim 1$  fm, the size of particle physics experiments  $D$  is of the order of centimetres and larger. The long distance requirement is then always fulfilled with  $R/D \lesssim 10^{-13}$ . For high-energy particles with  $|\vec{p}| \gtrsim 50$  GeV, also the short wavelength condition  $R|\vec{p}| \sim 50$  is met<sup>4</sup>. And even for very high-momentum particles in the TeV range the Fraunhofer condition  $R^2/(\lambda D) \ll 1$  is still well satisfied. The considerations for the optical diffraction amplitude then also hold for the particle scattering amplitude. In this context, observed differential hadronic cross-sections (compare Figure 2.3) suggest that hadrons are intransparent (*black*) discs with rather hard edges. This reflects the short range of the strong interaction.

### 2.2.2 Regge Theory

Regge theory (after Tullio Regge [74, 75]) attempts to describe hadronic cross-sections from basic principles of scattering theory. First developed in the 1950s and '60s, it predates QCD. It builds on the idea that hadron-exchange carries the strong force over larger distances. However, instead of individual hadrons, the correlated exchange of whole hadron families (orbital excitations) is considered. The exchanges are characterized by *Regge trajectories* that interpolate between resonances in the (complex) angular momentum and mass plane. In the following, some of the key ideas are discussed for the example of elastic  $2 \rightarrow 2$  scattering with the goal to gain some insight on the energy dependence of hadronic cross-sections. A textbook introduction to basic scattering theory can be found in Peskin and Schroeder [45], for example. Introductions to Regge theory are provided by Collins [76], Forshaw and Ross [77], or Donnachie et al. [78].

<sup>4</sup>Using a conversion factor  $200 \text{ MeV fm} = 1$ .

### Scattering Theory

The transition of the asymptotic initial state  $|i\rangle = |a, b\rangle$  to the asymptotic final state  $|f\rangle = |c, d\rangle$  is described by a scattering matrix  $\mathbf{S}$  that relates to the transition probability of  $|i\rangle$  going to  $|f\rangle$ :

$$P_{i \rightarrow f} = |\langle f | \hat{S} | i \rangle|^2 \quad (2.11)$$

Typically,  $\mathbf{S}$  is written in terms of the scattering amplitude  $\mathbf{A}$  by factoring out the case where no interaction takes place:

$$S_{if} = \delta_{if} + i(2\pi)^4 \delta^4(p_i - p_f) A_{if}. \quad (2.12)$$

Here,  $\delta_{if} = 1$  for  $i = f$  and  $\delta_{if} = 0$  otherwise and similarly  $\delta^4(p_i - p_f)$  ensures four-momentum conservation  $p_i = p_f$  with  $p_i = p_a + p_b$  and  $p_f = p_c + p_d$ . The scattering amplitude is related to the differential scattering cross-section as defined in Equation (2.7). Expressing the scattering angle in terms of the momentum transfer  $t$  and neglecting all particle masses in the high-energy limit, one finds:

$$\frac{d\sigma}{dt} = \frac{1}{16\pi s^2} |A_{if}(s, t)|^2. \quad (2.13)$$

Irrespective of the underlying interaction,  $\mathbf{S}$  is expected to have several fundamental properties:

**1. Lorentz invariance:**

$\mathbf{S}$  should be Lorentz invariant and thus be a function of only Lorentz invariant variables, i.e.,  $\mathbf{S} \equiv \mathbf{S}(s, t)$ .

**2. unitarity and the optical theorem:**

To conserve total probability,  $\mathbf{S}$  should be unitary, i.e.:

$$1 = \mathbf{S} \cdot \mathbf{S}^\dagger = \mathbf{S}^\dagger \cdot \mathbf{S}. \quad (2.14)$$

To ensure the unitarity condition, the imaginary part of the scattering amplitude  $\mathbf{A}$  must satisfy:

$$2\Im[A_{if}] = (2\pi)^4 \delta^4(p_i - p_f) \sum_k A_{ik} A_{kf}^\dagger. \quad (2.15)$$

An interesting consequence of the unitary condition for the scattering amplitude arises for the case of elastic forward scattering ( $f = i$ ) with vanishing momentum transfer ( $t = 0$ ). Then,

$$2\Im[A_{ii}(s, t = 0)] = (2\pi)^4 \sum_k \delta^4(p_i - p_k) |A_{ik}|^2 \propto \sigma_{\text{tot}}, \quad (2.16)$$

where the sum of the squared amplitude over all final states  $k$  is proportional to the total scattering cross-section  $\sigma_{\text{tot}}$ . Consequently, the total scattering cross-section  $ab \rightarrow \text{anything}$  is given by the imaginary part of the elastic forward amplitude. This relation is called the *optical theorem* and central to the study of hadronic cross-sections. In the high-energy limit the proportionality constant is a flux factor  $\Phi \simeq 2s$  and the total cross-section is given by:

$$\sigma_{\text{tot}}(s) = \frac{1}{s} \Im[A_{\text{elas}}(s, t = 0)]. \quad (2.17)$$

**3. analyticity and crossing-symmetry:**

Typically, it is also assumed that  $\mathbf{A}$  is a (complex) analytic function. The analyticity assumption is connected to causality. It has multiple consequences, e.g., on the

singularity structure of  $\mathbf{A}$  or on the dispersion relation that connects the imaginary with the real part of the amplitude. Furthermore, analyticity is a necessary requirement for *crossing-symmetry* to hold. Assuming the scattering amplitude  $A_{ab \rightarrow cd}(s, t)$  for a process  $a(p_a) b(p_b) \rightarrow c(p_c) d(p_d)$  is an analytic function, it can be continued beyond the physical region of the scattering process ( $s \gtrsim 4m^2$ ,  $t \lesssim 0$ , and  $u \lesssim 0$ ) to all (complex) values of  $s$ ,  $t$ , and  $u$ . Crossing-symmetry then is the requirement that the crossed process  $a(p_a) \bar{c}(-p_c) \rightarrow \bar{b}(-p_b) d(p_d)$ <sup>5</sup> with:

$$\begin{aligned} s_t &= (p_a + (-p_c))^2 \equiv t \gtrsim 4m^2 \\ t_t &= (p_a - (-p_b))^2 \equiv s \lesssim 0 \end{aligned}$$

is described by the same amplitude  $A_{ab \rightarrow cd}(s, t)$  once  $s$  and  $t$  are interchanged:

$$A_{ab \rightarrow cd}(s, t) = A_{a\bar{c} \rightarrow \bar{b}d}(t, s). \quad (2.18)$$

Crossing symmetry holds order by order in perturbative quantum field theory where amplitudes are constructed with Feynman rules. Here, it is assumed to also be true in general. A crucial consequence of crossing-symmetry is the concept that an  $s$ -channel resonance in  $a\bar{c} \rightarrow \bar{b}d$  can be exchanged in the  $t$ -channel in the crossed scattering process  $ab \rightarrow cd$ , as is illustrated with a generic leading order diagram in Figure 2.5.

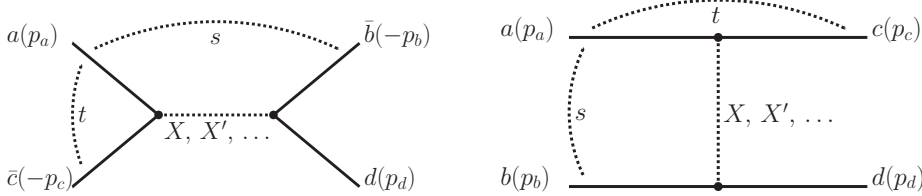


**Figure 2.5:** Diagrams for  $s$ -channel resonances in  $a\bar{c} \rightarrow \bar{b}d$  (left) that are exchanged in the  $t$ -channel in the crossed process  $ab \rightarrow cd$  (right).

### $t$ -Channel Resonance Exchange Amplitude

Regge theory aims to understand the high-energy behavior of the amplitude  $A_{ab \rightarrow cd}(s, t)$  for  $t$ -channel exchange. Using crossing symmetry,  $A_{ab \rightarrow cd}(s, t)$  can be expressed in terms of the crossed amplitude  $A_{a\bar{c} \rightarrow \bar{b}d}(t, s)$  that is continued to the regime  $s \gtrsim 4m^2$ ,  $t \lesssim 0$ . In general, the amplitude  $A_{a\bar{c} \rightarrow \bar{b}d}(s, t)$  can be expanded in a *partial wave expansion* as a series of Legendre polynomials:

$$A_{a\bar{c} \rightarrow \bar{b}d}(s, t) = \sum_{l=0}^{\infty} (2l+1) a_l(s) P_l(\cos \theta(s, t)), \quad (2.19)$$

The sum runs over the contributing angular momenta  $l$ ,  $a_l(s)$  is the so-called partial wave amplitude, and  $P_l(x)$  a Legendre polynomial of order  $l$ . Figuratively, the presence of a resonance with spin  $J$  and mass<sup>6</sup>  $m_J$  it gives rise to a *pole* in  $s$  around which it becomes the dominant contribution<sup>7</sup>:

$$A_{a\bar{c} \rightarrow \bar{b}d}(s, t) \sim A_{res}(s, t) \sim \frac{P_J(\cos \theta(s, t))}{s - m_J^2} \quad (2.20)$$

<sup>5</sup> $\bar{b}$  and  $\bar{c}$  denote the anti-particles of  $b$  and  $c$ , respectively

<sup>6</sup>For hadron resonances, a finite resonance width can be absorbed into a (complex) mass  $m_J$  and is ignored in the following.

<sup>7</sup>A more formal argument is given for example by Forshaw and Ross [77]. It involves continuing the amplitude to complex and continuous angular momentum and, using Cauchy's integral formula, write the partial wave equation as a contour integral in the complex  $l$ -plane. By choosing appropriate boundary conditions  $a_l(t)$  can be uniquely continued to  $a(l, t)$  with  $a(l, t) = a_l(t)$  for integer  $l$  such that the integral/series converges.

Using crossing symmetry and expressing the scattering angle  $\theta$  in terms of the momentum-transfer  $t$  via Equation (2.5), the amplitude for  $t$ -channel exchange of the resonance can be written as:

$$A_{ab \rightarrow cd}(s, t) = A_{a\bar{c} \rightarrow \bar{b}d}(t, s) \sim \frac{P_J(1 + \frac{2s}{t-4m^2})}{t - m_J^2}. \quad (2.21)$$

As  $|t| \ll s$  (for diffractive scattering), for large enough  $s \rightarrow \infty$  the Legendre polynomials  $P_J$  are dominated by the leading exponent,  $P_J(1 + \frac{2s}{t-4m^2}) \sim s^J$ . Using the optical theorem, this allows to find the asymptotic dependence of the total cross-section for single particle exchange:

$$\sigma_{tot} \xrightarrow{s \rightarrow \infty} \sim \frac{s^J}{s} = s^{J-1} \begin{cases} s^{-1}, & \text{for } J=0 \\ s^0, & \text{for } J=1 \\ s^1, & \text{for } J=2 \end{cases}. \quad (2.22)$$

Unfortunately, applying this to hadronic scattering processes by considering the exchange of hadrons fails to describe experimental data. Baryon exchange is negligible mainly due to large particle masses and quantum number constraints. Mesons, on the other hand, all have integer spin. They are then not able to reproduce measured cross-sections; compare the  $pp$  scattering cross-section presented in Figure 2.3 for an example. Furthermore, the presence of hadrons with large spin  $J > 1$  is problematic because their exchange leads to cross-sections in violation of unitarity.

## Regge Trajectories and Resonance Families

The idea of hadron exchange governing diffractive hadron-hadron scattering is saved by the realization that the hadronic resonances that are exchanged are not elementary particles but composite objects made from quarks. As such they can have orbital excitations which can also be exchanged<sup>8</sup>. To get the correct  $t$ -channel exchange amplitude, all exchange contributions have to be summed up coherently. The sum is performed by introducing so-called *Regge trajectories*  $\alpha_{\mathbb{R}}(t)$  that interpolate between resonance poles of a single family in the (complex) angular momentum versus mass plane. The trajectories are defined such, that the value at a pole gives the angular momentum of the corresponding resonance:

$$\alpha_{\mathbb{R}}(t = m_J^2) = J. \quad (2.23)$$

As first observed by Chew and Frautschi [79], and Gribov [80], the real part of hadronic Regge trajectories in the resonance region ( $t > 0$ ) is very well described by a linear function<sup>9</sup>:

$$\alpha_{\mathbb{R}}(t) = \alpha_0 + \alpha' t. \quad (2.24)$$

In Figure 2.6, the spin of mesons from the  $\rho$ ,  $\omega$ ,  $f_2$  and  $a$  families is plotted against their mass squared. They all lie on degenerate Regge trajectories with  $\alpha_0 \sim 0.5$  and  $\alpha' \sim 0.9 \text{ GeV}^{-2}$ .

If the exchange of a resonance family is considered instead of a single resonance, the sum over all resonances in Equation (2.21) can be performed by employing the Regge trajectories.

<sup>8</sup>For example for the spin-1  $\rho(770)$  meson in the ground state, one can also observe a spin-3  $\rho(1690)$  and spin-5  $\rho(2350)$  excited state [1].

<sup>9</sup>This can be simply taken as an experimental observation. However, it also follows from simple hadron string models where the hadrons are assumed to be rotating systems of quarks connected by an open color string. If the force between any two points of the string is constant, then the contribution from the string to  $J$  is proportional to its contribution to the mass squared:  $J_{string} \propto m_{string}^2$ . As a consequence, the Regge trajectories are linear with a universal slope [81]. For real hadrons, the linearity has to break down eventually when the energy stored in string becomes large enough for fragmentation to occur.

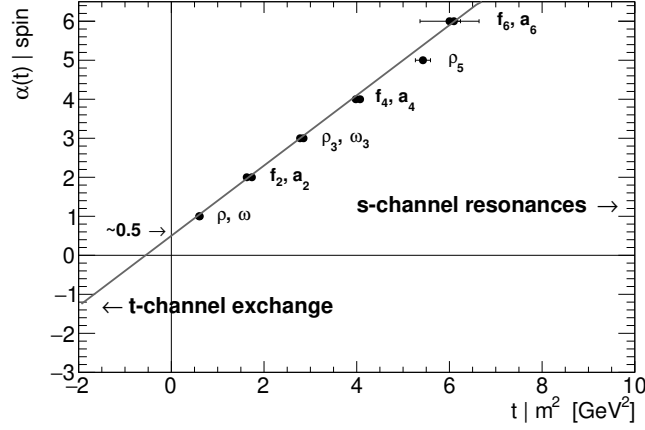


**Figure 2.6:** Chew-Frautchi plot for the four dominant and degenerate Regge trajectories from the  $\rho$ ,  $\omega$ ,  $f_2$  and  $a$  meson families. Data from [1].

For this, the trajectories need to be continued into the scattering region ( $t < 0$ ). For small negative  $t$ , they are found to continue linearly, such that one can replace the mass poles by

$$t - m_J = \frac{\alpha_{\mathcal{R}}(t) - J}{\alpha'}. \quad (2.25)$$

The  $t$ -channel Reggeon exchange amplitude then approximately becomes

$$A_{ab \rightarrow cd}(s, t) \xrightarrow{s \rightarrow \infty} \sim \sum_{l=0}^{\infty} \frac{s^l}{t - m_l^2} = \sum_{l=0}^{\infty} \frac{\alpha'}{l - \alpha_{\mathcal{R}}(t)} s^l. \quad (2.26)$$

The dominant contribution comes from the pole at  $l = \alpha_{\mathcal{R}}(t)$  and in the high-energy limit, the amplitude asymptotically behaves like

$$A_{ab \rightarrow cd}(s, t) \xrightarrow{s \rightarrow \infty} \sim s^{\alpha_{\mathcal{R}}(t)}. \quad (2.27)$$

A proper formal derivation results in the asymptotic Regge amplitude [77]:

$$A_{ab \rightarrow cd}(s, t) \xrightarrow{s \rightarrow \infty} \sim \frac{\eta + e^{-i\pi\alpha_{\mathcal{R}}(t)}}{2 \sin \pi\alpha_{\mathcal{R}}(t)} \frac{\beta_{ac}(t)\beta_{bd}(t)}{\Gamma(\alpha_{\mathcal{R}}(t))} s^{\alpha_{\mathcal{R}}(t)} \quad (2.28)$$

Formally, this resembles the exchange of a single resonance with  $t$ -dependent spin  $\alpha_{\mathcal{R}}(t)$  and with couplings  $\beta_{ac}(t)$  and  $\beta_{bd}$  to the scattering particles.  $\eta = \pm$  specifies the so-called *signature* of the amplitude, and  $\Gamma(\alpha_{\mathcal{R}}(t))$  absorbs a remaining pole structure. It is thus sometimes spoken of *Reggeon exchange*, as depicted in Figure 2.7. However, Reggeons are not actual particles but the combined effect of the coherent exchange of multiple resonance excitation states.

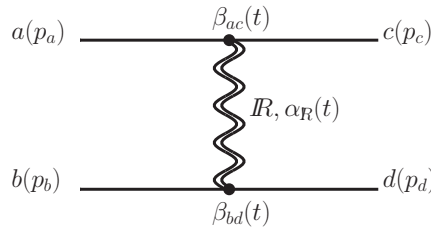


**Figure 2.7:** Diagram for Reggeon exchange.

## Reggeon Phenomenology

Elastic differential diffractive cross-sections are experimentally found to exponentially depend on the momentum transfer  $t$  for small values of  $|t|$ . Taking also the energy dependence of the Reggeon exchange cross-section into consideration, the differential elastic cross-section can be parametrized as:

$$\frac{d\sigma_{\text{elas}}}{dt}(s, t) \xrightarrow{s \rightarrow \infty} \frac{d\sigma_{\text{elas}}}{dt}(s_0, 0) \left(\frac{s}{s_0}\right)^{2(\alpha_R(t)-1)} e^{b_0 t} = \left(\frac{s}{s_0}\right)^{2(\alpha_R(0)-1)} e^{b(s)t} \quad (2.29)$$

with

$$b(s) = b_0 + 2\alpha' \ln(s/s_0) \quad (2.30)$$

and a reference energy  $s_0$ . The intercept  $\alpha_R(0)$  thus dominantly controls the variation of the cross-section with the center-of-mass energy  $s$ , while the slope  $\alpha'$  results in an effective *shrinkage* of the diffractive forward peak with increasing energy.

The Regge amplitude in Equation (2.28) suggests *factorization* of hadronic cross-sections, i.e., scattering processes in which the same Regge trajectories are exchanged differ only in the couplings  $\beta_{ac}(t)$  and  $\beta_{bd}(t)$  but otherwise exhibit the same energy dependence that is governed by the Reggeon trajectory.

Using again the optical theorem, total scattering cross-sections governed by Reggeon exchange have the asymptotic energy dependence

$$\sigma_{\text{tot}} \xrightarrow{s \rightarrow \infty} s^{\alpha_R(0)-1}. \quad (2.31)$$

The dominant Regge trajectories have  $\alpha_R(0) \sim 0.5$  and thus reproduce the measured hadronic cross-section up to energies of approximately  $s \lesssim 10$  GeV.

### 2.2.3 The Pomeron

Hadronic cross-sections are experimentally observed to slowly rise with the scattering energy above  $s \gtrsim 10$  GeV. For reference, the total cross-sections for selected processes are shown as a function of  $s$  in Figure 2.8.

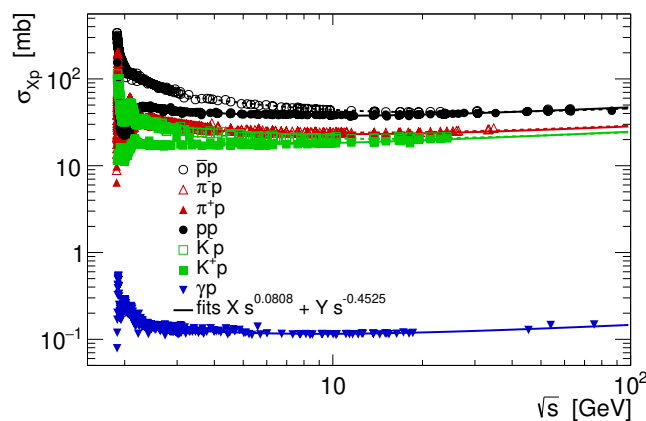


**Figure 2.8:** Energy dependence of total hadronic cross-sections for selected scattering processes. Data from the PDG [1].

In the Reggeon exchange picture, this requires a Regge trajectory with an intercept larger than 1. However, there is no evidence for a hadron family providing that. Instead, an ad-hoc trajectory is introduced to describe the high-energy behavior. It is typically called *Pomeron*

trajectory ( $\mathbb{P}$ ) and named after the physicist Isaak Pomerantschuk [82]. The canonical parameters of the Pomeron trajectory have been determined by Donnachie and Landshoff [83, 84] from proton-proton and proton-antiproton scattering cross-sections:

$$\alpha_{\mathbb{P}}^{DL}(t) = 1.0808 + 0.25 \text{ GeV}^{-2}t. \quad (2.32)$$

A further defining property of the Pomeron trajectory is that it corresponds to color-singlet states that have no strong isospin and transform even under charge and parity conjugation. One central phenomenological consequence is that particle-particle and particle-antiparticle Pomeron exchange interactions have the same cross-sections; compare Figure 2.8.

At first glance, the Pomeron trajectory appears to violate unitarity. The Froissart-Martin bound [85, 86] sets an upper limit on the maximally allowed rise of a cross-section with energy:

$$\sigma_{\text{tot}} < C \ln^2 s, \quad (2.33)$$

The proportionality factor  $C$  is typically estimated from the pion mass to be of the order of 60 mb [77]. While the Pomeron exchange cross-section mathematically rises more steeply, the limit then is only crossed for scattering energies beyond the Planck scale ( $s \gg 10^{38} \text{ GeV}^2$ ). Furthermore, it is expected that eventually at very high energies the exchange of multiple Pomerons results in a softer energy dependence [87, 88].

At energies currently accessible at particle colliders, the total hadronic scattering cross-sections for two particles  $a b \rightarrow \text{anything}$  can be simply parametrized by:

$$\sigma_{\text{tot}}^{ab}(s) = X^{ab} s^{\alpha_{\mathbb{P}}(0)-1} + (Y_+^{ab} + Y_-^{ab}) s^{\alpha_{\mathbb{R}}(0)-1}, \text{ and} \quad (2.34)$$

$$\sigma_{\text{tot}}^{\bar{a}b}(s) = X^{ab} s^{\alpha_{\mathbb{P}}(0)-1} + (Y_+^{ab} - Y_-^{ab}) s^{\alpha_{\mathbb{R}}(0)-1}, \quad (2.35)$$

with a universal Pomeron intercept  $\alpha_{\mathbb{P}}(0)$  and a degenerate, universal mesonic Reggeon intercept  $\alpha_{\mathbb{R}}(0)$  [78]. The normalization factors  $X^{ab}$ ,  $Y_+^{ab}$ , and  $Y_-^{ab}$  absorb previously introduced Pomeron and Reggeon coupling.  $Y_+^{ab}$  and  $Y_-^{ab}$  take into account Reggeon trajectories transforming even and odd under charge-conjugation. In principle, also a Pomeron trajectory that transforms odd under charge-conjugation is expected [89]. It is typically referred to as an *Odderon* trajectory and as of yet lacks solid experimental evidence.

### The Pomeron in QCD

Since the Pomeron is a phenomenon of the strong interaction, it is desirable to embed it into the framework of QCD. One way to do this is to associate the Pomeron trajectory in the resonance region with *glueballs* [90], i.e., hadrons with only valence gluons instead of quarks. These lack strong experimental evidence, but mass spectra can be calculated in lattice QCD [91] or by classical potential model approaches [92, 93]. Alternatively, there have been attempts to describe Pomeron exchange in terms of QCD. Indeed, to lowest order, it can be associated with the simultaneous exchange of two gluons [94, 95]; compare Figure 2.9. However, while two-gluon models provide the correct color and parity, they fail entirely to describe the energy dependence of diffractive interactions. The underlying reason is that the colored gluons strongly interact with one another so that higher-order corrections need to be taken into account.

In the presence of gluon self-coupling, QCD calculations of Pomeron exchange can then only be performed perturbatively. A necessary requirement is the presence of a hard scale like a large momentum transfer  $|t|$ . If such a scale is provided, and if the scattering energy  $s$  is much larger than  $|t|$ , the two-gluon exchange can be described by the Balitzky, Fadin, Kuraev, Lipatov (BFKL) evolution equation [96–99]. In the BFKL picture, it takes the form of a gluon ladder; compare Figure 2.9. A more detailed introduction to the topic is given by Forshaw and Ross [77], for example. Soft hadronic interactions, such as measured in

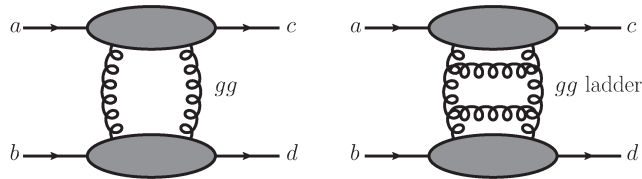


**Figure 2.9:** Two gluon (left) and gluon ladder exchange (right).

this thesis, typically do not provide a hard scale and are thus not amenable to this or other perturbative QCD approaches but only to Regge theory.

Nonetheless, (perturbative) QCD calculations at hard scales have implications also for the soft regime. In the context of this thesis, QCD constraints of the Regge trajectories are particularly interesting. While these are observed to be linear in the resonance region and also in the scattering region at small negative  $t$ , they obtain a hard lower bound from QCD [100–102]. The bound is approached from above [103]. The linearity can thus not continue to arbitrarily large negative  $t$ , and the trajectories must flatten. Indeed, it has been suggested that deviations from linearity might already be present around  $t \lesssim -1$  GeV in exclusive electroproduction of  $\rho^0$ ,  $\phi$ , and  $J/\psi$  vector mesons [93, 104].

The phenomenology of the *hard BFKL-Pomeron* is very different from the *soft Pomeron* that governs soft diffractive interactions. Typically, there is a much steeper energy dependence of the cross-sections and very little or no shrinkage of the forward peak with energy. This raises the question of whether the two Pomerons are really two phenomena of one single underlying dynamic or something different, entirely. In order to address this question from a theoretical standpoint, it is desirable to find a unified approach that allows describing both regimes in a single framework. A focus of these attempts typically lies on an understanding of the Pomeron trajectory. Simple approaches try to find the asymptotics in the hard scattering region ( $t \rightarrow -\infty$ ) and the glueball resonance region ( $t \rightarrow +\infty$ ), e.g., in classical strong potential ansatzes [93], and aim to interpolate between the regions; compare Figure 2.10.

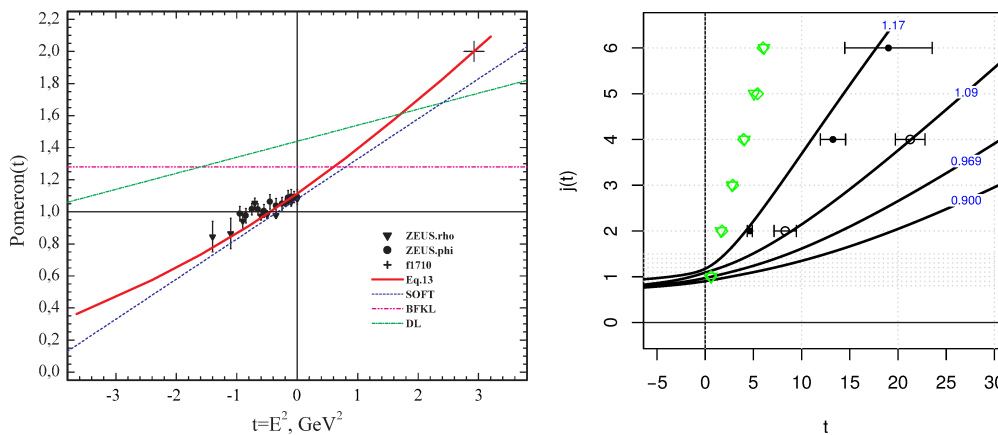


**Figure 2.10:** Pomeron trajectories extracted from a potential model (left) [93] and from a string theory approach (right) [105].

More comprehensive attempts to find a common description build on the idea that strongly interacting quantum field theories are dual to string theories on a suitable higher dimensional background space. This so-called AdS/CFT duality<sup>10</sup> [106–108] has been used to study the Pomeron trajectory [105, 109, 110]. In string theory, the Pomeron is associated with the graviton. Since that is a massless spin-2 particle, a priori the intercept of the Pomeron

<sup>10</sup>The duality between Anti-de-Sitter space, defined by the properties of the metric, and conformal field theories.

trajectory is at 2. However, it can be lowered by higher-order corrections to bring it into better agreement with the experimentally measured intercept close to 1. Trajectories extracted like that resemble the canonical linear Pomeron trajectory at large positive  $t$  and transition smoothly into a flat BFKL-like trajectory at large negative  $t$ . Qualitatively, they thus manage to connect the two regimes; compare Figure 2.10. However, the duality becomes invalid in the region of small negative  $t$  because confinement effects break the conformal symmetry. The exact structure of the transition can thus not be understood from such approaches.

### 2.2.4 Diffractive Dissociation

Another phenomenon of diffractive scattering that is relevant for this thesis is *diffractive dissociation* [111, 112]. Diffractive dissociation is an inelastic scattering process  $ab \rightarrow Y + b$  where one of the incoming particles,  $a$ , breaks up into a system of several particles  $Y$  which have typically the same quantum numbers as  $a$ . The characteristic kinematic variable of diffractive dissociation is the mass  $m_Y$  of the dissociative system. Cross-sections are then expressed double-differentially in  $t$  and  $m_Y$ .

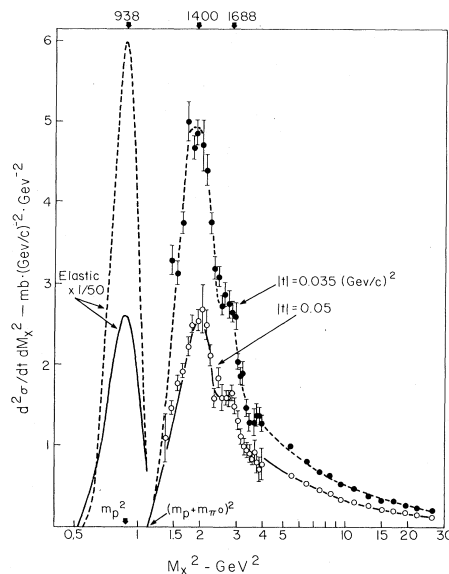


**Figure 2.11:** Double-differential proton-dissociative cross-section  $d^2\sigma(pd \rightarrow Yd)/dtdm_Y^2$  as a function of  $m_Y$  (labeled as  $M_X$  in the figure). Data is taken at a center-of-mass energy  $\sqrt{s} \simeq 10$  GeV and in two ranges of proton-momentum transfer  $t$  as labeled in the figure. Figure from [113]

For this thesis, in particular, dissociation of the proton target is of relevance. In Figure 2.11 the double-differential cross-section for proton-dissociative proton-deuteron scattering  $pd \rightarrow Yd$  is shown as a function of the dissociative mass  $m_Y$ . At low values, the cross-section exhibits multiple resonance peaks corresponding to excited proton states. At high values, the cross-section falls off continuously following an approximate  $1/m_Y^2$  behavior.

Several theoretical approaches aim to describe diffractive dissociation. For detailed reviews see Zotov and Tsarev [114], or Kaidalov [115], for example. The resonance region is often described in the optical analogy (*eikonal* models) as a partial absorption effect and the excitation of internal degrees of freedom. In the Good and Walker formalism [112] a physical state undergoing a diffractive scattering is described as a superposition of bare eigenstates of the interaction. These states are absorbed by the target in different ways. As a consequence, their composition is modified, which results in the apparent generation of new states in the scattering. The high mass continuum region can be understood in a Regge approach in so-called *triple Regge models*. A graphical illustration of the principle considerations

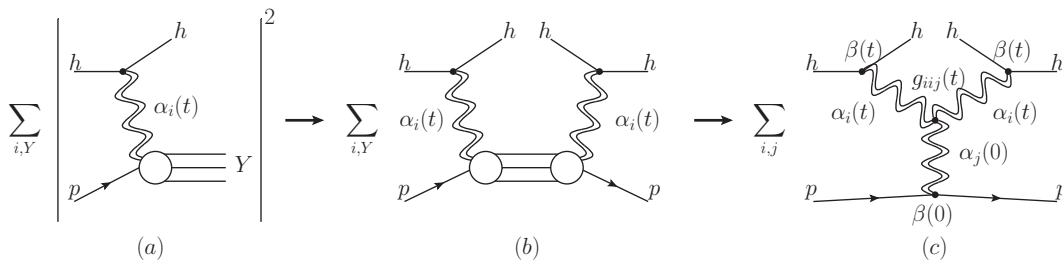


**Figure 2.12:** Illustration of the triple Regge approach to describe diffractive dissociation. The squared dissociative amplitude (a) is interpreted as  $s$ -channel resonance exchange (b) and replaced by the crossed  $t$ -channel Reggeon exchange diagram (c). Figure inspired by Reference [114].

underlying these models is given in Figure 2.12. The squared amplitude of diffractive dissociation scattering is interpreted as a sum over  $s$ -channel resonances. To reproduce the continuum spectrum, these are assumed to be manifold and wide. Using crossing-symmetry, the resonances can again be interpreted in terms of Reggeon exchange, giving rise to a triple Reggeon coupling. Considering only Pomeron contributions in the high-energy limit, the triple Reggeon diffractive cross-section can be written in the form [114]:

$$\frac{d^2\sigma}{dt dm_Y^2} \sim G_{\mathbb{P}\mathbb{P}\mathbb{P}}(t) s^{2\alpha_{\mathbb{P}}(t)-2} (m_Y^2)^{\alpha_{\mathbb{P}}(0)-2\alpha_{\mathbb{P}}(t)}, \quad (2.36)$$

where the coupling factor

$$G_{\mathbb{P}\mathbb{P}\mathbb{P}} \sim \beta^2(t) \beta(0) g_{\mathbb{P}\mathbb{P}\mathbb{P}}(t) \quad (2.37)$$

combines the particle-Pomeron and triple Pomeron couplings. The triple Pomeron coupling can be experimentally determined from measured dissociative spectra [115]. Equation 2.36 suggests factorization also holds for diffractive dissociation. As a consequence, the same energy dependence is expected for elastic and proton-dissociative amplitudes.

## Large Rapidity Gaps

In the QCD picture, a central feature of both elastic and dissociative diffractive scattering is that the exchange objects are color-singlets, i.e., there is no color flow between the scattering objects. As a consequence, a characteristic experimental signature of diffractive scattering events is the presence of *large rapidity gaps*<sup>11</sup> in the measured activity in a particle detector. In deep inelastic or hard interactions, on the contrary, color can flow between the scattering objects. Due to confinement, radiation and hadronization occurs along the color connection and populates the region between the scattering objects with new particles. The topology of the rapidity gaps gives insights into the diffractive scattering. Besides elastic and single-diffractive dissociation, there are further diffraction phenomena such as central diffraction, with topologies as illustrated in Figure 2.13.

The idea of large rapidity gaps to identify diffractive events has its limitations, though. There is a significant chance that the gaps are filled with secondary particles arising from additional soft interactions occurring in parallel to the diffractive exchange. This effect has to be taken into account in the form of a *rapidity gap survival probability*, which in practice is often very difficult to calculate. For electron-proton scattering, the survival probability is expected to be large and thus does not play a role in the present analysis.

<sup>11</sup>The rapidity is a measure for the polar coordinate in a particle detector. Typically the pseudorapidity  $\eta = -\ln[\tan(\theta/2)] \in (-\infty, \infty)$  is used with  $\theta$  being the polar angle coordinate.

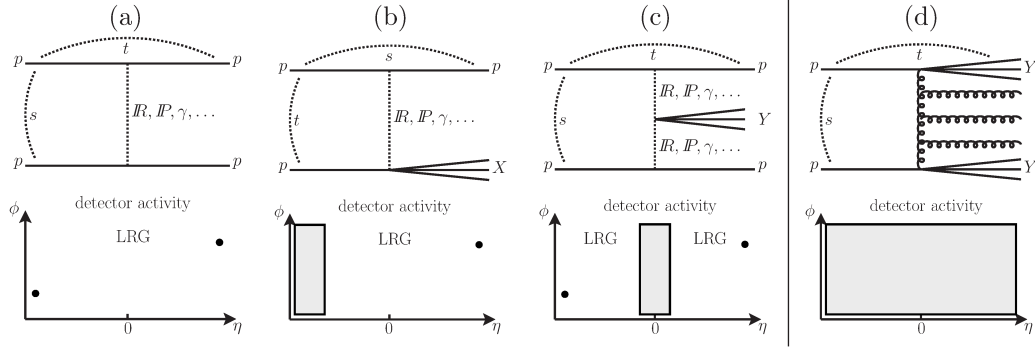


**Figure 2.13:** Basic types of diffractive two-particle scattering with the expected activity to be observed in a particle detector: elastic (a), single-diffractive dissociation (b), central diffraction (c), and non-diffractive (d). The diffractive types can be arbitrarily combined to form more complex topologies.

## 2.3 Photoproduction

Photon-hadron interactions are a special case of diffractive scattering interactions. As quantum-mechanical objects, photons can fluctuate into virtual quark-antiquark pairs. The time-scales over which these fluctuations exist are large enough to allow for the formation of (virtual) bound hadron states and the subsequent strong interaction with other hadrons [116]. These bound states can only be *vector mesons* such as the  $\rho^0(770)$ ,  $\omega(782)$ ,  $\phi(1020)$  mesons because they need to preserve the photon quantum numbers; namely a spin of one and negative parity and charge conjugation. Historically, this led to the modeling of the photon as a superposition of light vector mesons in so-called vector meson dominance (VMD) models [117].

The strong contributions dominate the total photon-hadron cross-sections which then behave

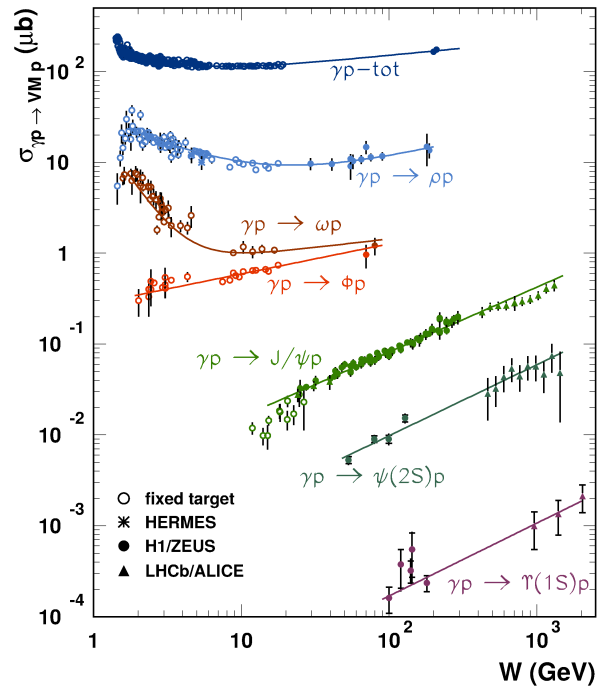


**Figure 2.14:** Vector meson photoproduction and total photon-hadron cross-sections as a function of the scattering energy  $W$ . Figure from [118].

largely like other hadron-hadron cross-sections [119]; compare also Figure 2.8. They are however suppressed by a factor  $1/\alpha_{em}$  compared to other hadron-hadron cross-sections from the coupling of the photon to the quark-antiquark pair. Through the scatterings, the virtual vector mesons can be pushed onto the mass shell and become real particles in the final state. Photon-hadron scatterings in which real vector mesons are produced are thus called *vector meson photoproduction*.

In Figure 2.14, an overview of various vector meson photoproduction cross-sections as a function of the scattering energy is given. The universality of the Pomeron trajectory breaks down for diffractive vector meson production. Possible explanations encompass contributions from the *hard* Pomeron in addition to the (universal) *soft* Pomeron characterized by Equation (2.32) [120, 121], or perturbative effects arising in the presence of a hard scale provided by the mass of heavy vector mesons.

### 2.3.1 $\pi^+\pi^-$ Photoproduction

Vector meson dominance can not be the complete picture of photon-hadron interactions. This can be well observed for the case of  $\pi^+\pi^-$  photoproduction that is studied in this thesis. At first glance,  $\pi^+\pi^-$  photoproduction is dominated by  $\rho^0$  resonance production with a subsequent decay into two charged pions. It also obtains smaller contributions from other vector mesons, such as the  $\omega$  or excited  $\rho'$  mesons. However, as first proposed by Söding [122], there must also be a significant non-resonant contribution. It is necessary for example to explain the difference in the lineshape of the  $\pi^+\pi^-$  mass distribution as it is measured in direct  $\rho^0$  resonance production in electron-positron annihilation compared to the lineshape observed in  $\pi^+\pi^-$  photoproduction.

More recent models consider all these contributions. So does the effective field theory approach proposed by Ewerz et al. [123] that is applied to  $\pi^+\pi^-$  photoproduction in Reference [124].

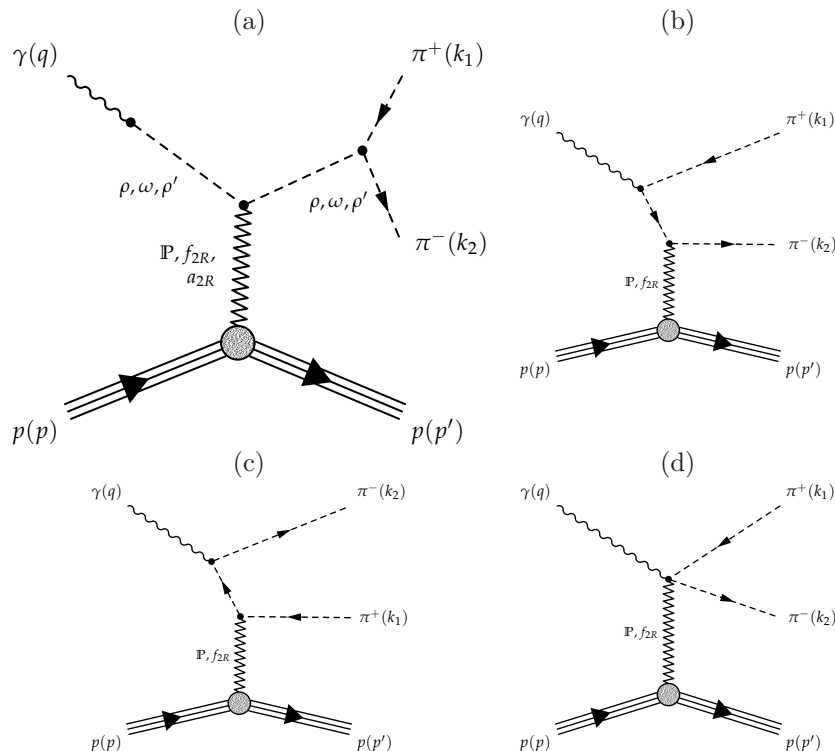


**Figure 2.15:** Diagrams for vector meson photoproduction (a), and non-resonant  $\pi^+\pi^-$  photoproduction (b-d) considered in the model by Ewerz et al. [123][124]. Figures from Reference [124].

Exemplary diagrams for vector meson and non-resonant  $\pi^+\pi^-$  photoproduction that are considered in the model amongst many others are shown in Figure 2.15. The invariant  $\pi^+\pi^-$  mass distribution predicted by the model is shown in Figure 2.16. In particular, the interference between resonant and non-resonant amplitudes results in the significant characteristic skewing of the  $\rho^0$  peak towards lower mass values.

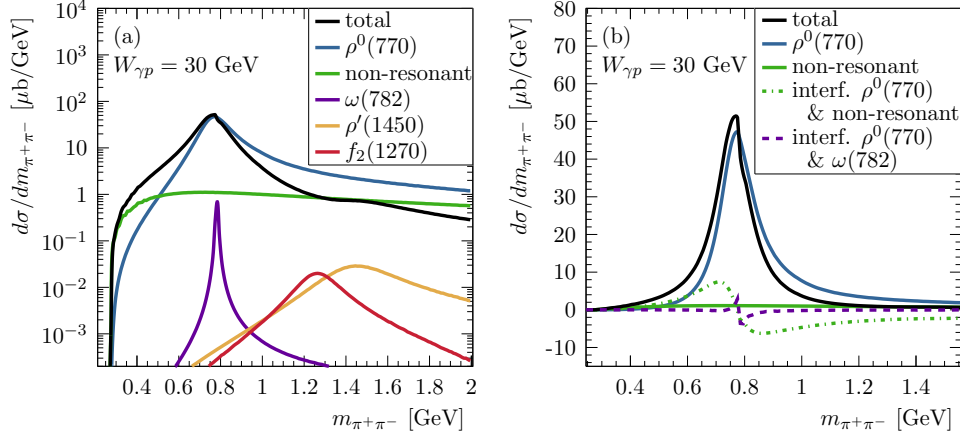


**Figure 2.16:** Differential cross-section  $d\sigma(\gamma p \rightarrow \pi^+\pi^- p)/dm_{\pi\pi}$  as a function of the invariant  $\pi^+\pi^-$  mass in the model by Ewerz et al. [123][124]. The left plot shows the individual resonant and non-resonant contributions considered in the model. The right plot illustrates the Söding mechanism which attributes the skewing of the  $\rho^0$  lineshape to an interference with non-resonant contributions. Figures from [124].

## 2.4 Diffractive Electron-Proton Scattering

The hadronic properties of the photon give rise to diffractive interactions in electron-proton scattering. Formally, they correspond to the reaction  $ep \rightarrow eXY$  with two distinct hadronic systems in the final state  $X$  and  $Y$ , which are separated by a large rapidity gap.  $X$  then is the distinct photon, and  $Y$  the proton remnant, such that for elastic scattering  $Y = p$  is the elastically scattered proton. A generic diagram for a diffractive  $ep$ -scattering in the Regge picture is depicted in Figure 2.17.

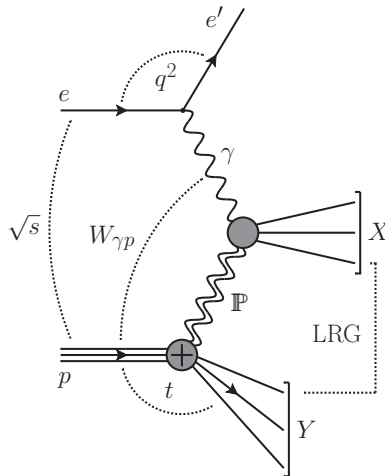


**Figure 2.17:** Diffractive electron-proton scattering.

### Kinematic Variables in $ep$ Scattering

The four-momenta of the incoming (outgoing) electron and proton are denoted with  $e$  ( $e'$ ) and  $p$  ( $p'$ ), respectively,  $k$  is the four-momentum of the system  $X$  and  $q = (e - e')$  the four momentum of the photon. Five Lorentz-invariant variables are then used to describe the kinematics of diffractive  $ep$  scattering:

- the *photon-virtuality*  $Q^2$ , i.e., the momentum transfer at the electron vertex (by convention,  $Q^2$  is defined to be positive):

$$Q^2 = -q^2 = (e - e')^2, \quad (2.38)$$

- the *photon-proton center-of-mass energy*  $W_{\gamma p}$ :

$$W_{\gamma p} = (q + p)^2, \quad (2.39)$$

- the *momentum transfer at the proton vertex*  $t$ :

$$t = (p - p')^2, \quad (2.40)$$

- the *mass of the photon remnants*  $m_X$ :

$$m_X^2 = k^2, \quad (2.41)$$

- and the *mass of the proton remnants*  $m_Y$ :

$$m_Y^2 = (p')^2. \quad (2.42)$$

In particular, in the context of diffractive  $ep$  interactions  $W_{\gamma p}$  takes over the role of the hadron-hadron center-of-mass energy.

Further relevant variables regularly used in the context of  $ep$  scattering are

- the *electron-proton center-of-mass energy*

$$s = (e + p)^2, \quad (2.43)$$

- the *inelasticity*  $y$ , i.e., the fraction of the electron's energy carried by the photon:

$$y = \frac{q \cdot p}{e' \cdot p}, \quad (2.44)$$

- and the *Bjorken scaling variable*  $x$ :

$$x = \frac{Q^2}{2q \cdot p'}. \quad (2.45)$$

They are related to the other variables by the equations:

$$Q^2 = xys, \quad (2.46)$$

and

$$W_{\gamma p} = ys - Q^2 - m_Y^2. \quad (2.47)$$

The photon virtuality is used to distinguish two distinct kinematic regimes. In *photoproduction*  $Q^2 \simeq 0 \text{ GeV}^2$  and a quasi-real photon interacts with the proton. Real photoproduction is not accessible in  $ep$  collisions as  $Q^2$  is kinematically constrained to [125]:

$$Q^2 > Q_{\min}^2 \simeq \frac{m_e^2 y^2}{1 - y}. \quad (2.48)$$

However,  $Q_{\min}^2$  typically is negligibly small. In the kinematic range of the present photoproduction analysis  $Q_{\min}^2 \sim 10^{-12} \text{ GeV}^2$ . Events with large  $Q^2 \gg 0 \text{ GeV}^2$  are then referred to as *deep inelastic scattering* (DIS) and production of vector mesons in DIS called *electroproduction*. In an experimental context, the definition of the two kinematic regimes is often loosened. In the context of this thesis, photoproduction refers to the regime  $Q^2 \lesssim 2.5 \text{ GeV}^2$ .

### The Electron as a Photon Source

In this analysis, a priori an electron-proton cross-section  $\sigma_{ep}$  is measured. However, in the context of diffractive scattering, the photon-proton cross-section  $\sigma_{\gamma^*p}$  is of interest. By interpreting the electron as a photon source emitting a flux of photons  $\Phi_{\gamma/e}$ , the electron-proton cross-section can be expressed in terms of the photon-proton cross-section:

$$\sigma_{ep} = \int_y \int_{Q^2} \sigma_{\gamma^*p}(W^2, Q^2) \Phi_{\gamma/e}(y, Q^2) dy dQ^2. \quad (2.49)$$

As the emitted photons are virtual, they can in particular also be longitudinally polarized. Introducing a longitudinal (superscript  $L$ ) and transverse (superscript  $T$ ) cross-section, Equation (2.49) can be decomposed into:

$$\sigma_{ep} = \int_y \int_{Q^2} \left( \sigma_{\gamma^*p}^T(W^2, Q^2) \Phi_{\gamma/e}^T(y, Q^2) + \sigma_{\gamma^*p}^L(W^2, Q^2) \Phi_{\gamma/e}^L(y, Q^2) \right) dy dQ^2. \quad (2.50)$$

In the *equivalent photon* or *Weizsäcker-Williams* approximation [126–129], the flux of both transversely and longitudinally polarized photons can be calculated:

$$\Phi_{\gamma/e}^T(y, Q^2) = \frac{\alpha_{em}}{2\pi} \frac{1}{yQ^2} \left( 1 + (1-y)^2 - 2m_e^2 \frac{y^2}{Q^2} \right) \quad (2.51)$$

$$\Phi_{\gamma/e}^L(y, Q^2) = \frac{\alpha_{em}}{\pi} \frac{1}{yQ^2} (1-y). \quad (2.52)$$

It is particularly noteworthy that the photon-flux decreases steeply with  $1/Q^2$  and the longitudinal component vanishes for  $y \rightarrow 1$ .

For the photoproduction regime studied in this thesis  $\sigma_{\gamma^*p}^L(W^2, Q^2)$  vanishes as  $Q^2 \rightarrow 0 \text{ GeV}^2$  and only the transverse component of Equation (2.50) is of relevance. Photoproduction cross-sections are then approximated for average center-of-mass energy  $\langle W_{\gamma p} \rangle$  and virtuality  $\langle Q^2 \rangle$  by normalizing the measured electron-proton cross-section by the integrated photon flux:

$$\sigma_{\gamma p}(\langle W_{\gamma p} \rangle, \langle Q^2 \rangle \simeq 0 \text{ GeV}^2) \simeq \frac{\sigma_{ep}}{\Phi_{\gamma/e}^{\text{int}}}, \quad (2.53)$$

with

$$\Phi_{\gamma/e}^{\text{int}} = \int_{y_{\text{min}}}^{y_{\text{max}}} \int_{Q_{\text{min}}^2}^{Q_{\text{max}}^2} \Phi_{\gamma/e}^T(y, Q^2) dy dQ^2. \quad (2.54)$$

It should be kept in mind that Equation (2.53) is only an approximate inversion of Equation (2.50) and only valid for (infinitesimally) small  $Q^2$  and  $y$ , i.e.,  $W_{\gamma p}$ , intervals.

## 3 HERA AND THE H1-DETECTOR

The measurement presented in this thesis is based on  $ep$  collision data recorded by the H1 experiment at the HERA collider. The collider is briefly described in Section 3.1 followed upon by an overview of the main H1 detector in Section 3.2. The H1 components most relevant to the analysis are described in more detail. Those are the central tracking detector (Section 3.2.1), the calorimetry system (Section 3.2.2), and the forward detectors (Section 3.2.3). The H1 trigger is described in Section 3.3. The luminosity measurement explained in Section 3.4.

### 3.1 The HERA Collider

The HERA (Hadron Elektron Ring Anlage) was a high-energy particle collider at the DESY (Deutsches Elektronen Synchrotron) laboratory in Hamburg, Germany. In a unique setup, HERA combined a proton and an electron synchrotron storage ring within a single, 6.3 km long tunnel. The full HERA machine, including pre-accelerator structures, is illustrated in Figure 3.1.

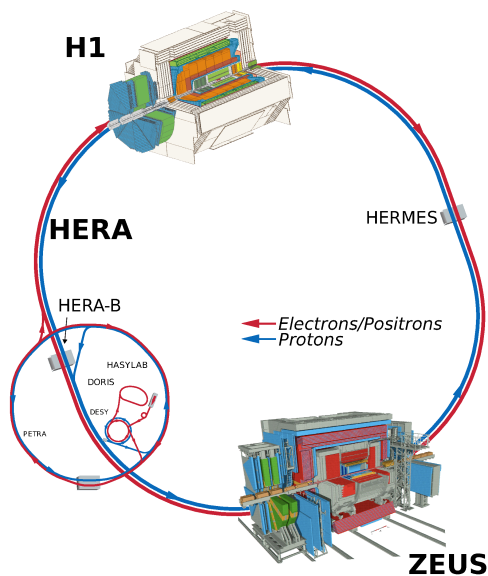


**Figure 3.1:** HERA and its pre-acceleration facilities. The positions of the H1 and ZEUS detectors is indicated by the respective detector drawings (not to scale). Figure provided by DESY [130] and adapted.

HERA's electron machine provided two operation modes to accelerate beams of either electrons or positrons<sup>1</sup> to an energy of 27.5 GeV. In the proton machine, proton beams circulating in the opposite direction could be brought to energies up to 920 GeV. The beams were collided at a center-of-mass energy of up to  $\sqrt{s} = 318$  GeV at two interaction points. The HERA machine was operated from 1992 until 2007. Over the turn of the century, it received a major luminosity upgrade for the HERA-II running period. The key design parameters of the HERA-II machine are summarized in Table 3.1.

<sup>1</sup>In the following, the word "electron" is used for both electrons and positrons indiscriminately.

	proton beam	electron beam
energy [GeV]	$\leq 920$	27.5
number of bunches total/colliding	180/174	180/174
particles per bunch	$10 \cdot 10^{10}$	$4.2 \cdot 10^{10}$
beam current [mA]	140	58
beam size $\sigma_x \times \sigma_y$ [ $\mu\text{m} \times \mu\text{m}$ ]	$118 \times 32$	$118 \times 32$
bunch spacing [ns] / bunch crossing rate [Mhz]	96 / 10.4	
luminosity [ $\text{cm}^{-2}\text{s}^{-1}$ ]	$7.36 \cdot 10^{31}$	
specific luminosity [ $\text{cm}^{-2}\text{s}^{-1}\text{mA}^{-2}$ ]	$1.64 \cdot 10^{30}$	
total integrated luminosity (2004-2007) [ $\text{pb}^{-1}$ ]	645 [131]	

**Table 3.1:** HERA-II design parameters given by the H1 Collaboration [132].

The HERA's electron-proton scattering events were recorded by two large, multi-purpose detectors built around the two interaction points: H1 and ZEUS. To this day, the collected data is used to study a wide range of particle physics' questions. The investigation of the internal structure and dynamics of the proton stands at the core of the physics program. The main legacy of the HERA experiment is the precise measurement of the parton distribution functions [133]. However, H1 and ZEUS also contributed to a better understanding of many other topics. They provided for example measurements of the scale dependence of the strong coupling constant over a wide energy range [134], found first direct evidence for electroweak unification [135, 136], and gave insights into the hadronic structure of the photon and hadronic scattering at high energies. It is to the latter topic where this thesis aims to contribute. The complete lists of H1 and ZEUS publications can be found at Refs. [137–139].

In addition to H1 and ZEUS, HERA also accommodated two fixed target experiments: In HERA-B [140], the proton beam was collided with various targets to study b-hadron decays. In HERMES [141], the electron beam was scattered off target nuclei from various elements to study their respective spin structures.

## 3.2 The H1 Detector at HERA

This analysis is based on data taken with the H1 detector during the HERA-II phase. H1 is a multi-purpose detector covering almost the full  $4\pi$  solid angle. At a size of  $12 \times 10 \times 15 \text{ m}^3$ , it weighs around 2800 tons. It consists of three main subsystems for tracking, calorimetry, and muon detection that are each built from various subdetectors. The asymmetry in the electron and proton beam energies is reflected in an asymmetric detector design. A schematic drawing of the detector in its HERA-II configuration is given in Figure 3.2.

The coordinate system used by H1 has its origin at the nominal interaction point (IP). The right-handed system is defined with the  $z$ -axis pointing *forward* in the flight direction of the protons and the  $x$ -axis pointing towards the center of the HERA ring. The  $y$ -axis then points upwards. In spherical coordinates the polar angle  $0 < \theta < 180^\circ$  is defined with respect to the  $z$ -axis such that  $\theta = 0^\circ$  corresponds to the proton beam direction. The azimuthal angle  $-180^\circ < \phi < 180^\circ$  in the  $xy$ -plane is defined such that  $\phi = 0^\circ$  corresponds to the  $x$ -axis. Alternatively to the polar angle  $\theta$ , often the *pseudorapidity*  $\eta$  is used, which is defined as:

$$\eta = -\ln \left[ \tan \left( \frac{\theta}{2} \right) \right] \quad (3.1)$$

and covers a range from  $\eta = \infty$  for  $\theta = 0^\circ$  to  $\eta = -\infty$  for  $\theta = 180^\circ$  with  $\eta = 0$  for  $\theta = 90^\circ$ .

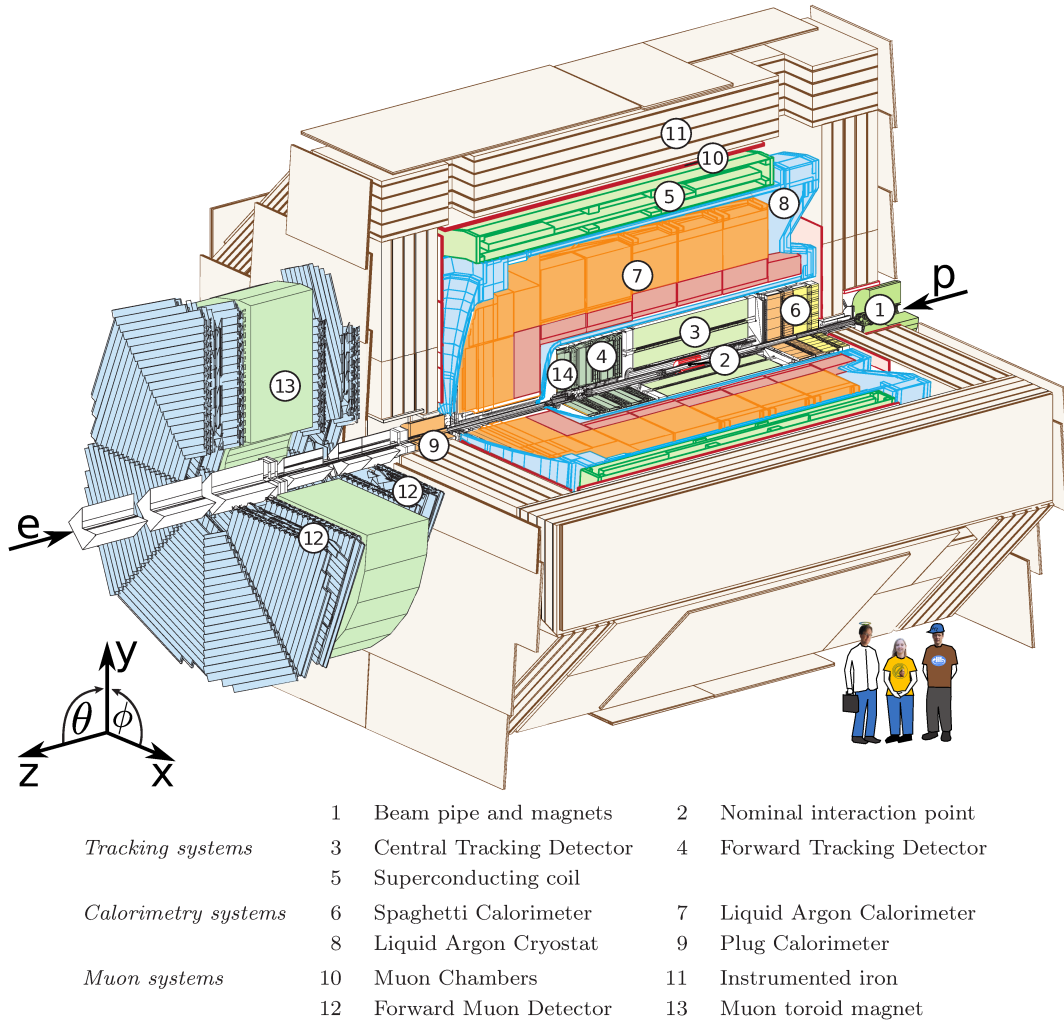


**Figure 3.2:** Illustration of the H1 detector based on the GEANT detector simulation. The detector is built from various subcomponents that are arranged in the typical onion structure. The most relevant components are labeled in the figure. The forward-backward asymmetry of the detector is reflective of the asymmetric beam configuration. In the used right-handed coordinate system the proton enters in positive  $z$ -direction and the  $x$ -axis points towards the center of the HERA-accelerator as illustrated by the arrows. Average sized scientists are shown for scale. Some detector systems are not included in the figure because they are placed far up and down the beam-pipe. Among those are for example the luminosity system, proton taggers and spectrometers, and others. Image provided by the H1 Collaboration and modified.

The innermost part of the H1 detector is occupied by a tracking system built directly around the IP. The tracking system is further subdivided into a Central Tracking Detector (CTD), a Forward Tracking Detector (FTD), and the Backward Proportional Chambers (BPC). The trackers are surrounded by calorimeters: the backward region is covered by the Spaghetti Calorimeter; the forward and central region by the Liquid Argon Calorimeter. The coverage in the forward direction is further increased by a Plug calorimeter. The tracking and calorimetry systems are embedded into a uniform axial-symmetric magnetic field of 1.15 T. The field is provided by a superconducting solenoid magnet built around the calorimeter. The iron return yoke outside of the solenoid is instrumented with streamer tube detectors for muon detection. Additional dedicated muon detectors are installed in the forward direction.

Auxiliary systems, e.g., for proton tagging or the luminosity measurement, are placed further up- and down-stream of the nominal interaction point and not included in Figure 3.2. A detailed description of the H1 detector is provided in Refs. [142, 143]. This analysis relies on the CTD for precise tracking, the calorimetry system, various forward detectors, and the luminosity system. They are described in more detail in the following sections.

### 3.2.1 The H1 Central Tracking Detector

The H1 central tracking system covers the full azimuthal angle and a range of roughly  $20^\circ < \theta < 160^\circ$  in the polar plane<sup>2</sup>. A detailed view of the inner part of the H1 detector in the polar plane, as well as a transverse view of the CTD are given in Figure 3.3.

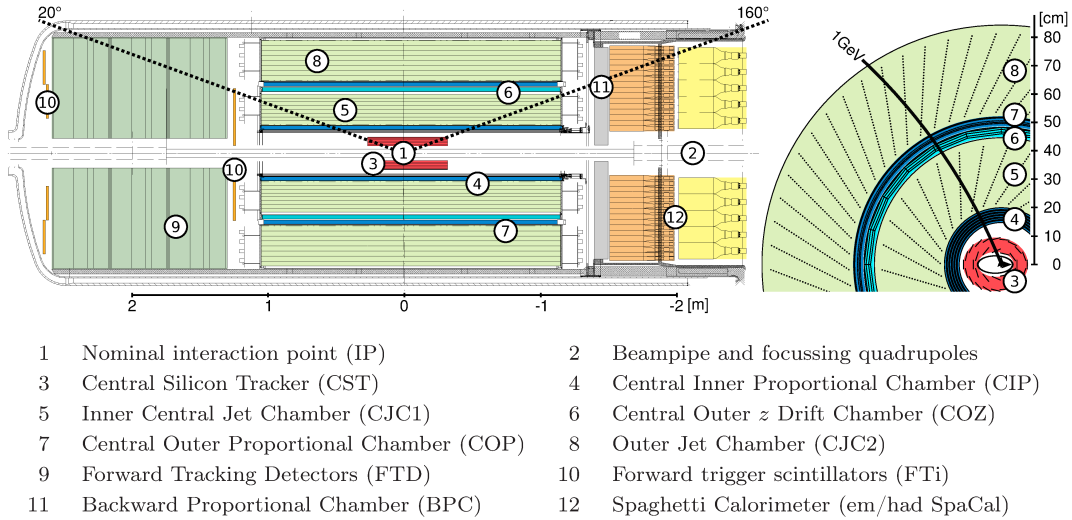


**Figure 3.3:** Left: Inner part of the H1 detector. Right: Transverse view of one quadrant of the CTD. Images provided by the H1 collaboration and modified.

As illustrated, the CTD consists of several components within a radius of roughly 90 cm. The innermost component is a silicon strip detector build closely around the beam pipe at a radius of  $r = 4$  cm. This Central Silicon Tracker (CST) [144, 145] provides high spatial resolution for a precise reconstruction of the primary vertex of an interaction and secondary decay vertices of long-lived particles. Around the CST, the Central Inner Proportional (CIP) chamber provides some very fast tracking and timing information. Built around the CIP, the two large Central Jet Chambers (CJC) are the backbone of the H1 tracking. They provide precise tracking information, in particular in the transverse plane. To improve the  $z$ -position information for tracking, the CJCs are supported by the Central Outer  $z$ -Drift Chamber (COZ) placed in between them. A second proportional chamber is placed around the COZ but is not used at all for the analysis.

#### The Central Inner Proportional Chamber

The CIP is a multiwire proportional chamber [146]. It provides fast tracking and timing information. In particular, it allows reconstructing the  $z$ -vertex position of an interaction at trigger level. The chamber is built from 5 radial layers with the innermost being placed at  $r \simeq 15$  cm and the outermost at  $r \simeq 20$  cm. 16 azimuthal segments cover the full circle. Along the  $z$ -axis it extends from  $z = -112.7$  cm up to  $z = 104.3$  cm. The CIP's 9600 readout pads are positioned in a *projective geometry*, as is illustrated in Figure 3.4. In this geometry,

<sup>2</sup>Further tracking is provided by the CTD in the forward direction ( $7^\circ < \theta < 20^\circ$ ) and the BPC in backward direction ( $160^\circ < \theta < 175^\circ$ ).

all tracks that originate from the same  $z$ -position produce the same hit pattern in the radial layers. The pattern is only shifted by a constant number of pads for different track  $\theta$ .

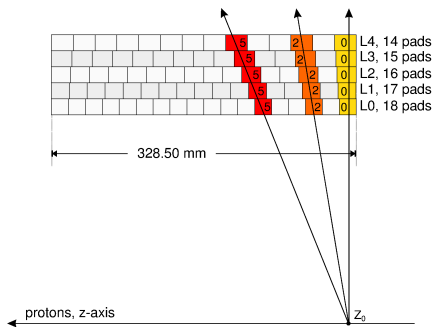


**Figure 3.4:** Projective geometry of the CIP. Tracks originating from the same position along the  $z$ -axis create the same hit pattern. The pattern is shifted along the  $z$ -axis by a constant number of pads depending on the track  $\theta$ . Figure from Urban [147] and adapted.

### The Central Jet Chambers

The Central Jet Chambers [148] are two large, concentric drift chambers that are used to track charged particles. The geometries of the two chambers are specified in Table 3.2. The chambers are filled with an argon and ethane based gas mixture. In the transverse plane, the inner CJC1 is segmented into 30, the outer CJC2 into 60 *drift cells* as is illustrated in Figure 3.3. The boundary planes of the cells are tilted by  $30^\circ$  with respect to the radial direction. They are formed by cathode wires strung parallel to the  $z$ -axis. Centrally in each drift cell 24 (CJC1) or 32 (CJC2) anode wires are strung parallel to the cathode wires. By applying a high voltage to the cathode wires, a static electric field is created inside of the drift cells. In this field, charge carriers that are ionized when a charged particle traverse the gas volume drift to the anode and cathode wires. The field is further shaped to optimize the drift behavior by adding additional potential wires to the cells. In the CJCs the electrostatic field is superimposed by the magnetostatic field from the solenoid. The electrostatic field is shaped such that the isochrones of the combined fields, i.e., the lines of constant field strength, form circles in the near field around the anode wires. The charge carriers then always drift to the closest wire. The Lorentz angle of that configuration, i.e., the angle between the drift direction in the superimposed electric and magnetic field and the field lines of the electric field alone, is approximately  $25^\circ$ . The tilt of the drift cells goes in the opposite direction to the Lorentz angle so that charge carriers ionized by a straight high  $p_T$  track always drift perpendicular to the track. The isochrones in a drift cell and the drift behavior of charge carriers are illustrated in Figure 3.5.

	CJC1	CJC2
number of cells	30	60
number of sense wires/cell	24	32
inner radius [cm]	20.3	53.0
outer radius [cm]	42.6	84.4
active radius [cm]	22.5	29.6
$z$ -min [cm]		-112.5
$z$ -max [cm]		+107.5

**Table 3.2:** CJC geometry as described by Burger et al. [148].

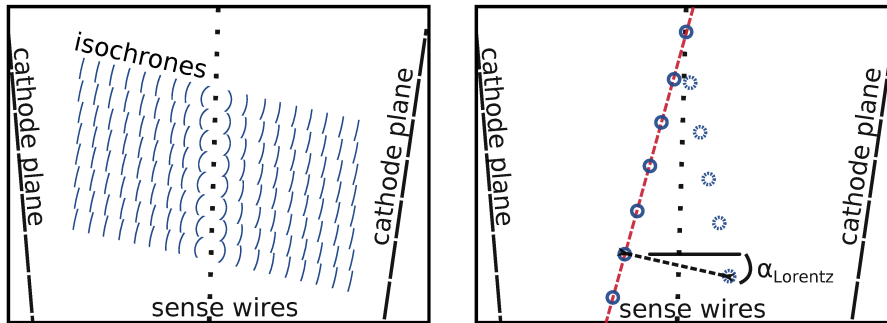


**Figure 3.5:** Schematic structure of a CJC drift cell constructed from cathode planes and anode wires. Additional potential wires that are present in the actual cells are not shown. The drawings illustrate the isochrones of the combined electro- and magnetostatic field (left) and the drift behavior of charge carriers (right). Charge carriers drift to the closest anode wire along a direction perpendicular to the track. Real charges can not be distinguished from mirror charges. Figure provided by Bolz [149].

The anode wires in the CJCs are used as sense wires and the signals induced in them by the drifting charge carriers are read out. A measurement of the drift times can be combined with the precise knowledge of the drift behavior of free charge carriers in the field to calculate the *hit* position of an ionization in the  $r\phi$ -plane. The achievable transverse hit resolution is about  $160\ \mu\text{m}$ . However, with the given field configuration, it can not be distinguished whether a hit occurred on the left or right side of the anode wire. Hits thus always come with a mirror hit as is illustrated in Figure 3.5. While traversing the jet chambers, a charged particle produces multiple hits. This allows reconstructing the associated track as is described further down in the text. The left-right ambiguity of hits within a single drift cell can be resolved for tracks crossing a cell boundary<sup>3</sup>. The  $30^\circ$  tilt of the drift cells ensures that a straight track always crosses at least two cells. In addition, a straight track also crosses at least one anode plane. Hits produced close to the crossing point have the shortest drift times. The minimum drift time of an associated hit is used to measure the timing of a track with a resolution of  $\sim 2\ \text{ns}$ . This allows in particular to distinguish tracks originating from different bunch crossings.

The  $z$ -positions of hits can also be measured with the CJCs. For this, the anode wires are read out at both ends. The total charge induced in the wire by a hit is divided between both ends. The further a hit is away from the wire end, the weaker is the fraction of the signal that is read out there. However, the available  $z$ -resolution is limited to  $2 - 8\ \text{cm}$  depending on the total induced charge. The  $z$ -information from the CJCs is combined with the hits measured by the COZ for an improved measurement of the  $z$ -position of tracks,

### Track Reconstruction

Charged particles in the central detector are bent onto circular trajectories in the transverse plane by the H1's solenoidal magnetic field  $B$ . The  $z$ -momentum component is not affected so that the particles travel on a helix trajectory in three dimensions. The helix can be described by a set of 5 parameters: These are in the transverse plane the curvature  $\kappa$ , the radial distance of closest approach to the IP  $d_{ca}$  and the azimuthal angle  $\phi_0$  at the point of closest approach to the IP. In the  $rz$ -plane, they are the  $z$ -position at the point of closest approach to the IP and the polar angle  $\theta$ .  $\kappa$  is the inverse of the bending radius  $R$  and thus varies with the transverse momentum of a particle:

$$\kappa = 1/R = \frac{zeB}{p_T} \quad (3.2)$$

<sup>3</sup>In fact, the anode wires are positioned in a *staggering* scheme, i.e., wires are alternatively shifted by  $\pm 150\ \mu\text{m}$  away from the nominal plane. This already helps to resolve the ambiguity within a single cell.

where  $ze$  is the charge of the particle. For the field configuration in the H1 detector, the bending radius for a track with  $p_T = 1$  GeV is approximately 3 m. A corresponding track is illustrated in Figure 3.3.

From the hits left by a charged particle along its trajectory, the helix, i.e., the particle track can be reconstructed. The track reconstruction starts by first finding and then fitting all tracks in an event. For an improved track reconstruction then further corrections might be applied. The cornerstones of the track reconstruction are:

- **Track Finding:**

The track finding algorithm aims to identify tracks from all hits in the jet chambers. In a first step, a pattern recognition algorithm tries to identify hit triplets from adjacent or next-to-adjacent wires. The triplets are then fitted in the transverse plane with a circle going through the nominal beam-axis to extract approximate values for  $\kappa$  and  $\phi_0$ . Triplets from a single track give similar values for  $\kappa$  and  $\phi_0$  and thus cluster in the  $\kappa\phi$ -plane. Based on this clustering, triplets are merged in an iterative procedure and the fits are repeated. Small deviations from the helix trajectory, e.g., because of multiple scattering with the detector material are considered by performing a *broken-lines fit* [150]. Once outlier hits are rejected and the beam-axis constraint is released, a final track fit provides a set of *non-vertex-fitted* tracks with parameters  $\kappa$ ,  $\phi_0$  and  $d_{ca}$ . In a second step,  $z_0$  and  $\theta$  for a given track are obtained from a straight-line fit in the polar plane.

- **Vertex Fit:**

Tracks from a single scattering event originate from the same primary vertex. This can be used as a constraint to improve the track fits and resolution. The  $z$ -vertex position varies strongly from event to event. A provisional value is determined from the weighted mean of the measured  $z_0$  values of the non-vertex-fitted tracks. The beam position in the transverse plane only changes little over time and is thus averaged over many events. However, the actual beams are slightly tilted with respect to the H1 coordinate system so that the actual  $x$ - and  $y$ -vertex positions need to be corrected for the measured  $z$ -vertex. All tracks are then individually refitted in the transverse plane using the calculated vertex as a constraint. Finally, the new track parameters are used for a common  $z$ -vertex fit with all tracks. The vertex-refitting procedure is repeated iteratively with the fitted  $z$ -vertex if necessary.

- **Energy Loss Corrections and Particle Identification:**

Particles can lose a significant amount of energy in interactions with the material in front of or in between the two jet chambers. To improve the fitted track parameters, the material is modeled in detail, and the energy loss is corrected for. The ionization energy loss  $dE/dx$  in the CJC can directly be measured. It is described by the Bethe-Bloch-Formula and in particular, depends on the velocity of the charged particle [1]. Together with the momentum measurement, this allows to identify the mass and thus type of low-momentum particles. The energy loss corrections and the  $dE/dx$  measurement for particle identification in the CJC are described in more detail by Berger [42], for example.

All details on the track fitting procedure can be found on the H1 Tracking Group homepage [151].

### 3.2.2 The H1 Calorimetry System

The H1 calorimetry system provides precise energy measurements of individual particles and jets. It is composed of the Liquid Argon (LAr) and Spaghetti Calorimeter (SpaCal). Both consist of an electromagnetic section surrounded by a hadronic section. To perform the energy measurement incident particles are stopped in the calorimeters and their energy deposition is turned into an electronic signal.

### The Liquid Argon Calorimeter

The Liquid Argon Calorimeter [152] covers the full azimuthal angle and a range  $4^\circ < \theta < 154^\circ$  in the polar plane. It is a *sampling calorimeter* consisting of alternating layers of passive and active material. The passive layers are made from high  $Z$  materials which facilitate the generation of cascades of secondary particles (*showers*) from the incident particle. Lead absorber plates are used for the electromagnetic part of the calorimeter. They add up to a total of 20 to 30 radiation lengths. In the hadronic part, plates of stainless steel are used. For the active material, argon is cooled down to 90 K to liquefy. The liquid argon is contained in a large vessel that the whole calorimeter is submerged in. Charged particles ionize the liquid argon and a signal is measured by collecting the ionization charge. The whole calorimeter is subdivided into 45 000 individual calorimeter cells. For reconstruction, the energy deposits above noise from neighboring cells are grouped into energy *clusters* [153].

The LAr is a *non-compensating* calorimeter with a different response to electromagnetically induced particle showers as compared to hadronic showers. For electromagnetic showers, the deposited energy is proportional to the total collected charge. Electromagnetic clusters can thus easily be calibrated. For hadronic showers, a significant fraction of the energy deposit is invisible to the charge collection, e.g., because it is used to free nucleons from nuclei in hadronic interactions or carried by invisible neutrinos within the shower. A complex software compensation and energy calibration are applied to recover the missing energy fraction [154]. The energy deposits in each of the cells contributing to a shower are calibrated separately. The fine granularity of the LAr cells allow to distinguish electromagnetic and hadronic subcomponents of a hadronically induced shower and calibrate them accordingly.

### The Spaghetti Calorimeter

The Spaghetti Calorimeter [155] covers the backwards region in a range  $153^\circ < \theta < 177.5^\circ$ . It consists of an electromagnetic and a hadronic section, that are both made from lead absorbers interlaced with scintillating fibers. The lead absorbers correspond to a total of 28 radiation lengths. Similar to the LAr, they initiate the cascading decay of incoming particles. Secondary particles can then be counted using the scintillation signals they produce in the fibers. The 2340 fibers in the SpaCal are grouped into  $4 \times 4$  cm<sup>2</sup> cells whose combined light output is read out by a photo-multiplier tube. The SpaCal's main purpose is the precise measurement of the energy and scattering angle of the scattered electron in interactions with medium momentum transfer at the electron vertex ( $Q^2 \sim 2 - 100$  GeV<sup>2</sup>).

## 3.2.3 H1 Forward Instrumentation

The H1 detector is equipped with forward detectors that are essential for diffractive analyses. For this analysis, the forward region of the LAr calorimeter is used both on trigger and analysis level to select events with a *large rapidity gap* (LRG) between the scattered proton and the centrally produced diffractive system. This ensures the diffractive nature of the selected processes. On trigger level, the LRG requirement is also ensured by the forward scintillator wall FTi2.

Furthermore, several forward detectors are used to tag proton-dissociative events on analysis level. Those are the Plug Calorimeter, the Forward Muon Detectors (FMD), and the Forward Tagging Stations (FTS). H1 is also equipped with spectrometers to reconstruct the elastically scattered proton, but they cover only a very limited acceptance region and are thus not used for this analysis<sup>4</sup>.

<sup>4</sup>E.g., the H1's Very Forward Proton Spectrometer (VFPS) requires a fractional proton momentum loss  $1 - E_{p'}/E_p \gtrsim 0.008$  to detect the elastically scattered proton [156]. For centrally produced  $\rho^0$  mesons that are studied here, a typical value is  $1 - E_{p'}/E_p \sim 0.0004$ .

### Forward Veto Counters

H1 is equipped with two scintillator rings placed in front of and behind the FTD; compare Figure 3.3. According to Berger [42], the first ring (FTi1), which is placed between the central and forward trackers has never been operational. The second ring (FTi2) is placed between forward tracker and LAr and used in the H1 trigger as a veto for non-diffractive events. Unfortunately, it appears that the technical drawings of the scintillators and with them the knowledge of their precise position in the detector are lost. One particular consequence of this is that the scintillators are not included in the detector simulation.

### The Plug Calorimeter

The plug calorimeter consists of a lead absorber followed by four scintillator layers. It covers the pseudorapidity range  $3.5 < \eta < 5.5$  and can be used to tag proton-dissociative events on analysis level.

### The Forward Muon Detector

The Forward Muon Detectors are positioned outside of the iron return yoke and in front of the main H1 detector. Meant primarily for the detection of forward muons, it covers a range of  $1.9 < \eta < 3.7$ . The detector consists of six double-layer drift chambers that allow the measurement of  $\phi$  and  $\theta$  hit coordinates. A toroid magnet between the third and fourth chamber provides bending strength necessary for momentum measurements. For this analysis, the first three chambers are used parasitically for tagging proton-dissociative events. Particles from the dissociative system which are scattered under small angles can hit the beampipe or one of several collimators that are placed inside of it to protect the central detector from synchrotron radiation. Secondary particles produced in these interactions can reach the FMD and produce a signal. The effective acceptance of the CMD can thus be lowered to  $\eta \simeq 6.5$  for tagging proton-dissociative events [157].

### The Forward Tagging System

The Forward Tagging System consists of four scintillator stations positioned around the proton beam pipe at  $z = 26$  m,  $z = 28$  m,  $z = 53$  m, and  $z = 92$  m. Generally, only the two closest stations are useful for tagging proton-dissociative events because elastically scattered protons often hit the beampipe and produce secondary particles that imitate the proton-dissociative signature in the far-away stations. The station at  $z = 26$  m was not fully operational during the considered run periods. For this analysis, thus only the station at  $z = 28$  m is used to tag proton-dissociative events. It covers a range of approximately  $6.0 < \eta < 7.5$ .

## 3.3 The H1 Trigger System

The bunch crossing rate at HERA is 10.4 MHz giving rise to an event rate of a similar magnitude. At the same time, the H1 detector can only be read out completely at a rate of roughly 50 Hz. Storing data permanently on tape is then only possible for 10 to 20 events per second. The data rate thus needs to be reduced by a factor of roughly one million in a short amount of time. This is achieved by the H1 Central Trigger (CT), an event filter operating in four levels.

At the first trigger level (L1 [158]) dedicated hardware operates on a small subset of signals produced by the H1 detector to generate a trigger signal. In parallel, various algorithms scan the signals from different sub-detectors for *interesting* event signatures such as muon tracks

in the muon systems, large energy deposits in the calorimeter or specific track topologies in the central tracker. From this information, 256 individual Trigger Elements (TEs) are derived. They are combined by the Central Trigger Logic (CTL) via logical AND and OR operations to 128 raw L1 subtriggers. If a subtrigger condition is met, the second stage of the trigger system is initiated. Some subtriggers with a particularly high rate are artificially scaled down by a factor  $n$  so that only every  $n$ -th occurrence produces an actual trigger signal. The trigger scales are dynamically adapted to the present run conditions [159]. The L1 trigger is operated dead-time free so that every event is analyzed. However, trigger signals are produced with a latency of up to  $2.3 \mu\text{s}$  corresponding to 24 bunch-crossings. The detector signals recorded in the meantime have to be temporarily stored in pipelines. Detectors with a good timing resolution like the CIP or SpaCal define a L1 trigger reference time that is used to identify a bunch-crossing. This allows reading out the correct position in the pipeline when a positive trigger decision is reached. The L1 trigger reduces the event rate to roughly 1 kHz.

At the software-based second trigger level (L2 [160]) events are analyzed in more detail by combining L1 information from various sub-detectors. Many L1 subtriggers, do not have L2 conditions and are validated by default. In the case of a positive L2 decision, data-taking is halted, and the full detector is read out. The readout can take up to 2 ms depending on the size of an event. A third trigger level (L3 [161]) was commissioned in 2005 to reduce dead time. It uses the information available early during readout, such as tracks provided by the Fast Track Trigger, to perform a partial event reconstruction. If the L2 decision can not be validated by the L3, the readout can be stopped after around  $100 \mu\text{s}$ . Once the detector is fully read out, all buffers are cleared and data taking and L1 operation is resumed. The L2 and L3 triggers reduce the event rate to approximately 200 Hz and 50 Hz, respectively.

After the detector is completely read out, further processing of the data happens asynchronously to the detector operation. In a fourth trigger level (L4) a complete event reconstruction is performed by the H1 reconstruction software (H1Rec). A final event filtering is performed to discard remaining unwanted events, e.g., events not originating from  $ep$  interactions. Also, specific high-rate processes can be further down-scaled. All other events are stored permanently on Production Output Tapes (POT). For faster analysis, reconstructed high-level objects such as tracks and clusters are also written onto Data Summary Tapes (DST).

### 3.3.1 The Fast Track Trigger

Track reconstruction is typically slow and computing-intensive because of the combinatorial problem that needs to be solved when assigning a large number of hits to a large number of tracks. Nonetheless, in H1 some tracking information is already available at the trigger level. It is provided by the Fast Track Trigger (FTT), an FPGA and associative-memory-based fast tracking engine [162, 163]. With the FTT it is possible to reconstruct tracks down to a transverse momentum of 100 MeV at the first trigger level. With a refined track reconstruction at the second trigger level, track parameter resolutions comparable to the offline reconstruction can be achieved. The FTT contributes to an improvement of the performance of many subtriggers. In particular, it is essential for triggering photoproduction events of light vector mesons. For these, the scattered electron is not reconstructed and only small energies are deposited in the LAr calorimeters. A detailed description of the FTT system is provided by Berger [42] and Baird et al. [162], for example. The main working principles are outlined in the following.

#### FTT Working Principle

The FTT uses partial information from the Central Track Chambers to reconstruct tracks. Twelve radial trigger layers are defined, consisting of a single wire per drift cell. Only the signals from those wires are read out by the FTT at a rate of 20 MHz, i.e., approximately

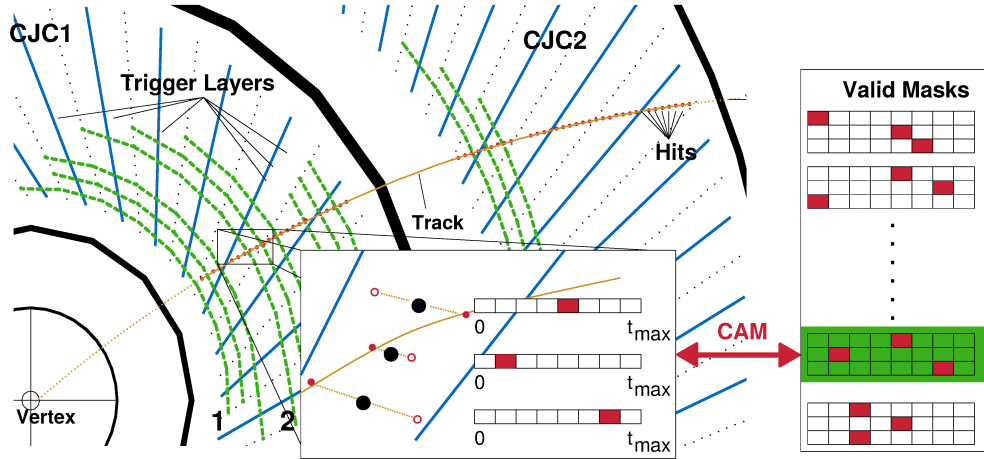


**Figure 3.6:** Illustration of the FTT's working principle. In the first trigger stage CJC hits from 4 radial trigger groups with three wires each are read out. The hit patterns from each group are compared on FPGAs to predefined patterns using Content Addressable Memories. Curvature and angular position of a track segment can be determined from the respective values of a matching pattern. Figure from Berger [42] and adapted.

twice the L1 rate. Sets of three neighboring wires each form one of 4 trigger groups. Three of the groups lie in the inner, the fourth in the outer jet chamber. For track finding, the hits from all wires are filled into shift registers. If all three wires of one trigger group in a drift cell have a hit, the resulting *hit pattern* is tested for compatibility with a track. For this purpose, hit pattern masks for a large set of possible tracks are a priori generated using the detector simulation and stored on Content Addressable Memory (CAM) chips. Usage of CAMs allows for a parallel and fast comparison of the measured hit pattern with all stored masks. If a matching mask can be found, an L1 FTT track segment is created using the track parameters corresponding to that mask. The track segments are characterized by the track curvature  $\kappa \propto 1/p_T$  and the azimuthal angle  $\phi$  of the CJC drift cell they originate from. The pattern masks are generated in  $2 \times 16 \kappa$  bins for positive and negative tracks. The granularity in  $\phi$  is given by the 30 drift cells of the inner CJC1. The structure of the FTT inputs and pattern recognition is also illustrated in Figure 3.6.

In a second step, the identified track segments are combined to complete tracks by the FTT's L1 Linker algorithm. First, the  $\kappa$  and  $\phi$  values from each trigger group are filled into a 2D histogram. To increase a potential overlap of track segments from the four groups, the resulting histograms are smeared. Along  $\phi$ , the number of bins is doubled and the bin content copied to both new bins. Along the  $\kappa$  dimension, bins containing an actual track segment weighted by a factor of 3, while neighboring bins get filled with a weight of 1. Since curved tracks produce patterns at different angles in the 4 trigger groups, a Hough-transform is performed to match the  $\phi$  values from the first, second and fourth trigger group to  $\phi(r_3)$  as it would have been measured at the radius of the third trigger group  $r_3$ . The construction of the track segment histograms is illustrated in Figure 3.7.

The track segment linking is then performed by adding the 4 histograms. Patterns from the same track tend to cluster in the  $\kappa\phi$ -plane. Among the bins exceeding a threshold of 4, i.e., obtaining contributions from at least two track segments, local maxima are searched. Each local maximum gives rise to an L1 FTT track candidate, with  $\kappa$  and  $\phi(r_3)$  defined by the position of the maximum. To avoid double counting of tracks, bins adjacent to a local maximum are vetoed. See also Figure 3.8.

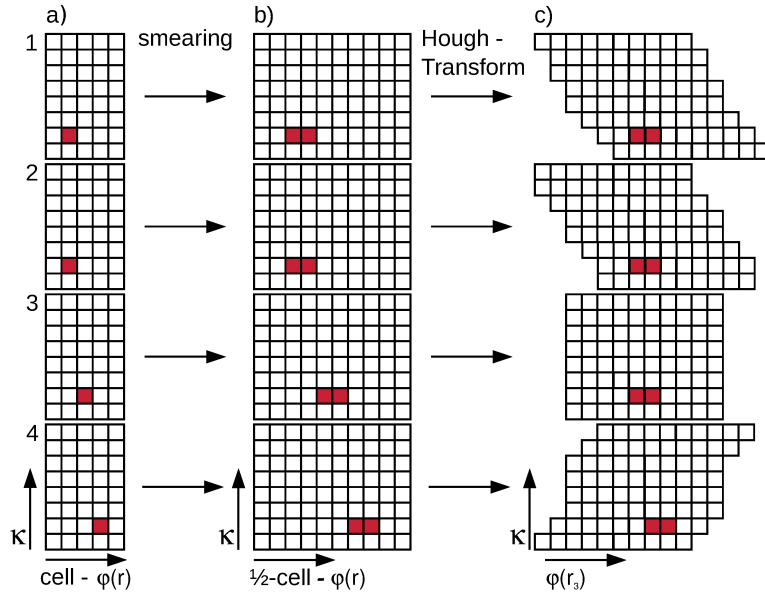


**Figure 3.7:** Illustration of the smearing and *Hough-transform* performed on the trigger group track segment histograms by the FTT L1 Linker. a) Track segment parameters for the 4 trigger groups in a schematic  $\kappa\phi$ -plane, where  $\phi$  corresponds to the position of the CJC cell the track segment lies in. b) Histograms are shown after smearing, i.e., duplicating each  $\phi$  column. In a Hough-transform, which also takes into account the cell tilt, the track parameters are shifted so that in each histogram  $\phi$  corresponds to the angle  $\phi(r_3)$  measured in the third trigger group. c) Track segments with compatible parameters sit in the same place in the transformed  $\kappa\phi(r_3)$ -plane. Figure from Berger [42].

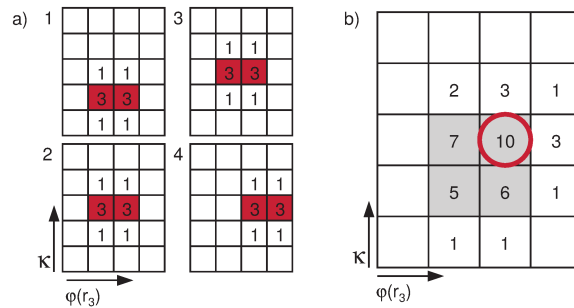


**Figure 3.8:** Working principle of the FTT L1 Linker algorithm. a) Track segment histograms in the 4 trigger groups after the Hough-transform. The numbers represent the weights given to the bins. b) For linking of track segments, the 4 histograms are added. Shaded bins exceed a threshold of 4 and are considered in the search for track candidates. If several adjacent bins exceed the threshold, only the local maximum is considered as indicated by the red circle. Figure from Berger [42].

### FTT at Level 1

The reconstruction of Level 1 FTT track candidates can be performed within the  $2.3 \mu\text{s}$  time frame available for the H1 L1 trigger. Track reconstruction itself is very fast, and a majority of the time is needed to wait for charge collection and readout of the CJC. From the track candidates, 16 FTT L1 trigger bits are constructed. They encode information on track multiplicities, the summed charge of all tracks, and the topological structure of the event. The track multiplicities are defined for various momentum thresholds, as defined in

Table 3.3. Charge information is available from the sign of the measured  $\kappa$  values. For the topological structure, the transverse plane is segmented into 10 slices in  $\phi$  and considering rotational symmetries 78 distinct topologies are defined, depending on the pattern of segments containing at least one track.

$\kappa$ bins	$p_T$ [GeV]	$1/p_T$ [GeV $^{-1}$ ]	trigger element	$n_{max}$
0, 15	0.100	10.00	FTT_mul-Ta	7
1, 14	0.125	8.00	–	–
2, 13	0.160	6.25	FTT_mul-Tb	3
3, 12	0.250	4.00	–	–
4, 11	0.400	2.50	FTT_mul-Tc	3
5, 10	0.600	1.66	–	–
6, 9	0.900	1.11	FTT_mul-Td	3
7, 8	1.800	0.55	FTT_mul-Te	3

**Table 3.3:** FTT L1 track momentum thresholds. 6 L1 trigger elements are defined from the multiplicities of tracks exceeding a given threshold. Only a limited number of bits are available for the FTT trigger elements resulting in a maximum track multiplicity that can be encoded for each threshold.

### FTT at Level 2 and 3

At the second H1 trigger stage, FTT track reconstruction is performed at much higher precision. Not only is the resolution in  $\kappa$  and  $\phi$  increased to 40 and 640 bins, respectively, but also the  $z$ -coordinate of tracks is determined by a measurement of the charge division in the CJC wires. Thus the full 3D track information for up to 48 tracks can be measured at a resolution similar to that provided by the offline track reconstruction. In particular, the full tracking information allows the reconstruction of more complex event variables, such as the  $z$ -vertex position, invariant masses, etc. to be used by the H1 L2 trigger. In the third trigger stage, L2 FTT tracks can be combined with objects from other sub-detectors for a more complete event reconstruction.

### 3.3.2 The CIP Trigger

The CIP's projective geometry allows for fast track recognition and  $z$ -vertex reconstruction already at trigger level. For the  $z$ -vertex reconstruction all valid CIP track patterns with hits in at least 4 layers are identified and their measured  $z$ -coordinates filled into a histogram. From this histogram a CIP *significance* and *multiplicity* can be calculated and used to distinguish signal from background events. The multiplicity corresponds to the number of entries in the histogram. The significance gives the fraction of signal-like central ( $z < 50$  cm) with respect to background like backward ( $z \geq 50$  cm) entries. Background events identified by the CIP mainly originate from interactions of the proton beam with collimators in front of the detector or with remaining gas in vacuum of the beampipe. An example CIP  $z$ -vertex histogram is provided in Figure 3.9.

The fast CIP signal also provides good timing information with a resolution of  $\sigma = 7.1$  ns. This is well below the 96 ns bunch spacing in HERA so that the CIP timing can be used to identify the exact bunch crossing an event originates from.

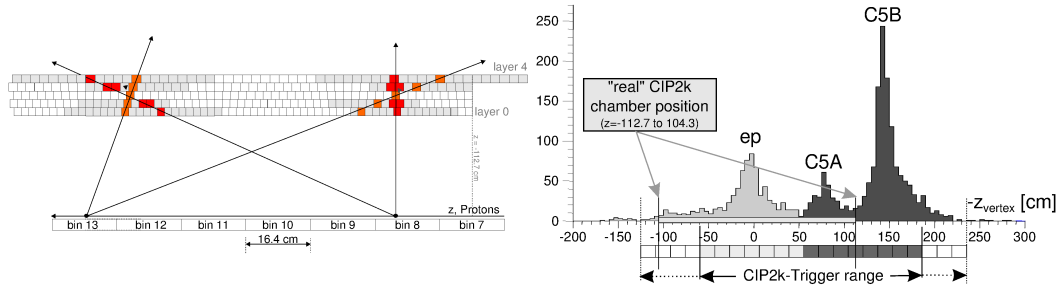


**Figure 3.9:** Illustration on the construction of the CIP trigger  $z$ -vertex histogram (left) and example histograms (right). Histograms are shown for signal events from  $ep$  collisions (light gray) and for background events from collisions of the incoming proton beam with the collimators C5A and C5B (dark gray). For the trigger, histograms are only evaluated within the specified trigger range. Light gray bins are considered as signal and dark gray bins as background. Figure from Urban [147] and adapted.

### 3.4 Luminosity Measurement

The (instantaneous) luminosity  $\mathcal{L}$  relates the event rate  $dN/dt$  of a process to the underlying cross-section  $\sigma$ :

$$dN/dt = \mathcal{L}\sigma \quad (3.3)$$

To measure a cross-section via a counting experiment in which all events are recorded and counted over a period of time, the luminosity integrated over that time,  $\mathcal{L}_{\text{int}}$ , thus needs to be precisely known. The instantaneous luminosity delivered by the HERA machine is monitored using the Bethe-Heitler-process  $ep \rightarrow ep\gamma$  [164] for which the cross-section can be precisely calculated in perturbative QED. Dedicated detector systems are installed upstream of the H1 detector to monitor the rate of Bethe-Heitler events by measuring the scattered electron and photon.

For a more precise measurement of the integrated luminosity an offline analysis of the QED Compton (QEDC) process [165] is performed. The QEDC final state is the same as for the Bethe-Heitler process but photon and scattered electron emerge with a large transverse momentum. QEDC events can thus be reconstructed with the main H1 detector using events with back-to-back energy deposits in the SpaCal. For the HERA-II period, the luminosity measurement from the QEDC analysis yields a total uncertainty of 2.7% that is dominated by systematic effects.

## 4 $\pi^+\pi^-$ PHOTOPRODUCTION DATA SAMPLE

The  $\rho^0$  meson decays almost exclusively into a pair of charged pions. The  $\rho^0$  cross-section measurement presented here is thus based on a sample of  $\pi^+\pi^-$  photoproduction events. The event topology is very simple, with only the two pions in the central detector. In the photoproduction regime, the scattered electron leaves the interaction point undetected, as does the diffractively scattered proton. The transverse momentum of the  $\pi^+\pi^-$  system, which balances the proton and electron momentum transfer, then is very small. As a consequence, the two pions emerge from the interaction point back-to-back in the transverse plane and with small transverse momenta  $p_T \lesssim 1$  GeV. An exemplary event can be seen in the H1 event display shown in Figure 4.1.

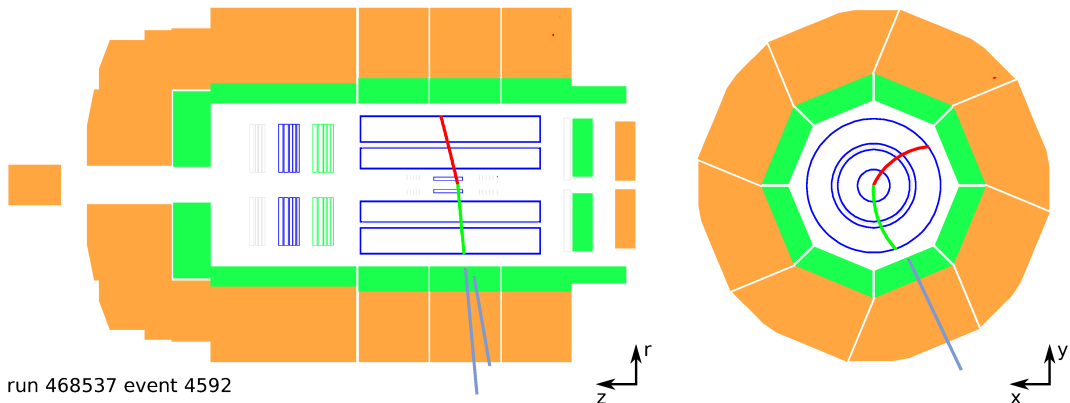


**Figure 4.1:** H1 event display of a  $\pi^+\pi^-$  photoproduction event candidate. The detector is empty but for two central, low  $p_T$ , back-to-back tracks and associated calorimeter clusters.

Measuring  $\pi^+\pi^-$  photoproduction events with the H1 detector is more complicated than the simple topology might suggest. A main experimental challenge is that they have to be triggered with track information only. For the H1 experiment, tracking information was available on the first trigger level mainly from the Fast Track Trigger (FTT). In Section 4.1 the trigger strategy for  $\pi^+\pi^-$  photoproduction events is described. The reconstruction of events then has also to be performed using mostly information from the two pion tracks. How various kinematic variables that are relevant for this thesis can be reconstructed is detailed in Section 4.2. The selection cuts applied on top of the trigger in order to enhance the purity of the  $\pi^+\pi^-$  photoproduction data sample are documented in Section 4.3. The section also describes the definition of dedicated signal and control regions to study remaining events from wrongly or partially reconstructed background processes. The dataset contains contributions from elastic and proton-dissociative events. Their respective fractions are determined using information from forward detectors to tag the proton-dissociative events, as is explained in Section 4.4. Throughout the chapter, the data is compared to the MC model introduced in Chapter 5.

### 4.1 H1 Dataset and Trigger

The analysis is based on  $ep$  scattering data collected by the H1 experiment during the 2006/2007 HERA running period. Only runs with a positron beam and at the high proton

beam energy of  $E_p = 920$  GeV are considered. During the running period, the H1 detector configuration was stable, and in particular, the FTT reached peak performance. Events are preselected to ensure all sub-detectors used in the analysis were operational during the corresponding data acquisition runs. The total, QED Compton-corrected luminosity in the considered run range is  $\mathcal{L}_{HE+06/07} = 130.0 \text{ pb}^{-1} \pm 2.7\%$  (syst.). A dedicated  $\pi^+\pi^-$  photoproduction trigger, the **s14** subtrigger, is used to trigger events. Due to the large  $\rho^0$  photoproduction cross-section, the trigger is heavily prescaled with an average prescale of  $\langle p_{\text{s14}} \rangle_{HE+06/07} = 97.6$ . The effective, prescale corrected luminosity thus is:

$$\mathcal{L}_{HE+06/07}^{\text{s14}} = 1.33 \text{ pb}^{-1} \pm 2.7\% \text{ (syst.)}. \quad (4.1)$$

It relates the number of triggered  $\pi^+\pi^-$  photoproduction events to the production cross-section and thus serves as the normalization factor for the cross-section measurement; compare Chapter 7.

### Beam-Gas Template

The vacuum in the HERA beampipe is not perfect, and some free atoms remain in it. Interactions between the particle beams and these restgas atoms are possible. They contribute as a background component to the present dataset. A dedicated data subset exists that can be used to study these interactions. It is obtained from so-called *pilot bunch* events collected from bunch-crossings in which one of the colliding electron or proton bunches is purposefully left empty. As a consequence, the incoming beam particles can only interact with atoms from the restgas. Events from these pilot bunches are weighted to match the luminosity of the main dataset, put through the full data selection and then used to construct a template for the beam-gas induced background contribution to the dataset. The event weights are obtained from the ratio of pilot-bunch to colliding-bunch currents, which are proportional to the instantaneous luminosity for the respective process.

### The **s14** Subtrigger

The **s14** trigger mainly exploits FTT information to identify events with the  $\pi^+\pi^-$  photoproduction topology. Information from other trigger systems is added to suppress events from various background processes. A positive trigger decision requires at least 2 L1 FTT tracks with transverse momenta above 160 MeV and at most 3 tracks with  $p_T > 100$  MeV. An additional third track is allowed in order to accommodate a considerable rate of fake, wrongly reconstructed FTT tracks. Two of the three tracks have to be of opposite charge. Besides the FTT requirements, cuts on the CIP significance, multiplicity, and timing ensure events originate from  $ep$  collisions at the nominal interaction point. Vetoes on activity in the inner forward liquid argon calorimeter and the forward FTI2 veto wall mainly suppress non-diffractive events or diffractive proton-dissociation events with a large invariant mass of the dissociative final state. The remaining trigger elements are a set of standard H1 vetoes against events from beam-gas and beam-machine interactions; in particular, from outside the nominal interaction region. In between the considered runs, the online trigger definition was subject to slight changes. For consistency, the trigger definition is harmonized in the offline event selection. Also, in 2007 the **s14** was extended by an L2 FTT vertex selection that cannot be applied to earlier runs. In practice, it is found to be almost fully efficient and can thus be ignored. The formal definition of the **s14** is given in Chapter 6. There, the trigger is studied in more detail, and trigger correction factors for the H1 detector simulation are derived. In all of the following plots, the trigger correction has been applied to the MC.

In Figure 4.2, the **s14** event yield is shown as a function of the run number. The yield is defined as the number of triggered events within a given time period divided by the corresponding prescale corrected luminosity. For better visualization, consecutive runs are combined to bins corresponding to a luminosity of approximately  $2 \text{ pb}^{-1}$  before trigger prescaling. The yield is shown for the online **s14** definition, the offline harmonized trigger, and

for events passing the full offline selection. The step in the online yield can be attributed to the FTI2 veto being temporarily taken out of the online trigger definition. After harmonizing the trigger definition offline, the yield becomes constant over time. This indicates a stable detector performance. The pull distribution of the offline harmonized yield is also shown in the figure, to illustrate this better. The pull is defined as the difference between the yield measured in run ranges of roughly  $1 \text{ pb}^{-1}$  and the average yield of the full dataset divided by the statistical yield uncertainty. Within uncertainties, the pull is roughly consistent with a normal distribution with zero mean and a width of 1.

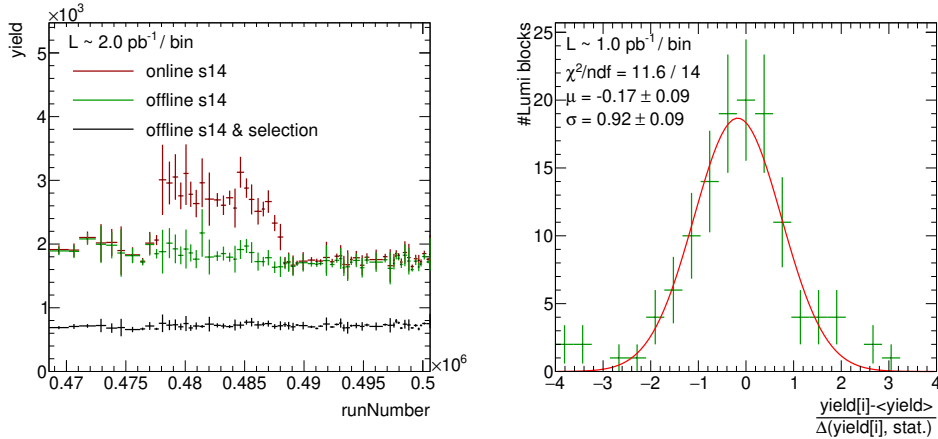


**Figure 4.2:** Left: Event yield against run number in blocks corresponding to  $2 \text{ pb}^{-1}$ . The yield is shown for online `s14` accepted events, events accepted by the offline harmonized `s14` trigger, and events accepted by the full offline selection as labeled in the legend. Right: Pull distribution of the harmonized `s14` yield with respect to the average yield. The pull distribution is fitted with a Gaussian function to validate consistency with a zero-mean and a variance of one.

## 4.2 Event Variables Reconstruction

In the photoproduction  $\pi^+\pi^-$  event topology, only the two pion tracks are precisely measured. All kinematic variables thus have to be reconstructed from the two pion four-vectors alone.

The momentum transfer at the electron vertex  $Q^2$  can be measured in deep inelastic scattering from the electron scattering angle  $\theta_{e'}$  and the initial and final state electron energies  $E_e$  and  $E_{e'}$ , respectively:

$$Q^2 = 2E_e E_{e'} (1 + \cos \theta_{e'}). \quad (4.2)$$

The experimental signature of photoproduction is that the scattered electron is not reconstructed. Scattered electrons can be measured up to  $\theta_{e'} \lesssim 177.5^\circ$  only, given the limited acceptance of the SpaCal. This limits  $Q^2 \lesssim 2.5 \text{ GeV}^2$ ; compare Section 7.1. Momentum conservation also enforces a lower bound of

$$Q_{\min}^2 = \frac{m_e^2 y^2}{1 - y}, \quad (4.3)$$

with the electron mass  $m_e$  and the inelasticity of the scattering process  $y$ , as defined in Section 2.4. MC studies suggest  $Q_{\min}^2 \simeq 10^{-12} \text{ GeV}^2$  and an average value of  $\langle Q^2 \rangle \simeq 0.02 \text{ GeV}^2$  for the kinematic range of the present analysis. Compared to other scales of the process, such as the center-of-mass energy,  $Q^2$  is very small and for practical purposes  $Q^2 \simeq 0 \text{ GeV}^2$  is assumed in the reconstruction of further kinematic variables.

Since the two pion tracks are directly measured, the kinematics of the di-pion system are precisely known apart from the inherent tracking resolution. In particular, the invariant  $\pi^+\pi^-$  mass can be calculated from the 4-vectors of the two pions,  $p_{\pi^+}$  and  $p_{\pi^-}$ :

$$m_{\pi\pi} = |p_{\pi^+} + p_{\pi^-}| = \sqrt{(E_{\pi\pi}^2 - |\vec{p}_{\pi\pi}|^2)}. \quad (4.4)$$

$E_{\pi\pi}$  and  $\vec{p}_{\pi\pi}$  are the energy and three-vector of the  $\pi^+\pi^-$  system, respectively.

The photon-proton center-of-mass energy  $W_{\gamma p} = |p_p + p_e - p_{e'}|$ , can be approximately calculated from the two tracks via

$$W_{\gamma p} \simeq \sqrt{2E_p(E_{\pi\pi} - p_{z,\pi\pi})}. \quad (4.5)$$

Only the known the proton beam energy  $E_p$ , the reconstructed di-pion energy, and the longitudinal di-pion momentum  $p_{z,\pi\pi}$  enter the expression. However, an approximation is made wherein contributions of the order of  $m_p^2$ ,  $Q^2$ ,  $m_Y^2$ , and  $t$  are neglected relative to the actual  $W_{\gamma p}^2$ ; compare derivation in Appendix C. For the higher end of the energy range probed by this analysis ( $W_{\gamma p} \sim \mathcal{O}(80 \text{ GeV})$ ), these are all valid assumptions. However, at the lower end ( $W_{\gamma p} \sim \mathcal{O}(20 \text{ GeV})$ ) and for proton-dissociative events with large  $m_Y \sim \mathcal{O}(10 \text{ GeV})$  the approximation breaks down. In Figure 4.3, the relative difference between the actual and approximated value of  $W_{\gamma p}$  is plotted against the mass of the proton-dissociative system using generated events from the  $\pi^+\pi^-$  signal MC samples. At large  $m_Y \sim 10 \text{ GeV}$  the relative error on the average approximated  $W_{\gamma p}$  value is roughly 3% but can be expected to be more significant for small  $W_{\gamma p}$ .

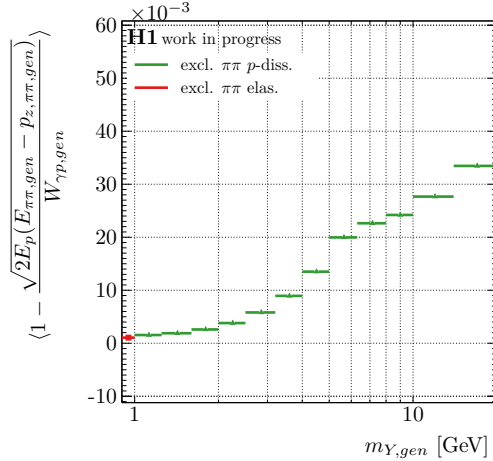


**Figure 4.3:** Average relative error for the approximation of  $W_{\gamma p}$  using only di-pion information as a function of  $m_Y$ . The curve is constructed using generated tracks from the elastic and proton-dissociative  $\pi^+\pi^-$  signal MC samples as indicated in the legend.

The momentum transfer at the proton vertex  $t = |p_p - p_{p'}|^2$  roughly equals the negative squared transverse momentum of the di-pion system:

$$t \simeq -p_{T,\pi\pi}^2. \quad (4.6)$$

The expression is precisely valid only for  $Q^2 = 0 \text{ GeV}^2$  and if  $m_p$  and  $m_Y$  are neglected relative to a much larger  $W_{\gamma p}$ ; compare derivation in Appendix C. These assumptions become problematic in some regions of the probed phasespace. In Figure 4.4, the relative error in the approximated value for  $t$  is plotted as a function of both  $Q^2$  and  $m_Y$  using generated events from the signal  $\pi^+\pi^-$  MC samples. For large  $Q^2 \sim 2.5 \text{ GeV}^2$  the average error grows to around 20-40%<sup>1</sup> and for large  $m_Y \sim 10 \text{ GeV}$  to roughly 30%.

<sup>1</sup>The structure in the  $Q^2$  dependence of the error is related to the  $\rho^0 \rightarrow \pi^+\pi^-$  decay topology that changes qualitatively once  $Q^2$  is larger than the average  $|t|$ ; compare e.g., Chapter 6.

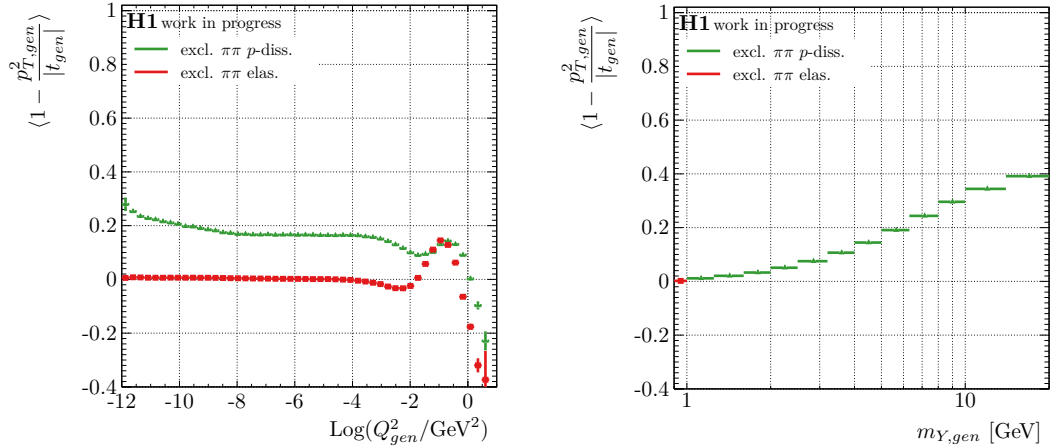


**Figure 4.4:** Average relative error for the approximations of  $t$  using only di-pion information as a function of  $Q^2$  (left) and  $m_Y$  (right). The curves are constructed using generated tracks from the elastic and proton-dissociative  $\pi^+\pi^-$  signal MC samples as indicated in the legend.

The remaining unknown variable in the final state is the mass of the proton-remnants  $m_Y$ , in events where the proton dissociates. It can not be determined from the two pions alone. The event selection applied on the dataset constrains it to roughly below 10 GeV; compare Section 7.1. However, dedicated forward detectors are used to separate elastic ( $m_Y = m_p$ ) from dissociative events ( $m_Y > m_p$ ) as is explained further on in the chapter in Section 4.4.

### 4.3 Event Selection

To select a clean sample of  $\pi^+\pi^-$  photoproduction events, various event and track quality cuts are applied on top of the run period and trigger selection. The selection procedure is further split into two stages. First, a common base selection is applied. Events satisfying the base selection are then split into a signal and multiple background control regions. The signal region is very pure in  $\pi^+\pi^-$  events. However, it is still contaminated by misreconstructed events from various background processes. Those are studied in more detail in multiple background control regions that are enriched in a given kind of process. All selection steps are described in the following. For a compact overview, all cuts are also summarized in Table B.2 in Appendix B. Throughout the description, the measured data is compared to the MC template model via control distributions of various kinematic variables. The MC template is defined in Chapter 5.

#### 4.3.1 Base Selection

##### Photoproduction and Event Quality

The selection of photoproduction events is ensured by a veto on the scattered electron. It is required that no electron candidate is found in neither the SpaCal nor LAr calorimeter and that the energy deposited in the SpaCal is below 10 GeV. Out of time events are rejected by cuts on the liquid argon and CJC timing. Background events from beam-gas and beam-machine interactions are suppressed by selecting the  $z$ -vertex position of the interaction to be within 40 cm of the nominal interaction point.

### Central Tracks

Only events with exactly two reconstructed central tracks of good quality are considered. The selected tracks have to be fitted to the primary vertex with a distance of closest approach below 10 mm in the transverse plane. They need to satisfy minimum requirements on the fit quality, the track length, and the associated number of hits in the CJs and be within the acceptance of the central tracking detector. The central tracker acceptance is defined by the requirements  $p_{T, \text{trk}} > 160$  MeV and  $25^\circ < \theta_{\text{trk}} < 155^\circ$  on the track parameters. The polar acceptance is slightly reduced compared to the actual CJC geometry for an improved trigger performance; compare Chapter 6. The two tracks have to have opposite charges. Cuts on the CJC timing ensure that the tracks originate from the same bunch crossing. To improve the performance and modeling of the FTT, a minimum opening angle of  $\Delta\phi_{FTT} > 20^\circ$  between the tracks in the transverse plane is required.  $\Delta\phi_{FTT}$  is evaluated at the position of the third FTT trigger group at a radius of 22 cm. Additionally, the transverse opening angle between the tracks at the vertex is required to be larger than  $50^\circ$ . The cut reduces contributions from backgrounds with additional neutral particles in the final state, which are not well modeled by the available MC samples. Finally, a veto on tracks originating from cosmic muons is applied as described by Huber [43]. The two tracks are then considered to be candidates for the  $\pi^+$  and  $\pi^-$  particles.

### Large Rapidity Gap

The diffractive nature of the selected events is ensured by requiring a large rapidity gap (LRG) between the centrally produced pions and the forward energy flow from the scattered proton system. The LRG selection comprises a veto on events with more than a single track in the forward tracking detector. A single track is allowed to account for detector noise or proton-dissociative scattering events. Furthermore, no energy cluster above a noise level of 600 MeV is allowed in the forward region,  $\theta < 20^\circ$ , of the liquid argon calorimeter. The cut is defined conservatively in order to supersede the forward trigger vetoes and improve the modeling thereof.

### Visible Analysis Phasespace

The analysis phasespace is explicitly defined by the cuts  $0.3 \text{ GeV} < m_{\pi\pi} < 2.3 \text{ GeV}$ ,  $15 \text{ GeV} < W_{\pi\pi} < 90 \text{ GeV}$ , and  $p_{T, \pi\pi}^2 < 3 \text{ GeV}^2$  on the reconstructed event variables. It is further discussed in Section 7.1.

## 4.3.2 Signal Region Selection

For the  $\pi^+\pi^-$  signal, only two (pion) tracks are expected in the detector. The base selection does not explicitly suppress background events with additional neutral particles, events with additional charged particles outside of the CJC acceptance, or events with the two tracks topology but with final state particles other than pions. A signal region is defined by implementing additional cuts to suppress such background contributions.

### Beam-Gas Events

The  $z$ -vertex distribution is shown in Figure 4.5. The sidebands are dominated by events from beam-gas interactions. These events are suppressed in the signal region by applying a tighter cut  $|z_{\text{vtx}}| < 25$  cm on the  $z$ -vertex.

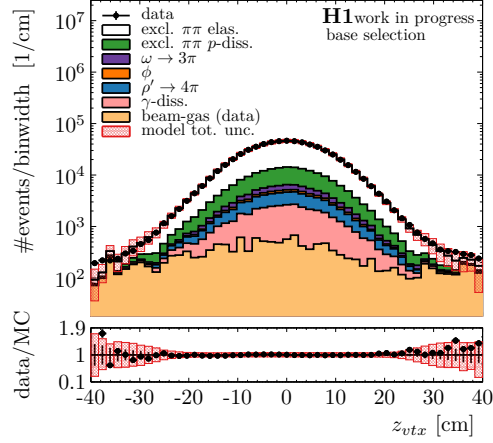


**Figure 4.5:**  $z$ -vertex distribution for events satisfying the base selection. The black data points are compared to the MC template with stacked contributions shown as labeled in the legend.

## Energy Deposits

Energy clusters from the liquid argon and spaghetti calorimeter are summed to give the respective total energy deposits in the LAr and SpaCal. Only clusters above a noise level of 600 MeV for the LAr and 300 MeV for the SpaCal are considered. A geometric cluster-to-track matching is performed to associate clusters with the two selected tracks. A cylindrical cluster-to-track distance is calculated at the particle's entry point into the calorimeter and with a cylinder axis along its momentum direction upon entry. Calculating the entry point at the calorimeter is essential for performing a proper matching with low  $p_T$ , i.e., strongly bent tracks. In figures 4.7 and 4.6, the distribution of the distance measure is shown for LAr and SpaCal clusters, respectively. Clusters within a cylinder with a radius of 60 cm are considered to be originating from a track. The large radius ensures that secondary particles emerging from nuclear interactions of the pions with the detector material are also attributed to a track. A significant excess of clusters associated with a track in data compared to the MC template is attributed to an underestimation of the nuclear interaction cross-section by the detector simulation; compare Section 5.2. This is not corrected, but potential consequences are mitigated by the cluster-to-track matching and consequently not using the associated energy any further.

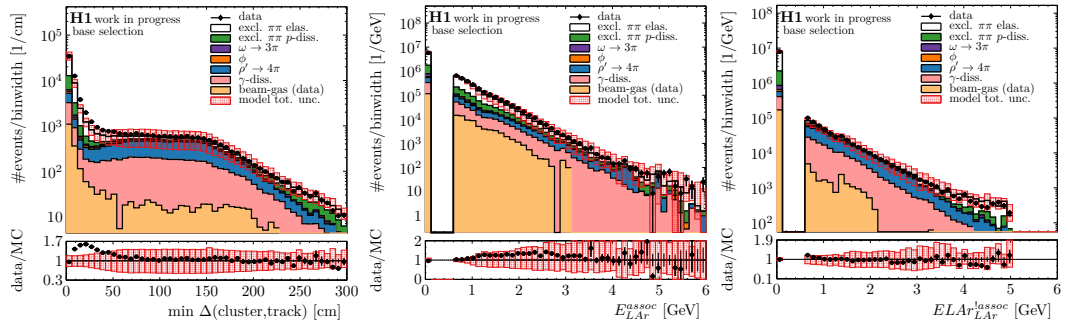


**Figure 4.6:** LAr control distributions for events satisfying the base selection. Left: Minimum cylindrical distance between clusters and either of the two tracks as defined in the text. Center: Energy associated with either of the tracks. Right: Energy not associated with either of the tracks. The black data points are compared to the MC template with stacked contributions shown as labeled in the legend.

### 4.3. EVENT SELECTION

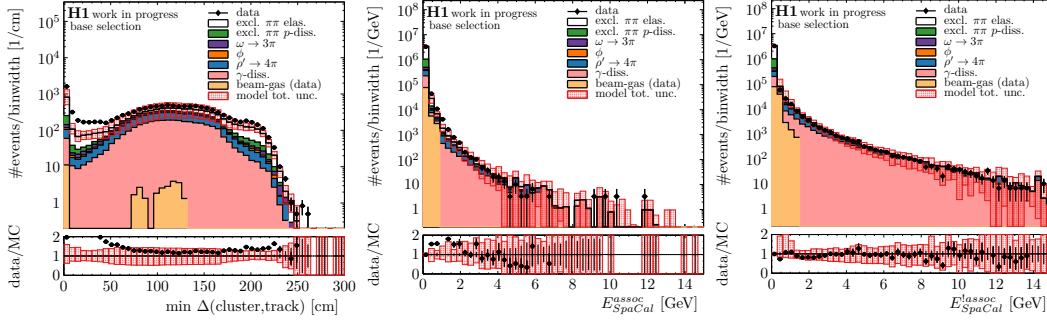


**Figure 4.7:** SpaCal control distributions for events satisfying the base selection. Left: Minimum cylindrical distance between clusters and either of the two tracks as defined in the text. Center: Energy associated with either of the tracks. Right: Energy not associated with either of the tracks. The black data points are compared to the MC template with stacked contributions shown as labeled in the legend.

For signal  $\pi^+\pi^-$  events, significant energy deposits that are not matched to a track are not expected. However, they can occur in background processes with additional particles in the final state. If those particles are neutral, e.g., for  $\omega \rightarrow \pi^+\pi^-\pi^0$  photoproduction, or lie outside of the CJC acceptance such events are not rejected by the track selection. Instead, they are suppressed by cuts on the un-associated energy  $E_{LAr}^{!assoc} < 0.8$  GeV, and  $E_{SpaCal}^{!assoc} < 4$  GeV in the LAr and SpaCal, respectively. The distributions of the total energy deposits which are either associated and not associated with a track are shown in figures 4.6 and 4.7 for the LAr and SpaCal, respectively.

### Particle Identification

The specific energy loss by ionization  $dE/dx$  in the central tracker is measured for each track. The loss depends primarily on a particle's velocity and thus can be used together with the momentum measurement to discriminate particles of different mass. Due to a limited resolution of the momentum and  $dE/dx$  measurements, only low-momentum particles can be well separated. In Figure 4.8, the measured  $dE/dx$  in units of the energy loss of a minimum ionizing particle (MIP) is plotted for selected tracks as a function of the track momentum. Three distinct bands clearly separate low momentum pions from kaons and protons.

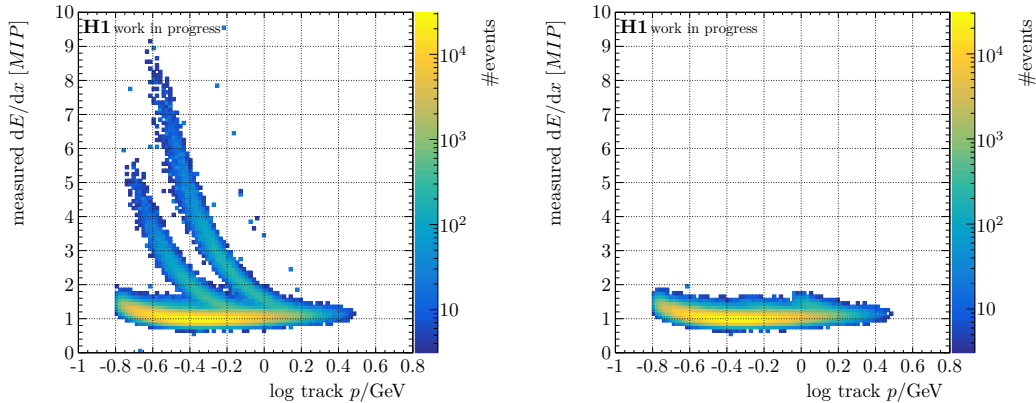


**Figure 4.8:** Measured  $dE/dx$  distribution as a function of the log of the track momentum for data events satisfying the base selection (left) and additionally the particle identification selection (right). The four distinct bands differentiate pion, kaon, proton, and deuteron tracks.

Tracks are tested for compatibility with a particle hypothesis by comparing the measured  $dE/dx$  value to the expected value for that hypothesis. The expected values are calculated with the Bethe-Bloch formula [1]. The compatibility is quantified in terms of a  $\chi^2$  probability. The probability is calculated from the difference in the measured and calculated  $dE/dx$  values relative to the resolution of the  $dE/dx$  measurement. Details on the procedure are given by Berger [42]. A loose pion selection is applied by requiring the pion probability to exceed  $10^{-9}$ . Furthermore, kaon, proton, and deuteron vetoes are applied for tracks with momenta below 400 MeV, 900 MeV, and 2 GeV respectively if the corresponding likelihood exceeds 10%. The veto mostly reduces backgrounds from beam-gas interactions with a pion-proton track topology and  $\phi \rightarrow K^+K^-$  events. The impact of the selection is also illustrated in Figure 4.8.

### Control Plots

After the full signal selection, over 900 000 di-pion photoproduction events remain in the data sample. Using the MC model, the fraction of exclusive  $\pi^+\pi^-$  signal events is approximately 90%. The exact event yields, as well as the fractional contributions from all background processes, are summarized in Table 4.1.

	N(signal region)
data	$943\,962 \pm 0.12\%$ (stat.)
MC model	$944\,380 \pm 0.30\%$ (stat.) $\pm 6.04\%$ (syst.)
	contribution [%]
excl. $\pi^+\pi^-$	89.2
$\gamma$ -dissociation	3.4
$\omega \rightarrow 3\pi$	2.7
$\rho' \rightarrow 4\pi$	2.6
beam-gas	1.7
$\phi$	0.4

**Table 4.1:** Number of events in the  $\pi^+\pi^-$  photoproduction signal region after applying all selection cuts and fractional contributions from the various signal and background processes considered in the MC model.

Control distributions of the invariant di-pion mass, the photon-proton scattering energy, and the squared transverse  $\pi^+\pi^-$  momentum for events satisfying the signal selection are shown in Figure 4.9. The sample is indeed dominated by the  $\rho^0$  resonance, which gives rise to a large peak around  $m_{\pi\pi} \sim 0.770$  GeV. A second  $\pi^+\pi^-$  resonance can be seen on the logarithmic scale at a higher mass of around  $m_{\pi\pi} \sim 1.6$  GeV. Various wrongly reconstructed background processes then contribute over the whole mass range. The falling  $W_{\gamma p}$  distribution is mostly a feature of the photon flux decreasing with increasing energy; compare Section 2.4. The lower and upper energy range is restricted by the polar acceptance of the central tracker. The  $p_{T,\pi\pi}^2 \sim -t$  distribution is steeply falling, as is expected for diffractive processes. At low  $p_{T,\pi\pi}^2$ , it is dominated by elastic scattering, whereas at large  $p_{T,\pi\pi}^2 \gtrsim 0.5$  GeV<sup>2</sup>, proton-dissociation becomes dominant. All distributions are well described by the MC model. This can only be achieved after tuning the MC samples to the present data; compare Section 5.3.

Further control plots showing distributions of the pion track variables are presented in Figure 4.10. Most notably, they illustrate the low transverse momenta of the pion tracks with typical values of  $p_{T,\text{high}} \sim 0.4$  GeV for the leading and  $p_{T,\text{low}} \sim 0.3$  GeV for the sub-leading track. Another important topological property of the events is illustrated by the distribution of the transverse opening angle between the two pions. Due to the small momentum transfer at both the electron- and proton-vertex in diffractive photoproduction and the consequently

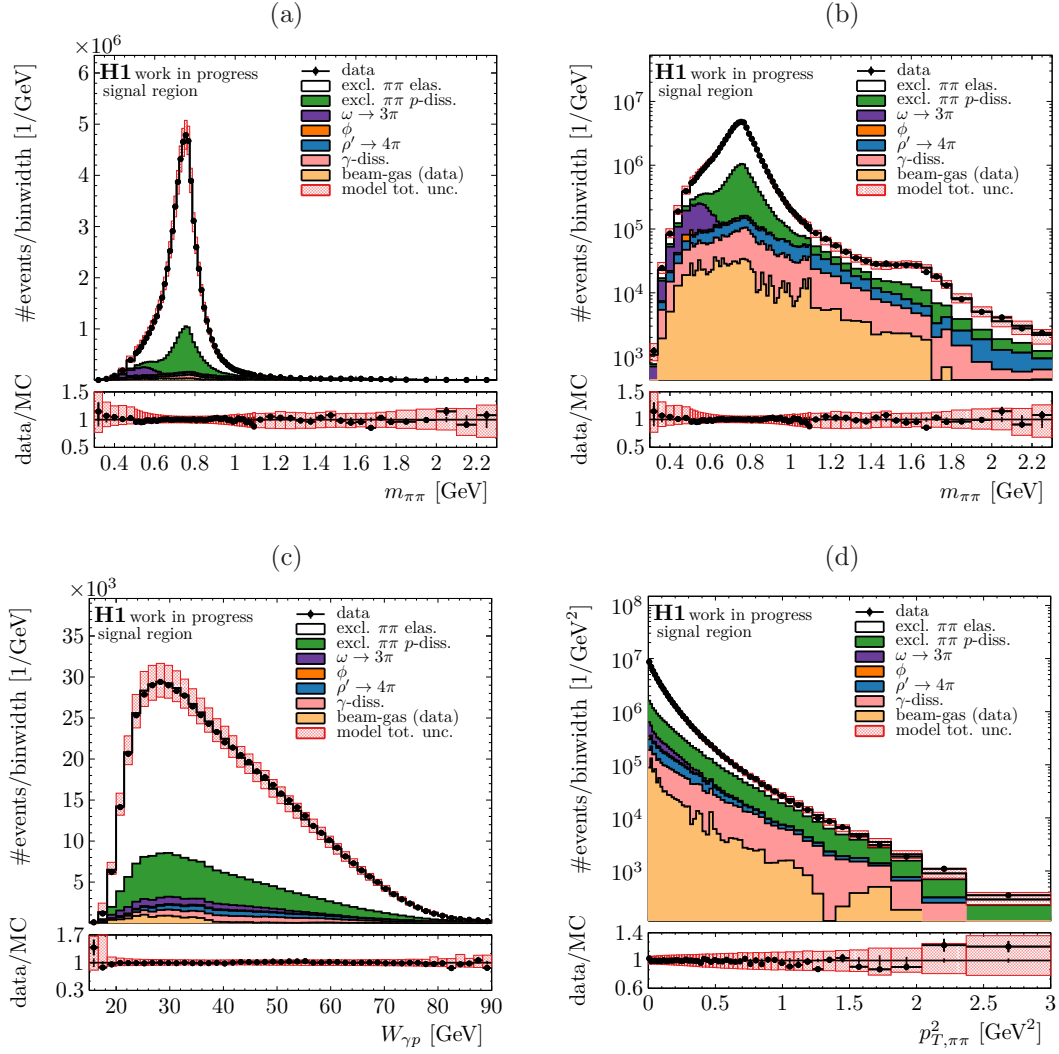


**Figure 4.9:**  $m_{\pi\pi}$  distribution on a linear (a) and logarithmic  $y$ -axis scale (b),  $W_{\gamma p}$  distribution (c), and  $p_{T,\pi\pi}^2$  distribution (d) for events satisfying the signal selection. The black data points are compared to the full MC model with stacked contributions shown as labeled in the legend.

small transverse momentum of the  $\pi^+\pi^-$  system, the two pion tracks mostly emerge back to back. The distributions of the polar angles of the two tracks are shown because they are very sensitive to good modeling of many detector effects with polar dependencies. In particular, the polar angle of the less central of the two tracks is used for the correction of the trigger simulation; compare Chapter 6. Overall, the MC template model describes the data quite well in all studied variables. Some discrepancies between data and the nominal MC distribution persist, but the full systematic uncertainty band typically covers them.

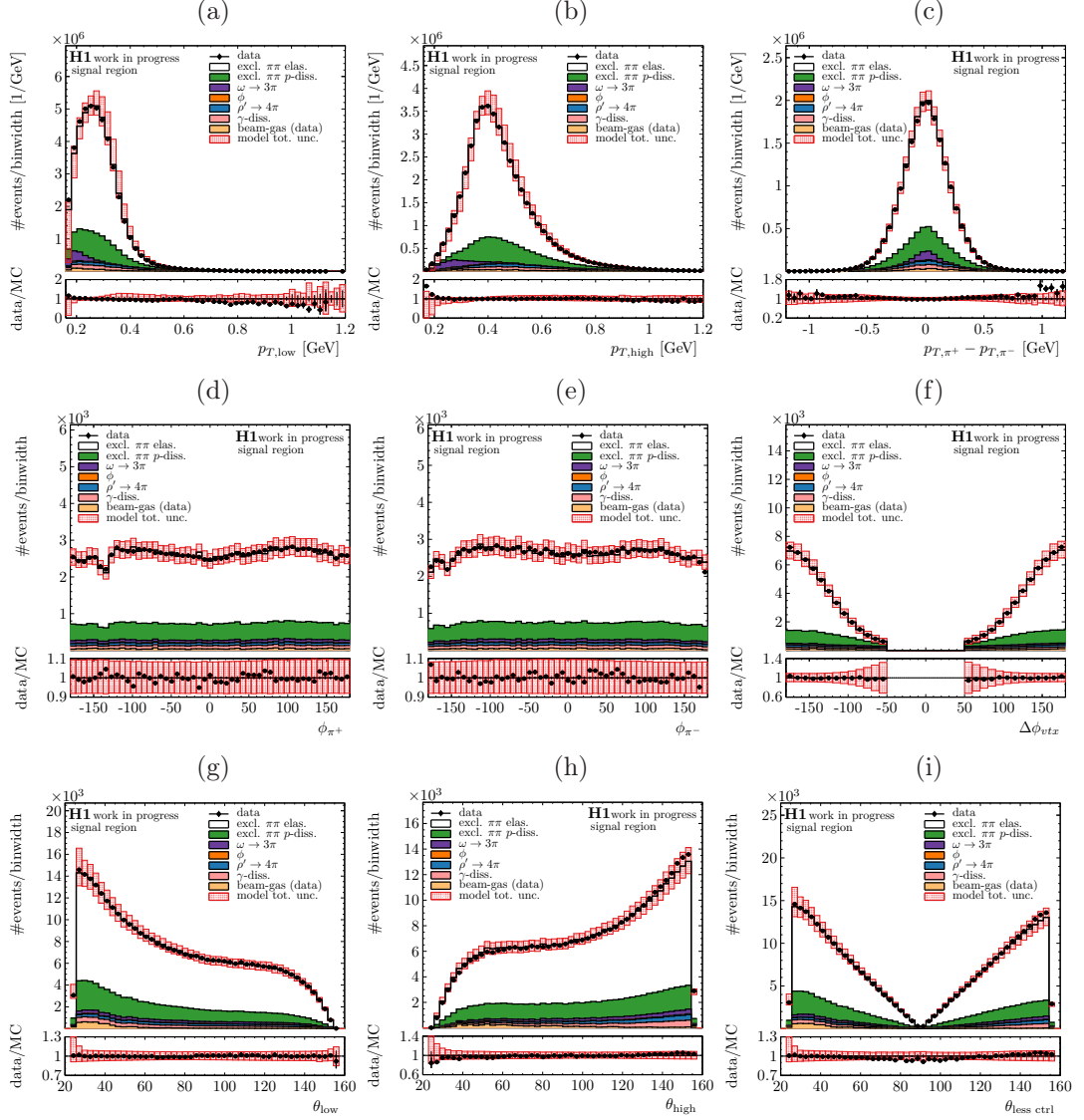


**Figure 4.10:** Control plots of track variables for events satisfying the signal selection. Distribution of the lower (a) and higher of the two track transverse momenta (b), of the difference between the two track transverse momenta (c), of the azimuthal angle of the positive (d) and negative track (e), of the difference between the azimuthal angles (f), of the lower (g) and higher of the two track polar angles (h), and of the less central polar angle (i). The black data points are compared to the full MC model with stacked contributions shown as labeled in the legend.

### 4.3.3 Background Control Regions

Several wrongly or partially reconstructed background processes populate the  $\pi^+\pi^-$  photo-production dataset even after the full signal event selection that is described in the previous section. The dominant processes to be considered are diffractive photoproduction of other vector mesons, such as the  $\omega(782)$ ,  $\phi(1020)$ ,  $\rho(1450)$ , or  $\rho(1700)$  mesons, and diffractive photon-dissociation. A generic diagram for these processes is depicted in Figure 4.11. Some of the considered vector mesons can decay into a pure  $\pi^+\pi^-$  final state, which is then indistinguishable from the signal and treated as such; compare Chapter 5. However, the dominant decay modes generally include multiple pions, kaons, and other particles in the final state; compare Table 5.1 in Chapter 5. Another important background comes from interactions between either of the incoming particle beams and remaining atoms in the imperfect vacuum in the beam-pipe. Further backgrounds are not considered and assumed to be negligibly small.

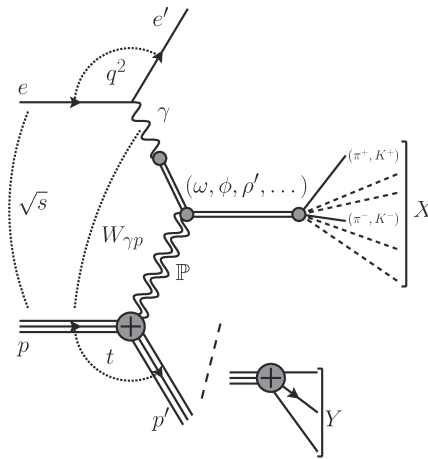


**Figure 4.11:** Diagram of generic vector meson production with multiple particles in the final state. If only two charged particles are reconstructed, these processes can give background contaminations to the selected  $\pi^+\pi^-$  dataset.

Due to the limited acceptance and efficiency of the H1 tracking detectors and the limited sensitivity of the calorimeter, charged and neutral particles are easily missed in the event reconstruction. If only two charged particles from a multi-particle background event are reconstructed, it can satisfy the  $\pi^+\pi^-$  criteria and be wrongly selected. Event displays of two background event candidates that satisfy the base selection are shown in Figure 4.12. The two events show additional activity in the calorimeters that can not be associated with the two selected tracks.

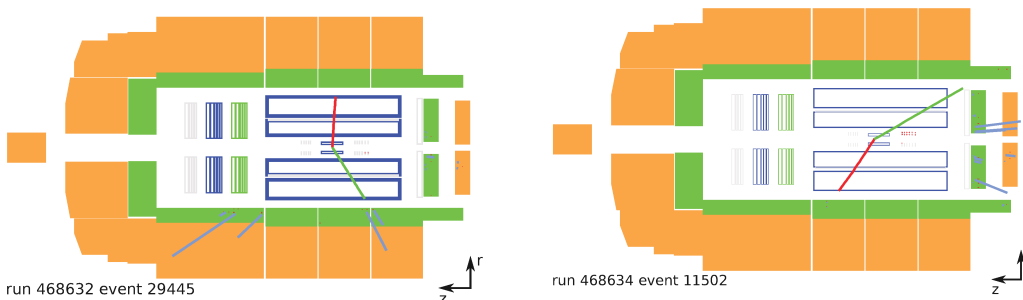


**Figure 4.12:** H1 event displays for events with the dipion photoproduction track topology and additional activity in the LAr (left) or SpaCal calorimeter (right).

For the analysis, various background control regions are defined in which a specific background component is enhanced. They allow to study the respective components and modeling thereof in more detail. More importantly, they are used for normalizing the background MC samples; compare Chapter 5 and Chapter 7. The control regions are defined orthogonally by inverting or replacing a subset of the previously defined  $\pi^+\pi^-$  signal selection cuts on top of the base selection.

### Photon-Dissociation Control Region

The final state particles from photon-dissociation typically emerge in the direction of the photon, i.e., they preferably produce signals in the backward region of the H1 detector. To identify photon-dissociation events thus the cut on the unassociated energy deposited in the SpaCal is replaced by the requirement  $4 \text{ GeV} < E_{SpaCal}^{assoc} < 10 \text{ GeV}$ . An exemplary event with two tracks plus un-associated energy deposits in the SpaCal calorimeter is shown in Figure 4.12. The lower energy bound distinguishes photon-dissociation from  $\rho' \rightarrow 4\pi$  and  $\omega \rightarrow \pi^+\pi^-\pi^0$  events. The upper bound is retained as a veto against DIS events.

Control distributions of event variables in the photon-dissociation control region are presented in Figure 4.13. Generally, the data appears to be well described by the MC model, though the size of the sample is rather small. The purity of  $\gamma$ -dissociation events in the control region is roughly 78%.

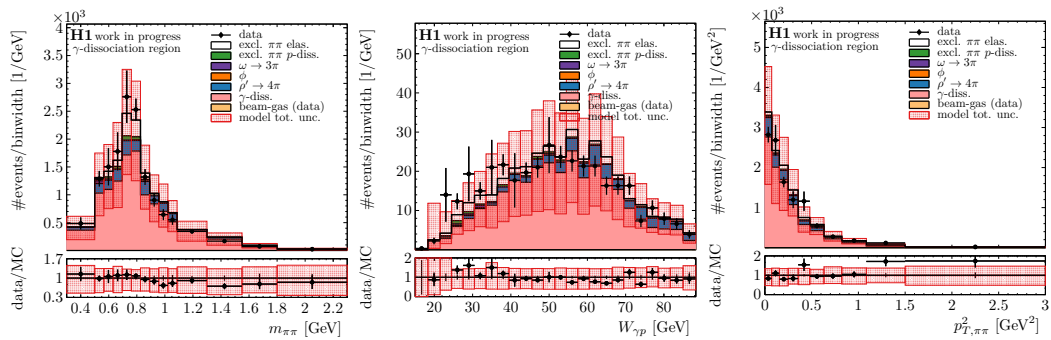


**Figure 4.13:**  $m_{\pi\pi}$  (left),  $W_{\gamma p}$  (center), and  $p_{T,\pi\pi}^2$  (right) distribution in the  $\gamma$ -dissociation control region. The black data points are compared to the MC template with stacked contributions shown as labeled in the legend.

### $\omega \rightarrow 3\pi$ Control Region

The  $\omega$  meson decays primarily into two charged and a neutral pion. For an enhanced selection of such  $\omega \rightarrow \pi^+\pi^-\pi^0$  events, the cut on the energy deposit in the LAr that is not associated with the tracks is inverted, i.e., it is required that  $E_{LAr}^{assoc} > 0.8 \text{ GeV}$ . An exemplary data event with two tracks plus unassociated energy deposits in the LAr calorimeter is shown in Figure 4.12. On detector level,  $\omega$  and  $\rho'$  events with unassociated energy deposits are very similar. As the  $\omega$  meson is lighter than the considered  $\rho'$  resonances, it can be distinguished by requiring the mass of the  $\pi^+\pi^-$  system to be below 0.55 GeV in the  $\omega$  control region. Furthermore, an *event mass*  $m_{\text{evt}}$  is constructed, which is calculated from the four-vectors of the two pion tracks and all the four-vectors of unassociated LAr and SpaCal clusters. A control distribution of the event mass is given in Figure 4.14 for events satisfying the base selection. For the  $\omega$  control region,  $m_{\text{evt}} < 1.2 \text{ GeV}$  is required.

Control distributions of event variables in the  $\omega \rightarrow 3\pi$  control region are presented in Figure 4.15. Generally, the data appears to be well described by the MC model. The purity of  $\omega$  events in the control region is roughly 54%. A better purity could not be achieved because of the similarity of  $\omega$  events to  $\rho'$  and  $\gamma$ -dissociation events on detector level.

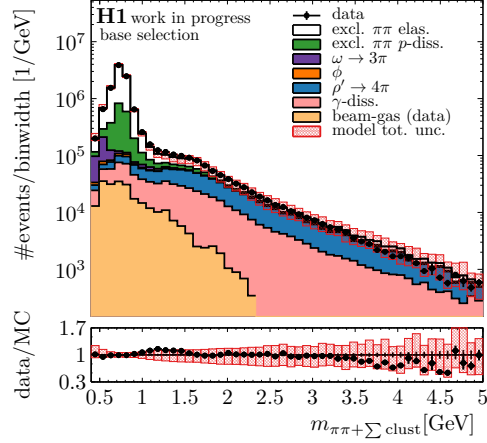


**Figure 4.14:** Control distribution of the event mass variable  $m_{\text{evt}}$  for events passing the base selection. The black data points are compared to the MC template with stacked contributions shown as labeled in the legend.

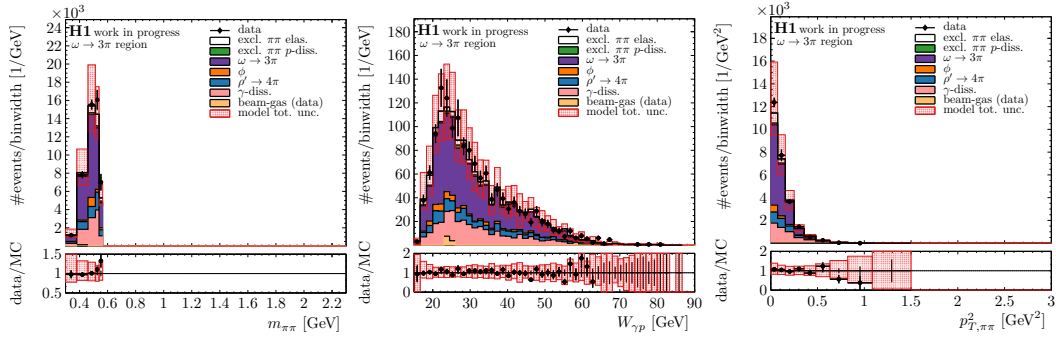


**Figure 4.15:**  $m_{\pi\pi}$  (left),  $W_{\gamma p}$  (center), and  $p_{T,\pi\pi}^2$  (right) distribution in the  $\omega \rightarrow 3\pi$  control region. The black data points are compared to the MC template with stacked contributions shown as labeled in the legend.

### $\rho' \rightarrow 4\pi$ Control Region

Excited  $\rho'$  mesons decay primarily into four pions with various different charge configurations. For an enhanced selection of such  $\rho' \rightarrow 4\pi$  events, the cut on the energy deposit in the LAr that is not associated with the tracks is inverted to the requirement  $E_{LAr}^{\text{assoc}} > 0.8$  GeV.  $\rho'$  events are separated from  $\omega$  events, by requiring the event mass to be larger than 1.2 GeV. Ideally, additional tracks would be used to identify  $\rho'$  decaying into multiple charged pions. However, this is not possible for this analysis. Additional central tracks can not be used because of the poor MC modeling of the FTT fake track rate and the track multiplicity requirements on trigger level. Forward tracks can not be used because of the forward FTI2 veto in the trigger which is not included in the simulation but can be expected to have a significant impact on  $\rho'$  events; compare Chapter 6.

Control distributions of event variables in the  $\rho' \rightarrow 4\pi$  control region are presented in Figure 4.16. Some mismodelings might be present in the  $m_{\pi\pi}$  distribution. Structures in  $m_{\pi\pi}$  are sensitive to the  $\rho'$  decay modes, in particular to those with and without an intermediate  $\rho^0$  resonance. Those are only roughly estimated in the  $\rho'$  MC samples; compare Section 5.3. A dedicated systematic uncertainty on the decay modes is estimated to cover potential discrepancies; compare Section 5.5. The purity of  $\rho'$  events in the control region is roughly 48%. A better purity could not be achieved because of similarities between  $\omega$ ,  $\rho'$ , and  $\gamma$ -dissociation events on detector level.

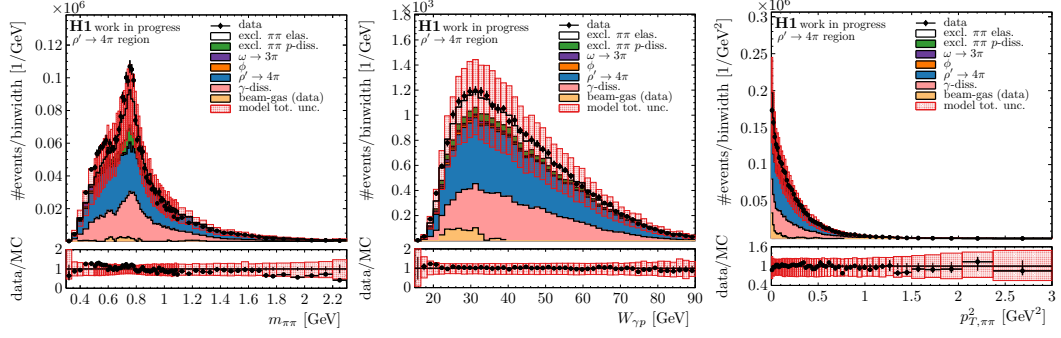


**Figure 4.16:**  $m_{\pi\pi}$  (left),  $W_{\gamma p}$  (center), and  $p_{T,\pi\pi}^2$  (right) distribution in the  $\rho'$  control region. The black data points are compared to the MC template with stacked contributions shown as labeled in the legend.

### $\phi \rightarrow KK$ Control Region

The  $\phi$  meson decays primarily into a pair of charged kaons. Those can be identified via their specific energy loss in the CJs. The signal pion  $dE/dx$  selection is thus replaced by a requirement that the  $dE/dx$  likelihood under a kaon hypothesis exceeds 1% for both tracks. Selected kaons are ensured to originate from  $\phi$  mesons by requiring the invariant mass of the two tracks reconstructed under a kaon hypothesis to be within 15 MeV of the  $\phi$  meson's mass. The  $\phi$  meson tends to have a larger transverse momentum so that also the cut on the transverse opening angle between the two tracks at the vertex must be removed.

Control distributions of event variables in the  $\phi \rightarrow KK$  control region are presented in Figure 4.17. Generally, the data appears to be well described by the MC model. The purity of  $\phi$  events in the control region is roughly 89%.

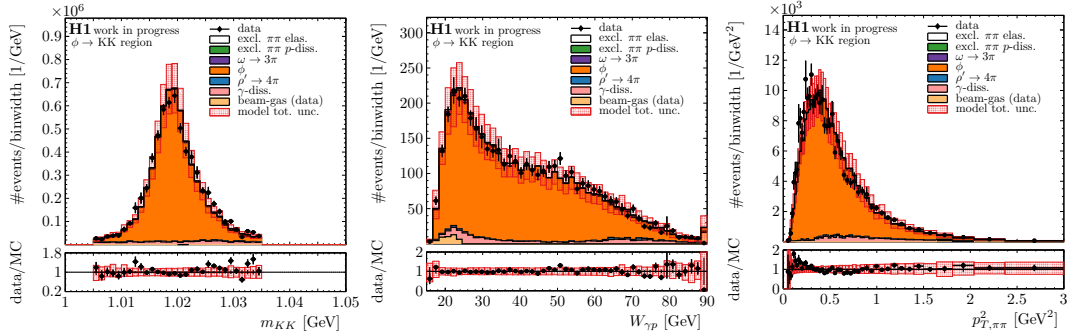


**Figure 4.17:**  $m_{KK}$  (left),  $W_{\gamma p}$  (center), and  $p_{T,\pi\pi}^2$  (right) distribution in the  $\phi$  control region. Only the invariant mass is calculated under a kaon track hypothesis. The black data points are compared to the MC template with stacked contributions shown as labeled in the legend.

### Beam-Gas Control Region

The remaining gas in the beam-pipes is homogeneously distributed. Events from beam-gas interactions are thus also uniformly distributed along the  $z$ -vertex position. Unlike signal events that peak at  $z_{\text{vtx}} = 0$  cm. A corresponding beam-gas control region is thus defined from the  $z_{\text{vtx}}$  sidebands  $25 < |z_{\text{vtx}}| < 40$  cm.

Control distributions of event variables in the beam-gas control region are presented in Figure 4.18. Generally, the data appears to be well described by the MC model. The purity of beam-gas induced events in the control region is roughly 42%.

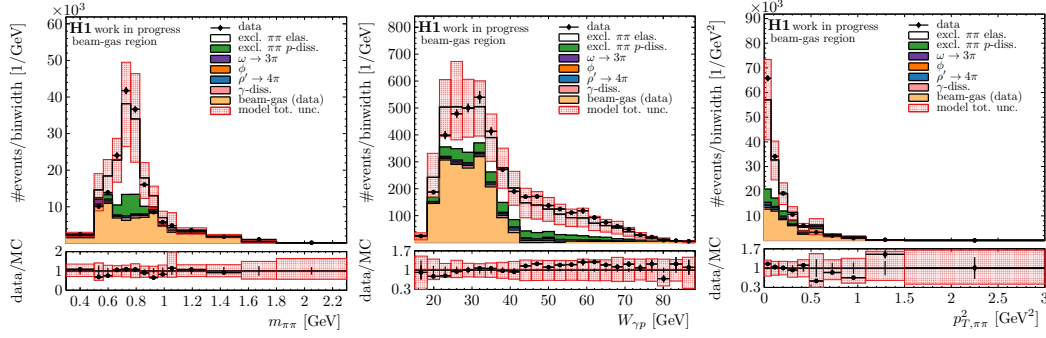


**Figure 4.18:**  $m_{\pi\pi}$  (left),  $W_{\gamma p}$  (center), and  $p_{T,\pi\pi}^2$  (right) distribution in the beam-gas control region. The black data points are compared to the MC template with stacked contributions shown as labeled in the legend.

### Control Region Yields

Event yields and purities in the signal and all control regions are summarized in Table 4.2.

CR	N data $\pm$ stat.	N MC model $\pm$ stat. $\pm$ syst.	purity
excl. $\pi^+\pi^-$	943962 $\pm$ 0.1%	944380 $\pm$ 0.3% $\pm$ 6.0%	89 %
$\gamma$ -diss.	1108 $\pm$ 5.0%	1117 $\pm$ 2.1% $\pm$ 39.5%	78 %
$\omega \rightarrow 3\pi$	2146 $\pm$ 2.7%	2144 $\pm$ 2.8% $\pm$ 21.2%	54 %
$\rho' \rightarrow 4\pi$	39355 $\pm$ 0.6%	39357 $\pm$ 1.5% $\pm$ 22.9%	48 %
$\phi \rightarrow KK$	6432 $\pm$ 1.5%	6432 $\pm$ 1.1% $\pm$ 14.7%	89 %
beam-gas	12602 $\pm$ 1.1%	12704 $\pm$ 10.0% $\pm$ 21.3%	42 %

**Table 4.2:** Event yields and purity in the signal and control regions. The beam-gas region is dominated by weighted data events from pilot bunch interactions, hence the large statistical uncertainty.

A summary of all signal and control region cuts is given in Table B.2 in Appendix B.

## 4.4 Proton-Dissociation Tagging

The  $\pi^+\pi^-$  photoproduction data sample is dominated by elastic scattering events. However, it also contains contributions from proton-dissociative scattering where the final state proton decays into a system  $Y$  of multiple particles with a combined invariant mass  $m_Y > m_p$ . The event selection, most notably the veto on energy deposits in the forward LAr, limits  $m_Y \lesssim 10$  GeV; compare Section 7.1.

The proton remnants emerge in the very forward direction, which is not well covered by detector instrumentation. They can thus not be entirely or reliably reconstructed, but mostly leave the detector undetected through the beampipe. However, some of the remnant particles do occasionally induce signals in one of several forward detectors. Either by direct interaction or via indirectly produced secondary particles from collisions with the beampipe, collimators or other infrastructure. An exemplary event with activity in the forward Plug calorimeter is shown in Figure 4.19.

Not every dissociative event produces a signal in the forward detectors. Besides, signals can also occur in the presence of detector noise or when the elastically scattered proton produces secondary particles upon interacting with the detector infrastructure. Consequently, proton-dissociative scattering events can not be identified on an event-by-event basis. However,

information from the forward detectors can be used to define event *tags* that allow splitting the dataset into control regions enriched in either elastic or proton-dissociative events. These regions then allow the determination of the overall elastic and proton-dissociative contributions to the dataset.

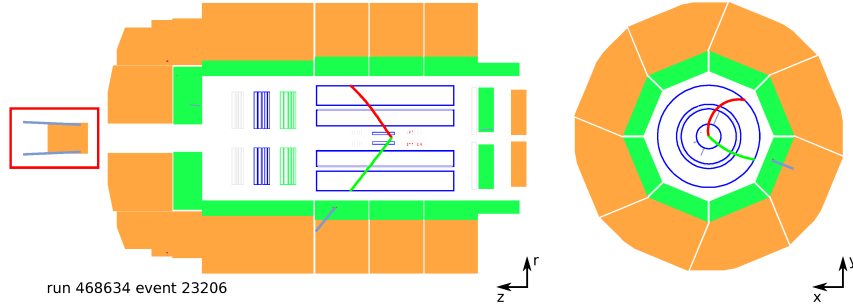


**Figure 4.19:** H1 event display for a proton-dissociative di-pion photoproduction event candidate with a signal in the Plug calorimeter (highlighted in red).

#### 4.4.1 Forward Detectors For Tagging

The forward detectors used by the present analysis for tagging proton-dissociative events are the Forward Tagging Station (FTS) at  $z=28$  m, the Plug calorimeter and the Forward Muon Detector (FMD). Neither of them provides complete coverage of the forward direction. However, in combination, they cover a large range in forward rapidity up to approximately  $\eta \lesssim 7.5$ ; compare Chapter 3. The usage of these detectors in an analysis is potentially problematic because the H1 simulation does not describe their respective responses very well. A two-step procedure is applied to make the simulation more robust and bring it into better agreement with the actual performance of the real detectors. First, only binary tagging information from the detectors is used to distinguish whether there was a signal or not. Secondly, the tagging information from the three detectors is combined in order to reduce dependence on good modeling of a single detector. A tagging rate is defined as the fraction of fully reconstructed events that are tagged by a single subdetector or a combination of multiple detectors:

$$\epsilon_{tag} = \frac{N(\text{tagged \&\& selected})}{N(\text{selected})}. \quad (4.7)$$

Tagging rates are used to study the tagging performance of each sub-detector in data and the MC model and to ensure that the combined tagging information is reasonably well described by the simulation.

$$\text{tag}_{\text{FTS}} : N_{\text{FTS}28}^{\text{hits}} > 0$$

An event is tagged by the FTS at  $z=28$  m if there is at least one hit recorded. A priori, the FTS has a significant fake tagging rate for elastic scattering events. For large momentum transfers and certain azimuthal scattering angles, the elastically scattered protons can hit a collimator in front of the FTS and induce signals via secondary particles. Unfortunately, the collimator appears not to be correctly positioned in the simulation resulting in a wrong description of the MC tagging rate for these events. The FTS can thus only reliably be used for events where the proton does not hit the respective collimator. Exploiting the momentum balance in an event, for  $\pi^+\pi^-$  signal events this can be ensured via acceptance cuts on the  $\pi^+\pi^-$  kinematics; namely on the azimuthal angle and transverse momentum of the  $\pi^+\pi^-$

system. The FTS is then only used for events which satisfy either of the requirements:

$$\begin{aligned} \text{FTS acceptance} = & (p_{T,\pi\pi}^2 \leq 100 \text{ MeV}) \\ & || (p_{T,\pi\pi}^2 > 100 \text{ MeV} \ \&\& \ |\phi_{\pi\pi}| > 120^\circ) \\ & || (p_{T,\pi\pi}^2 > 300 \text{ MeV} \ \&\& \ |\phi_{\pi\pi}| < 45^\circ). \end{aligned} \quad (4.8)$$

In Figure 4.20, the distribution of the number of FTS hits within this acceptance is shown for data and the MC model. The tagging rate for the FTS is shown in the same figure as a function of  $p_{T,\pi\pi}^2$  for data, the full MC template, and the elastic and proton-dissociative signal  $\pi^+\pi^-$  MC samples. While the number of FTS hits is ill-described by the MC, the tagging rate measured in data seems to be well reproduced by the full MC model within systematic uncertainties. The  $p_{T,\pi\pi}^2$  dependence of the tagging rate is significantly shaped by the FTS acceptance cuts and varies between 25% and 10% for proton-dissociative events. Elastic events are still wrongly tagged at a rate of about 1% because of noise in the FTS. The total MC rate rises from 5% at low  $p_{T,\pi\pi}^2$  to roughly 10% for  $p_{T,\pi\pi}^2 \gtrsim 1 \text{ GeV}$  because of an increasing contribution from proton-dissociative events towards higher  $p_{T,\pi\pi}^2$ ; compare also Figure 4.9 (d).

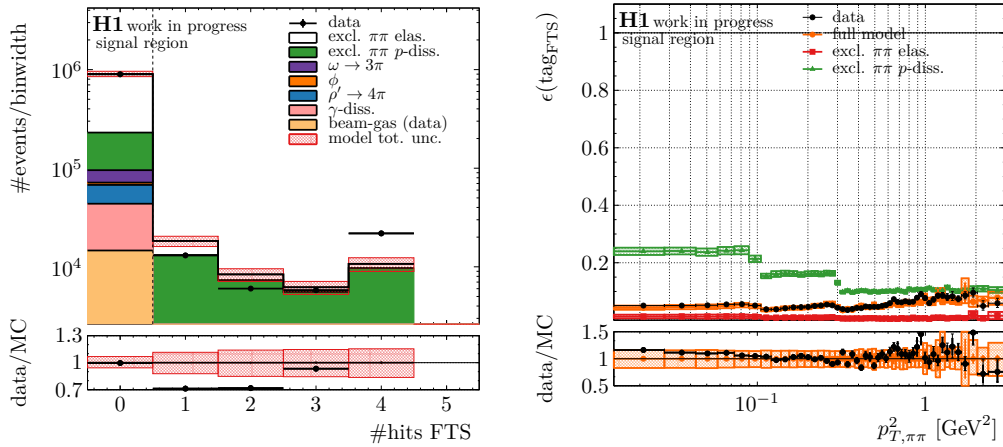


**Figure 4.20:** Left: Distribution of the number of FTS hits within the FTS acceptance as it is defined in the text. The black data points are compared to the MC model with stacked contributions as labeled in the legend. Right: FTS tagging rate as a function of  $p_{T,\pi\pi}^2$ . The rate is shown for data, the full model, and the elastic and proton-dissociative signal  $\pi^+\pi^-$  MC as labeled in the legend.

$$\text{tag}_{\text{Plug}} : N_{\text{Plug}}^{E_c > 1.2 \text{ GeV}} > 1$$

The Plug calorimeter suffers from a high noise level. Also, its energy response is not well modeled. For tagging purposes thus only the number of Plug clusters above a noise threshold of 1.2 GeV is considered. If there is more than one such cluster in an event, it is considered to be tagged by the Plug. The distribution of the number of plug clusters above the noise is shown together with the plug tagging rate in Figure 4.21. For dissociative events, the rate is about 10% and varies only little with  $p_{T,\pi\pi}^2$ . For elastic events, the rate due to remaining noise is almost negligible. A change in the relative proton-dissociative contribution leads to a change in the tagging rate in data with  $p_{T,\pi\pi}^2$ . The remaining differences between the data and full model rates appear to be within the systematic uncertainty band.

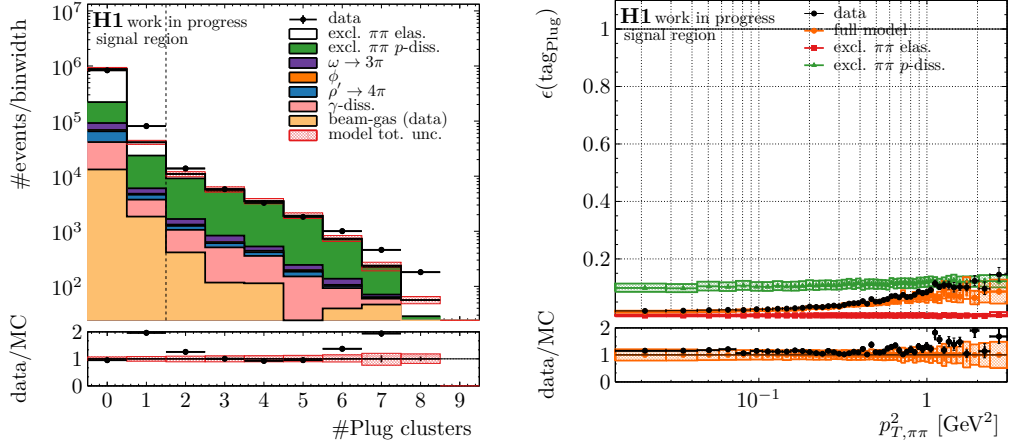


**Figure 4.21:** Left: Distribution of the number of Plug clusters above noise. The black data points are compared to the MC model with stacked contributions as labeled in the legend. Right: Plug tagging rate as a function of  $p_{T,\pi\pi}^2$ . The rate is shown for data, the full model, and the elastic and proton-dissociative signal MC as labeled in the legend.

$$\text{tag}_{\text{FMD}} : N_{\text{FMD}}^{123} > 0$$

An event is tagged by the FMD if there is at least 1 hit in any of the first three FMD layers. In Figure 4.22, the number of FMD hits in the first 3 layers is shown together with the tagging rate as a function of  $p_{T,\pi\pi}^2$ . The distribution of FMD hits is poorly described by the MC. The tagging rate, on the other hand, is much better modeled. Contrary to the other detectors the FMD suffers from a rather large noise level resulting in a roughly 20% mistag rate for elastic events. Naturally, the noise level is independent of kinematic variables. Simultaneously, the FMD provides a high tagging rate for dissociative events that varies from  $\sim 55\%$  at low  $p_{T,\pi\pi}^2$  to  $\sim 65\%$  at  $p_{T,\pi\pi}^2 \simeq 3 \text{ GeV}$ . The data rate is described by the MC within uncertainties and exhibits a similar  $p_{T,\pi\pi}^2$  dependence as observed for the previous detectors.

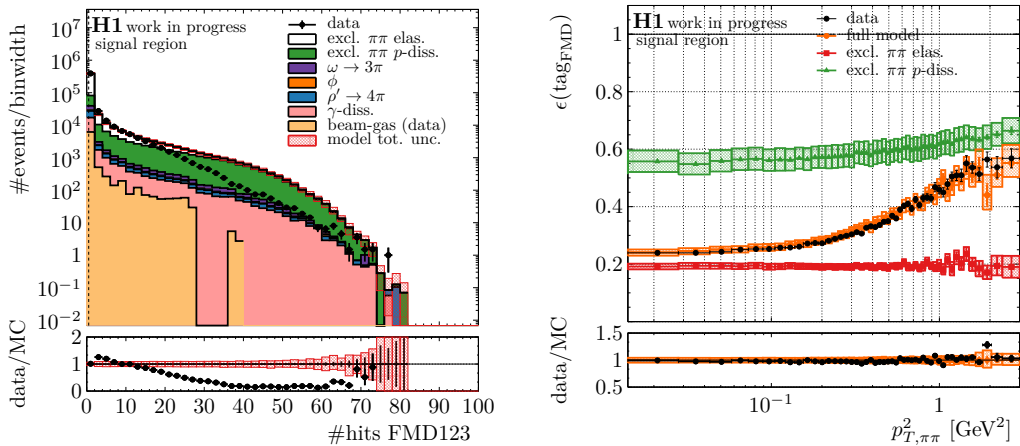


**Figure 4.22:** Left: Distribution of the number of hits in the first three FMD layers. The black data points are compared to the MC model with stacked contributions as labeled in the legend. Right: FMD tagging rate as a function of  $p_{T,\pi\pi}^2$ . The rate is shown for data, the full model, and the elastic and proton-dissociative signal MC as labeled in the legend.

### 4.4.2 Application of Tagging Information

#### Tagging Categories

The tagging information from the 3 forward detectors is combined to reduce the dependence on the individual detectors and in turn reduce a potential impact from the mismodeling they are subject to. For the combination, the tags from FTS, FMD and the Plug calorimeter in an event are counted to give the total number of tags in an event:

$$N_{\text{tags}} = \text{tag}_{\text{Plug}} + \text{tag}_{\text{FTS}} + \text{tag}_{\text{FMD}}, \quad 0 \leq N_{\text{tags}} \leq 3, \quad (4.9)$$

Only this combined tag information is used. Four different tagging categories are defined. The requirements  $N_{\text{tags}} = 0$ ,  $N_{\text{tags}} = 1$ , and  $N_{\text{tags}} > 1$  define orthogonal *zero-tag*, *single-tag* and *multi-tag* categories, respectively. The two latter categories can be combined to an *inclusive-tag* category corresponding to the requirement  $N_{\text{tags}} > 0$ .

The tagging rates for the zero-tag, single-tag, and multi-tag categories are shown in Figure 4.23 as a function of  $p_{T,\pi\pi}^2$ . The rates appear to be well described by the MC within uncertainties.

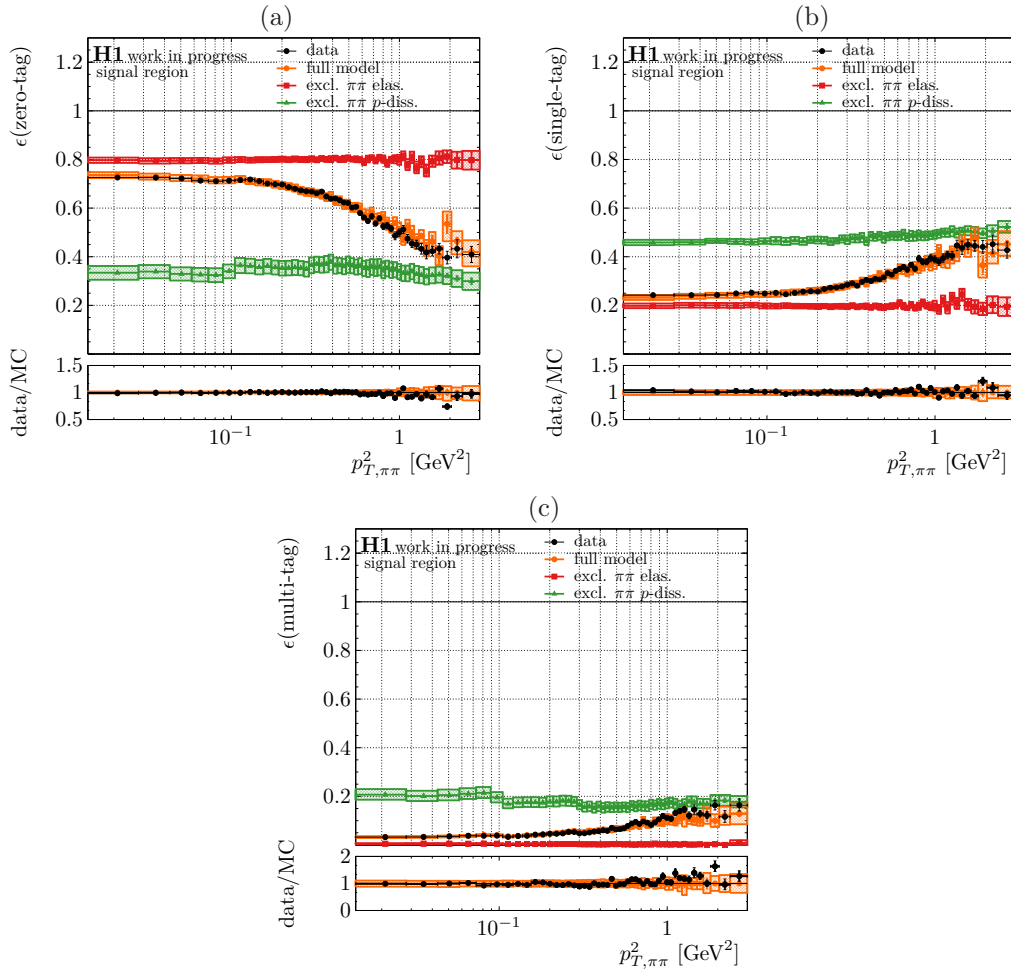


**Figure 4.23:** Zero-tag (a), single-tag (b), and multi-tag tagging rate (c) as a function of  $p_{T,\pi\pi}^2$ . The rate is shown for data, the full model, and the elastic and proton-dissociative signal MC as labeled in the legend.

The event yields in the three tagging categories in the signal region are summarized in Table 4.3. The respective fractions of proton-dissociative  $\pi^+\pi^-$  events are also listed. The

zero-tag and multi-tag categories provide two control regions that are very pure in elastic and proton-dissociative events, respectively. The single-tag category can then be considered as a transition region where the respective contributions are of a more similar size.

tagging region	N data $\pm$ stat.	N MC model $\pm$ stat. $\pm$ syst.	$N_{\text{pd}}^{\pi\pi}/N^{\pi\pi}$
zero-tag	$661755 \pm 0.14\%$	$664052 \pm 0.28\% \pm 5.58\%$	10 %
single-tag	$243472 \pm 0.23\%$	$240895 \pm 0.37\% \pm 8.53\%$	36 %
multi-tag	$38735 \pm 0.61\%$	$39432 \pm 0.75\% \pm 13.31\%$	91 %
inclusive-tag	$282207 \pm 0.21\%$	$280327 \pm 0.39\% \pm 8.77\%$	44 %

**Table 4.3:** Event yields for the tagging categories in the signal region and fraction of proton-dissociative  $\pi^+\pi^-$  events.

### Application of Tagging Information

The tagging categories allow determining the elastic and proton-dissociative contribution to the dataset. For a simplified argument, background contributions are neglected for the moment, and it is assumed that the  $N$  measured data events are constituted of  $N_{\text{el}}$  elastic and  $N_{\text{pd}}$  proton-dissociative events. Using any two orthogonal tagging categories with tagging rates  $\epsilon_{\text{tag1}}$  and  $\epsilon_{\text{tag2}}$  the dataset can be split into two categories:

$$N_{\text{tag1}} = \epsilon_{\text{tag1}} N = \epsilon_{\text{el,tag1}} N_{\text{el}} + \epsilon_{\text{pd,tag1}} N_{\text{pd}} \quad (4.10)$$

$$N_{\text{tag2}} = \epsilon_{\text{tag2}} N = \epsilon_{\text{el,tag2}} N_{\text{el}} + \epsilon_{\text{pd,tag2}} N_{\text{pd}} \quad (4.11)$$

If the tagging rates are correctly described by the elastic and proton-dissociative MC, the MC rates can be inserted, and equations (4.10) and (4.11) be solved for  $N_{\text{el}}$  and  $N_{\text{pd}}$ :

$$N_{\text{el}} = \frac{\epsilon_{\text{pd,tag2}}^{mc} N_{\text{tag1}} - \epsilon_{\text{pd,tag1}}^{mc} N_{\text{tag2}}}{\epsilon_{\text{pd,tag1}}^{mc} \epsilon_{\text{el,tag2}}^{mc} - \epsilon_{\text{pd,tag2}}^{mc} \epsilon_{\text{el,tag1}}^{mc}} \quad (4.12)$$

$$N_{\text{pd}} = -\frac{\epsilon_{\text{el,tag2}}^{mc} N_{\text{tag1}} - \epsilon_{\text{el,tag1}}^{mc} N_{\text{tag2}}}{\epsilon_{\text{pd,tag1}}^{mc} \epsilon_{\text{el,tag2}}^{mc} - \epsilon_{\text{pd,tag2}}^{mc} \epsilon_{\text{el,tag1}}^{mc}} \quad (4.13)$$

However, this simple approach (“ABCD” method) poses a risk. Since two equations are used to determine two unknown parameters, there is always a unique solution. The validity of the solution then relies on the tagging rates being correctly simulated. Judging from the control distributions of the tagging inputs from FMD, FTS, and the Plug calorimeter, a priori, this is not a save assumption for the present analysis<sup>2</sup>.

In order to determine the elastic and proton-dissociative contributions more robustly, three tagging categories are used instead of two: the zero-tag, single-tag, and multi-tag category. Equations (4.10) and (4.11) are then extended by a third. In the presence of mismodeling of the tagging detectors, statistical, and systematic uncertainties, the three equations can not be analytically solved using MC tagging rates. Instead, a fit has to performed to determine optimal  $N_{\text{el}}$  and  $N_{\text{pd}}$  that best satisfy all three conditions. Similar considerations also apply in the presence of additional background contributions where additional constraints on the event yields come from the background control regions. As the number of events in these regions is rather small, they are only split into two tagging categories, the zero- and inclusive-tag category.

<sup>2</sup>The argument remains the same even when distributions are considered instead of total event yields because the DiffVM MC generator does not predict kinematic cross-section dependencies. Instead, those have to be tuned to data. Equations (4.10) and (4.11) then simply have to be solved independently to every bin in a considered distribution. This is achieved in the unfolding approach for the cross-section measurement; compare Chapter 7.

This fitting procedure is applied twice in the present analysis. First, it is used to determine the normalizations of the MC samples for the construction of the MC template model. Details are described in Section 5.3. Furthermore, a fit in the tagging categories is performed in the unfolding procedure for the cross-section measurement; compare Section 7.2.

Using the single- and multi-tag categories instead of the inclusive-tag category has another advantage: It provides some sensitivity to the distribution of the mass of the proton-dissociative system. The three tagging categories perform differently in different  $m_Y$  ranges. In Figure 4.24, the respective rates are shown for the  $\pi^+\pi^-$  signal MC samples as a function of  $m_Y$ . At low masses around  $m_Y \simeq 1$  GeV, most events do not obtain any tag. A single tag dominates moderate masses around  $m_Y \simeq 3$  GeV. For higher masses, increasingly two or more of the forward detectors receive a hit from the proton remnants. This is found to greatly reduce the dependence of the cross-section measurement on the MC modeling of the  $m_Y$  distribution. For the final result, using 3 instead of 2 tagging categories is found to reduce the uncertainty of the proton-dissociative cross-section associated with the  $m_Y$  shape by a factor of approximately 2.

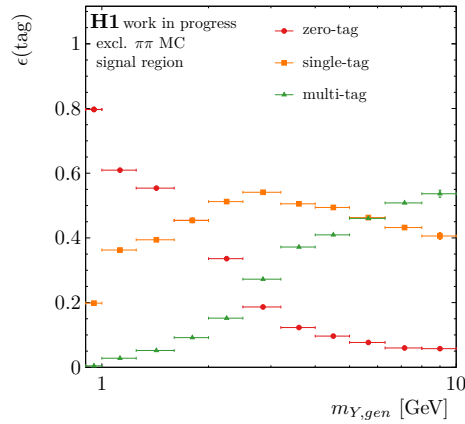


**Figure 4.24:** Zero-tag, single-tag, and multi-tag tagging rate as a function of  $m_Y$  for the elastic and dissociative  $\pi^+\pi^-$  signal MC as labeled in the legend.

### Control Plots

Throughout this section, the MC model can simultaneously describe all tagging rates reasonably. Both for the individual forward detectors and the combined tagging categories. This consistency is taken as an important validation for a reasonable modeling of the forward tagging information and for the procedure applied to normalize the elastic and proton-dissociative MC contributions. For further validation, the  $m_{\pi\pi}$ ,  $W_{\gamma p}$ , and  $t$  control distributions are shown for the three tagging categories in the signal region in Figure 4.25. Within uncertainties, the MC also reproduces the kinematic dependencies in the tagging categories quite well.

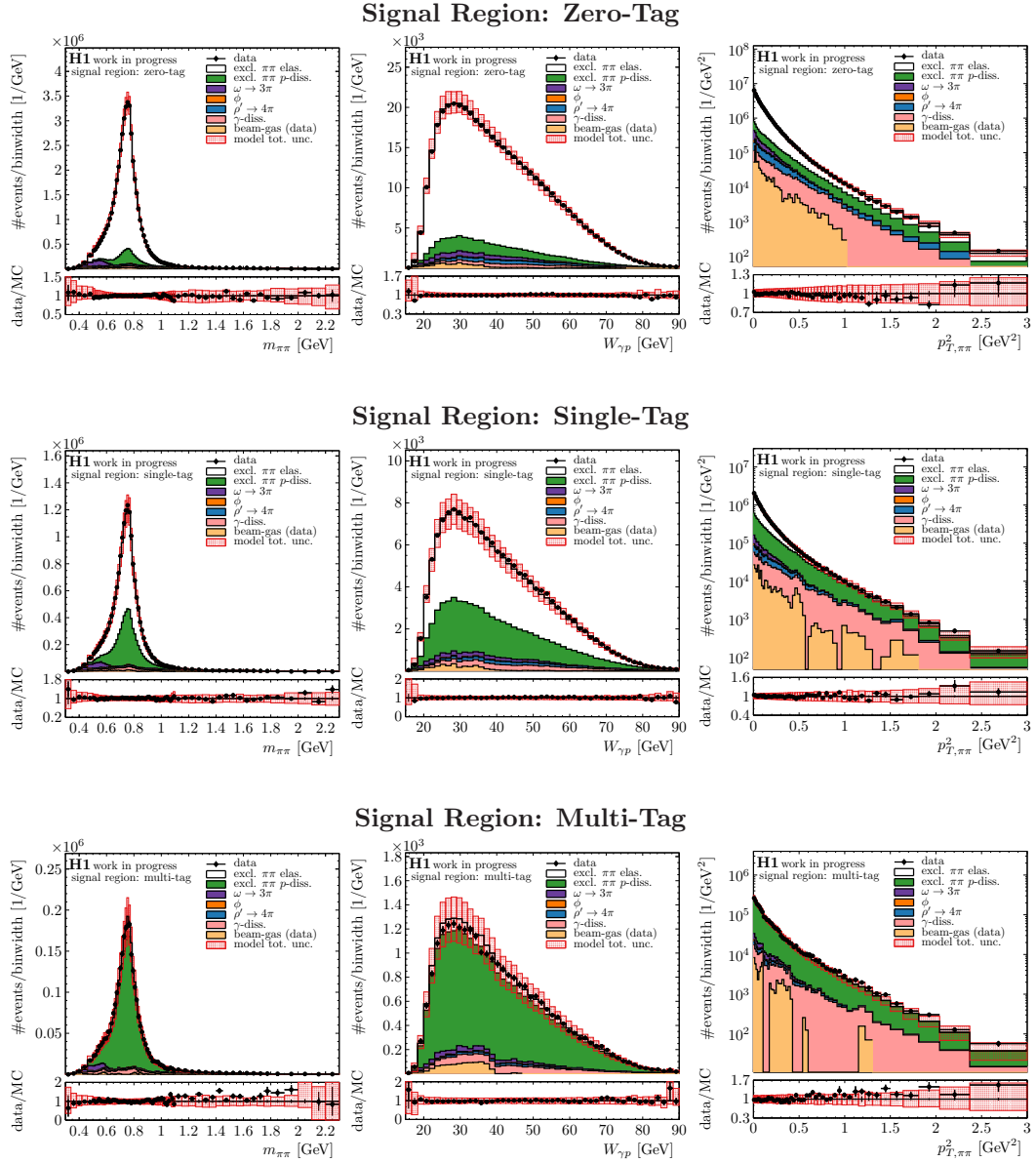


**Figure 4.25:** Control distributions for  $m_{\pi\pi}$  (left column),  $W_{\gamma p}$  (center column), and  $p_{T,\pi\pi}^2$  (right column) for events from the signal region in the zero-tag (top row), single-tag (center row), and multi-tag category (bottom row). The black data points are compared to the full MC model with stacked contributions shown as labeled in the legend.



## 5 SIMULATION OF $\pi^+\pi^-$ PRODUCTION

The present analysis relies on the simulation of  $\pi^+\pi^-$  electroproduction and various background processes at HERA and their measurement with the H1 detector. For once, simulated events that mimic the measured data are used to validate the understanding of the dataset; compare Chapter 4. More importantly, the simulation is used to model the response of the H1 detector to  $\pi^+\pi^-$  production. The detector simulation can then be used to correct the measured data distributions for detector effects; compare Chapter 7. With the corrected distributions,  $\pi^+\pi^-$  photoproduction cross-sections can be measured on *particle level*, i.e., before the final state particles have interacted with the detector. Simulated events are built in two stages: First, a Monte Carlo (MC) *event generator* is used to randomly generate events that reproduce the event rate distributions to be expected from an underlying physics model. The generated events are then processed through a *simulation* of the experimental setup, i.e., of HERA and the H1 detector.

This analysis makes use of the DiffVM event generator that is introduced in Section 5.1. The detector simulation is described in Section 5.2. In Section 5.3, the various MC samples that are used for this analysis are introduced. They model relevant signal and background processes and are combined to a template model aiming to reproduce the photoproduction H1 dataset; compare Chapter 4. For an improved description of the data, the MC samples are tuned; which is described in Section 5.4. A good description of the data is only possible once systematic model uncertainties are accounted for. The sources of systematic uncertainties considered for this analysis are discussed in Section 5.5.

### 5.1 The DiffVM Generator

This analysis uses the DiffVM [166] event generator to simulate diffractive vector meson production in  $ep$  collisions. Both elastic scattering and proton-dissociation are modeled. The description of the diffractive interaction is based on the Vector Meson Dominance Model (VDM) [117, 119, 167–169] and Regge theory. DiffVM is both used to model signal  $\pi^+\pi^-$  photoproduction as well as various diffractive background processes. The generator is briefly described in the following.

#### Vector Meson Production

DiffVM assumes the incoming electrons emit virtual photons. The  $ep$  cross-section then is modeled in terms of a photon flux  $\Phi_{\gamma/e}$  and the photon-proton cross-section  $\sigma_{\gamma^*p}$ :

$$\frac{d^2\sigma_{ep}}{dydQ^2} = \Phi_{\gamma/e}^T(y, Q^2) \sigma_{\gamma^*p}^T(W_{\gamma p}, Q^2) + \Phi_{\gamma/e}^L(y, Q^2) \sigma_{\gamma^*p}^L(W_{\gamma p}, Q^2). \quad (5.1)$$

$Q^2$ ,  $y$ , and  $W_{\gamma p}$  are the photon-virtuality, inelasticity, and photon-proton center-of-mass energy, respectively, as they are introduced in Section 2.4. For virtual photons with non-zero  $Q^2$ , both transverse and longitudinal polarization states as indicated by the superscripts  $T$  and  $L$  can contribute. The longitudinal and transverse photon flux is simulated according to the Weizsäcker-Williams approximation as introduced in Section 2.4.

The photon-proton cross-section is expressed in terms of the real photoproduction ( $Q^2 = 0 \text{ GeV}^2$ ) cross-section modified by a phenomenological  $Q^2$  dependence. For transversely

polarized photons it is parametrized as

$$\sigma_{\gamma^*p}^T(Q^2) = \sigma_{\gamma p} \left( \frac{1}{1 + \frac{Q^2}{\Lambda^2}} \right)^{n_q}, \quad (5.2)$$

with phenomenological parameters  $\Lambda$  and  $n_q$ . The longitudinal cross-section then is parametrized in terms of the transverse cross-section as

$$\sigma_{\gamma^*p}^L(Q^2) = R_{L/T} \sigma_{\gamma^*p}^T(Q^2) = \frac{\xi \frac{Q^2}{\Lambda^2}}{1 + \chi \xi \frac{Q^2}{\Lambda^2}} \sigma_{\gamma^*p}^T(Q^2), \quad (5.3)$$

with additional free model parameters  $\xi$  and  $\chi$ . In particular,  $\sigma_{\gamma^*p}^L$  vanishes for  $Q^2 \rightarrow 0$  GeV<sup>2</sup> while  $\sigma_{\gamma^*p}^T$  approaches the photoproduction cross-section. The parameters for the  $Q^2$  dependence are roughly chosen to reproduce measured cross-section distributions.  $\Lambda$  is set to the mass of the simulated vector meson. For the other parameters the values  $n_q = 2.4$ ,  $\xi = 0.42$  and  $\chi = 0.12$  are chosen. They roughly reproduce the spectra measured for  $\rho^0$  electroproduction by the H1 Collaboration [2]. Since the present analysis only considers events at low  $Q^2$  values, it is not very sensitive to the precise modeling of the  $Q^2$  dependence.

In the spirit of vector meson dominance,  $\sigma_{\gamma p}$  is assumed to be a superposition of vector meson cross-sections  $\sigma_{\gamma p}^{\text{VM}}$ . However, no assumption on the coupling between photons and vector mesons is made. Instead, every process can only be simulated independently, and the coupling is absorbed into a global normalization factor that has to be provided externally. A simple, non-relativistic Breit-Wigner function is assumed for the lineshape of the vector meson mass distributions:

$$\frac{d\sigma_{\gamma p}^{\text{VM}}}{dm}(m) \propto \mathcal{BW}_{\text{non-rel}}(m) = \frac{\Gamma_{\text{VM}}^2}{(m - m_{\text{VM}})^2 + \frac{1}{4}\Gamma_{\text{VM}}^2}. \quad (5.4)$$

In the parametrization,  $m$  is the generated invariant vector meson mass, and  $m_{\text{VM}}$  and  $\Gamma_{\text{VM}}$  are the Breit-Wigner mass and width parameters, respectively. Various decay channels can be modeled with branching-ratios again having to be provided by external measurements. The angular decay distributions are modeled under assumption of  $s$ -channel helicity conservation, where the vector mesons retain the helicity state of the photon. The mass shape of the DiffVM samples used for the present analysis is further discussed in Section 5.4.

### Pomeron Exchange

The meson-proton interaction is modeled following Regge phenomenology by considering the exchange of a single leading Pomeron trajectory

$$\alpha(t) = \alpha(0) + \alpha' t = 1 + \epsilon + \alpha' t, \quad (5.5)$$

with free parameters  $\epsilon$ , and  $\alpha'$ .  $t$  is the momentum transfer at the proton vertex as introduced in Section 2.4. The cross-section is then assumed to rise exponentially as a function of  $W_{\gamma p}$  and  $t$ :

$$\frac{d\sigma_{\gamma p}^{\text{VM}}}{dt}(W_{\gamma p}, t) = \frac{d\sigma_{\gamma p}^{\text{VM}}}{dt}(W_{\gamma p} = W_0, t = 0) \left( \frac{W_{\gamma p}}{W_0} \right)^{4(\epsilon + \alpha' t)} e^{bt} \quad (5.6)$$

Again, any couplings are absorbed into the global cross-section normalization at a reference energy  $W_0$  and zero momentum transfer. The  $t$ -dependence is parametrized by an additional parameter  $b$ . For this analysis, different values for  $\epsilon$ ,  $\alpha'$ , and  $b$  are assumed for various simulated processes. A detailed discussion follows further on in the text in Section 5.4.

### Diffractional Dissociation

DiffVM can model both elastic scattering and diffractive dissociation of the final state proton. However, the processes are simulated independently, and no assumption is made on the relative normalization. For proton-dissociation, the mass spectrum of the proton remnants  $Y$  is modeled according to

$$\frac{d\sigma}{dm_Y^2} \propto \frac{f(m_Y^2)}{(m_Y^2)^{1+\epsilon_Y}}, \quad (5.7)$$

with a free model parameters  $\epsilon_Y$ . The function  $f(m_Y^2)$  models the resonance structure of the excited proton. For low masses  $m_Y^2 \leq 3.6 \text{ GeV}^2$ ,  $f(m_Y^2)$  is obtained from a parametrization and fit of the resonance structure observed in proton-dissociative proton-deuteron scattering [170, 171]. In particular, several  $N^{*+}$  resonances observed in data are included in the model, such as the  $N(1440)$ ,  $N(1520)$ ,  $N(1680)$ , and  $N(1700)$  resonances. For resonance production, the proton decay is modeled according to the measured resonance decay modes. In the continuum regime with  $m_Y^2 \gtrsim 3.6 \text{ GeV}^2$ , the function  $f(m_Y^2)$  is set to 1 and the proton modeled as a quark-diquark system. The quark is assumed to be set free in the scattering. For the subsequent fragmentation, a Lund string model as implemented in JETSET [172] is used.

The photon can also dissociate diffractively instead of forming a bound vector meson state. This is modeled in DiffVM by assuming that the photon forms a quark-antiquark pair collinear with the photon flight direction. For the mass  $m_X$  of the diffractive system, the cross-section is expected to behave like

$$\frac{d\sigma}{dm_X^2} \propto \frac{1}{(m_X^2)^{1+\epsilon_X}} \quad (5.8)$$

with a free parameter  $\epsilon_X$ . The fragmentation is again modeled in JETSET.

From Regge theory, it is expected that diffractive dissociation is governed by triple Pomeron exchange; compare Chapter 2. The dissociative cross-section dependencies modeled by DiffVM have a simpler form. In particular, they do not model a  $t$ -dependence of the dissociative mass spectrum. For  $\epsilon_Y = \epsilon_X = 0.0808$  the Donnachie and Landshoff Pomeron intercept is chosen.

## 5.2 The H1 Detector Simulation

The H1 detector is precisely modeled and its response to particles is simulated in the H1Sim [173] program. H1Sim is based on GEANT3 [174] to simulate the interaction of particles with the detector material. Events generated by the Monte Carlo event generators are passed through the simulation to produce detector signals similar to those obtained for events observed with the real H1 detector. These signals are then processed by the standard H1 reconstruction software that is also used for real data. This provides simulated events on detector level that can be compared to measured events.

This analysis relies mainly on the central tracker and thus precise modeling of it. Unfortunately, there are some flaws in the simulation that need to be accounted for. They mostly affect the simulated detector response on trigger level and require a correction of the simulated trigger efficiencies. The trigger correction factors are derived in Chapter 6. Another known problem of the simulation is an inadequate description of nuclear interactions between particles traversing the detector and the detector material itself. Nuclear interactions are simulated with the GEISHA program, which is not reliable in the intermediate track momentum range of 100 to 500 MeV [175]; also compare the discussion by Berger [42]. Unfortunately, this range is most relevant for the process studied in this thesis. The simulated tracking efficiency is retroactively corrected for an underestimation of the nuclear

interaction cross-section [176]. The simulated tracking resolution and response of other detector components such as the calorimeters are not. Instead, conservative uncertainties are assumed to cover a potential impact on the analysis; compare Section 5.5.

### 5.3 Modeling the $\pi^+\pi^-$ Photoproduction Dataset

Several MC samples are used to model the  $\pi^+\pi^-$  photoproduction dataset that is introduced in Chapter 4. They model elastic and proton-dissociative production of  $\rho^0(770)$ ,  $\omega(782)$ ,  $\phi(1020)$ ,  $\rho(1450)$ , and  $\rho(1700)$  vector mesons, as well as photon-dissociation. All samples are generated with the DiffVM generator, and the events are propagated through the H1 simulation. Table 5.1 summarizes all used samples and lists the decay modes considered by the generator.

i	process	N events	decay modes	BR [%]
0	$\rho^0(770)$	$10^7$ elastic	$\pi^+\pi^-$	99.0
		$10^7$ $p$ -dissociative	$\pi^+\pi^-\gamma$	1.0
$\leftrightarrow$ reweighted to describe all $\pi^+\pi^-$ final states				
1	$\omega(782)$		$\pi^+\pi^-\pi^0$	89.2
		$10^6$ elastic	$\pi^0\gamma$	8.6
		$10^6$ $p$ -dissociative	$\pi^+\pi^-$	2.2
$\leftrightarrow$ $\pi^+\pi^-$ removed, included in signal				
2	$\phi(1020)$		$K^+K^-$	49.0
			$K_L K_S$	34.4
		$10^6$ elastic	$\pi^+\rho^-, \pi^-\rho^+, \pi^0\rho^0$	each 4.3
		$10^6$ $p$ -dissociative	$\pi^+\pi^0\pi^0$	2.4
$\eta\gamma$				
3	$\rho(1450)$ & $\rho(1700)$		$\rho^0\pi^+\pi^-, \rho^+\pi^-\pi^0, \rho^-\pi^+\pi^0$	each 25.0
			$\pi^+\pi^-\pi^+\pi^-$	15.0
		each $10^6$ elastic	$\pi^+\pi^-\pi^0\pi^0$	8.0
		each $10^6$ $p$ -dissoc.	$\pi^+\pi^-$	2.0
		$\leftrightarrow$ $\pi^+\pi^-$ removed, included in signal		
$\leftrightarrow$ merged $\rho(1450) : \rho(1700) = 1 : 1$				
4	$\gamma$ -dissoc.	$10^7$ elastic	JETSET	
		$10^7$ $p$ -dissociative	$\leftrightarrow$ $\pi^+\pi^-$ removed, included in signal	

**Table 5.1:** DiffVM MC samples used to model the  $\pi^+\pi^-$  photoproduction dataset. All decay modes with a branching fraction  $\gtrsim 1\%$  are simulated. For the  $\rho(1450)$  and  $\rho(1700)$  samples the branching fractions are only estimates. For the other vector meson decays the measured PDG [1] values are used. The  $\pi^+\pi^-$  final states are removed from background samples and modeled instead by reweighting the  $\rho^0$  sample.

Several of the considered processes result in an exclusive  $\pi^+\pi^-$  final state. Since they are simulated by DiffVM independently, interference effects are not considered. However, these can be quite significant. For example, the interference between the  $\rho^0$  resonance and non-resonant  $\pi^+\pi^-$  production causes a strong skewing of the  $\rho^0$  lineshape; compare Section 2.3. Better modeling of dipion production is achieved by removing the exclusive  $\pi^+\pi^-$  final state from all background samples and modifying the  $\rho^0$  samples to account for every  $\pi^+\pi^-$  contribution, instead. The modification is done in a way to include also interference contributions. The exact procedure is described below in the text in Section 5.4.1.

Redefining the  $\rho^0$  to an exclusive  $\pi^+\pi^-$  MC results in a small inconsistency with respect to the  $\rho^0 \rightarrow \pi^+\pi^-\gamma$  contribution. For technical reasons, it is kept in the sample but treated as background in the final  $\pi^+\pi^-$  cross-section measurement; compare Chapter 7. For a good description of the measured distributions, further optimizations for the MC samples are needed; these are also described in the following section.

A template model is constructed from the tuned MC samples in order to describe the measured  $\pi^+\pi^-$  photoproduction data. The two samples for  $\rho(1450)$  and  $\rho(1700)$  production are experimentally not distinguishable in the present analysis in which only two charged pions are reconstructed. They are thus merged one-to-one to a combined  $\rho'$  sample. An additional background contribution from beam-gas interactions is considered using data events from pilot bunch crossings; compare Section 4.1. The complete model then has the form:

$$\mathcal{M} = \sum_{i=0}^4 (f_i^{\text{el}} MC_i^{\text{el}} + f_i^{\text{pd}} MC_i^{\text{pd}}) + BG. \quad (5.9)$$

$MC_i^{\text{el}}$  and  $MC_i^{\text{pd}}$  are the elastic and proton-dissociative component of the  $i^{\text{th}}$  MC sample. They are scaled by factors  $f_i^{\text{el}}$  and  $f_i^{\text{pd}}$ , respectively.  $BG$  is the luminosity normalized beam-gas background contribution; compare Section 4.1. In principle, the scaling factors  $f_i^{\text{el}}$  and  $f_i^{\text{pd}}$  could be calculated from the cross-sections of the given processes and the integrated luminosity. However, for many of the considered MC processes, cross-section measurements are not available. Instead, the scaling factors are obtained by fitting the MC template to the present dataset. For the fit, the selected event yields in the signal and background control regions as they are defined in Section 4.3 are considered. In order to independently normalize the elastic and proton-dissociative MC samples, the signal region is split into three, and the background control regions into two orthogonal forward-tagging categories; compare Section 4.4. The fit is performed by varying  $f_i^{\text{el}}$  and  $f_i^{\text{pd}}$  in order to minimize the  $\chi^2$  between the event yield distribution in data  $D$  and the MC template  $\mathcal{M}$ :

$$\chi^2(f_i^{\text{el}}, f_i^{\text{pd}}) = \sum_j^{CR} \frac{(D[j] - \mathcal{M}[j])^2}{(\Delta_{\text{stat}} D[j])^2 + (\Delta_{\text{stat}} \mathcal{M}[j])^2}. \quad (5.10)$$

The fitted event yield distribution is shown in Figure 5.1. The MC scaling factors are summarized in Table 5.2.

i	DiffVM sample	scale factor	stat. unc.
0	$\rho^0(770)$ elastic	0.350	0.002
0	$\rho^0(770)$ $p$ -dissociative	0.163	0.002
1	$\omega(782)$ elastic	1.12	0.14
1	$\omega(782)$ $p$ -dissociative	0.55	0.14
2	$\phi(1020)$ elastic	0.43	0.02
2	$\phi(1020)$ $p$ -dissociative	0.32	0.02
3	$\rho(1450) + \rho(1700)$ elastic	0.80	0.06
3	$\rho(1450) + \rho(1700)$ $p$ -dissociative	0.24	0.10
4	$\gamma$ -dissociative elastic	0.21	0.03
4	$\gamma$ -dissociative $p$ -dissociative	0.21	0.05

**Table 5.2:** Scaling factors for the DiffVM samples obtained from the template fit to data that is described in the text.

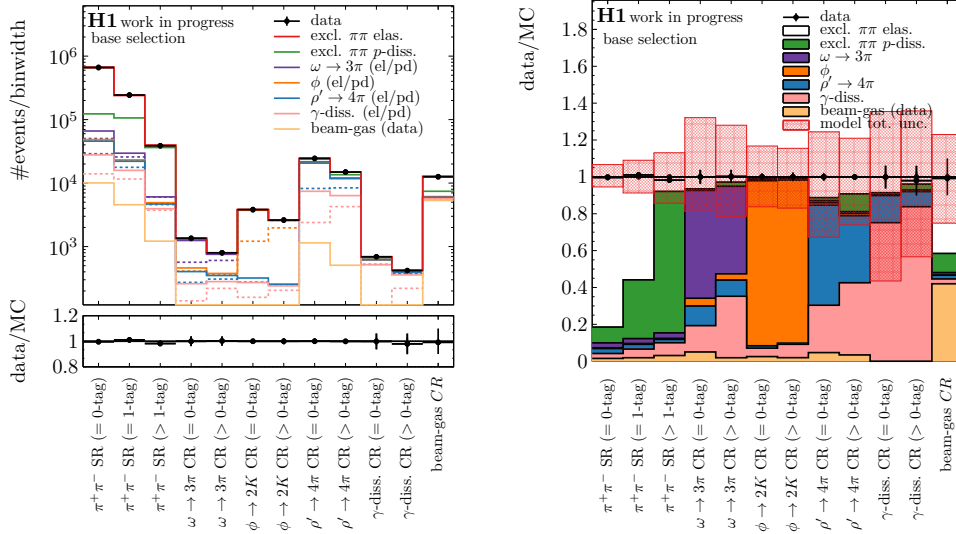


**Figure 5.1:** Event yields (left) and event fractions (right) in the signal and control regions of the  $\pi^+\pi^-$  photoproduction dataset. The MC template is fitted to the data. Individual contributions are stacked on top of one another as labeled by the legend. The dashed lines show the proton-dissociative background samples that are not listed.

## 5.4 DiffVM Sample Tuning

Besides the normalizations, DiffVM is also not predictive in the cross-section shapes and does only provide phenomenological parametrizations for the kinematic cross-section dependencies. The DiffVM distributions thus also need to be adapted to real data. The approach taken to achieve this is that all samples are first generated with a default set of model parameters. The kinematic distributions are then reweighted retroactively to describe the data distributions better. For this analysis, the reweighting serves a second essential purpose: the  $\rho^0$  sample is adapted to describe all contributions to exclusive  $\pi^+\pi^-$  production. That includes contributions from non-resonant,  $\omega$ , and  $\rho'$  production as well as interference effects between them; compare Section 2.3. In order to avoid double-counting, simultaneously all exclusive  $\pi^+\pi^-$  final states are removed from the background MC samples.

### 5.4.1 Signal $\rho^0$ MC Tuning

The generated  $m$ ,  $W_{\gamma p}$ , and  $t$  distributions of the  $\rho^0$  MC samples are simultaneously reweighted to describe the data better. The reweighting is achieved via two (multiplicative) event weights  $w_{mt}^{\text{evt}}(m_{\text{gen}}, t_{\text{gen}}; \vec{\Theta})$  and  $w_{Wt}^{\text{evt}}(W_{\text{gen}}, t_{\text{gen}}; \vec{\Theta})$  that depend on the generator level variables  $m_{\text{gen}}$ ,  $W_{\text{gen}}$ , and  $t_{\text{gen}}$  and a set of weighting parameters  $\vec{\Theta}$ .

#### $\rho^0 \rightarrow \pi^+\pi^-$ Weight

The generated  $m_{\pi\pi}$  distributions of the elastic and proton-dissociative DiffVM  $\rho^0$  samples are reweighted to the extended Söding model  $S_{\text{ext}}$  that is defined in Equation (A.3) in Section A.1. The model includes contributions from a non-resonant, an  $\omega$ , and a single  $\rho'$  amplitude and takes into account also interference effects. For the reweighting, the model parameters are assumed to be the same for the elastic and dissociative MC. The sole exception is the non-resonant phase  $\phi_{\text{nr}}$ , which is tuned independently. In Chapter 8, it is observed that the non-resonant background changes with  $t$ . That change is approximately modeled by a

$t$ -dependence of the parameter  $\Lambda_{\text{nr}}$  that is parameterized as:

$$\Lambda_{\text{nr}}(t) = 4m_\pi^2 + \Lambda_0 t. \quad (5.11)$$

Events from the  $\rho^0$  samples resulting in the exclusive  $\pi^+\pi^-$  final state are then weighted by the weight:

$$w_{mt}^{\text{evt}}(m_{\text{gen}}, t_{\text{gen}}) = \frac{\mathcal{S}_{\text{ext}}(m_{\text{gen}}, t_{\text{gen}})}{\mathcal{BW}_{\text{non-rel}}(m_{\text{gen}})} \quad (5.12)$$

The generated and tuned  $m_{\pi\pi}$  distributions of the elastic and proton-dissociative DiffVM MC samples are shown in Figure 5.2. Differences between the tuned lineshapes of the two processes are mainly due to the  $t$ -dependence of the parameter  $\Lambda_{\text{nr}}(t)$  and different  $t$  spectra.

### Diffractive Cross-Section Weight

The generated  $W_{\gamma p}$  and  $t$  distribution are also modified to describe the data better. At large  $|t|$ , the simple exponential cross-section  $t$ -dependence assumed by DiffVM does not describe the data spectra anymore. Instead, the MC distributions are reweighted to the parameterization

$$\left. \frac{d\sigma}{dt} \right|_{\text{tune}}(W_{\text{gen}}, t_{\text{gen}}) \propto \left( \frac{W_{\text{gen}}}{W_0} \right)^{4(\epsilon + \alpha' t)} \left( 1 - \frac{bt}{a} \right)^{-a}. \quad (5.13)$$

For the  $t$ -dependence, it interpolates between an exponential behavior  $\propto e^{bt}$  at low and a  $|t|^{-a}$ -behavior at high  $|t|$ . An event weight for all events in the  $\rho^0$  samples is then defined as

$$w_{Wt}^{\text{evt}}(W_{\text{gen}}, t_{\text{gen}}) = \left( \left. \frac{d\sigma}{dt} \right|_{\text{tune}}(W_{\text{gen}}, t_{\text{gen}}) \right) / \left( \left. \frac{d\sigma}{dt} \right|_{\text{DiffVM}}(W_{\text{gen}}, t_{\text{gen}}) \right) \quad (5.14)$$

All weight parameters are assumed to be independent for the elastic and proton-dissociative MC samples so that they can have different kinematic distributions. The generated and tuned  $W_{\gamma p}$  and  $t$  distributions of the elastic and proton-dissociative DiffVM MC samples are shown in Figure 5.2.

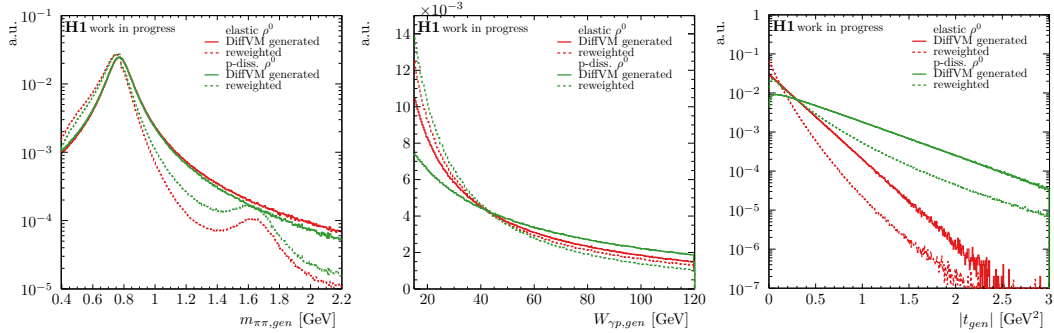


**Figure 5.2:** Generated and tuned lineshapes for the elastic and proton-dissociative DiffVM  $\rho^0$  MC sample as a function of  $m_{\pi\pi}$  (left),  $W_{\gamma p}$  (center), and  $t$  (right).

### Sample Normalization

In order to preserve the normalization of the MC samples, every sample is retroactively scaled with the average event weight:

$$w^{\text{sample}} = \frac{1}{\langle w_{mt}^{\text{evt}}(m_{\text{gen}}, t_{\text{gen}}) \cdot w_{Wt}^{\text{evt}}(W_{\text{gen}}, t_{\text{gen}}) \rangle_{\text{events}}}. \quad (5.15)$$

### Weight Parameter Optimization

In order to obtain optimal weight parameters, the weighted MC samples are fitted to the three-dimensional detector level  $m_{\pi\pi} \otimes W_{\gamma p} \otimes t$  distribution. The distribution is split into the three signal tagging categories to provide constraints on elastic and proton-dissociative reweighting parameters. For technical reasons, it is difficult to directly optimize the parameters in the fit because every variation requires a time-intensive reprocessing of the affected MC samples. Instead, optimal parameters are only approximated. The approximation is performed by starting with an initial set of parameter values and associated uncertainties. The uncertainty  $\Delta\Theta_k$  of a parameter  $\Theta_k$  then gives rise to a corresponding uncertainty of the weighted MC template:

$$\Delta\mathcal{M}_k = \mathcal{M}(\vec{\Theta} + \Delta\Theta_k \vec{e}_k) - \mathcal{M}(\vec{\Theta}) \quad (5.16)$$

Instead of fitting the parameters  $\vec{\Theta}$  directly, a  $\chi^2$  function is defined in which the template uncertainties are included via unconstrained nuisance parameters  $\vec{\beta}$ :

$$\chi^2(f^{\text{el}}, f^{\text{pd}}, \vec{\beta}) = \sum_j^{CR} \sum_l^{(t, W, m)} \frac{(D[j, l] - \mathcal{M}[j, l] - \sum_k \beta_k \Delta\mathcal{M}_k[j, l])^2}{(\Delta_{\text{stat}} D[j, l])^2 + (\Delta_{\text{stat}} \mathcal{M}[j, l])^2}. \quad (5.17)$$

The  $\chi^2$  is then minimized by varying  $\vec{\beta}$ . The scale factors  $f^{\text{el}}$  and  $f^{\text{pd}}$  depend on the weighting parameters and are thus also re-fitted. The background MC samples are constrained again by the event yields in the background control regions split into two tagging categories as described in the previous section. In an iterative procedure, the nominal weight parameters and uncertainties are varied in the direction of  $\vec{\beta}$  as obtained from the fit. Optimal weight parameters are defined by requiring they result in fitted values  $\vec{\beta} \simeq 0$ . One-sigma parameter uncertainties are estimated by requiring the fitted uncertainties to be  $\Delta\vec{\beta} \simeq \vec{1}$ . Uncertainty correlations are not considered.

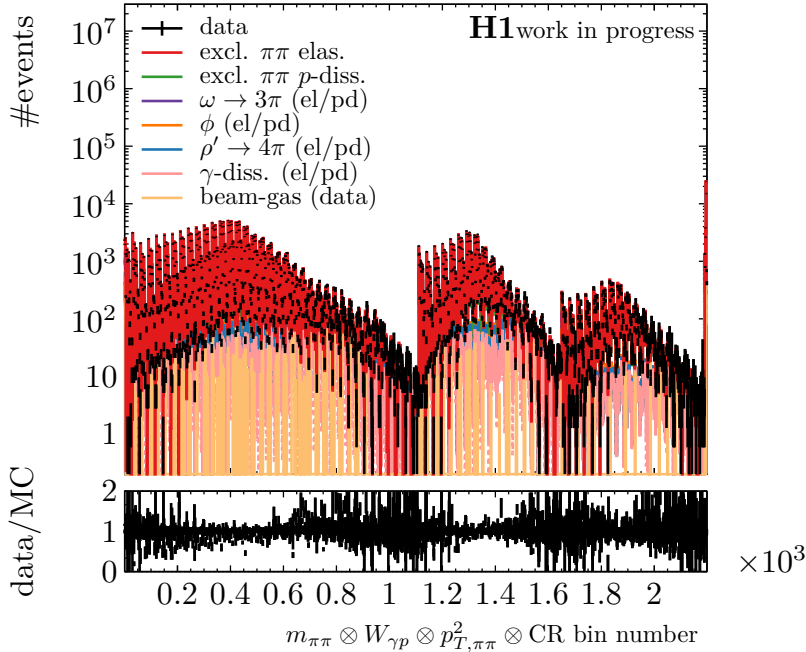


**Figure 5.3:** Tuning distributions  $m_{\pi\pi} \otimes W_{\gamma p} \otimes t$  in the  $\pi^+\pi^-$  signal region split into three tagging categories. The distributions are projected onto a one-dimensional bin-number distribution. Additional bins consider the event yields in the background control regions split into two tagging categories per region. The MC template is fitted to data. Individual contributions are stacked on top of one another as labeled in the legend.

The best tuning parameters provide a  $\chi^2/\text{ndf} = 2776/1874 = 1.5$ . The corresponding fitted distribution is shown in Figure 5.3. Considering that the tuning model is quite crude and still has to describe the three-dimensional distribution  $m_{\pi\pi} \otimes W_{\gamma p} \otimes t$  in all tagging categories, this is deemed to be good enough. Also, only statistical uncertainties are considered in the fit while generally systematic uncertainties play a dominant role for the present dataset; compare Section 5.5.

The optimal tuning parameters for the  $\rho^0$  MC samples are summarized in Table 5.3. At this point, the parameters are not required to be physical. For once, no proper fit is performed and some of the reweighting parameters are strongly correlated. Moreover, it is not clear if the model is valid for the three-dimensional cross-section as a function of  $m_{\pi\pi}$ ,  $W_{\gamma p}$ , and  $t$ . The mass reweighting parameters could be compared to those discussed in Appendix A.1. However, the assumptions on the  $t$ -dependence of the non-resonant background certainly affect the parameters obtained in the tuning. The parameters for the  $W_{\gamma p}$  and  $t$  reweighting can certainly not be compared to those measured in Section 8.2. First, the reweighting is for the full  $\pi^+\pi^-$  cross-section while in Section 8.2, only the  $\rho^0$  cross-section is analyzed. Secondly, while the reweighting is done in the full phasespace, the cross-sections are measured in the fiducial phasespace only, and the phasespace restriction significantly shapes the measured distributions; compare Section 7.1. What is surprising at first though, is that the elastic and proton-dissociative tuned values for  $\epsilon$  and  $\alpha'$  are very different and thus might appear to violate factorization. However, it is not clear if factorization should be expected to hold here. It applies to amplitudes or differential cross-sections in  $m_Y$ . However, the reweighting is done for cross-sections that are integrated over  $m_Y$ . The  $m_Y$  distribution assumed by DiffVM is simplified and does not follow the parameterization expected from a Regge approach for which factorization would hold. In particular, no  $t$ -dependence of the  $m_Y$  spectrum is assumed. It is thus not clear what the consequences of the integration are and whether  $\epsilon_{\text{pd}}$  and  $\alpha'_{\text{pd}}$  might simply compensate for a poorly modeled  $m_Y$  distribution. Furthermore, the considered phasespace extends to rather large  $|t| < 3$  GeV. It is not clear whether the Regge trajectory is linear over that range as assumed in the model. With the proton-dissociative contribution probing larger  $|t|$  on average, this might also lead to different parameter values for the (linearised) trajectory.

parameter	$w_{mt}^{\text{evt}}$		parameter	$w_{Wt}^{\text{evt}}$	
	DiffVM	tuned value		DiffVM	tuned value
$m_\rho$ [MeV]	770	$772.9 \pm 0.4$	$W_0$	90	90
$\Gamma_{\rho,0}$ [MeV]	151	$149.1 \pm 0.8$	$\epsilon_{\text{el}}$	0.0808	$0.068 \pm 0.002$
$f_{\text{nr}}$	-	$0.227 \pm 0.003$	$\alpha'_{\text{el}}$ [GeV $^{-2}$ ]	0	$0.23 \pm 0.01$
$m_\omega$ [MeV]	-	$780 \pm 1$	$a_{\text{el}}$	$\infty$	$18.2 \pm 0.6$
$\Gamma_\omega$ [MeV]	-	0.85 (PDG fix)	$b_{\text{el}}$ [GeV $^{-2}$ ]	5	$11.04 \pm 0.06$
$f_\omega$	-	$0.154 \pm 0.006$	$\epsilon_{\text{pd}}$	0.0808	$-0.061 \pm 0.005$
$\phi_\omega$	-	$-0.08 \pm 0.09$	$\alpha'_{\text{pd}}$ [GeV $^{-2}$ ]	0	$0.04 \pm 0.01$
$m_{\rho'}$ [GeV]	-	$1671 \pm 6$	$a_{\text{pd}}$	$\infty$	$7.8 \pm 0.4$
$\Gamma_{\rho'}$ [GeV]	-	$282 \pm 14$	$b_{\text{pd}}$ [GeV $^{-2}$ ]	2	$5.7 \pm 0.1$
$f_{\rho'}$	-	$0.017 \pm 0.001$			
$\phi_{\rho'}$	-	$1.64 \pm 0.07$			
$\delta_{\text{nr}}$	-	$1.47 \pm 0.01$			
$\Lambda_0$	-	$1.81 \pm 0.02$			
$\phi_{\text{nr,el}}$	-	$-0.198 \pm 0.006$			
$\phi_{\text{nr,pd}}$	-	$-0.14 \pm 0.02$			

**Table 5.3:** Parameters for reweighting the  $\rho^0$  MC samples obtained from tuning the MC model to data.

Given this ignorance about the model, no definite conclusion can be drawn as to whether the tuned parameters make physical sense. However, they result in a reasonable description of the data in all accessible variables; compare Chapter 4. Concerning the measurement performed in this thesis, the unfolding approach to extract cross-sections greatly reduces the sensitivity to the  $m_{\pi\pi}$ ,  $W_{\gamma p}$ ,  $t$  and even the  $m_Y$  distribution in the visible phasespace; compare Chapter 7. However, the limitations of the DiffVM model certainly do not allow to extrapolate measured cross-sections to regions of the phasespace that are not accessible by the analysis.

### 5.4.2 Background Sample Tuning

The mass distributions of the resonance background samples are reweighted to follow a relativistic Breit-Wigner shape:

$$\mathcal{BW}_{\text{rel}} = \frac{m\Gamma(m)}{(m^2 - m_{\text{VM}}^2)^2 + m_{\text{VM}}^2\Gamma^2(m)}. \quad (5.18)$$

A mass-dependent width is assumed. In the numerator, it accounts for the phasespace threshold. The width is calculated according to

$$\Gamma(m) = \Gamma_{\text{VM}} \left( \frac{m^2 - (n_{\text{dec}}m_{\text{dec}})^2}{m_{\text{VM}}^2 - (n_{\text{dec}}m_{\text{dec}})^2} \right)^{\frac{3}{2}} \frac{m_{\text{VM}}}{m}. \quad (5.19)$$

The formula is a simple extension from a two-body decay to decays with  $n_{\text{dec}}$  final state particles of mass  $m_{\text{dec}}$ . Strictly, this extension is invalid. Furthermore, only the dominant decay mode is considered for resonances with multiple modes. However, the approach was found to lead to an improved and reasonable description of mass related variables in the background control regions; compare Section 4.3.3. It is thus good enough for the present analysis. Event weights are then defined as

$$w_{\text{bkg}}^{\text{evt}}(m) = \frac{\mathcal{BW}_{\text{rel}}(m)}{\mathcal{BW}_{\text{non-rel}}(m)}. \quad (5.20)$$

The background samples are also reweighted in their respective  $W_{\gamma p}$  and  $t$  distributions. The weight is defined analogously to Equation (5.14), but also for the tuned distributions a simple exponential  $t$ -dependence is assumed ( $a = \infty$ ). For elastic  $\phi$  photoproduction, the ZEUS Collaboration has measured  $b_{\phi,\text{el}} = 6.3 \pm 1$  (tot.) [16]. For elastic  $\omega$  photoproduction the ZEUS Collaboration has measured  $b_{\omega,\text{el}} = 10.0 \pm 1.8$  (tot.) [19]. The parameters for the elastic  $\rho'$  and  $\gamma$ -dissociation samples are estimated to provide a good description of the measured  $p_{T,\pi\pi}^2$  distributions in the respective control regions; compare Section 4.3.3. For the  $\rho^0$  sample it is found that  $b_{\text{pd}} \simeq 0.5 b_{\text{el}}$ , which is also assumed for all background samples. For the elastic trajectories, the Donnachie-Landshoff parameters are assumed. For the proton-dissociative samples, values closer to those determined for the dissociative  $\rho^0$  sample are used. All background reweighting parameters are summarized in Table 5.4. In order to preserve the sample normalization, the background samples are also retroactively scaled by the average event weight.

### 5.4.3 Detector Level Corrections

The distribution of the  $z$ -vertex position in the simulation does not quite reproduce the data distribution. For an improved description of the data, the MC distributions are reweighted. To extract reweighting parameters, the beam-gas background is subtracted from the  $z_{\text{vtx}}$  distribution of selected data events and the original MC template model. The resulting  $z$ -vertex distributions are parametrized by the function:

$$N(z_{\text{vtx}}) = N_0 \left( e^{-\frac{1}{2} \left( \frac{z-z_0}{\sigma_z} \right)^2} + c \right). \quad (5.21)$$

	$n_{\text{dec}}$	$m_{\text{dec}}$	$b$ [GeV $^{-2}$ ]	$\epsilon$	$\alpha'$ [GeV $^{-2}$ ]
$\omega$ elas.	3	$m_\pi$	$10.0 \pm 1.8$ (5)	$0.0808 \pm 0.04$ (0.0808)	0.25 (0)
$\omega$ $p$ -diss.	3	$m_\pi$	$5.0 \pm 0.9$ (2)	$-0.0500 \pm 0.05$ (0.0808)	0.00 (0)
$\phi$ elas.	2	$m_K$	$6.3 \pm 1.0$ (4)	$0.0808 \pm 0.04$ (0.0808)	0.25 (0)
$\phi$ $p$ -diss.	2	$m_K$	$3.2 \pm 0.5$ (1.5)	$-0.0500 \pm 0.05$ (0.0808)	0.00 (0)
$\rho'$ elastic	4	$m_\pi$	$9.4 \pm 2.0$ (8/8)	$0.0808 \pm 0.04$ (0.0808)	0.25 (0/0.25)
$\rho'$ $p$ -diss.	4	$m_\pi$	$4.7 \pm 1.0$ (4/2)	$-0.0500 \pm 0.05$ (0.0808)	0.00 (0/0.25)
$\gamma$ -diss. elas.	-	-	$3.0 \pm 1.0$ (0.5)	$0.0808 \pm 0.04$ (0.0808)	0.25 (0.25)
$\gamma$ -diss. $p$ -diss.	-	-	$1.5 \pm 0.5$ (0.5)	$-0.0500 \pm 0.05$ (0.0808)	0.00 (0)

**Table 5.4:** Reweighting parameters for the background DiffVM samples. The original DiffVM production values are given in brackets.

Optimal parameters for the data and MC distributions are obtained with a  $\chi^2$  fit. The resulting values are summarized in Table 5.5. MC events with a reconstructed  $z_{\text{vtx}}$  are then weighted with the factor

$$w_{\text{vtx}}(z_{\text{vtx}}) = \frac{N_{\text{data}}(z_{\text{vtx}})}{N_{\text{MC}}(z_{\text{vtx}})}. \quad (5.22)$$

	$z_0$ [cm]	$\sigma_z$ [cm]	$c$
data	$-0.019 \pm 0.014$	$8.50 \pm 0.01$	$0.0041 \pm 0.0003$
MC	$-0.037 \pm 0.014$	$8.54 \pm 0.01$	$0.0013 \pm 0.0004$

**Table 5.5:** Parameters for reweighting the simulated  $z$ -vertex distribution.

## 5.5 Systematic Uncertainties

The MC model is not perfect. For example, in comparison to data some mismodeling is observed that is not covered by statistical uncertainties alone; compare Chapter 4. However, more generally, it can not be expected to be. The underlying DiffVM event generator has many known limitations, as has the simulation of the H1 detector. In order to account for these limitations, systematic uncertainties are assigned to the model.

Deriving meaningful systematic uncertainties for this analysis is challenging. The high statistical precision of the  $\pi^+\pi^-$  photoproduction dataset at hand ideally requires the MC models and the detector to be understood on a similar level of precision. This in particular means that any mismodeling with an impact on the cross-section measurement of the size of the statistical uncertainty or larger need to be understood and the effect size and potential kinematic dependencies covered by appropriate systematic uncertainties. Such a detailed understanding could not be achieved in the context of this thesis. The study of the trigger mismodeling that is documented in Chapter 6 illustrates the challenges or even impossibility of assigning *good* uncertainties in the absence of a reliable control-region with sufficient statistical precision. As a consequence of these challenges, uncertainties for known limitations are often only estimated to cover the respective effect sizes approximately. Beyond that, it can not always be ensured that shapes and kinematic dependencies are also meaningfully covered.

Two types of mismodeling are considered: such that affect the model underlying the DiffVM event generator and such that are present in the detector simulation. Uncertainties on the DiffVM model are estimated by reweighting the generated kinematic distributions of the MC samples. Uncertainties on the detector simulation are estimated by either varying the

detector response to the MC events or by simultaneously varying the selection in MC and data.

### Model Uncertainties

The parameters for re-weighting the MC samples as described in Section 5.3 are independently varied up and down by the uncertainties listed in Table 5.3 and Table 5.4. Uncertainties on the  $Q^2$  and  $m_Y$  dependences of the MC samples are estimated following the procedure described in Reference [24]. The  $Q^2$  dependence of the MC samples is varied by applying a weight  $(1 + Q_{\text{gen}}^2/m_{VM}^2)^{\pm 0.09}$ . And the  $m_Y$  dependence of the proton dissociative sample is varied by applying a weight  $(1/m_{Y,\text{gen}}^2)^{\pm 0.15}$ .

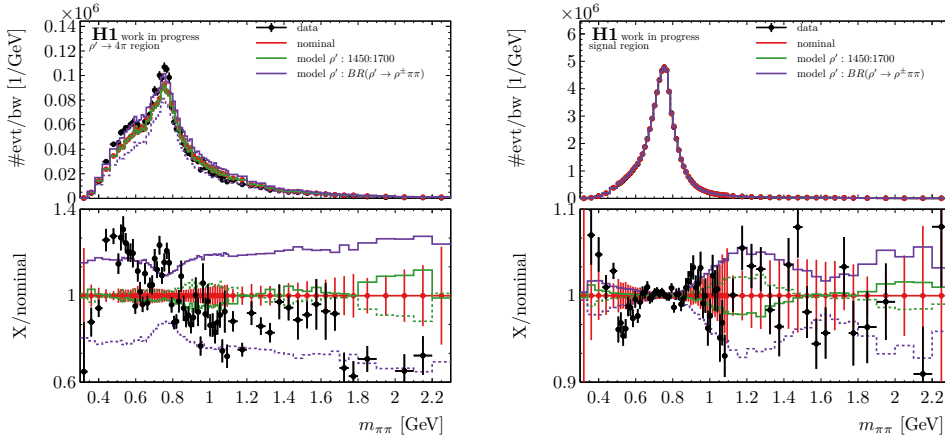


**Figure 5.4:** Impact of the variation of the  $\rho'$  mass and branching fraction on the reconstructed di-pion mass in  $\rho'$  control region (left) and the signal region region (right).

For the  $\rho'$  background MC samples, further model uncertainties are considered for the relative  $\rho(1450)$  and  $\rho(1700)$  contributions and resonance decay modes. The first is estimated by varying the relative  $\rho(1450) : \rho(1700)$  weight from 1:1 up and down to 2:1 and 1:2, respectively. An uncertainty on the  $\rho'$  decay channels is estimated by varying  $BR(\rho' \rightarrow \rho^\pm \pi^\mp \pi^0) = (0.50 \pm 0.25)\%$  while simultaneously scaling all other decay modes proportionally. The impact of these variations on the  $m_{\pi\pi}$  distribution in the signal and  $\rho'$  control region is shown in Figure 5.4. The mismodeling in the  $m_{\pi\pi}$  distribution in the  $\rho'$  control region is roughly enclosed by the variation of the branching fraction. But the variation does not provide the correct shape. Neither could another configuration of varied branching fractions. It is assumed, that the difference in the line-shape originates from a  $\rho' \rightarrow \rho^0 \pi^0 \pi^0$  mode, which is not included in the MC sample, at all. This could not be further investigated in the context of this thesis.

A shape uncertainty on the mass distribution of the photon-dissociative mass is conservatively estimated by reweighting the distribution by  $(1/m_{X,\text{gen}}^2)^{\pm 0.15}$ . This mostly affects the normalization of the photon-dissociative sample. The reconstructed  $\pi^+\pi^-$  mass appears to be largely decoupled from  $m_X$ .

### Simulation Uncertainties

An uncertainty of 20% on the simulated track  $p_T$  resolution is assumed [176]. It is applied on the signal  $\pi^+\pi^-$  MC samples only by smearing the reconstructed track  $p_{T,\text{rec}}$  with respect to the generated true  $p_{T,\text{gen}}$ :

$$p_{T,\text{rec}} \rightarrow p_{T,\text{rec}} \pm 0.2 (p_{T,\text{rec}} - p_{T,\text{gen}}). \quad (5.23)$$

	tagging rate ( $p$ -dissociative samples )	noise rate (elastic samples)
tag <sub>F<sub>TS</sub></sub>	5%	50%
tag <sub>Plug</sub>	5%	100%
tag <sub>F<sub>MD</sub></sub>	5%	5%

**Table 5.6:** Uncertainty on the tagging rate and noise for the FTS, Plug and FMD tag that are applied to proton-dissociative and elastic MC samples, respectively.

The track  $p_{z,rec}$  and  $\phi_{rec}$  as well as the reconstructed vertex are preserved by the procedure. The smearing is applied track-by-track and event-by-event and the impact is propagated to all kinematic variables reconstructed directly from the two pion four-momenta. Similarly, a 20% uncertainty is assumed on the resolution of the polar angle measurement. It is applied to the signal  $\pi^+\pi^-$  MC samples only by smearing the reconstructed track  $\theta_{rec}$  with respect to the generated true  $\theta_{gen}$ :

$$\theta_{rec} \rightarrow \theta_{rec} \pm 0.2 (\theta_{rec} - \theta_{gen}). \quad (5.24)$$

The track  $p_{T,rec}$  and  $\phi_{rec}$  as well as the reconstructed vertex are preserved by the procedure. The smearing is applied track-by-track and event-by-event and the impact is propagated to all kinematic variables reconstructed directly from the two pion four-momenta. The uncertainties aim to cover the effect the mismodeling of the nuclear interaction cross-section has on the tracking resolution, as well as potential inhomogeneities of the  $B$ -field that might affect the track  $p_T$  measurement.

The energy scales of the LAr and SpaCal clusters are independently varied by  $\pm 10\%$ . The variations are assumed to be independent of the cluster energies in the energy range that is relevant for this analysis. The variations are applied before the respective cluster noise cut is applied. The impact of the variations on the energy deposits in LAr and SpaCal not associated to a track is shown in Figure 5.5. The variations are more conservative than the actual energy resolution provided by the detectors and aim to also cover the impact of the mismodeling of nuclear interactions on calorimeter variables.

Uncertainties on the trigger correction factors are considered as discussed in Chapter 6. They cover parameter uncertainties for the parametrizations of the correction factors, as well as an uncertainty to account for phasespace effects when applying correction factors derived in DIS to the photoproduction event topology. The uncertainties related to the correction of the central tracker CIP+FTT trigger elements are shown in Figure 5.6.

In order to estimate an uncertainty on the forward tagging, the tagging rates and noise levels of the FTS, Plug and FMD detectors are independently varied. For the tagging rate uncertainty, the tagging rate of the proton-dissociative MC samples is scaled down by randomly discarding a fraction of events with positive tags. Similarly, to estimate the noise uncertainty the noise level in the elastic MC samples is scaled down by randomly discarding a fraction of events with a positive tag. The relative uncertainties for the tagging rates and noise levels of the three detectors are summarized in Table 5.6. They are roughly estimated so that data-MC discrepancies in the individual tagging rates are covered by the systematic uncertainty band; compare the figures in Section 4.4. No kinematic dependence is assumed.

An uncertainty on the MC  $z$ -vertex distribution is estimated by independently varying the  $z$ -vertex reweighting factors within the uncertainties listed in Table 5.5.

### Selection Uncertainties

The noise cut on LAr and SpaCal energy clusters is independently varied up and down to 800 MeV and 400 MeV, respectively, corresponding to the noise uncertainty assumed in Reference [177].

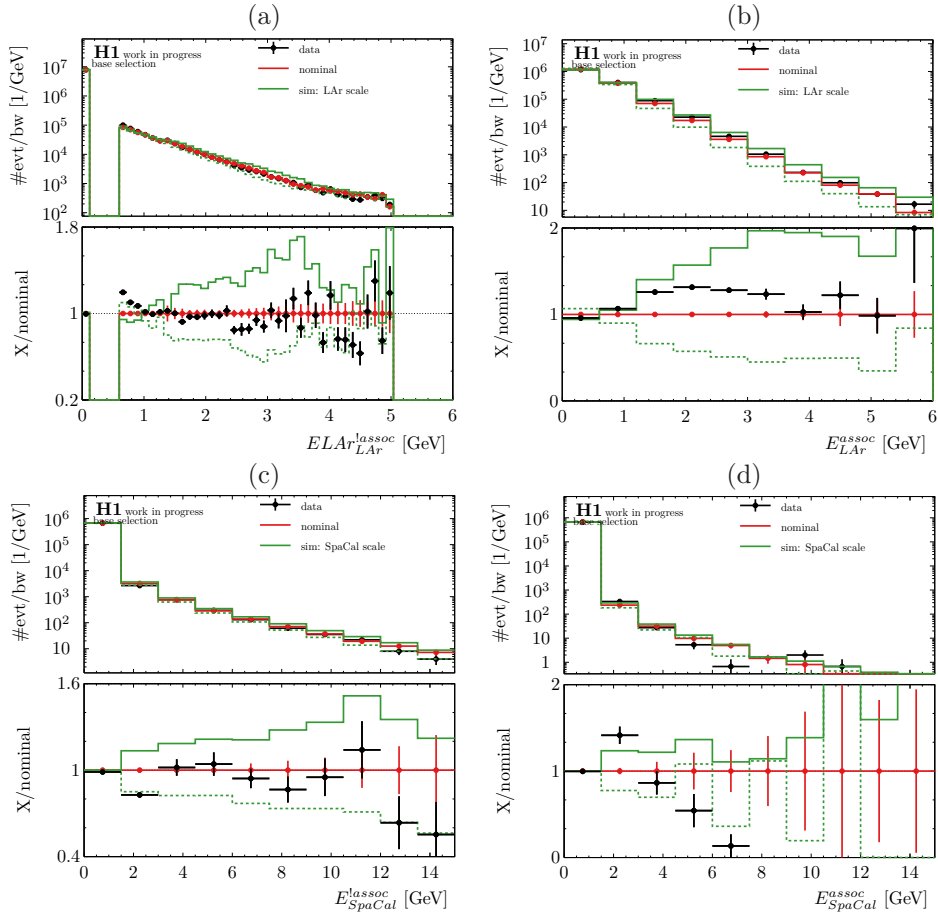


**Figure 5.5:** Impact of the LAR and SpaCal energy scale variations of the respective total energy deposits for events satisfying the base selection. (a) SpaCal energy associated to the tracks, (b) SpaCal energy not associated to the tracks, (c) LAR energy associated to the tracks, and (d) LAR energy not associated to the tracks. The black data points are compared to the nominal and varied MC samples as labeled by the legend.

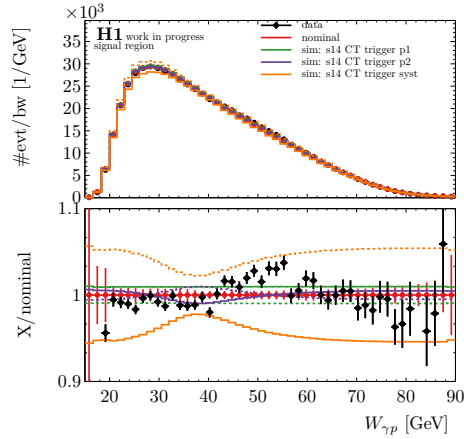


**Figure 5.6:** Uncertainties for the CIP & FTT trigger elements correction as a function of  $W_{\gamma p}$  for events in the  $\pi^+\pi^-$  signal region. The black data points are compared to the nominal and varied MC samples as labeled by the legend.

The cut applied for associating clusters to tracks is varied up and down to 70 cm and 50 cm, respectively. This estimates a potential impact from wrongly assigning clusters from secondary particles due to nuclear interactions to the two pion tracks. The cover a potential mismodeling of the nuclear interactions in the simulation; compare Figure 4.6.

In the particle identification, the cut on the Kaon, Proton, and Deuteron  $dE/dx$  rejection likelihoods is varied up and down to 0.12 and 0.08. Simultaneously, the cut on the pion  $dE/dx$  selection likelihood is varied down and up to  $10^{-10}$  and  $10^{-8}$ , respectively.

The veto on the number of forward tracks is varied up and down to allow either zero or up to two tracks in the forward tracking detector.

The geometric acceptance of the CJC in  $\theta$  and  $p_T$  is independently varied. The  $\theta$ -acceptance cut is varied up and down to  $20^\circ < \theta < 160^\circ$  and  $30^\circ < \theta < 150^\circ$ , respectively. The  $p_T$  acceptance cut is varied up to  $p_T > 180$  MeV. The  $\theta$  variation is also meant to cover a potential mismodeling of the impact of the two pions on the forward and backwards trigger vetoes; compare Chapter 6.

### Normalization Uncertainties

Normalization uncertainties are only applied to the unfolded cross-sections. The luminosity is measured with a 2.7% uncertainty [165]. The uncertainty on the track reconstruction efficiency is 1% per track [176]. No kinematic dependency is assumed and both tracks are affected coherently. For the two tracks in the analysis, this results in a 2% overall normalization uncertainty.

### Others

A 25% uncorrelated normalization uncertainty is assumed for the beam-gas background templates corresponding to the variance of the pilot bunch event weights.

### Uncertainty Calculation

Uncertainties are calculated from the MC variations. Most variations are two-sided resulting in two-sided systematic uncertainties. If  $\mathcal{M}_{\text{nom}}$  is the nominal MC template and  $\mathcal{M}_{\text{up}}$  and  $\mathcal{M}_{\text{dn}}$  a systematic up and down variation, the associated up and down uncertainty is calculated as:

$$\mathcal{M}_{\text{nom}} \pm \Delta_{\text{syst}}^{\text{up/dn}} = \mathcal{M}_{\text{nom}} \begin{matrix} +(\mathcal{M}_{\text{up}} - \mathcal{M}_{\text{nom}}) \\ -(\mathcal{M}_{\text{nom}} - \mathcal{M}_{\text{dn}}) \end{matrix}. \quad (5.25)$$

In particular, two-sided variations are not symmetrized. One-sided systematic variations  $\mathcal{M}_{\text{var}}$  are always symmetrized to give a two-sided uncertainty:

$$\mathcal{M}_{\text{nom}} \pm \Delta_{\text{syst}} = \mathcal{M}_{\text{nom}} \pm (\mathcal{M}_{\text{var}} - \mathcal{M}_{\text{nom}}). \quad (5.26)$$

For the control plots presented in Chapter 4, a special procedure is applied to the selection uncertainties that arise from simultaneous variations of data and the MC template. In order to give a more realistic representation of the actual impact of the selection uncertainties on the final result, only the relative variation between the MC sample and the data is included as a MC uncertainty. For a one-sided variation it is calculated as:

$$\mathcal{M}_{\text{nom}} \pm \Delta_{\text{syst}}^{\text{sel}} = \mathcal{M}_{\text{nom}} \pm \left( \frac{\mathcal{M}_{\text{var}}}{\mathcal{D}_{\text{var}}} - \frac{\mathcal{M}_{\text{nom}}}{\mathcal{D}_{\text{nom}}} \right) \mathcal{D}_{\text{nom}}, \quad (5.27)$$

and correspondingly for two-sided variations. The propagation of uncertainties through the unfolding for the final cross-section uncertainties is described in Chapter 7.



## 6 TRIGGER SIMULATION CORRECTION

The  $\pi^+\pi^-$  photoproduction data sample that is used for the cross-section measurement presented in this thesis is collected with the H1 **s14** subtrigger. The **s14** subtrigger is a dedicated track-based  $\pi^+\pi^-$  photoproduction trigger using mainly FTT and CIP trigger elements. From past analyses, it is known that the modeling of the trigger elements by the simulation is flawed and needs to be corrected retroactively [41, 149, 177]. The correction factors derived in those past analyses can not be reused for this measurement. The analysis by Weber [41] is based on a different dataset that was collected in 2005. The detector conditions then were very different compared to the 2006/2007 running periods during which the present dataset was recorded. Notably, different high voltage settings in the CJC resulted in a significantly different FTT performance. The correction factors used in Reference [177] can also not be used because a different unfolding approach is taken in the present analysis compared to the reference. In particular, the present approach requires a different treatment of correction factors for elastic and proton-dissociative events. Instead, a dedicated study of the **s14** performance is conducted for this thesis. It results in the derivation of dedicated scaling factors to correct the mismodeling of the trigger simulation for the present measurement.

The performance of the trigger is studied in an independent  $\pi^+\pi^-$  sample from deep inelastic scattering (DIS) events. The sample is selected using independent triggers based on the detection of the scattered electron in the SpaCal. The DIS  $\pi^+\pi^-$  dataset used for the trigger study is introduced in Section 6.1. The performance of the FTT, the **s14** subtrigger, and its constituting trigger elements is analyzed in data and MC in Section 6.2. Indeed, some mismodeling is observed, and trigger scaling factors to correct the simulation are derived in Section 6.3.

### 6.1 DIS $\pi^+\pi^-$ Data Set

The DIS  $\pi^+\pi^-$  sample is collected from the 2006/2007 high-energy positron run period using a combination of L1 subtriggers that are solely based on SpaCal information. The employed triggers all require a local energy deposit in the SpaCal but at different energy thresholds of either 6 GeV or 9 GeV. They also consider different geometric trigger regions in the SpaCal, effectively probing different ranges of the electron scattering angle  $\theta_e$ . The subtriggers are all independently scaled down. In combination with the topological requirements, this would result in discontinuities in the measured data spectra. These are removed by weighting data events with appropriate prescale correction factors.<sup>1</sup>

#### Event Reconstruction and Selection

The event selection for the DIS  $\pi^+\pi^-$  sample mimics the selection for photoproduction signal events that is described in Section 4.3. Mostly the electron veto and cuts on the SpaCal energy deposits are replaced by an electron selection. Also, some background rejection and

---

<sup>1</sup>The H1 subtriggers **s0**, **s1**, **s2** and **s3** are used and combined with a logical OR. While the raw trigger conditions are partially inclusive, the actual triggers could fire independently because of different scale factors. In the considered run period, the average scale factors are 5.2, 31.5, 1.5, and 1 for the four subtriggers, respectively. Data events are weighted to correct for the combined scale factor. The weight is calculated by taking overlaps between the triggers into account following the procedure described by Sauter [178, Appendix E].

**s14** performance improvement cuts are not applied in the DIS sample. All selection cuts are summarized in Table B.1 in Appendix B. For the electron selection, a single electron candidate has to be found in the SpaCal. Candidates within ill-performing SpaCal regions are rejected following the selection procedure by Jung [179]. In order to ensure that a candidate is really the scattered electron, the associated cluster energy has to pass the cut  $E_{\text{SpaCal},e'} > 17$  GeV. For large scattering angles, the scattered electron can traverse the central tracker. In order to study the **s14** subtrigger performance in a two-track topology similar to  $\pi^+\pi^-$  photoproduction this is to be avoided. The radial position of the electron trajectory at the edge of the CIP  $z_{\text{CIP}}$  can be calculated from the scattering angle  $\theta_{e'}$  and under consideration of the reconstructed  $z$ -vertex position:

$$r_{\text{CT},e'} = \tan(\pi - \theta_{e'}) \cdot (z_{\text{vtx}} - z_{\text{CIP}}). \quad (6.1)$$

In order to avoid the electron penetrating the CIP and thus any other component of the central tracker relevant for the **s14** subtrigger,  $r_{\text{CT},e'} < 16$  cm is required. Cutting on  $r_{\text{CT},e'}$  is found to perform better than a simple cut on  $\theta_{e'}$  to keep the electron out of the CI, because of the large variation of the  $z_{\text{vtx}}$  position.

The kinematics of elastic  $\pi^+\pi^-$  production are over-constrained with the detection of the scattered electron. The energy of the scattered electron can be reconstructed with higher resolution from the scattering angle  $\theta_{e'}$ :

$$E_{e'} = \frac{2e_E - E_{\pi\pi} + p_{z,\pi\pi}}{1 - \cos(\theta_{e'})}, \quad (6.2)$$

where  $E_e$  is the electron beam energy. Furthermore,

$$Q^2 = 4E_e E_{e'} \cos^2\left(\frac{\theta_{e'}}{2}\right), \quad (6.3)$$

$$W_{\gamma p} = |p + e - e'|, \quad \text{and} \quad (6.4)$$

$$t \simeq -(p_{T,\pi\pi} + e'_T)^2, \quad (6.5)$$

where  $p$  and  $p'$  and  $e$  and  $e'$  are the four vectors of the incoming and scattered proton and electron, respectively, and  $E_{\pi\pi}$ ,  $p_{T,\pi\pi}$  and  $p_{z,\pi\pi}$  denote the energy, and the transverse and longitudinal momenta of the  $\pi^+\pi^-$  system, respectively.

The visible DIS phasespace varies slightly compared to the considered photoproduction phasespace. It is defined in terms of the reconstructed  $Q^2$ ,  $m_{\pi\pi}$ ,  $W_{\gamma p}$ , and  $t$  in Table 6.1. The range in  $Q^2$  is implicitly restricted by the SpaCal acceptance and the requirement to keep the scattered electron out of the central tracker. The considered range in the invariant  $\pi^+\pi^-$  mass is explicitly limited to the region around the  $\rho^0$  mass peak so that background processes can be neglected. The visible  $W_{\gamma p}$  range is determined by the CJC acceptance in the polar angle. In DIS, the acceptance allows for higher  $W_{\gamma p}$  values compared to photoproduction because of the larger momentum transfer at the electron vertex. The  $t$ -range in DIS is chosen to match the photoproduction phasespace.

min		variable		max
2.5	<	$Q^2$ [GeV <sup>2</sup> ]	<	20
0.6	<	$m_{\pi\pi}$ [GeV]	<	1.0
20	<	$W_{\gamma p}$ [GeV]	<	180
-3	<	$t$ [GeV <sup>2</sup> ]	<	0

**Table 6.1:** Phasespace for the DIS  $\pi^+\pi^-$  dataset defined in terms of  $m_{\pi\pi}$ ,  $W_{\gamma p}$ ,  $t$ , and  $Q^2$ .

## Control Plots

The data is compared to an MC model of exclusive elastic and proton-dissociative  $\pi^+\pi^-$  events. Contributions from misreconstructed background processes are not considered. Like the photoproduction samples, the DIS MC samples are tuned in  $m_{\pi\pi}$ ,  $W_{\gamma p}$ , and  $t$  describe the data better [149]. The respective elastic and proton-dissociative normalizations are determined using the tagging information from the forward detectors; compare Section 5.3 and Section 4.4, but in DIS only two tag categories are used. Control distributions for  $Q^2$ ,  $m_{\pi\pi}$ ,  $W_{\gamma p}$ , and  $t$  are shown in Figure 6.1. The data distributions are compared to the nominal MC models. Systematic uncertainties are not evaluated. Generally, the agreement seems reasonable within statistical uncertainties.

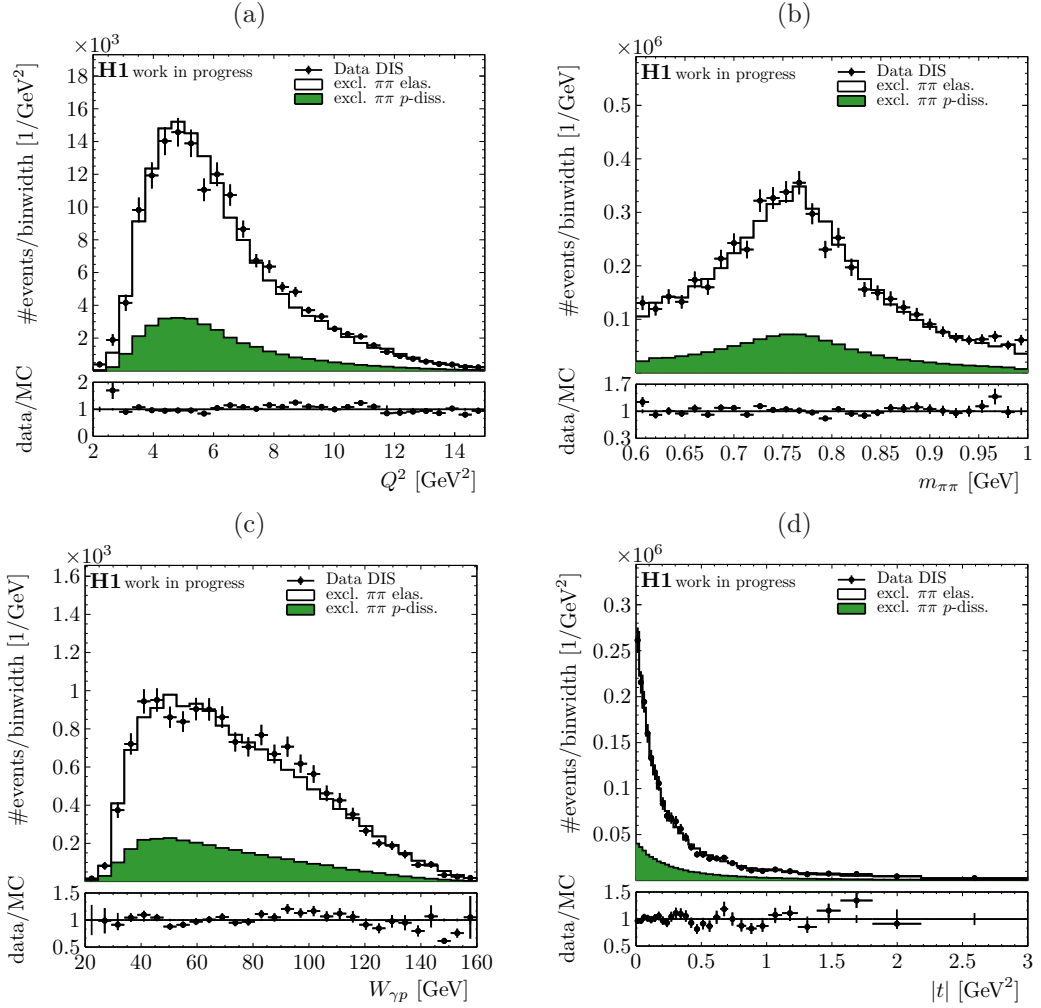


**Figure 6.1:**  $Q^2$  (a),  $m_{\pi\pi}$  (b),  $W_{\gamma p}$  (c), and  $t$  (d) control distributions in the DIS  $\pi^+\pi^-$  sample. The black data points are compared to the MC model with contributions from elastic and proton-dissociative  $\pi^+\pi^-$  production as labeled in the legend. Systematic uncertainties are not evaluated, and only the statistical data and MC uncertainties are shown.

## DIS vs Photoproduction Topology

The event topology and kinematics of the two pions in the DIS and photoproduction samples are compared in Figure 6.2. The distributions are shown for selected signal events from the  $\pi^+\pi^-$  MC that satisfy either the DIS selection criteria described in this chapter and the photoproduction criteria described in Chapter 4.

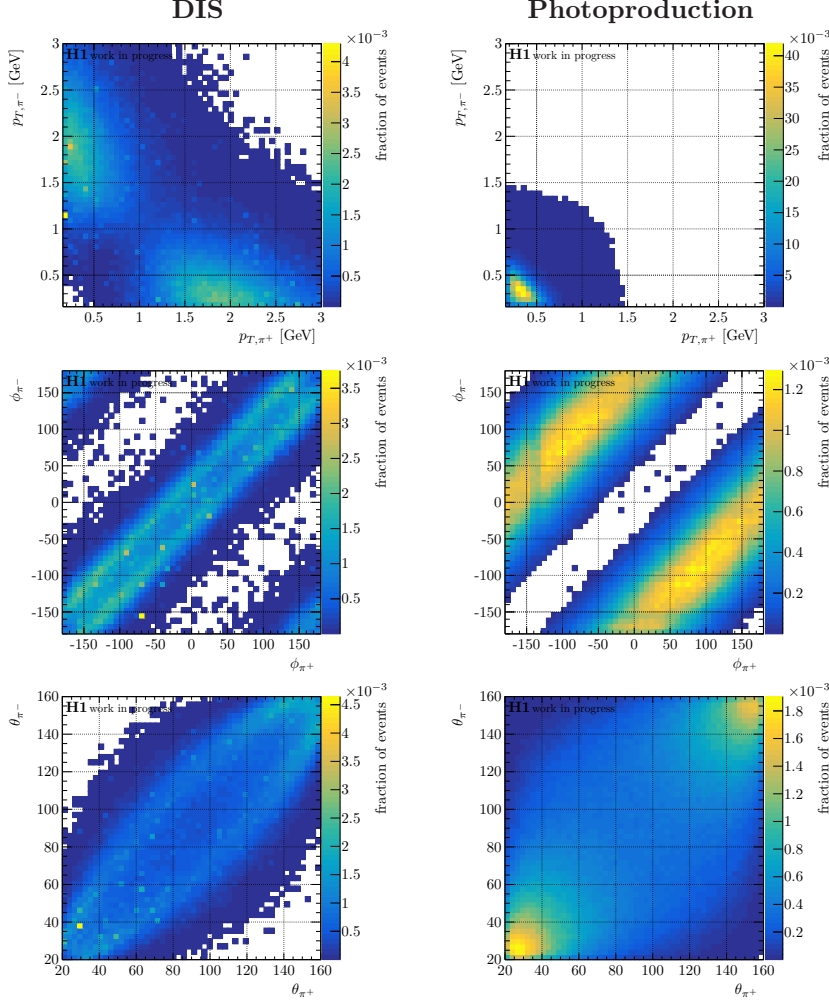


**Figure 6.2:** Di-pion kinematics and topology for events from the  $\pi^+\pi^-$  signal MC samples that satisfy the DIS (left column) or photoproduction selection (right column). The 2D generator level distributions of the negative against the positive pion  $p_T$  (top) ,  $\phi$  (center), and  $\theta$  (bottom) are shown.

The topologies are very different. In DIS, the  $\rho^0$  meson obtains a large transverse boost from the momentum transfer at the electron vertex. The angular structure of  $\rho^0$  electroproduction and decay is such that the two pions emerge primarily in and opposite to the flight direction of the  $\rho^0$  meson in the lab frame [180]. As a result, there is only a small transverse opening angle between the two tracks as well as a large imbalance in their respective transverse momenta. In photoproduction, on the other hand, the  $\rho^0$  meson has a very small transverse momentum. Consequently, also both pions have small transverse momenta and emerge back-to-back in the transverse plane. The difference in the DIS and photoproduction  $\pi^+\pi^-$  kinematics is of great relevance for applying trigger correction factors derived in DIS to the photoproduction samples because the trigger performance strongly depends on the  $\pi^+\pi^-$  kinematics and topology.

## 6.2 s14 Subtrigger Performance

### Trigger Definition

The `s14` trigger is constituted from several L1 trigger elements. The exact composition used in the online trigger changed slightly in between run periods and for the actual analysis a unified offline definition is used:

$$\begin{aligned}
 \text{s14}_{L1} = & \text{CIP\_T0} \ \&\& \text{CIP\_sig}>2 \ \&\& \text{CIP\_mul}<6 \\
 & \&\& \text{FTT\_mul\_Tb}>1 \ \&\& \text{FTT\_mul\_Ta}<4 \ \&\& \text{FTT\_chg\_1} \\
 & \&\& \text{!LAr\_IF} \ \&\& \text{!FTi2\_G1} \\
 & \&\& \text{!SPCLh\_AToF\_E\_1} \ \&\& \text{!SPCLh\_ToF\_E\_2} \\
 & \&\& \text{!BToF\_VETO} \ \&\& \text{!SToF\_BG} \ \&\& \text{!VETO\_BG}
 \end{aligned}
 \tag{6.6}$$

The central trigger elements come from the FTT and CIP. The  $\pi^+\pi^-$  event topology is selected by the FTT trigger requirements. At least 2 L1 FTT tracks above a transverse momentum threshold of  $p_T > 160$  MeV (`FTT_mul_Tb>1`) and at most 3 tracks above a threshold of  $p_T > 100$  MeV are required (`FTT_mul_Ta<4`). The summed charge of all FTT tracks must not exceed  $\pm 1e$  to ensure that two of the tracks have opposite charge (`FTT_chg_1`). The CIP has to provide the right timing (`CIP_T0`), and the CIP significance and multiplicity have to meet the requirements for  $ep$  interactions (`CIP_sig>2` and `CIP_mul<6`). Two vetoes on a significant energy deposit in the inner forward LAr trigger tower (`!LAr_IF`) and on activity in the FTi2 scintillator wall (`!FTi2_G1`) limit the forward energy flow and thus ensure the diffractive nature of the events. The trigger is complimented by various standard H1 vetoes against events from beam-gas and beam-machine interactions from outside the detector.

Most of these trigger elements are not part of the SpaCal triggers used for selecting the DIS data sample and thus their performance can be studied without introducing a bias. In particular the SpaCal vetoes (`!SPCLh_AToF_E_1` and `!SPCLh_ToF_E_2`) are on energy deposits in the *hadronic* section of the SpaCal and thus are not affected by the DIS selection because the scattered electron deposits energy in the electromagnetic section only. An overlap between the triggers exists however for the global H1 vetoes `!BToF_VETO`, `!SToF_BG`, and `!VETO_BG`. These then can not be investigated with the DIS dataset at hand and are assumed to be either well modeled or to have negligible impact on the analysis.

### Trigger Performance

In the following, trigger efficiencies for individual trigger elements and combinations thereof are defined with respect to the full  $\pi^+\pi^-$  signal selection:

$$\epsilon_{\text{trigger}} = \frac{N(\text{trigger accept} \ \&\& \ \text{selected})}{N(\text{selected})}
 \tag{6.7}$$

The overall trigger efficiencies for the `s14` subtrigger and the trigger elements constituting it are shown in Figure 6.3. The efficiency measured in the DIS data sample is compared to the efficiency measured with the corresponding MC model. The figure shows large discrepancies between data and the MC that can be traced back to a significant mismodeling of the CIP and FTT trigger elements. The LAr veto is superseded by the event selection and thus almost fully efficient and overall well described. The FTi2 veto is not implemented in the trigger emulation at all and thus is fully efficient in the MC. In data, however, a significant amount of proton-dissociative events are rejected by the veto<sup>2</sup>. The SpaCal vetoes appear to be almost fully efficient in both data and the MC.

<sup>2</sup>The offline selection limiting the energy deposit in the forward region of the LAr ensures that no non-diffractive events are selected. The inefficiency is thus solely attributed to a rejection of diffractive dissociation events.

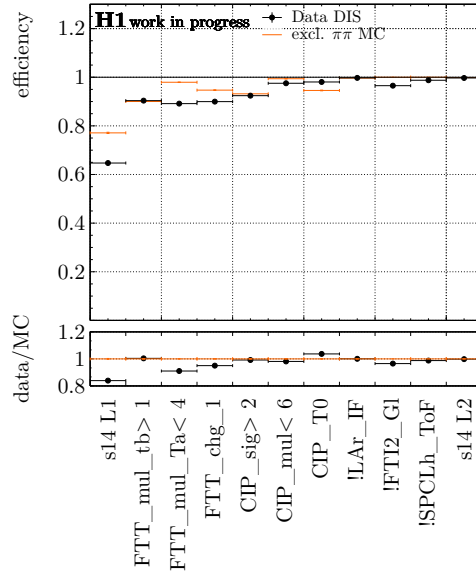


**Figure 6.3:** Efficiencies of the **s14** subtrigger and the trigger elements constituting it as measured in the DIS  $\pi^+\pi^-$  sample. The black data points show the efficiencies measured in data and are compared to the orange MC model. Only statistical uncertainties are shown.

In order to be able to perform a meaningful cross-section measurement, the mismodeling of the trigger efficiency needs to be corrected. This is challenging because the efficiencies and in particular the data-MC discrepancies have strong kinematic dependencies. Furthermore, the kinematics of photoproduction and DIS events are very different. If correction factors are to be derived from the DIS sample, they need to be defined in such a way that these differences factorize out. For  $\pi^+\pi^-$  events, the FTT and CIP trigger elements are constructed only from the two tracks. It thus suggests itself to understand the trigger performance and data-MC discrepancies in terms of the track kinematics.

### s14 L2/L3 Performance

In 2007 an FTT vertex constraint was added in the second trigger level to the **s14** subtrigger. The constraint can also best be studied with the matching part of the DIS data sample. It is found to reject much fewer than 1% of events; compare Figure 6.3. The effect of the trigger on the photoproduction dataset is thus neglected. Potential impacts on the measurement are assumed to be covered by the luminosity uncertainty.

#### 6.2.1 FTT Performance

The performance of the FTT trigger elements in the **s14** subtrigger relies on the FTT track reconstruction. Of most relevance for the trigger are the track reconstruction efficiency, the fake rate and the accuracy of the charge measurement.

In order to study the efficiency, the FTT L1 tracks are geometrically and exclusively matched to offline reconstructed and selected tracks as described by Bolz [149]. The single track reconstruction efficiency is then defined as the ratio of offline tracks with a matched FTT track to the total number of offline tracks:

$$\epsilon_{\text{FTT, track}} = \frac{N(\text{offline tracks w/ FTT match})}{N(\text{offline tracks})}. \quad (6.8)$$

The tracking efficiency is measured using both tracks in the DIS sample. It is shown in Figure 6.4 as a function of the offline reconstructed track  $p_T$ ,  $\phi$ , and  $\theta$ . The efficiency measured

in data appears to be well modeled by the simulation within statistical uncertainties. In particular, the dependence of the efficiency on the effective track length is reproduced by the MC sample. A larger track length results in more charges being ionized in the CJC and thus in a higher efficiency. It expresses itself in a rise of the efficiency at very low  $p_T$  and in a drop around  $\theta \sim 90^\circ$  and at the edges of the CJC. Even more complex features appear to be reasonably described by the simulation, e.g., efficiency losses due to dead CJC wires, which are visible in the  $\phi$  dependence. The good description of the FTT tracking efficiency is consistent with the previous observation that the minimum track multiplicity trigger requirement is well modeled.

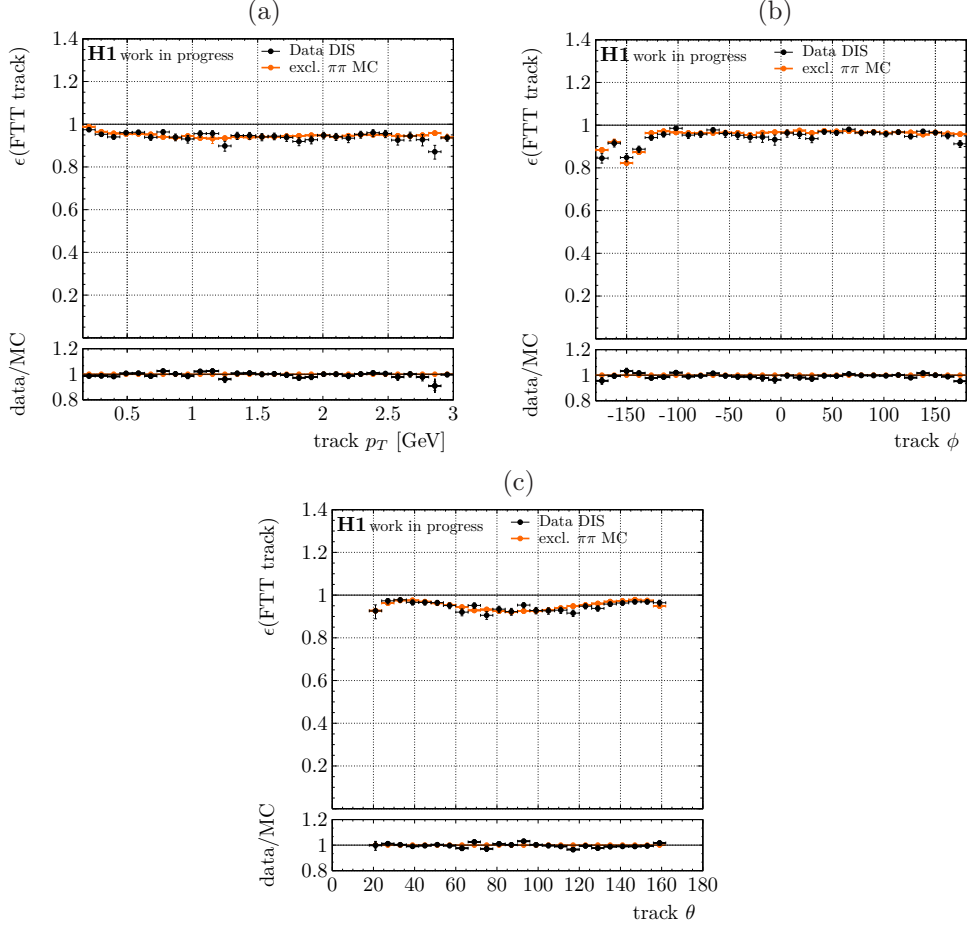


**Figure 6.4:** FTT single track reconstruction efficiency measured in DIS as a function of the offline reconstructed track  $p_T$  (a),  $\phi$  (b), and  $\theta$  (c). Only statistical uncertainties are considered.

Separate from a good tracking efficiency, the FTT suffers from a considerable rate of *fake* L1 tracks. These are FTT track candidates that can not be matched to an actual offline track and are wrongly reconstructed by the FTT. Given the coarse resolution of the FTT track patterns and the indistinguishability between actual and mirror charge carriers, two FTT track segments can easily form a false match and be reconstructed as a track. An illustration is given in Figure 6.5. The rate of fake FTT tracks is particularly high in dense topologies. In these, actual tracks are close in the transverse plane, thus increasing the chance of randomly matching track segments.

Here, the rate of fake FTT tracks is studied in terms of the track multiplicity veto in the s14 subtrigger, which requires  $\text{FTT\_mul\_Ta} < 4$ . Since there are two real tracks in the DIS sample, there need to be at least two fake FTT tracks for an event to be rejected by the veto.

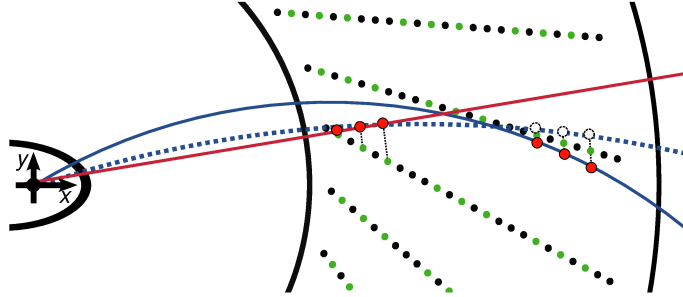


**Figure 6.5:** Illustration of the reconstruction of a fake FTT track. Shown is an drawing of the inner CJC with the sense wires used by the three inner FTT trigger groups marked in green. The fake track (dashed line) is reconstructed from a combination of a real (red dots) and a mirror charge triplet (white dots) that are produced by two real, proximate tracks (continuous lines). The event resembles an actual DIS  $\pi^+\pi^-$  data event.

In Figure 6.6, the efficiency of the veto is plotted as a function of the azimuthal opening angle between the two tracks evaluated at the radius of the third FTT trigger group  $\Delta\phi_{FTT}$ . Indeed, the efficiency goes down, i.e., the rate of fake tracks goes up, when the two tracks are very close together.

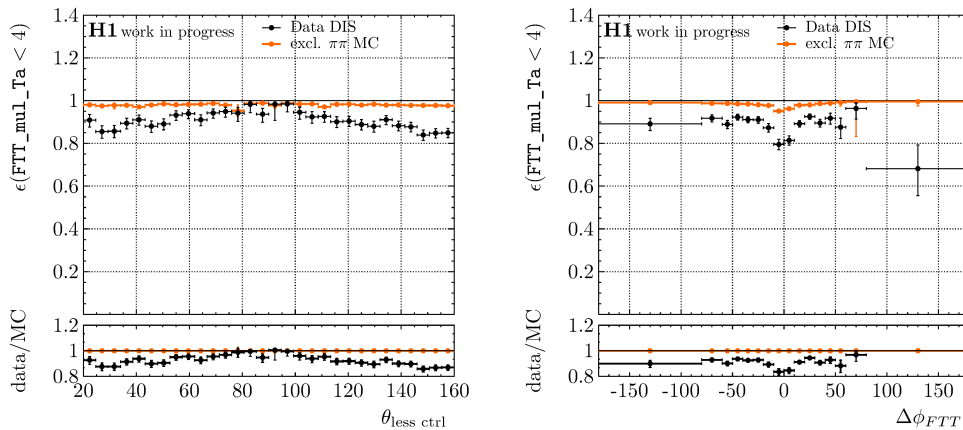


**Figure 6.6:** FTT\_mul\_Ta<4 efficiency in DIS as a function of the azimuthal opening angle between the two tracks evaluated at the radius of the third FTT layer  $\Delta\phi_{FTT}$  (left), and as a function of the less central track angle  $\theta_{\text{less ctrl}}$  (right). Only statistical uncertainties are considered.

More importantly, the rate of fake tracks is much higher in data than in the simulation. There are several factors that can contribute to that. First of all, there are typically more actual FTT track segments in the real detector than in the simulation. They can originate from out-of-time pileup signals, such as *curler* tracks<sup>3</sup>, or from secondary tracks from nuclear interactions of signal particles with the detector material. Neither effect is well modeled by the simulation; compare Section 5.2. Beyond that, the chance of randomly matching track segments is also higher for the real FTT than in the simulation. The reason is that the resolution of the track segments is generally worse, e.g., because of slight variations of the charge carrier drift times in the CJC, to which the FTT is very sensitive [149]. However, not all details are understood in the context of this thesis.

The rate of fake FTT tracks has further kinematic dependencies. In Figure 6.6, the efficiency

<sup>3</sup>Those are particles with very low  $p_T$  that have closed trajectories in the inner CJC. They can circulate for many bunch-crossings before decaying or being absorbed in the detector material.

for the `FTT_mul-Ta<4` trigger requirement is also plotted as a function of the variable:

$$\theta_{\text{less ctrl}} = \begin{cases} \theta_{\pi^+}, & \text{if } |\theta_{\pi^+} - 90^\circ| > |\theta_{\pi^-} - 90^\circ| \\ \theta_{\pi^-}, & \text{else.} \end{cases} \quad (6.9)$$

$\theta_{\text{less ctrl}}$  always is the polar angle of the less central of the two tracks. The respective track tends to have a longer effective track length and thus deposits more charges in the CJs. The efficiency of the veto, i.e., the fake rate, has a strong dependence on  $\theta_{\text{less ctrl}}$ . Also here, multiple factors contribute but not all details are understood. For once, the single track efficiency and thus the number of valid FTT triplets increases with increasing track length. Beyond that, other factors might also play a role. For example, a larger track length also results in a higher rate of nuclear interactions and in a higher number of ionized charge carriers which might modify the local drift behaviour.

The performance of the FTT track multiplicity veto certainly needs to be corrected in the simulation. Lacking a more detailed understanding of all the mechanisms that affect the rate of fake FTT tracks, it is not clear how such a correction should best be performed. A pragmatic approach is chosen that is discussed further on in the text. This approach results in a large systematic uncertainty for the correction factor, which ends up being one of the most relevant uncertainties of the measurement presented in this thesis.

The third relevant feature of the FTT is its capability to measure track charges. This enters the `s14` trigger via the FTT charge requirement `FTT_chg_1`. For the charge requirement to be violated, either the charge of one of the two tracks has to be measured incorrectly by the FTT, or there have to be (multiple) fake tracks. For straight high  $p_T$  tracks, the charge measurement becomes increasingly challenging. In Figure 6.7, the fraction of FTT tracks with the same charge as the matched reconstructed track is plotted as a function of track  $p_T$ . For tracks with  $p_T \gtrsim 1$  GeV, the FTT fails to measure the correct charge at an increasing rate. However, the charge measurement is correctly modeled by the simulation. The efficiency of the `FTT_chg_1` trigger requirement is shown in Figure 6.7 as a function of the larger track  $p_T$ . It exhibits a small  $p_T$  dependence, as could be expected from the single track charge measurement. However, the data efficiency is not reproduced by the MC model. Since the charge measurement of individual tracks is well described by the simulation, the mismodeling of the total charge requirement has to be attributed to the mismodeling of the FTT fake track rate.

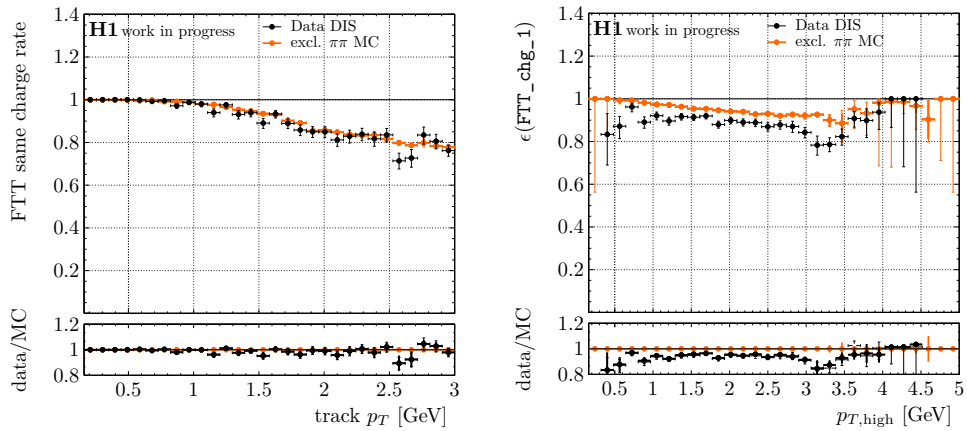


**Figure 6.7:** FTT charge mismeasurement rate in DIS as a function of track  $p_T$  (left). `FTT_chg_1` efficiency as a function of the larger pion track  $p_T$  (right). Only statistical uncertainties are considered.

## 6.2.2 Performance of Other Trigger Elements

### CIP Performance

The efficiencies of the three CIP trigger requirements are plotted as a function of  $\theta_{\text{less ctrl}}$  in Figure 6.8. Some mismodeling of the trigger elements is observed. Consistently with the CIP's geometry, it exhibits a dependence on the polar angles of the two pions. The precise underlying mechanism responsible for the mismodeling is not understood in the context of this thesis.

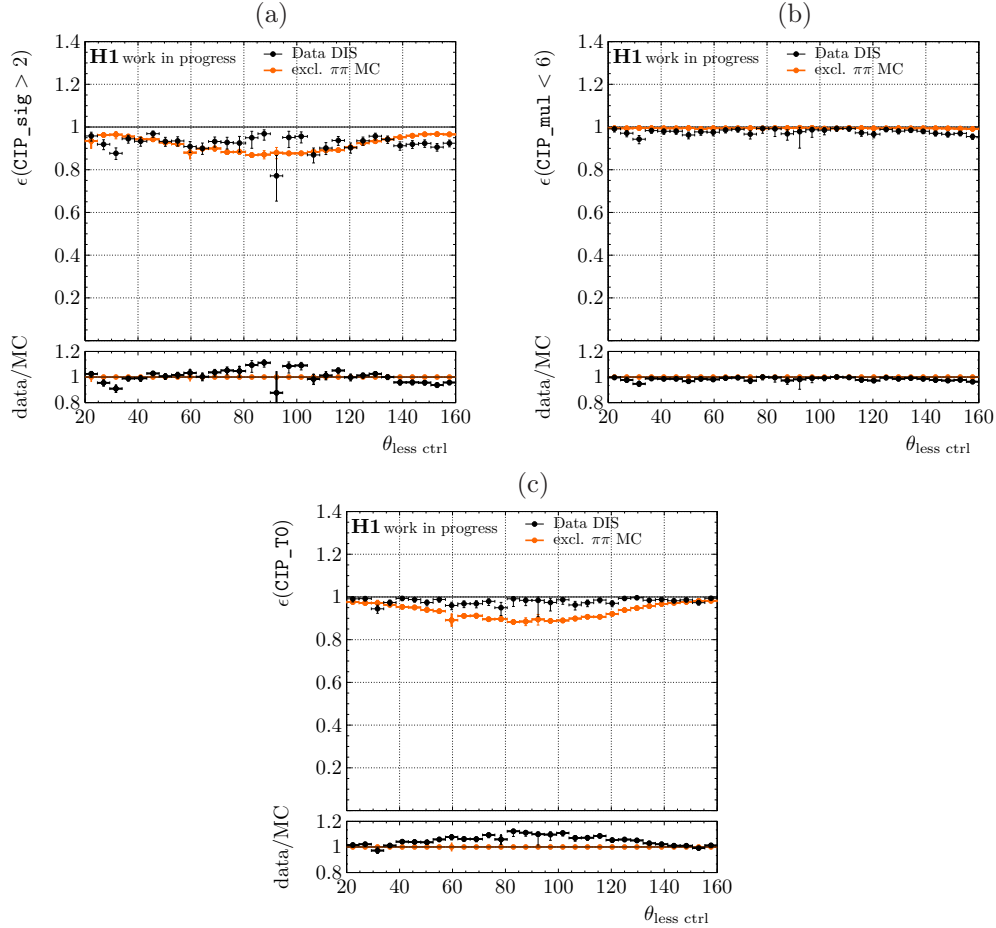


**Figure 6.8:** Efficiency of the CIP s14 trigger elements CIP\_sig>2 (a), CIP\_mul<6 (b), and CIP\_T0 (c) as a function of  $\theta_{\text{less ctrl}}$ . The efficiencies are measured in the DIS data sample and compared to the corresponding MC model. Only statistical uncertainties are considered.

### Forward and Backwards Veto Performance

The FTi2 trigger veto is based on signals from the FTi2 scintillator wall in front of the forward trackers. The scintillator covers an acceptance of roughly  $\theta \lesssim 20^\circ$ . However, as discussed in Section 3.2.3, its precise geometry is not known. Neither is it included in the H1 detector simulation, at all. While it was meant to reject non-diffractive events, the FTi2 veto also has a significant impact on selected (proton-dissociative) events.

In data, the performance of the FTi2 veto can be studied with the DIS sample. However, the veto was also taken out of the s14 online definition for an extended period of time. While the

trigger definition is harmonized offline for the selection of the photoproduction data sample, the subset collected without the veto can be used to study the FTi2 performance also in photoproduction. This is useful because the available photoproduction subsample is much larger than the DIS sample. Also, kinematic differences between DIS and photoproduction then do not need to be considered. In order to study the FTi2\_G1 performance consistently in DIS and photoproduction, its efficiency is evaluated for events passing the full  $\pi^+\pi^-$  signal event selection, as well as all other **s14** requirements. The efficiency defined that way is shown in Figure 6.9 as a function of the lower of the two track polar angles,  $\theta_{\text{low}}$ . The FTi2\_G1 veto was implemented to reject non-diffractive events. However, in the figure a dependence on  $\theta_{\text{low}}$  can be observed, such that the efficiency goes down at low angles. This suggests that also the pions can interfere with the performance of the veto when going very forward; potentially through secondary particles created in interactions with the detector material. Furthermore, the efficiency never reaches 1 even for very large  $\theta_{\text{low}}$ . Assuming that no non-diffractive events survive the offline event selection, this has to be attributed to diffractive dissociation events being rejected because some of the proton remnants hit and interact with the veto wall.

The combined efficiency of both the SpaCal vetoes applied in the trigger (`!SPCLh_AToF_E_1` && `!SPCLh_ToF_E_2`) is shown as a function of the larger of the two pion polar angles  $\theta_{\text{high}}$  in Figure 6.9. Generally, the vetoes are almost fully efficient in both data and the MC. A potential inefficiency might occur at very high  $\theta_{\text{high}}$  in data, but not the MC. This could again be a consequence of the two pions inducing a SpaCal signal through secondary particles from interactions with the detector material which are not well modeled by the simulation.

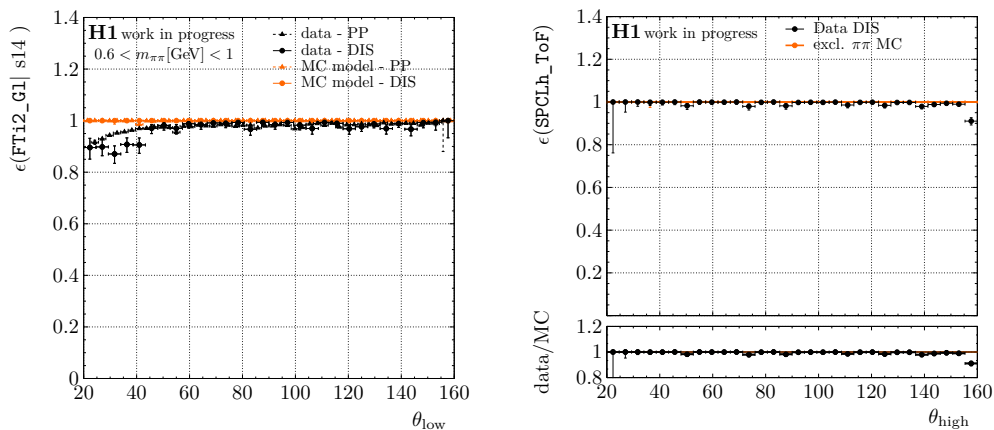


**Figure 6.9:** Left: FTi2\_G1 veto efficiency as a function of the lower of the two pion  $\theta$ . The efficiency is measured in the DIS sample and the subset of the photoproduction sample without the veto in the online **s14** subtrigger definition. Fluctuations in the photoproduction MC template away from 1 originate from contributions from the beam-gas data template; compare Section 5.3. Only statistical uncertainties are considered. Right: Efficiency of the SpaCal trigger vetoes as a function of the larger of the two pion polar angles. The efficiency is measured in the data DIS sample and compared to the corresponding MC model. Only statistical uncertainties are considered.

### 6.3 Trigger Correction Factors

The observed flaws in the trigger simulation need to be corrected in the MC model that is used for the photoproduction cross-section measurement. Only then can the MC be employed to correct the measured data distribution for detector effects. The available DIS sample is not ideal for deriving correction factors because it only provides limited statistics and covers

a kinematic region orthogonal to the photoproduction dataset. Unfortunately, no better alternative could be found in the context of this thesis. Correction factors are thus derived from the DIS sample for the photoproduction topology in a way that reduces the impact from the different kinematics as best as possible. As a first step, additional cuts are introduced to improve the overall  $s_{14}$  trigger performance:

- $|\Delta\phi_{FTT}| > 20^\circ$
- $25^\circ < \text{track } \theta < 155^\circ$

The cut on the transverse opening angle between the tracks reduces the rate of fake FTT tracks. By applying it on the angle evaluated at the third FTT trigger layer, a potential impact from the track  $p_T$  differences between DIS and photoproduction is mitigated. The reduction of the polar track acceptance region reduces the potential impact from the pions interfering with either the FTi2 or the SpaCal trigger vetoes. It also reduces a potential impact on the FTT performance from CJC edge effects. In a second step, two multiplicative correction factors are derived that correct the mismodeling in the combined CIP and FTT trigger elements performance on the one hand, and the FTi2 veto performance on the other.

### 6.3.1 FTT & CIP Correction

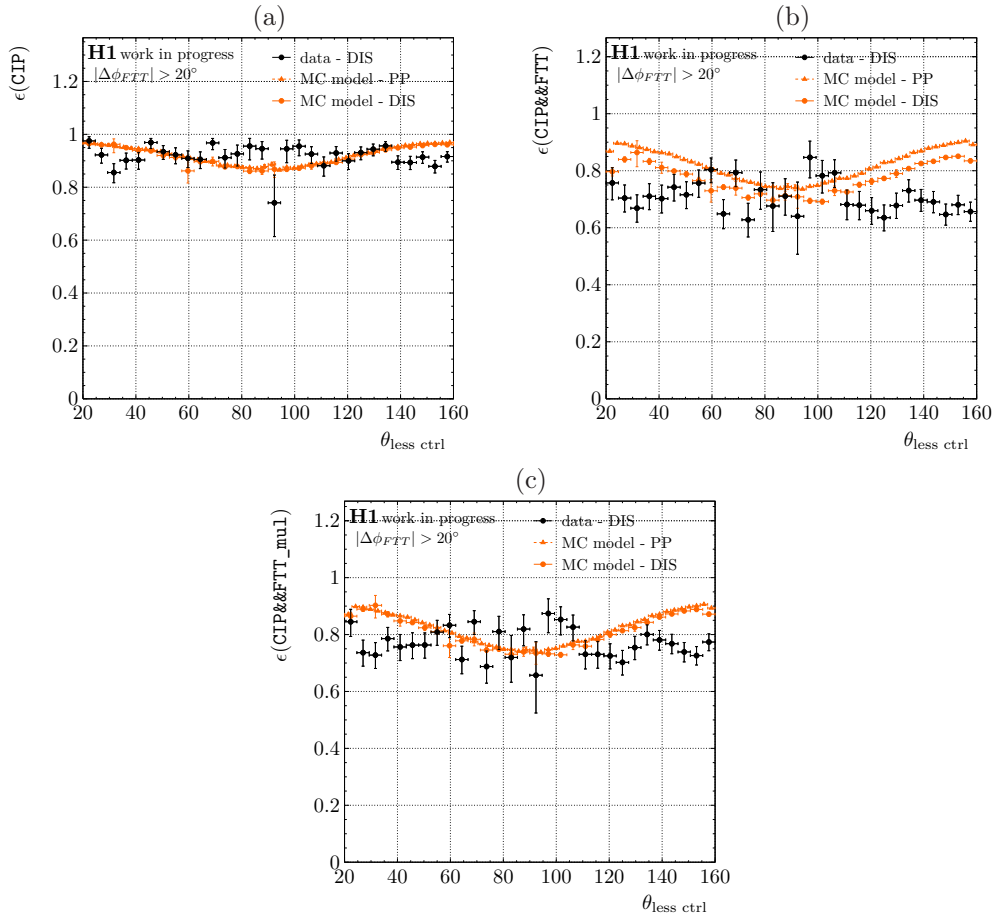


**Figure 6.10:** Efficiencies  $\epsilon_{CIP}$  (a),  $\epsilon_{CIP\&\&FTT}$  (b),  $\epsilon_{CIP\&\&FTT\_mul}$  (c) as a function of  $\theta_{\text{less ctrl}}$ . The efficiencies are measured in the DIS data sample and in the DIS and photoproduction MC samples as labeled in the legend. Only statistical uncertainties are considered.

The performance of the CIP and FTT trigger elements depends strongly on the kinematics and the topology of the two tracks, most notably on the track  $\theta$ ,  $p_T$  and  $\Delta\phi$ . The  $\Delta\phi$  dependence is significantly reduced by applying the trigger performance improvement cuts described in the text above. Without CJC edge effects, the qualitative  $\theta$  dependence of the CIP and FTT trigger elements is very similar. In Figure 6.10, the efficiency of three distinct combinations of trigger elements are studied: the combination of all CIP ( $\epsilon_{\text{CIP}}$ ), of all CIP and all FTT ( $\epsilon_{\text{CIP\&FTT}}$ ), and of all CIP and only the FTT track multiplicity elements ( $\epsilon_{\text{CIP\&FTT\_mul}}$ ). The efficiencies are measured in the DIS data sample and in the DIS and photoproduction MC samples. They are plotted as a function of  $\theta_{\text{less ctrl}}$ .

If adequate efficiency correction factors for the photoproduction MC sample are to be derived in DIS, a necessary condition is that kinematic differences between the DIS and photoproduction regimes are factorized out. This appears to be the case for the CIP trigger elements for which the DIS and photoproduction MC efficiencies agree very well when measured as a function of  $\theta_{\text{less ctrl}}$ . However, it is not true for the FTT. When all FTT trigger elements are considered, the MC performance in photoproduction is much better than in DIS. The underlying reasons are a better FTT track charge measurement, a higher FTT track reconstruction efficiency and a lower fake track rate. They are the consequence of a lower track  $p_T \lesssim 1$  GeV and a larger transverse opening angle between the two tracks in photoproduction.

The charge measurement can be expected to be very reliable in photoproduction and to be simultaneously well modeled by the MC; compare Figure 6.7. Thus, the `FTI_chg_1` requirement should not be corrected in photoproduction. It can not cause inefficiencies of the trigger directly. If the charges of the two real pion tracks are correctly measured, the charge requirement can only be violated in the presence of at least two additional fake FTT tracks. However, events with multiple fake tracks are simultaneously rejected by the track multiplicity veto. In photoproduction, it should thus be sufficient only to correct the CIP and FTT track multiplicity requirements. For these, i.e.,  $\epsilon_{\text{CIP\&FTT\_mul}}$ , the agreement between the DIS and photoproduction MC is indeed much better, though some small differences remain.

Unfortunately, the differences in the performance of the FTT track multiplicity veto are expected to be much larger in data than the MC. While the efficiency can not be measured in the photoproduction data sample, the observable rate of one additional fake FTT track is accessible. Among the DIS data events satisfying the `s14` trigger, 30% have an additional (fake) FTT track, while only 19% of the photoproduction events do. This difference also suggests a difference in the rate of events with two fake FTT tracks and thus a worse performance of the FTT multiplicity veto in the DIS than in the photoproduction topology. The difference can not be explained by slightly different  $\theta_{\text{less ctrl}}$  distributions alone. It is also the consequence of other topological differences in the  $p_T$  and  $\phi$  configurations of the two tracks. They can not all be considered simultaneously.

Neglecting CJC edge effects, the  $\theta_{\text{less ctrl}}$  dependence of the combined CIP and FTT trigger elements can be parametrized by the function:

$$\epsilon_{\text{CIP,FTT}}(\theta_{\text{less ctrl}}) = p_0 + p_1 [\sin^4(\pi/4) - \sin^4(\theta_{\text{less ctrl}}[\text{rad}])], \quad (6.10)$$

with free parameters  $p_0$  and  $p_1$ . The function is fitted to the efficiencies of the combined CIP and FTT trigger elements. The fits are shown in Figure 6.11 and the corresponding fit parameters are summarized in Table 6.2.

An efficiency correction factor can then be defined as the parametrized efficiency ratio between data and MC:

$$R(\theta_{\text{less ctrl}}) = \frac{\epsilon^{\text{data}}(\theta_{\text{less ctrl}})}{\epsilon^{\text{MC}}(\theta_{\text{less ctrl}})} \quad (6.11)$$

The efficiency correction is applied by weighting reconstructed MC events that pass the trigger requirement by  $R$ . For the DIS MC, the CIP and FTT correction factor is calculated

correction factor	$p_0^{\text{data}}$	$p_1^{\text{data}}$	$p_0^{\text{MC}}$	$p_1^{\text{MC}}$
$R_{\text{CIP}}$	$0.913 \pm 0.006$	$-0.034 \pm 0.018$	$0.940 \pm 0.001$	$0.102 \pm 0.003$
$R_{\text{CIP}\&\&\text{FTT\_mul}}$	$0.756 \pm 0.009$	$-0.049 \pm 0.028$	$0.851 \pm 0.002$	$0.169 \pm 0.005$
$R_{\text{CIP}\&\&\text{FTT}}$	$0.694 \pm 0.010$	$-0.057 \pm 0.030$	$0.813 \pm 0.002$	$0.165 \pm 0.005$

**Table 6.2:** Fit parameters for the fits of the  $\theta_{\text{less ctrl}}$  dependence of the efficiencies  $\epsilon_{\text{CIP}}$ ,  $\epsilon_{\text{CIP}\&\&\text{FTT}}$ ,  $\epsilon_{\text{CIP}\&\&\text{FTT\_mul}}$  measured in the DIS data and MC samples. Only statistical uncertainties are considered.

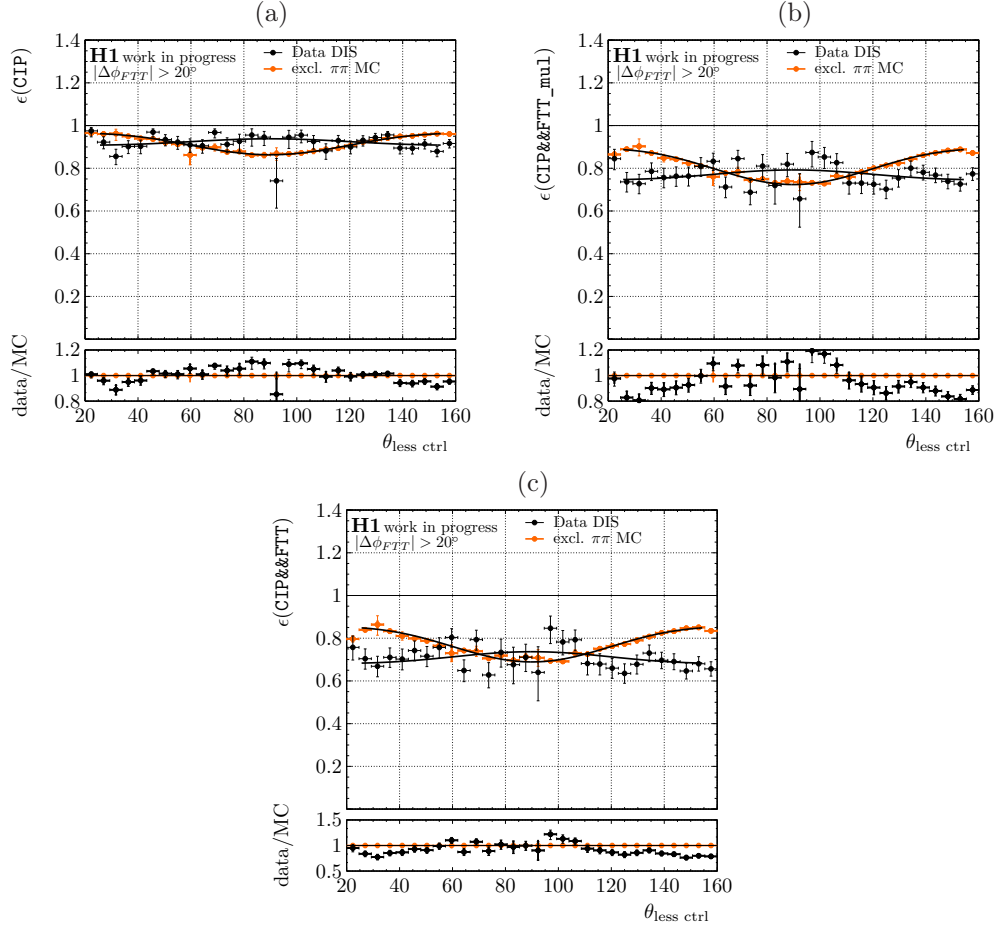


**Figure 6.11:** Fits of the  $\theta_{\text{less ctrl}}$  dependence of the efficiencies  $\epsilon_{\text{CIP}}$  (a),  $\epsilon_{\text{CIP}\&\&\text{FTT\_mul}}$  (b),  $\epsilon_{\text{CIP}\&\&\text{FTT}}$  (c) measured in the DIS data and MC samples. Only statistical uncertainties are considered.

from the combined efficiency of all CIP and FTT trigger elements:

$$R_{\text{CIP}\&\&\text{FTT}}^{\text{DIS}}(\theta_{\text{less ctrl}}) = \frac{\epsilon_{\text{CIP}\&\&\text{FTT}}^{\text{data}}(\theta_{\text{less ctrl}})}{\epsilon_{\text{CIP}\&\&\text{FTT}}^{\text{MC}}(\theta_{\text{less ctrl}})}. \quad (6.12)$$

Due to the discussed kinematic and topological differences, a derivation of the photoproduction correction factor is not as straight forward. Since the photoproduction  $\pi^+\pi^-$  kinematics are generally more favorable for a good FTT performance, two extreme scenarios are considered:

1. The FTT is assumed to be well described by the simulation in the photoproduction topology and does not need to be corrected, at all.
2. The FTT charge measurement is assumed to be well described by the simulation in

the photoproduction regime, but the fake rate is as poorly described as it is in the DIS topology.

No strong argument can be made in favor of either scenario. That is why the average correction factor for the two scenarios is used for correcting the (nominal) photoproduction MC. The difference between the scenarios is then used to estimate a systematic uncertainty for the correction:

$$R_{\text{CIP}\&\&\text{FTT}}^{PP} = \frac{1}{2} [R_{\text{CIP}} + R_{\text{CIP}\&\&\text{FTT\_mul}}] \pm \frac{1}{2} [R_{\text{CIP}} - R_{\text{CIP}\&\&\text{FTT\_mul}}] (\text{syst}). \quad (6.13)$$

A further uncertainty of the correction factors is considered from the statistical uncertainty of the fit parameters. Since the data uncertainties are dominant, MC uncertainties are neglected. For the used fit function, the two parameters  $p_0$  and  $p_1$  are only weakly correlated. The parameters for the fit of  $\epsilon_{\text{CIP}}$  and  $\epsilon_{\text{CIP}\&\&\text{FTT\_mul}}$ , on the other hand, are strongly correlated because the respective efficiency measurements are. For simplicity the first correlation is neglected, the second is assumed to be 100%. Two statistical variations of  $R_{\text{CIP}\&\&\text{FTT\_mul}}^{PP}$  are then assumed in which either  $p_0^{\text{data}}$  or  $p_1^{\text{data}}$  of both  $R_{\text{CIP}}$  and  $R_{\text{CIP}\&\&\text{FTT\_mul}}$  are simultaneously varied by their respective statistical uncertainties.

### Validation in DIS

The correction of the CIP and FTT trigger elements can be validated only in the DIS sample. For the validation, the trigger performance improvement cuts are applied and MC events passing the CIP and FTT s14 trigger requirements are weighted by the correction factor  $R_{\text{CIP}\&\&\text{FTT}}^{\text{DIS}}(\theta_{\text{less ctrl}})$  as defined in Equation (6.12). The corrected efficiency is shown in Figure 6.12 as a function of  $Q^2$ ,  $W_{\gamma p}$ ,  $m_{\pi\pi}$ , and  $t$  and is compared to the efficiency measured in the DIS data sample. Overall, the corrected MC agrees well with the MC and within statistical uncertainties and also kinematic dependencies appear to be reasonably described. However, a small difference in the  $Q^2$  dependence might remain, as should be expected from the previously observed difference of the trigger performance in the DIS and photoproduction MC samples. A potential consequence for the photoproduction correction factor is assumed to be covered by the systematic uncertainties assigned to it.

### 6.3.2 FTi2 Veto Correction

A correction factor for the FTi2 veto is derived from the photoproduction subsample that was collected without the FTi2 veto in the online s14 trigger definition. It then is defined for events passing the CIP and FTT trigger requirements and can thus be applied multiplicatively on top of the CIP and FTT correction. The derivation of the correction factor is not as straight forward as for the CIP and FTT. As the veto appears to be affected by forward going pions, it does reject not only proton-dissociative but also elastic events. Separate correction factors for both processes are thus needed. In order to separate elastic from proton-dissociative events, the forward tagging information is used; compare Section 4.4. The zero-tag and inclusive-tag categories are used to split the dataset into two parts with contributions from elastic and proton-dissociative events according to the respective tagging efficiencies:

$$N_{\text{data}}^{\text{tag}} = \epsilon_{\text{data}}^{\text{tag el}} N_{\text{data}}^{\text{el}} + \epsilon_{\text{data}}^{\text{tag pd}} N_{\text{data}}^{\text{pd}} \quad (6.14)$$

$$N_{\text{data}}^{\text{!tag}} = (1 - \epsilon_{\text{data}}^{\text{tag el}}) N_{\text{data}}^{\text{el}} + (1 - \epsilon_{\text{data}}^{\text{tag pd}}) N_{\text{data}}^{\text{pd}} \quad (6.15)$$

The data tagging efficiencies for elastic and dissociative events are not known. Assuming they are well modeled, they can be replaced by the MC efficiencies. Then the elastic and proton-dissociative number of events can be calculated:

$$N_{\text{data}}^{\text{el/pd}} \simeq \pm \frac{(1 - \epsilon_{\text{MC}}^{\text{tag pd/el}}) N_{\text{data}}^{\text{tag}} - \epsilon_{\text{MC}}^{\text{tag pd/el}} N_{\text{data}}^{\text{!tag}}}{\epsilon_{\text{MC}}^{\text{tag el}} - \epsilon_{\text{MC}}^{\text{tag pd}}}. \quad (6.16)$$

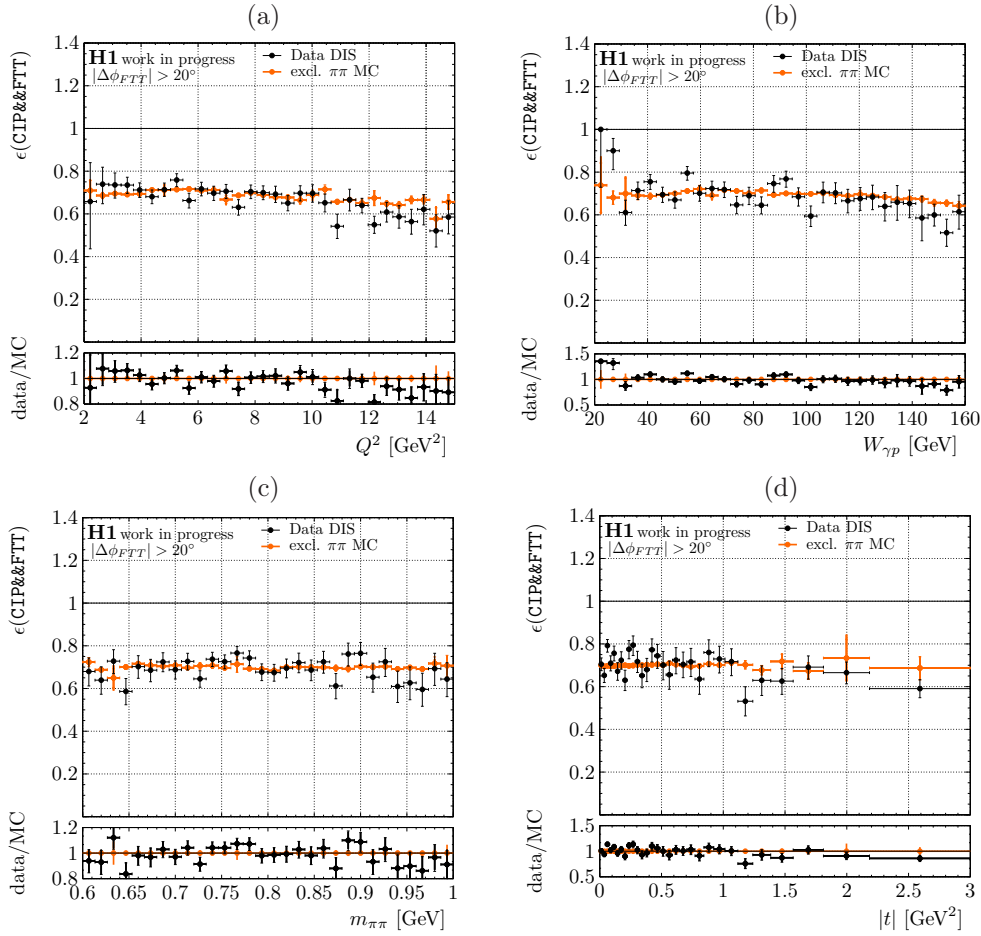


**Figure 6.12:** Efficiency of the combined CIP&&FTT  $s_{14}$  trigger elements measured in the DIS data and MC sample as a function of  $Q^2$  (a),  $W_{\gamma p}$  (b),  $m_{\pi\pi}$  (c), and  $t$  (d). The MC efficiency is corrected as described in the text. Only statistical uncertainties are considered.

Assuming the tagging efficiency is independent from the FTi2 veto, this allows to calculate the efficiency of the veto for elastic and dissociative events by calculating the respective fractions of events passing the veto:

$$\epsilon_{\text{FTi2}}^{\text{el/pd}} = \frac{N^{\text{el/pd}}(\text{!FTi2\_G1} \ \&\& \ s_{14}(\text{CIP}\&\&\text{FTT}) \ \&\& \ \text{selected})}{N^{\text{el/pd}}(s_{14}(\text{CIP}\&\&\text{FTT}) \ \&\& \ \text{selected})}. \quad (6.17)$$

In Figure 6.13, the FTi2 veto efficiency is shown for the photoproduction subsample recorded without the FTi2 veto in the online trigger definition. The efficiency is shown for the total sample as well as the elastic and proton-dissociative contributions.

A correction factor for the FTi2 veto can only be derived differentially in a single variable because of the limited size of the control dataset. In order to consider the impact of the pions on the veto, the variable  $\theta_{\text{low}}$  is chosen. In particular, an expected dependence of the efficiency on the mass of the dissociative system  $m_Y$  can not be considered nor studied because  $m_Y$  is experimentally not accessible. It is assumed that a potential impact on the measurement is covered by the uncertainty associated with the MC modeling of the  $m_Y$  distribution. Furthermore, it can also be expected that the efficiency is different for  $\pi^+\pi^-$  signal events and background processes with additional final state particles. Dedicated correction factors for the background processes can also not be derived. However, since the background MC samples are normalized to data on detector level, and are simply subtracted from the data

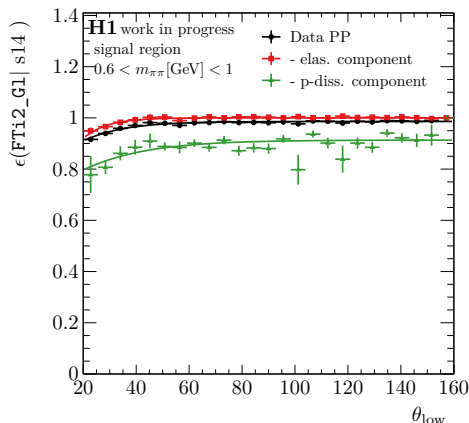


**Figure 6.13:** Efficiency of the FTi2 veto as a function of the lower track angle  $\theta_{\text{low}}$ . The efficiency is measured in the subsample of the photoproduction dataset that was recorded without the FTi2 veto in the online trigger definition. The efficiency is separated for elastic and proton-dissociative events as described in the text and as labeled in the legend. Only statistical uncertainties are considered.

distributions in the cross-section measurement, a correction is less critical. A correction factor for the  $\pi^+\pi^-$  signal samples is derived by parametrizing the  $\theta_{\text{low}}$ -dependence of the data efficiencies by the function:

$$R_{\text{FTi2}}(\theta_{\text{low}}) = \epsilon_{\text{FTi2}}(\theta_{\text{low}}) = \frac{p_0}{1 + \exp(-p_1 + p_2(\theta_{\text{low}} - 30^\circ)/180^\circ)} \quad (6.18)$$

Fits are performed to obtain optimal parameters for the efficiency in elastic and proton-dissociative events. The fit results are superimposed on the data points in Figure 6.13, and the fit parameters are summarized in Table 6.3.

correction factor	$p_0$	$p_1$	$p_2$
$R_{\text{FTi2}}$ elastic	$1 \pm 0$	$3.63 \pm 0.14$	$-21.3 \pm 3.9$
$R_{\text{FTi2}}$ proton-dissociative	$0.913 \pm 0.011$	$2.40 \pm 0.27$	$-8.86 \pm 6.62$

**Table 6.3:** Fit parameters for the fits of the  $\theta_{\text{low}}$  dependence of the elastic and proton-dissociative FTi2 veto efficiency in the photoproduction data subset. Only statistical uncertainties are considered.

The FTi2 veto trigger correction is applied by weighting reconstructed elastic and proton-dissociative MC events by the respective parametrized data efficiency. Systematic uncertainties on the correction are estimated as follows: For elastic events, a 100% uncertainty is assumed by not applying the correction at all. For the proton-dissociative events, a normalization uncertainty is assumed from the statistical uncertainty of the fitted parameter  $p_0$ , and a shape uncertainty is estimated by alternatively assuming no kinematic dependence of the trigger correction, i.e.,  $R_{\text{FTi2}} = p_0$ .

### Validation in Photoproduction

In order to validate the correction of the FTi2 veto efficiency in the MC, the efficiency of the corrected photoproduction MC is compared to the data efficiency as a function of  $m_{\pi\pi}$ ,  $W_{\gamma p}$ , and  $p_{T,\pi\pi}^2$  in Figure 6.14. After the correction the agreement is quite reasonable. Some mismodeling remains in the tails of the  $\rho^0$  mass peak below  $m_{\pi\pi} \lesssim 0.6$  GeV and above  $m_{\pi\pi} \gtrsim 1.1$  GeV. There, the dataset obtains a significant contribution from background processes (compare Chapter 4) for which no dedicated trigger correction is derived. A

potential impact on the final cross-section measurement is mitigated by subtracting the elastic and proton-dissociative background contributions independently on detector level; compare Chapter 7.

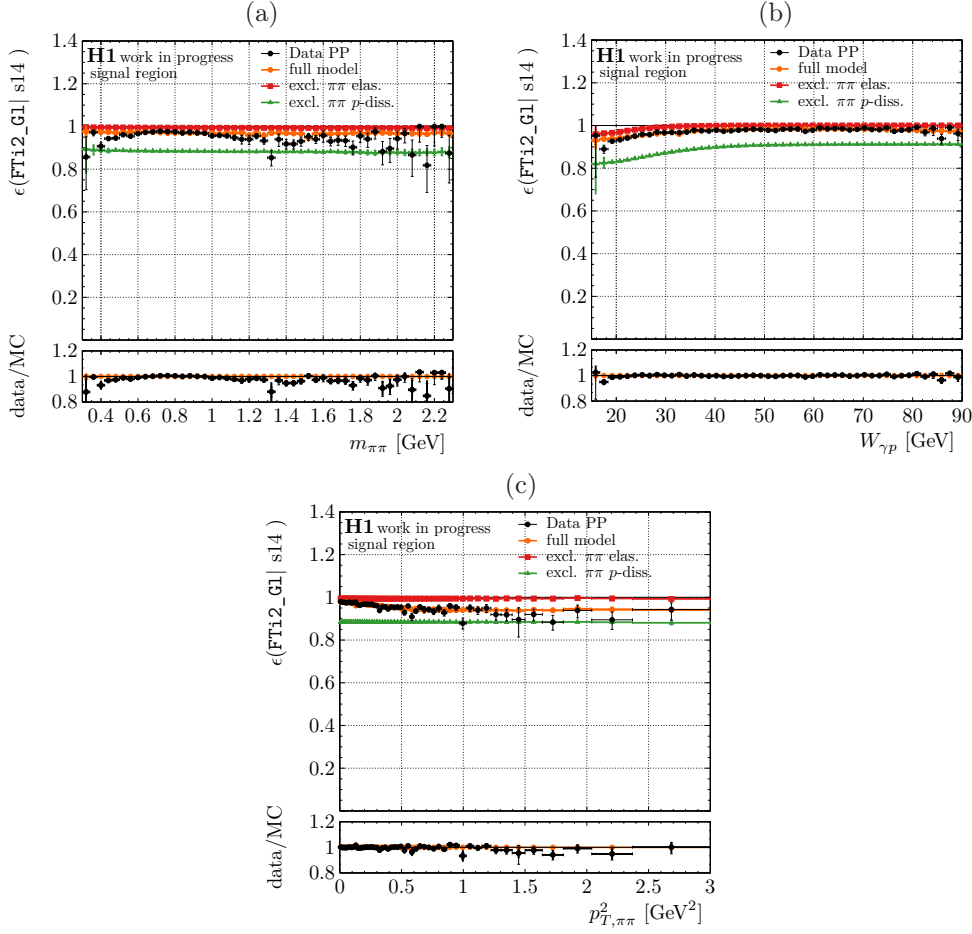


**Figure 6.14:** FTi2\_G1 veto efficiency in the photoproduction data subsample as a function of  $m_{\pi\pi}$  (a),  $W_{\gamma p}$  (b), and  $p_{T,\pi\pi}^2$  (c) after applying the trigger correction to the elastic and proton-dissociative MC samples. The black data points are compared to the full MC model and the elastic and proton-dissociative  $\pi^+\pi^-$  signal samples as labeled in the legend. Only statistical uncertainties are considered.

### 6.3.3 Applying Trigger Correction Factors

For the photoproduction MC samples two trigger correction factors  $R_{\text{CIP}\&\&\text{FTT}}^{PP}$  and  $R_{\text{FTi2}}$  are defined. They can be applied multiplicatively because  $R_{\text{CIP}\&\&\text{FTT}}^{PP}$  is defined for events passing the event selection and  $R_{\text{FTi2}}$  for events passing the event selection and all other s14 trigger requirements. Events passing the trigger and selection criteria are then simply weighted down by  $R_{\text{CIP}\&\&\text{FTT}}^{PP} \cdot R_{\text{FTi2}}$ . For the calculation of the response matrices used in the cross-section measurements (compare Chapter 7) the trigger correction is applied in a way to not destroy the normalization of the MC sample on generator level and thus allow for an efficiency correction to particle level.

## 7 $\rho^0 \rightarrow \pi^+\pi^-$ CROSS-SECTION MEASUREMENT

The goal of this analysis is to measure differential  $\rho^0$  photoproduction cross-sections as a function of the photon-proton center-of-mass energy  $W_{\gamma p}$  and the momentum transfer at the proton vertex  $t$ . Several experimental challenges need to be addressed and overcome to achieve that goal with the data at hand. They originate from the fact that only limited information is available for events observed through the H1 detector. At a fundamental level,  $\rho^0$  mesons themselves can not be directly observed. Due to their extremely short lifetime ( $\tau_\rho \sim 4.5 \cdot 10^{-24}$  s), they decay before they could ever interact with the detector. Only their decay products, i.e., the two pions, are directly measured. On a more technical level, the  $\pi^+\pi^-$  measurement is then also subject to various limitations of the H1 detector.

As a first step, the  $\pi^+\pi^-$  dataset at hand thus has to be corrected for features introduced by the detector. Relevant detector effects and their respective impacts on the dataset are described in Section 7.1. The correction is done via an unfolding procedure that is detailed in Section 7.2. The unfolding results in corrected  $\pi^+\pi^-$  event number distributions that are subsequently normalized to calculate differential  $\pi^+\pi^-$  photoproduction cross-sections. The  $\pi^+\pi^-$  cross-section obtains contributions from various processes in the considered kinematic region; compare Section 2.3. In order to measure the  $\rho^0$  cross-section, it needs to be isolated from the other contributions. This is achieved via a Söding model that is defined in Section 7.3. For the  $\rho^0$  extraction, the model is fitted to the measured invariant di-pion mass spectra. The fitting procedure explained in Section 7.4.

### 7.1 Detector Effects

Measuring the  $\pi^+\pi^-$  cross-section first requires the data to be corrected for detector effects. Broadly, two kinds of effects can be distinguished:

- The limited geometric detector *acceptance* and detector *inefficiencies* result in scattering events being recorded incompletely or not at all.
- The limited detector *resolution* results in measured kinematic variable values being smeared with respect to the true values.

#### 7.1.1 Detector Acceptance and Efficiency

Since this analysis relies heavily on the central tracking detector, the effective geometric acceptance for tracks is limited to  $20^\circ \lesssim \theta \lesssim 160^\circ$  and  $p_T \gtrsim 160$  MeV. Events in which either of the two pions goes outside of that range can not be measured at all. Even when both particles are within the central tracker's acceptance, they might not both be reconstructed because of detector inefficiencies. Insensitive regions due to detector support and readout structures, malfunctioning hardware, or more subtle effects can lead to tracks being missed by the trigger or offline track reconstruction. Additional events are lost in the data quality selection step. The full efficiency is defined for MC events as the fraction of generated events that are within the detector acceptance, are fully reconstructed, are triggered, and satisfy all selection requirements:

$$\epsilon_{\text{full sel}} = \frac{N(\text{acc. \&\& rec. \&\& trig. \&\& sel. \&\& gen.})}{N(\text{gen.})}. \quad (7.1)$$

In Figure 7.1, the efficiency is shown for the signal  $\pi^+\pi^-$  MC as a function of the true, i.e., generated  $m_{\pi\pi}$ ,  $W_{\gamma p}$ , and  $t$  variables. The steep drop in the efficiency at small  $m_{\pi\pi}$  and at small and large  $W_{\gamma p}$  is a direct consequence of the central tracker acceptance in  $p_T$  and  $\theta$ , respectively. The efficiency drop with increasing  $|t|$  is mainly a result of the event selection, with the restrictions of the forward energy flow of the dissociative system and on the transverse opening angles of the pions playing a major role.

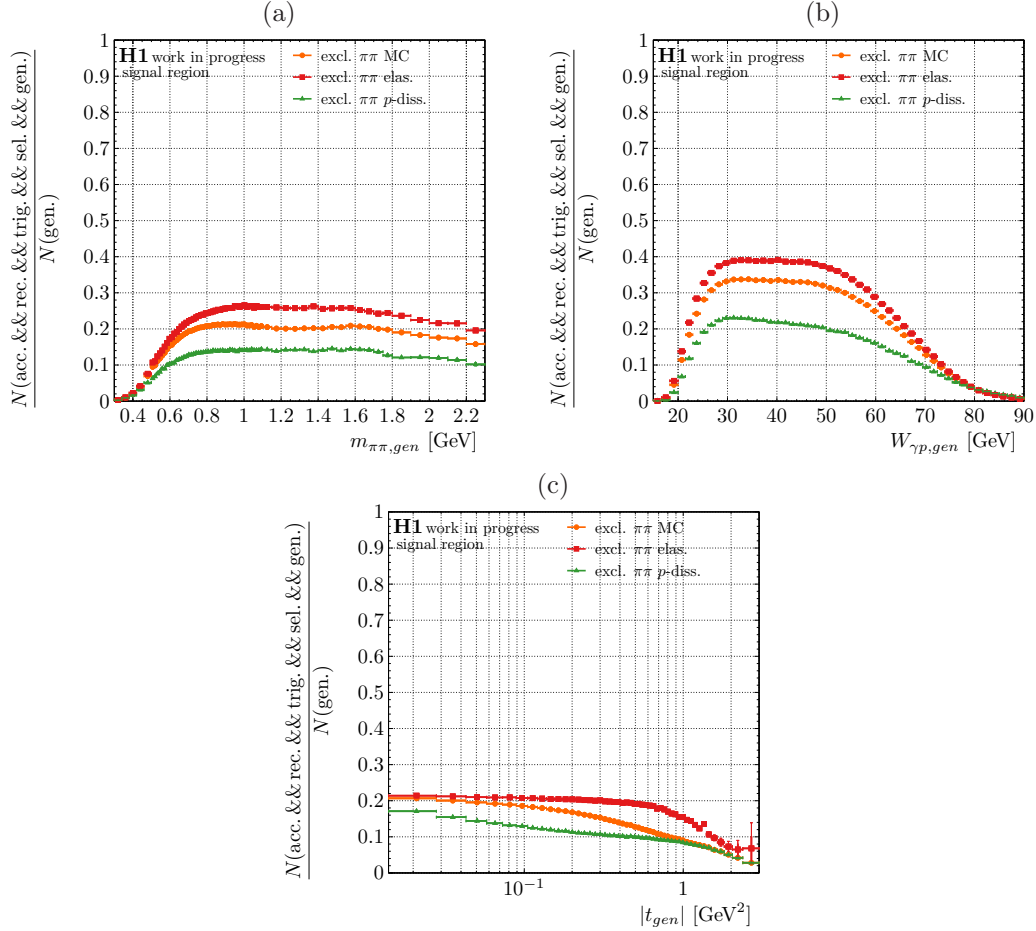


**Figure 7.1:** Efficiency for  $\pi^+\pi^-$  signal events to be within the detector acceptance, triggered, reconstructed, and selected  $\epsilon_{\text{full sel}}$ . The efficiency is shown for the elastic, proton-dissociative, and combined  $\pi^+\pi^-$  MC samples as labeled in the legends and as a function of the generated  $m_{\pi\pi}$  (a),  $W_{\gamma p}$  (b), and  $t$  (c). Only statistical uncertainties are shown.

Besides the central tracker for the di-pion reconstruction, the analysis also relies on the SpaCal to reject events with large momentum transfer  $Q^2$  and to ensure that only photoproduction-like events are selected. However, the SpaCal only extends down to  $\theta \lesssim 177.5^\circ$  and thus can only reject electrons with a minimal scattering angle, i.e., a minimal  $Q^2$ . Furthermore, the diffractive nature of the scattering is ensured by requiring a rapidity gap between the forward energy flow and the di-pion system. This is ensured by vetoing energy deposits in the forward LAr. However, the cut also rejects diffractive events where the proton dissociates into a system with large invariant mass  $m_Y$ . In Figure 7.2, the full selection efficiency is shown as a function of  $Q^2$  and  $m_Y$ . Events are selected within a kinematic range of roughly  $Q^2 \lesssim 2.5 \text{ GeV}^2$  and  $m_Y \lesssim 10 \text{ GeV}$ , respectively.

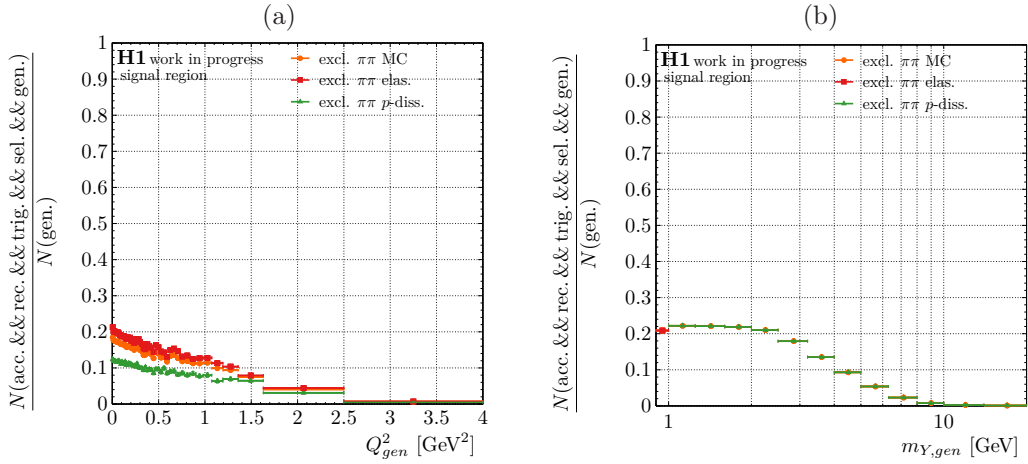


**Figure 7.2:** Efficiency for  $\pi^+\pi^-$  signal events to be within the detector acceptance, triggered, reconstructed, and selected  $\epsilon_{\text{full sel}}$  as a function of the true  $Q^2$  (left) and  $m_Y$  (right). The efficiency is shown for the elastic, proton-dissociative, and combined  $\pi^+\pi^-$  MC samples as labeled in the legends. Only statistical uncertainties are shown<sup>1</sup>.

### 7.1.2 Detector Resolution and Migrations

For this analysis, the kinematic event variables are reconstructed using only information from the two tracks. Their resolution is thus fundamentally restricted by the precision of the track measurement. However, for the photoproduction event topology, the resolution is deteriorated even further. In particular,  $W_{\gamma p}$  and  $t$  are reconstructed under the assumption that  $Q^2 = 0 \text{ GeV}^2$  and that all masses, including the mass of the dissociative system  $m_Y$ , can be neglected; compare Section 4.2. In this case, the full scattering kinematics are constrained by the knowledge of the initial state and the  $\pi^+\pi^-$  final state. For  $Q^2 \neq 0 \text{ GeV}$  or large  $m_Y$ , this is not a valid assumption anymore, and kinematic variables calculated from the two pions alone deviate systematically from the true values.

The relative difference between the reconstructed di-pion mass,  $W_{\gamma p}$ , and  $t$  and the respective true values are shown in Figure 7.3. A relative resolution is defined as the variation that encloses 68% of the reconstructed values, corresponding to a  $1\sigma$  variation assuming a Gaussian resolution. Lines indicating the relative resolution of each variable are included in each plot. The measured resolution of  $m_{\pi\pi}$  is roughly 1% and varies only little with the mass. It is solely given by the resolution of the track parameters. The resolution of  $W_{\gamma p}$  is of the order of 1%, too, but the reconstructed values exhibit a systematic shift on the permille level that changes with energy.  $W_{\gamma p}$  is strongly correlated with the polar angle  $\theta_{\pi\pi}$  of the  $\pi^+\pi^-$  system. The resolution and shift are thus dominated by the measurement of the track  $\theta$ . The reconstructed track  $\theta$  values deviate from the true values due to variations in the  $z$ -vertex position and the beam tilts. The deviation is in the opposite direction for forward and backward tracks, which results in the shift of  $W_{\gamma p}$  changing with energy. For proton-dissociative events, neglecting the mass of the proton remnant results in a further shift in the reconstructed  $W_{\gamma p}$ . Because that shift is independent of  $W_{\gamma p}$ , its relative size

<sup>1</sup>There is a slight inconsistency in the  $m_Y$  dependence of the efficiency, such that for small  $m_Y$  the efficiencies measured in the elastic and proton-dissociative MC differ by roughly 5%. This discrepancy is a feature of the independent (and inconsistent) treatment of the elastic and proton-dissociative MC samples. The samples are simulated and reweighted independently; compare Chapter 5. In particular, the  $m_{\pi\pi}$ ,  $t$ , and  $W_{\gamma p}$  MC distributions match those observed at an average  $m_Y$  and do not incorporate an  $m_Y$  dependence. For  $m_Y \rightarrow m_p$ , the distributions do not approach the elastic distributions. Phasespace restriction of low  $m_{\pi\pi}$  in particular then causes a higher efficiency in the proton-dissociative sample. As long as the proton-dissociative MC samples models the *average*  $m_Y$  well, the measured proton-dissociative cross-sections are not affected.

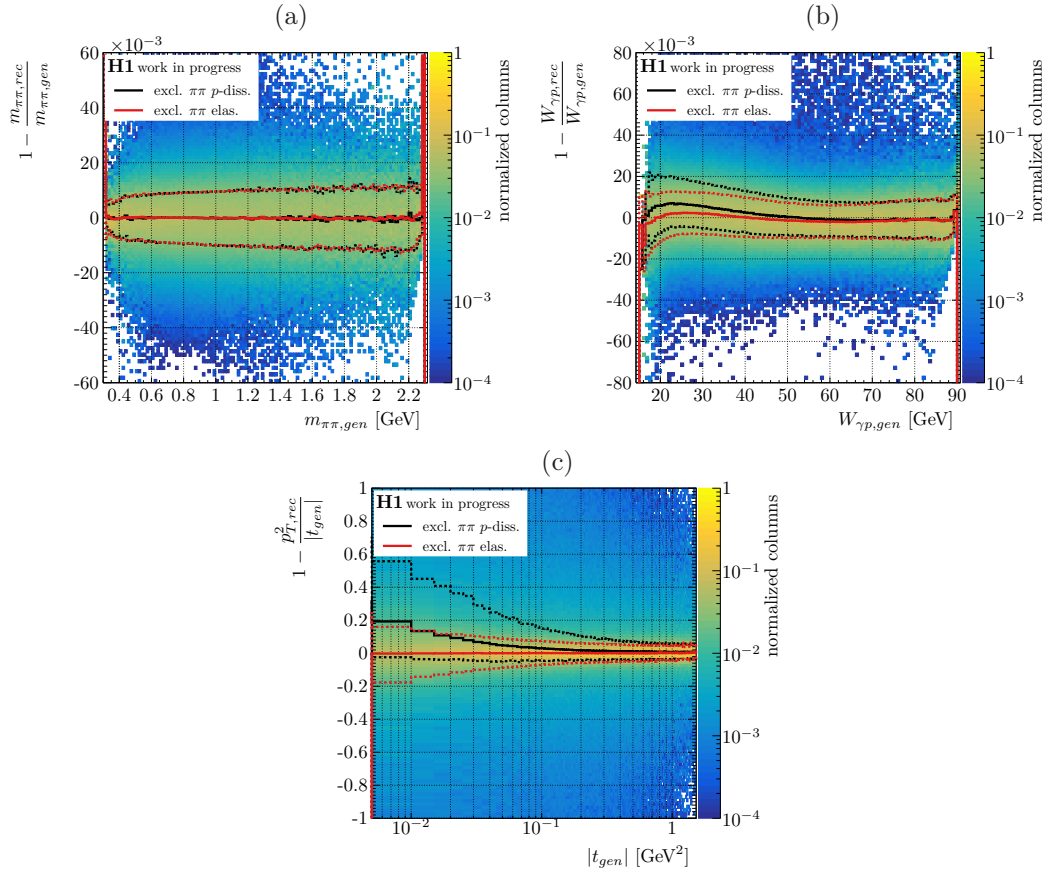


**Figure 7.3:** Relative resolution of the reconstructed variables with respect to the true values for  $m_{\pi\pi}$  (a),  $W_{\gamma p}$  (b) and  $t$  (c). Events are taken from the elastic and  $p$ -dissociative  $\pi^+\pi^-$  signal MC. The red and black lines indicate the 50% (continuous), and the 16% and 84% percentiles (dashed) of the elastic and proton-dissociative MC, respectively.

decreases with increasing  $W_{\gamma p}$ . The reconstruction of  $t \simeq -p_{T,\pi\pi}^2$  provides only a very poor relative resolution that varies from almost 20% at very small  $|t|$  down to roughly 5% at  $t = 1 \text{ GeV}^2$ . The driving factor behind the poor resolution is the disregard of larger photon-virtualities  $Q^2 \neq 0 \text{ GeV}^2$ . For proton-dissociative events, neglecting  $m_Y$  further deteriorates the measurement of  $t$  and results in values that are systematically shifted by up to 20% at very small  $|t|$ .

### Background Contributions

Another consequence of the limited detector acceptance, efficiency, and resolution is the contamination of the dataset by wrongly or incompletely reconstructed events from background processes. As is studied in Chapter 4, a small but considerable number of these events pass the full event selection and spoil the sample of  $\pi^+\pi^-$  photoproduction candidates. These contributions can not be identified event-by-event but still need to be removed from the data.

### 7.1.3 Visible and Fiducial Phasespace

The correction steps to be performed on the measured data are: first, the subtraction of events from non- $\pi^+\pi^-$  background processes and second, the correction of the signal

$\pi^+\pi^-$  events for detector resolution and inefficiencies. Acceptance corrections can not be performed when the underlying physical process is different outside and inside of the acceptance region. A measurement then is restricted to the visible kinematic range. The visible range of this analysis is mainly defined by the CJC acceptance, which limits the accessible energy range, and by the rapidity gap requirement, which limits the accessible mass of the dissociative system. However, also the size of the dataset and the MC samples restrict it. Most importantly, a lack of a sufficient number of measured and simulated events limits the  $m_{\pi\pi}$  range of the measurement. The *visible phasespace* for the present  $\pi^+\pi^-$  photoproduction measurement is formally defined in Table 7.1, taking these limitations into account. For the variables that can be reconstructed, i.e.,  $m_{\pi\pi}$ ,  $W_{\gamma p}$ , and  $t$  it is explicitly enforced by cuts on the reconstructed values. For the other variables, i.e.,  $Q^2$  and  $m_Y$ , it is only implicitly defined by selection restrictions on the accessible kinematic ranges, or by fundamental kinematic constraints.

	min		variable		max
	0.3	<	$m_{\pi\pi,\text{rec}}$ [GeV]	<	2.3
explicit:	15	<	$W_{\gamma p,\text{rec}}$ [GeV]	<	90
	-3	<	$t_{\text{rec}} = -p_{T,\pi\pi}^2$ [GeV <sup>2</sup> ]	<	0
implicit:	$Q_{\text{min}}^2$	<	$Q^2$	$\lesssim$	2.5 GeV <sup>2</sup>
	$m_p$	$\leq$	$m_Y$	$\lesssim$	10 GeV

**Table 7.1:** Visible phasespace defined in terms of the detector level, reconstructed variables  $m_{\pi\pi}$ ,  $W_{\gamma p}$ ,  $t$ ,  $Q^2$ , and  $m_Y$ . For the first three variables, which can be reconstructed from the two pions, it is explicitly enforced by cuts on the reconstructed values.  $Q^2$  and  $m_Y$  are kinematically constrained and implicitly by the event selection.

As discussed in the text above, the reconstructed variables can have a poor resolution. This can lead to problems at the kinematic boundaries where events can migrate into and out of the visible phasespace. To be able to correct these migrations, the actual measurement is performed in a *fiducial phasespace* only, which is slightly smaller than the visible phasespace defined above. The fiducial phasespace is defined in terms of the true MC variables and enforced by explicit cuts on the true values of  $m_{\pi\pi}$ ,  $W_{\gamma p}$ ,  $t$ ,  $Q^2$ , and  $m_Y$ . Besides migration effects, further considerations feed into the definition of the fiducial phasespace. Most importantly, the  $Q^2$  range is reduced to ensure the photoproduction kinematic regime.

	min		variable		max
	0.5	<	$m_{\pi\pi,\text{gen}}$ [GeV]	<	2.2
	20	<	$W_{\gamma p,\text{gen}}$ [GeV]	<	80
	-1.5	<	$t_{\text{gen}}$ [GeV <sup>2</sup> ]	<	0
	$Q_{\text{min}}^2$	<	$Q_{\text{gen}}^2$	<	0.1 GeV <sup>2</sup>
	$m_p$	$\leq$	$m_{Y,\text{gen}}$	<	10 GeV

**Table 7.2:** Fiducial cross-section phasespace defined in terms of the true, i.e., generated,  $m_{\pi\pi}$ ,  $W_{\gamma p}$ ,  $t$ ,  $Q^2$ , and  $m_Y$ .

Restricting the fiducial phasespace of a measurement can shape the measured differential cross-sections. For the present analysis, this is the case for the proton-dissociative component, in particular. As energy is needed to excite or break up the scattered proton, the accessible mass  $m_Y$  is restricted by the accessible range in the other kinematic variables. For a given

$W_{\gamma p}$ ,  $m_{\pi\pi}$ ,  $Q^2$ , and  $t$ , the maximally accessible mass  $m_Y$  is approximately [181]:

$$m_Y^2 \lesssim \frac{|t|W_{\gamma p}^4}{(m_{\pi\pi}^2 + Q^2)^2}. \quad (7.2)$$

In turn, limiting the range of  $m_Y$  in the fiducial phasespace definition strongly shapes the  $W_{\gamma p}$  and  $t$  dependence of the measured cross-sections. A smaller, yet still considerable effect comes from the restriction of the energy range, which can affect the measured  $t$  distributions. Both effects can be seen in Figure 7.4, where the fraction of generated events that pass the fiducial phasespace cuts, i.e.,

$$\epsilon_{\text{fid PS}} = \frac{N(\text{fid. PS \&\& gen.})}{N(\text{gen.})}, \quad (7.3)$$

are plotted as a function of  $m_{\pi\pi}$ ,  $W_{\gamma p}$ , and  $t$ . The effective impact of the cut on  $m_Y < 10$  GeV strongly varies with  $W_{\gamma p}$  and  $t$ , in particular. This is directly reflecting on the measured cross-section distributions. These shaping effects can not be corrected in the measurement unless models are used to extrapolate the measured cross-sections beyond the visible phasespace. Such an extrapolation is not done for the present analysis because the DiffVM event generator does not model the  $m_Y$  distribution very reliably. Instead, the phasespace shaping of the measured cross-sections has to be taken into account when they are interpreted.

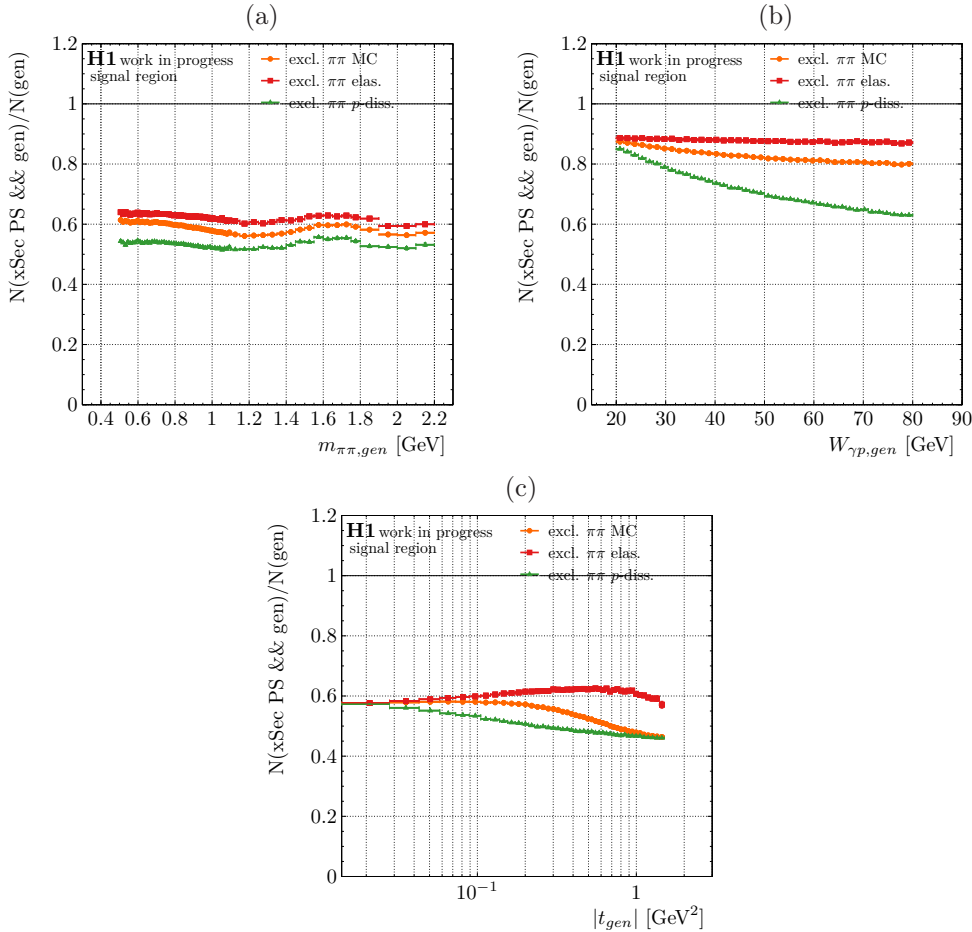


**Figure 7.4:** Fraction of generated events from the signal  $\pi^+\pi^-$  photoproduction MC that pass the fiducial phasespace cuts defined in Table 7.2. The fraction is shown for the elastic, proton-dissociative and combined MC as labeled in the legend and as a function of the generated  $m_{\pi\pi}$  (a),  $W_{\gamma p}$  (b), and  $t$  (c). Only statistical uncertainties are shown.

## 7.2 Unfolding $\pi^+\pi^-$ Cross-Sections

In order to correct detector efficiency and resolution, the measured distributions are *unfolded*. The principal concepts of unfolding and the procedure applied for this measurement are outlined in the following. Let the *true probability distribution* for a physical process be given by a function  $f(x)$  depending on a set of kinematic variables  $x$ . If the process is observed through a particle detector, a priori only *detector level distribution*  $g(y)$  can be measured depending on a set of reconstructed kinematic variables  $y$ . If the detector is imperfect,  $g(y)$  and  $y$  might be distorted in comparison to  $f(x)$  and  $x$ , respectively. Under the assumption of a linear detector response, the response can be described by a function  $A(y, x)$ , and the detector level distribution  $g(y)$  can be calculated by folding the true distribution  $f(x)$  with  $A(x, y)$ :

$$g(y) = \int_{x_{min}}^{x_{max}} A(y, x) f(x) dx. \quad (7.4)$$

In the case of limited efficiency or detector acceptance, the norm of the measured distribution  $\int g(y)dy$  is smaller than the norm of the true distribution  $\int f(x)dx$ . For a finite measurement resolution  $g(y)$  obtains contributions from a range of  $x$  values; even if the variables  $x$  and  $y$  correspond directly to one another. In that case, the relation in Equation (7.4) is by no means unique. Instead, any function that averages to zero over the contributing  $x$  range can be added to  $f(x)$  without changing  $g(y)$ . One example would be high-frequency noise, another, contributions from outside an acceptance region where  $A(y, x) = 0$  for all  $y$ .

Unfolding then refers to the inversion of Equation (7.4) so that from  $g(y)$  and given  $A(y, x)$  information about  $f(x)$  can be inferred. From the previous argument, it follows that on principle  $f(x)$  can never be determined unambiguously. In practical applications, the situation is often aggravated because the measured distribution  $g(y)$  is already not well known. For example, it might only be sampled by a finite number of measurements. Uncertainties of  $g(y)$  are then often amplified or lead to noise contributions to the estimate of  $f(x)$  during the inversion step. A common way to resolve these problems is to introduce external regularization constraints that enforce a specific behavior. Assuming, for example, that  $f(x)$  is a physical distribution, one could require it to be smooth and hence suppress any high-frequency variations.

A general and more detailed introduction to unfolding and regularization is given by Blobel and Lohrmann [182], for example. For this analysis, only binned distributions are considered, in which regions of the phasespace are grouped together. They are unfolded via a regularized template fit with the TUnfold software package [183]. The unfolding is described in more detail in the following section.

### 7.2.1 Regularized Template Fit

The goal of this analysis is to unfold binned distributions. For these, Equation (7.4) can be discretized by replacing  $f(x)$  by the number of true events  $x_j$  in bin  $j = 1 \dots n$  and  $g(y)$  by the number of detector level events  $y_i$  in bin  $i = 1 \dots m$ .  $A(y, x)$  becomes a transition matrix  $A_{ij}$  that describes the probability of an event from the truth level bin  $j$  migrating into detector level bin  $i$ . Integrals over  $x$  or  $y$  are replaced by sums over  $i$  and  $j$ , respectively. In vector notation Equation (7.4) then becomes<sup>2</sup>:

$$\vec{y} = \mathbf{A} \cdot \vec{x}. \quad (7.5)$$

The detector level distribution  $\vec{y}$  is not known precisely but only estimated from a finite number of experiments by counting the observed number of events  $\hat{y}_i$  in each bin  $i$ . Then

<sup>2</sup>In general  $f(x)$  and  $g(y)$  can be multi-dimensional physical distributions but in the following they are assumed to be projected onto a one-dimensional bin numbering scheme.

$\hat{y}_i$  is in particular subject to statistical uncertainties. It may also obtain contributions from misreconstructed background events  $\vec{b}$  that can not be identified on an event-by-event basis. For a square and invertible matrix  $\mathbf{A}$ ,  $\vec{y}$  could in principle be replaced by  $\hat{\vec{y}} - \vec{b}$  and Equation (7.5) be inverted in order to obtain an estimate  $\hat{\vec{x}}$  for  $\vec{x}$ . However, statistical uncertainties in  $\hat{\vec{y}}$  are often strongly enhanced by such a simple inversion. The unfolding result  $\hat{\vec{x}}$  then suffers from large statistical fluctuations that come with large (anti-)correlated uncertainties. While solutions obtained by inversion are statistically correct, they are often not desired for aesthetic and practical reasons, e.g., correlated uncertainties are difficult to visualize, document, or publish.

There are many approaches to unfolding that try to provide an estimated  $\hat{\vec{x}}$  with reduced fluctuations and correlated uncertainties by avoiding a direct inversion of Equation (7.5). For a comparison of various methods, see the review by Schmitt [184], for example. The approach taken in this analysis is to find an estimate  $\hat{\vec{x}}$  for the true distribution with a  $\chi^2$  template fit. The fit is performed using the TUnfold software package. The TUnfold  $\chi^2$  function is defined as:

$$\chi^2(\vec{x}, \lambda) = \left(\hat{\vec{y}} - \vec{b} - \mathbf{A} \cdot \vec{x}\right)^T \cdot \mathbf{V}_{\hat{\vec{y}}-\vec{b}}^{-1} \cdot \left(\hat{\vec{y}} - \vec{b} - \mathbf{A} \cdot \vec{x}\right) + \chi_{\text{reg}}^2 + \chi_{\text{norm}}^2 \quad (7.6)$$

It compares a truth level distribution  $\vec{x}$  smeared by the response matrix to the background-subtracted measured distribution. The uncertainties of the background-subtracted measured input distribution are given by the covariance matrix  $\mathbf{V}_{\hat{\vec{y}}-\vec{b}}$ . The  $\chi^2$  function is extended by a regularization constraint  $\chi_{\text{reg}}^2$  and a normalization constraint  $\chi_{\text{norm}}^2$ . They impose additional restrictions on  $\hat{\vec{x}}$  and are discussed further on in the text. Using a  $\chi^2$ -based instead of a likelihood-based method has the advantage that the minimization of Equation (7.29) can be analytically solved to give the best estimate  $\hat{\vec{x}}$  for  $\vec{x}$ . Of course, the underlying assumption then has to be that the uncertainties  $\mathbf{V}_{\hat{\vec{y}}-\vec{b}}$  are normally distributed. The minimization procedure is detailed in the TUnfold documentation [183]. In particular, it does not rely on the direct inversion of  $\mathbf{A}$ . As one consequence, the fit can also be performed with non-square response matrices. In fact, asymmetric response matrices with a larger number of detector level than truth level bins are desirable. They result in an over-constraining of the unfolded truth bins. The  $\chi^2$  is then minimized for  $n_{\text{df}} > 0$  degrees of freedom. Not only is the inversion more stable in this case, but it also allows interpreting the minimal  $\chi^2$  value statistically.

## 7.2.2 Background Subtraction

As a first step of the unfolding, background contributions to the detector level distributions need to be subtracted from the input data distributions. For this analysis, only the background from beam-gas events is directly subtracted. The subtraction of backgrounds estimated from MC samples is incorporated into the  $\chi^2$  minimization step. Doing so allows fitting their respective normalization factors. For this purpose, they are included in the definition of the response matrix.

## 7.2.3 Response Matrix Definition

The response matrix  $\mathbf{A}$  is determined from Monte Carlo events. For these, both truth and detector level information is available. The truth level is the generator level, i.e., the generated cross-section distributions and the generated four-momenta of all particles involved in the scattering. Propagating the generated events through the H1 detector simulation then provides also detector level information, i.e., the reconstructed four-momenta of the two pions. In order to calculate  $\mathbf{A}$  for unfolding a given kinematic distribution, a two-dimensional histogram  $\mathbf{N}$  of the generator level truth distribution against the detector level measured distribution is constructed and filled with events from the MC. To account for efficiency losses, events that are not reconstructed and selected are filled into an overflow bin  $i = 0$ .

For this analysis, MC events are weighted with generator level and detector level weights. Generator level weights are applied equally to reconstructed and non-reconstructed events. Detector level weights such as trigger efficiency scaling factors are only applied on detector level. In order to preserve the total number of MC events in  $\mathbf{N}$ , detector level weights need to be compensated. The compensation is achieved by filling every reconstructed event weighted by a factor  $R$  also in the non-reconstructed overflow bin with the complementary weight  $(1 - R)$ .

The elements of  $\mathbf{A}$ , i.e., the probability that an event generated in bin  $j$  is reconstructed in bin  $i$ , can then be calculated from  $\mathbf{N}$ :

$$A_{ij} = \frac{N_{ij}}{\sum_{i=0}^{i=m} N_{ij}}. \quad (7.7)$$

The efficiency correction is implicitly incorporated by the overflow bin, with the total efficiency given by

$$\epsilon_j = \frac{\sum_{i=1}^{i=m} N_{ij}}{\sum_{i=0}^{i=m} N_{ij}}. \quad (7.8)$$

Due to the normalization,  $\mathbf{A}$  is independent of the shape of the MC distribution in the unfolding variables. However, it is not entirely independent of the MC and can still strongly depend on the modeling of hidden MC distributions of variables that are not unfolded. As is discussed in Section 7.1, the reconstruction and selection efficiency exhibits strong kinematic dependencies. Thus, in order to obtain correct unfolded distributions, all hidden MC distributions in variables that are not directly unfolded need to be well described by the MC. Otherwise, the result might be biased. For this analysis, this is ensured by tuning the MC distributions to data, and verified with various control distributions; compare Chapter 5 and Chapter 4.

### Response Matrices For The $\pi^+\pi^-$ Cross-Section

For the present cross-section measurement, various multi-dimensional  $\pi^+\pi^-$  event yield distributions as a function of  $m_{\pi\pi}$ ,  $W_{\gamma p}$ ,  $t$ , and combinations thereof are unfolded. To match the formulation above, they are projected onto one-dimensional bin number distributions. The general structure of all the response matrices used for the unfolding of these is the same. It is illustrated in Figure 7.5.

In the illustration of the response matrix, the  $y$ -axis represents the generator level and the  $x$ -axis the detector level distributions. One fundamental property of the unfolding here is that it separates the elastic and proton-dissociative contributions. For emphasis, this is explicitly shown even though it could also be interpreted as merely unfolding two bins in  $m_Y$  as one extra dimension of the measured distributions. For both the elastic and proton-dissociative region, a distinction is made between events falling into the fiducial cross-section region as defined in Table 7.2 and outside of it. Events from outside the fiducial phasespace are considered in a single overflow bin per region. As a consequence, out-of-phasespace migrations into and out of that region are considered in the unfolding. For technical reasons, the  $\pi^+\pi^-$  signal MC obtains a small contribution from  $\rho^0 \rightarrow \pi^+\pi^-\gamma$  events; compare Chapter 5. These events are considered as background and removed in the unfolding. This is achieved by treating them as migrations from outside the fiducial phasespace and filling them in the corresponding bin in the migration matrix.

Another property of the response matrix is the incorporation of MC background contributions. For the eight considered MC background samples, i.e., for elastic and dissociative  $\omega$ ,  $\phi$ , and  $\rho'$  photoproduction as well as  $\gamma$ -dissociation, additional generator level distributions are added to the response matrix. Truth level  $\pi^+\pi^-$  information is not defined for these processes. Instead, the generator level distributions are filled with detector level variables, and only events inside of the visible phasespace are considered. In the unfolding, this effectively results

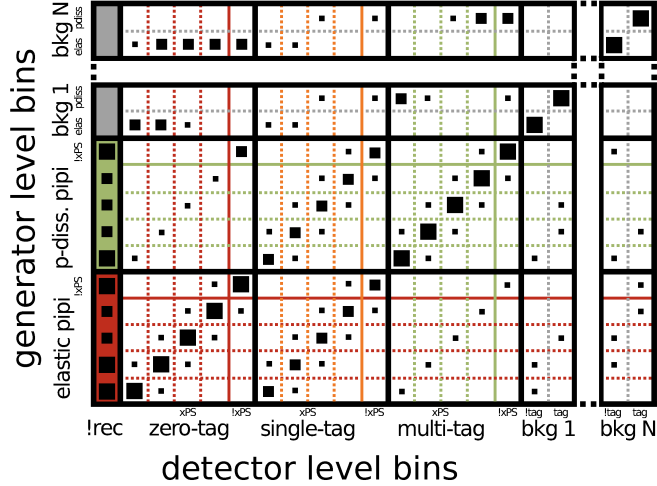


**Figure 7.5:** Illustration of the general structure of the response matrices used for the unfolding. The x-axis corresponds to reconstructed detector level variables, the y-axis to the true, generator level variables.

in a simple background subtraction on detector level. However, the background normalization in every generator level bin is obtained with the  $\chi^2$  fit.

On detector level, the reconstructed distributions are considered in the signal and the four background control regions as they are defined in Section 4.3.3. The signal region is further split into the three proton-dissociation tagging categories as defined Section 4.4, i.e., the zero-tag, single-tag, and multi-tag region. This allows constraining the elastic and proton-dissociative  $\pi^+\pi^-$  contribution independently. The four background regions are split into a zero-tag and inclusive-tag category to constrain the respective elastic and proton-dissociative background contributions. All events inside the visible phase space are considered. Events that are not reconstructed or selected in the visible phase space are accounted for in a dedicated overflow bin. For the three signal regions also a distinction between events inside and outside of the fiducial phase space is made. The phase space cuts defined in Table 7.2 are applied on the detector level variables. Events that are rejected are filled into one dedicated overflow bin per region. The number of bins per region is the same on detector and particle level. As there are three detector level signal control regions for two signal components, the total number of bins on detector level is larger than on generator level. Generally, this is a necessary though not sufficient requirement for all generator level bins to be constrained independently. The exact binning schemes of all unfolded distributions are summarized in Appendix E.

As an example for an actual response matrix used in the present analysis, the matrix for unfolding the one-dimensional  $m_{\pi\pi}$  distributions is shown in Figure 7.6. The response matrix for unfolding the  $m_{\pi\pi}$  distributions exhibits significant migrations, i.e., off-diagonal elements. These can pose a problem for the unfolding. Two types of migrations are to be considered: migrations from one generator level bin into multiple detector level bins (*stability*) and migrations from multiple generator level bins into one detector level bin (*purity*). The way it is normalized, the response matrix is a direct measure for the stability. Correspondingly, a purity matrix  $\mathbf{P}$  can be defined as:

$$P_{ij} = \frac{N_{ij}}{\sum_{j=1}^{j \leq n} N_{ij}}, \quad (7.9)$$

which gives the relative contribution of a given generator level bin  $j$  to a detector level bin  $i$ .

Generally, an unfolding problem is only well defined if every generator level bin is constrained by at least one detector level bin. The higher the purity in the constraining bin, the better its constraining power. For a stable solution, thus a high purity is more important than a high stability. The purity matrix for the one-dimensional  $m_{\pi\pi}$  distributions is shown in

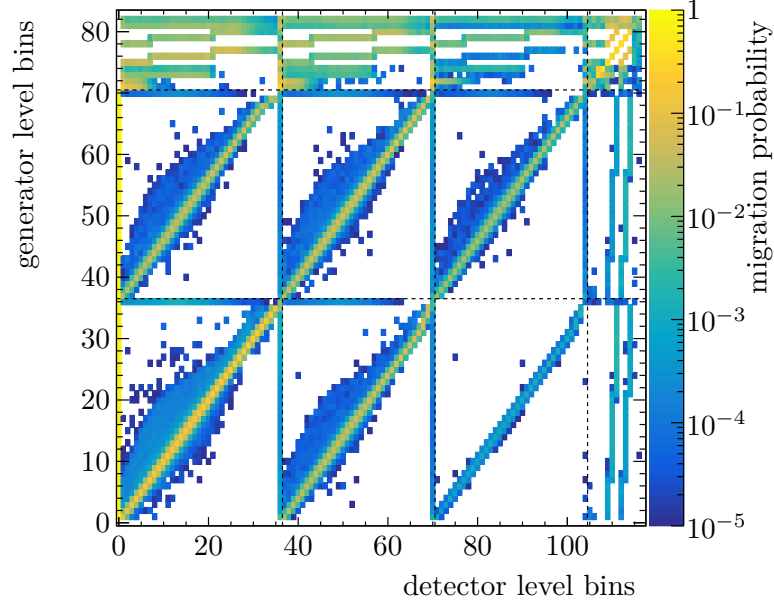


**Figure 7.6:** Response matrix  $A$  for unfolding the one-dimensional  $m_{\pi\pi}$  distributions. The matrix is constructed from the MC model as described in the text. The dashed lines indicate the boundaries of the elastic and proton-dissociative  $\pi^+\pi^-$  signal MC on generator level and the three signal tagging regions on detector level.

Figure 7.7. While there are significant migrations, most generator level bins are strongly constrained by at least one detector level bin. However, for the considered  $m_{\pi\pi}$  response matrix, the purity is not ideal. For some generator level bins, the best constraining bin has a purity of less than 50%. This is the case in the tails of the  $\rho^0$  resonance peak and for some background distributions, in particular.

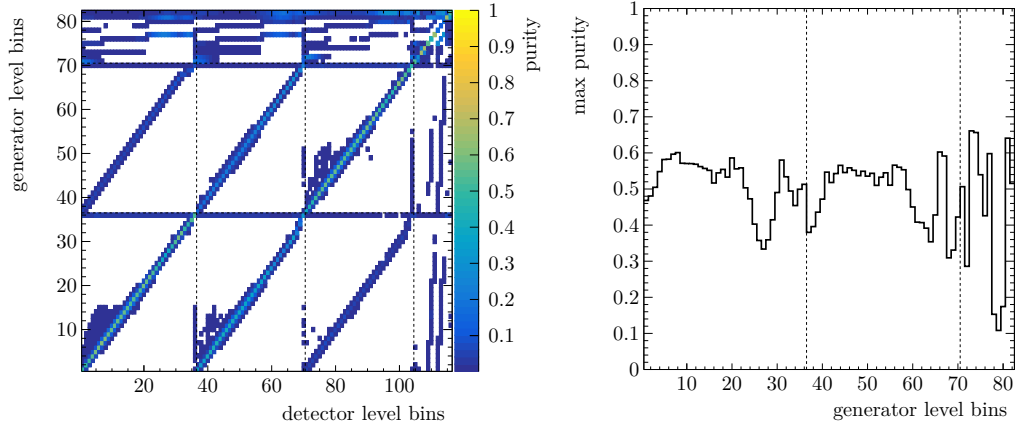


**Figure 7.7:** Purity matrix (left) and maximum entry for every generator level bin (right) for the one-dimensional  $m_{\pi\pi}$  response matrix. The dashed lines indicate the boundaries of the elastic and proton-dissociative  $\pi^+\pi^-$  signal MC on generator level and the three signal tagging regions on detector level.

Unfortunately, it is not straight forward to further improve the purity. Again, two types of migrations are to be considered: Migrations between control regions, e.g., from the generator level background regions into the detector level signal regions, and migrations between bins of a single region in the response matrix, e.g., due to a finite  $m_{\pi\pi}$  resolution. The first type of migrations is difficult to reduce. A reduction can only be achieved by defining detector level

control regions that better match the MC contributions. An example from this analysis is the implementation of a multi-tag signal category, which has a much higher purity ( $\sim 91\%$ ) in proton-dissociative events compared to an inclusive ( $\sim 44\%$ ) or exclusive single-tag category ( $\sim 37\%$ ). Beyond that, some background control regions in the analysis only provide a poor purity. Defining a good control region for proton-dissociative  $\rho'$  events is particularly challenging. The additional pions from the  $\rho' \rightarrow 4\pi$  decay often induce a tagging signal in the forward detectors. This results in a considerable tagging rate also for elastic  $\rho'$  events, which are then indistinguishable from proton-dissociative events. Unfortunately, better background control regions could not be found in the context of this thesis. The second kind of migrations due to the limited variable measurement resolution can be reduced by increasing the bin sizes of the generator level bins. Ideally, they should be larger than the variable resolution; compare Figure 7.3. For this analysis, bin sizes are chosen accordingly, where possible. However, it can not always be ensured. The poor resolution of the reconstructed  $t$  values poses a particular challenge. Large migrations between bins result in anti-correlated bin-by-bin fluctuations in the unfolded distribution. For neighboring bins within a distribution, these can be artificially suppressed by applying a regularization condition.

### 7.2.4 Regularization

The goal of regularization is to suppress unphysical behavior in unfolded distributions, such as large bin-by-bin fluctuations. Over time a wide variety of regularization schemes to achieve this goal have been proposed; see the review by Schmitt [184], for example. By construction, regularization always comes at the cost of introducing a bias in the unfolded distribution. The challenge then is to find a good compromise between unphysical behavior and the size of the bias. In the TUnfold package, a Tikhonov type regularization [185, 186] can be added to the  $\chi^2$  term. It has the general form

$$\chi_{\text{reg}}^2 = \tau^2 (\vec{x} - \vec{x}_b)^T \cdot (\mathbf{L}^T \mathbf{L}) \cdot (\vec{x} - \vec{x}_b). \quad (7.10)$$

Here,  $\tau$  is a meta-parameter that can be varied to change the overall strength of the regularization and  $\vec{x}_b$  is a bias distribution whose behavior  $\vec{x}$  is incentivized to imitate. The matrix  $\mathbf{L}$  can be chosen in order to implement different regularization schemes. This kind of regularization term has several desirable features. First of all, by explicitly providing a bias distribution, the potential bias introduced by the regularization is known. Furthermore, the strength of the regularization can be smoothly varied with the parameter  $\tau$ , and for  $\tau \rightarrow 0$  there is a continuous transition to the un-regularized solution. On a technical level, Equation (7.10) preserves the property of the TUnfold  $\chi^2$  function to have an analytic minimum.

The matrix  $\mathbf{L}$  allows implementing different regularization schemes. For  $\mathbf{L} = \mathbf{1}$  the absolute difference between  $\vec{x}$  and  $\vec{x}_b$  is regularized, and large deviations are suppressed. Other matrices  $\mathbf{L}$  then allow to also regularize the first or second derivative (curvature) of the unfolded relative to the bias distribution, or even more complicated schemes. For this thesis, regularization of the curvature is chosen because it matches the set goal of suppressing anti-correlated bin-by-bin fluctuations best. The curvature of the unfolded distribution in bin  $j$  is estimated via

$$(x_j)'' \simeq (x_{j+1} - x_j) - (x_j - x_{j-1}), \quad (7.11)$$

in disregard of the bin widths. Regularization of the curvature can then be implemented in Equation (7.10) by setting  $\mathbf{L} = 0$  except for  $L_{j,j} = -2$  and  $L_{j,j-1} = L_{j,j+1} = 1$  for  $j = 2 \dots n - 1$ . For the present analysis,  $\mathbf{L}$  is defined in awareness of the projection of the physical distributions to one-dimensional bin-number distributions. That is, physical and not bin-number distributions are regularized. In particular, the regularization stops at the edges of physical distributions, e.g., in between the elastic and proton-dissociative distributions. For multi-dimensional distributions, the curvature in every dimension is independently regularized, stopping at all distribution boundaries. This can also be achieved by a proper choice of  $\mathbf{L}$ .

For the bias distributions, the MC template constructed as detailed in Section 5.3 is used. An example of the regularization matrix for unfolding the one-dimensional  $m_{\pi\pi}$  distributions is provided in Figure 7.8.

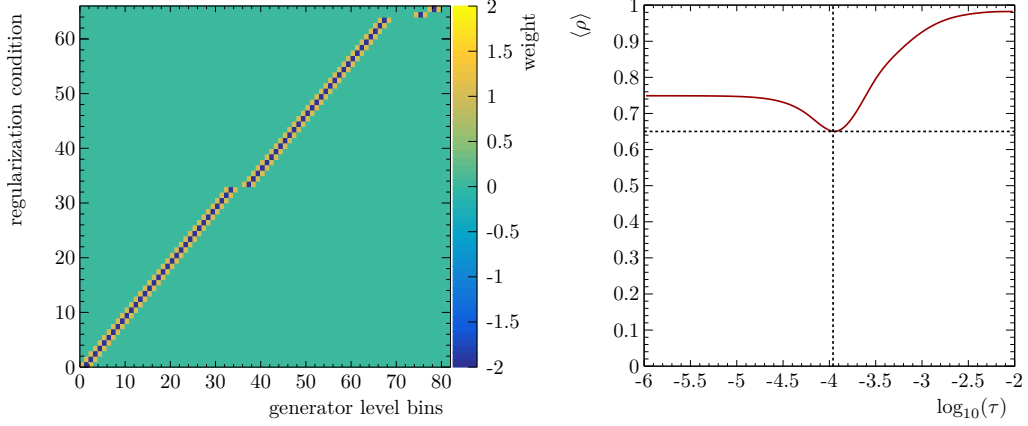


**Figure 7.8:** Regularization matrix  $L$  for the unfolding of the one-dimensional  $m_{\pi\pi}$  distributions (left) and scan of the average global correlation coefficient  $\langle \rho \rangle$  over the regularization strength  $\tau$  (right). For the actual unfolding  $\tau$  is chosen to minimize  $\langle \rho \rangle$  as is indicated by the dashed lines.

As stated previously, the goal of the regularization is to suppress bin-by-bin fluctuations which typically come with large (anti-)correlated uncertainties. The *global correlation coefficient* [187] is introduced as a measure for the size of the correlation between one unfolded generator level bin and all other bins:

$$\rho_i = \sqrt{1 - [(V_{\hat{x}})_{ii}(V_{\hat{x}}^{-1})_{ii}]^{-1}}. \quad (7.12)$$

$V_{\hat{x}}$  denotes the statistical covariance matrix of the unfolded distribution obtained by error propagation of the statistical input uncertainties, as detailed in the TUnfold documentation [183]. Following a recommendation given by Blobel [188], the strength of the regularization is chosen to minimize the *average global correlation coefficient*:

$$\langle \rho \rangle = \frac{1}{n} \sum_{j=1}^{j \leq n} \rho_j \quad (7.13)$$

A scan of the average global correlation coefficient over a range of regularization strengths  $\tau$  is shown in Figure 7.8 for the unfolded one-dimensional  $m_{\pi\pi}$  distributions. No regularization results in anti-correlated neighboring bins, whereas a strong regularization of the curvature results in strong positive correlations. Both situations result in a large average global correlation coefficient. As a consequence, there is always a local minimum in  $\langle \rho \rangle$  as a function of  $\tau$  that is used to choose the optimal value for the final regularization.

Introducing a regularization term can destroy the norm-preservation property of the  $\chi^2$  function, i.e.,  $\|\mathbf{A} \cdot \hat{x}\|^3$  is no longer ensured to be equal to  $\|\hat{y} - \vec{b}\|$ . To enforce preservation of the norm, a corresponding boundary constraint is explicitly added to the TUnfold  $\chi^2$  function:

$$\chi_{\text{norm}}^2 = \lambda \left( \|\hat{y} - \vec{b}\| - \|\mathbf{A}\hat{x}\| \right). \quad (7.14)$$

The Lagrange multiplier  $\lambda$  is obtained together with  $\hat{x}$  in the  $\chi^2$  minimization.

<sup>3</sup> $\|x\| := \sqrt{x^T \cdot x}$

### 7.2.5 Uncertainty Propagation

Statistical and systematic uncertainties need to be propagated through the unfolding.

#### Statistical Uncertainties

Two sources of statistical uncertainties are considered: statistical uncertainties of the input data (including contributions from the beam-gas background subtraction) and statistical uncertainties of the response matrix. Both are propagated to the unfolded distributions in the way described in the TUnfold documentation [183]. Due to migration effects, the statistical input uncertainties of the unfolded distribution are no longer uncorrelated. Statistical uncertainties of input and response matrix are combined and henceforth referred to as the *statistical uncertainty*. Generally, the input uncertainty is the dominant statistical uncertainty in the present measurement.

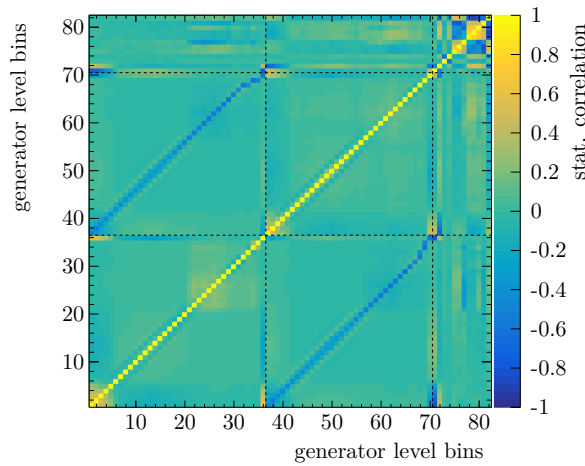


**Figure 7.9:** Statistical covariance matrix of the unfolded one-dimensional  $m_{\pi\pi}$  distributions.

The statistical covariance matrix of the unfolded one-dimensional  $m_{\pi\pi}$  distributions is shown in Figure 7.9. While correlations between neighboring bins are reduced by the regularization, large anti-correlated uncertainties between different regions remain. They are a consequence of the previously discussed limited purity in some detector level bins. As explained, they can not easily be avoided for the present analysis.

#### Systematic Uncertainties

Systematic uncertainties are propagated through the unfolding via an *offset* method: The unfolding is repeated with the systematically varied input components, and systematic uncertainties of the unfolded distribution are estimated from the differences between nominal and systematically varied distributions. Some systematic uncertainties are estimated via a two-sided variation. This does not always result in a symmetric variation of the unfolded distribution. No symmetrization is performed and instead an up and down uncertainty is defined as:

$$\hat{x}_{\text{nom}} \pm \Delta \hat{x}_{\text{up/dn}} = \hat{x}_{\text{nom}} \begin{array}{l} +(\hat{x}_{\text{up}} - \hat{x}_{\text{nom}}) \\ -(\hat{x}_{\text{nom}} - \hat{x}_{\text{dn}}) \end{array}. \quad (7.15)$$

For one-sided systematic variations the uncertainty of the unfolded distribution is estimated conservatively to be symmetrically two-sided:

$$\hat{x}_{\text{nom}} \pm \Delta \hat{x} = \hat{x}_{\text{nom}} \pm (\hat{x}_{\text{var}} - \hat{x}_{\text{nom}}). \quad (7.16)$$

No smoothing of the systematic variations relative to the statistical uncertainties is performed.

The different kinds of considered systematic variations affect different components of the unfolding:

- **Model variations** mainly come in the form of varied parameters for the reweighting of the MC distributions as described in Section 5.4. They affect the response matrix as well as the bias distribution used in the regularization. In order to propagate model uncertainties through the unfolding, it is repeated with the nominal input data and the simultaneously varied response matrix and bias distribution.
- **Simulation variations** affect MC events only on detector level. They come in the form of scaling weights of reconstructed variables, e.g., on the reconstructed  $z_{\text{vtx}}$  or track  $p_T$ , and as event weights, e.g., for the trigger correction factors. They are only applied on the detector level and thus only affect the response matrix but not the bias distribution. Simulation uncertainties are propagated by unfolding the nominal input distribution with the varied response matrix and the nominal bias distribution.
- **Event selection variations** affect both data and the MC. The MC is only affected on detector level so that only the response matrix is varied, whereas the bias remains the nominal distribution. Selection uncertainties are propagated by unfolding the varied input distribution with the varied response matrix.
- **Normalization uncertainties** are directly applied to the unfolded distributions.

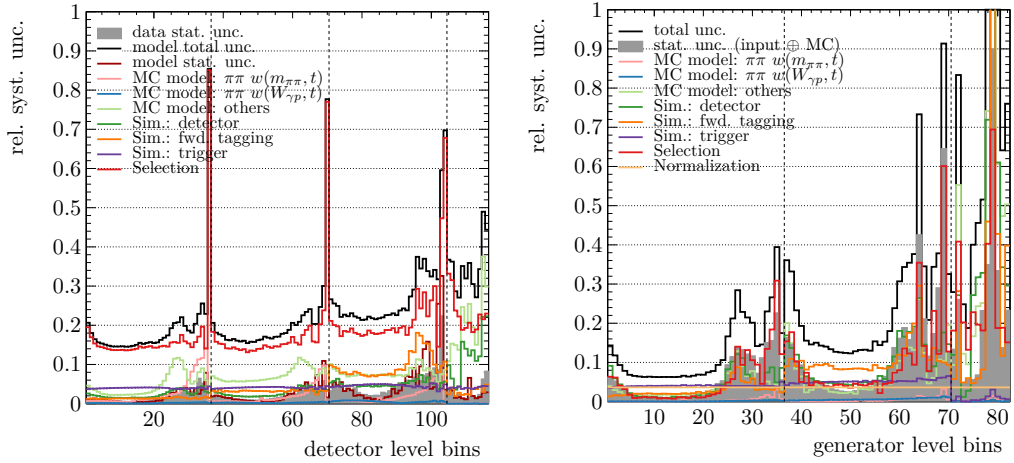


**Figure 7.10:** Uncertainty breakdown for the one-dimensional  $m_{\pi\pi}$  distributions before (left) and after unfolding (right). The impact of various sources of Uncertainties as labeled in the legends is compared.

In Figure 7.10, the uncertainty breakdown for the one-dimensional  $m_{\pi\pi}$  distributions is shown for the MC model on detector level and for the unfolded data distributions. Only combinations of selected groups of uncertainties are shown. Three things are particularly noteworthy. First, unfolding comes at the cost of increased statistical uncertainties. Second, the impact of model variations is strongly reduced by the unfolding. In fact, a reduction is to be expected for variations of the unfolded distributions. The way the response matrix is normalized, it is indifferent to the shape of the underlying MC distributions. However, these variations can still have a small impact through the bias in the regularization. Finally, also the apparent impact of the selection variations is reduced because they affect both data and the MC synchronously. On detector level, (absolute) selection uncertainties are only shown for the MC and not relative to data.

### 7.2.6 Unfolding Procedure Overview

In summary, the unfolding procedure is the following:

1. The (multi-dimensional) detector level data distributions in the signal and background tagging control regions are projected onto a one-dimensional binning scheme.
2. The beam-gas background is directly subtracted from the detector level data distribution.
3. The TUnfold  $\chi^2$  fit is performed with the unfolding matrix as defined in the text. Multiple transformations of the data are performed simultaneously by the fit:
  - The normalization of the MC background samples is determined and the respective contributions are subtracted from the detector level distribution.
  - The remaining  $\pi^+\pi^-$  distributions are corrected for migration effects and for the full reconstruction and selection efficiency within the fiducial phasespace.
  - Contributions with  $Q^2 > 0.1 \text{ GeV}^2$  are removed to get as close as possible to the true photoproduction regime.
  - The elastic ( $m_Y = m_p$ ) and proton-dissociative ( $m_p < m_Y < 10 \text{ GeV}$ ) contributions are separated.
4. The unfolding is performed with a regularization of the second derivative of the unfolded distributions. The regularization is aware of the physical distributions and uses the truth MC distributions as a bias. The regularization strength  $\tau$  is chosen to minimize the average global correlation coefficient  $\langle \rho \rangle$ . To find the corresponding optimal  $\tau$  value, a scan of  $\langle \rho \rangle$  over discrete values of  $\tau$  is performed.
5. Statistical and systematic uncertainties are propagated through the unfolding as described in the text.

The unfolding results in event number distributions on truth  $\pi^+\pi^-$  particle level. From these differential  $\pi^+\pi^-$  photoproduction cross-sections can be calculated.

### 7.2.7 $\pi^+\pi^-$ Cross-Section Definition

Differential  $\pi^+\pi^-$  photoproduction cross-sections are calculated from the number of unfolded  $\pi^+\pi^-$  events. The most general case considered in this analysis is the triple-differential elastic and proton-dissociative cross-section as a function of  $m_{\pi\pi}$ ,  $W_{\gamma p}$ , and  $t$ . In bin  $j$  of the unfolded distribution it is defined as:

$$\left[ \frac{d^2\sigma(\gamma p \rightarrow \pi^+\pi^- Y)(Y; m_{\pi\pi}, W_{\gamma p}, t)}{dt dm_{\pi\pi}} \right]_j = \frac{\hat{x}_j(Y; m_j, W_j, t_j)}{\Delta t_j \Delta m_j} \frac{1}{\mathcal{L}_{\text{int}} \Phi_{\gamma/e}^{\text{int}}(W_j)}. \quad (7.17)$$

$Y$  can be either the elastically scattered proton or the proton remnants in dissociative events.  $\hat{x}_j$  is the number of unfolded events in bin  $j$ , which spans a kinematic range  $(m_j \pm \frac{1}{2}\Delta m_j) \otimes (W_j \pm \frac{1}{2}\Delta W_j) \otimes (t \pm \frac{1}{2}\Delta t_j)$ . The derivative with respect to  $m_{\pi\pi}$  and  $t$  is estimated via the division by the respective bin widths  $\Delta m_j$  and  $\Delta t_j$ . A priori, no bin center correction is performed even though the cross-section may vary strongly within individual  $t$  and  $m_{\pi\pi}$  bins. The event yields are normalized by the integrated  $ep$  luminosity  $\mathcal{L}_{\text{int}}$ . They are turned into a photoproduction cross-section by normalization by the integrated photon-flux  $\Phi_{\gamma/e}^{\text{int}}$ . The flux is calculated in the Weizsäcker-Williams approximation by integrating Equation (2.51) over the considered photoproduction phasespace  $0 \leq Q^2 < 0.1 \text{ GeV}^2$  and the respective  $W_{\gamma p}$  bin; compare Section 2.4.

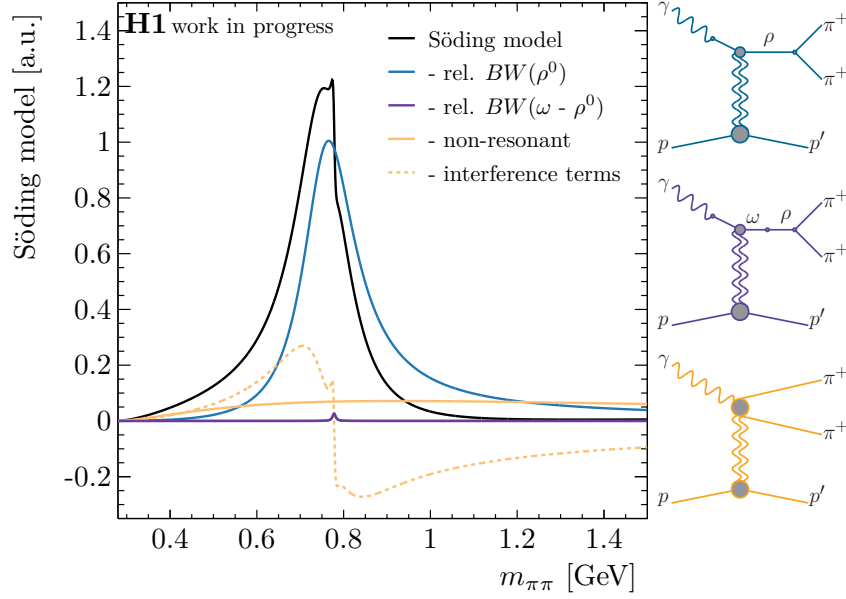


**Figure 7.11:** Söding model and individual contributions as labeled by the legend and illustrated by the color coded diagrams.

### 7.3 $\rho^0$ Cross-Section Definition

The  $\pi^+\pi^-$  photoproduction cross-section is dominated by the  $\rho^0$  resonance in the considered kinematic range. However, it has been observed to obtain also large contributions from non-resonant continuum  $\pi^+\pi^-$  production in similar past HERA analyses [6, 11, 13]. From DIS  $\pi^+\pi^-$  production measurements, also higher mass  $\rho'$  resonances can be expected to contribute [8]. Besides, in  $\pi^+\pi^-$  production in electron-positron annihilation a significant  $\omega(782)$  component is observed; for example, by Akhmetshin et al. [189]. In the past, this has been widely neglected in high-energy  $\pi^+\pi^-$  photoproduction where the experimental resolution often does not allow to resolve the narrow  $\omega(782)$  width.

In order to separate these contributions and to extract the  $\rho^0$  cross-section, the unfolded  $m_{\pi\pi}$  distribution is parametrized and fitted. Individual components of the fit model are then associated with the respective physical contributions. By integrating these components over the invariance di-pion mass, the contributions of the corresponding physical processes to the  $\pi^+\pi^-$  photoproduction cross-section are calculated.

#### 7.3.1 Söding Model

Around the  $\rho^0$  resonance peak, a Söding type model [122] is used to describe the  $m_{\pi\pi}$  spectrum. It considers a  $\rho^0$ , non-resonant, and  $\omega$  contribution. They are added on amplitude level, so that interference effects are taken into account. Further  $\rho'$  resonances are not considered as they are assumed to only contribute at high masses  $m_{\pi\pi} \gtrsim 1.2$  GeV, where the model then is not applicable. The model is defined as:

$$\frac{d\sigma_{\pi\pi}}{dm_{\pi\pi}}(m_{\pi\pi}) = N \frac{q^3(m_{\pi\pi})}{q^3(m_\rho)} \left| A_{\rho,\omega}(m_{\pi\pi}) + A_{\text{nr}}(m_{\pi\pi}) \right|^2. \quad (7.18)$$

$N$  is a global normalization factor.  $q(m_{\pi\pi})$  is the momentum of one of the pions in the  $\pi^+\pi^-$  center of mass frame:

$$q(m_{\pi\pi}) = \frac{1}{2} \sqrt{m_{\pi\pi}^2 - 4m_\pi^2} \quad (7.19)$$

The factor  $q^3(m_{\pi\pi})$  then describes the spin averaged  $\pi^+\pi^-$  contribution to the phasespace integrated over the decay angles as it is derived for example by Jackson [190]. It is normalized to the value at the  $\rho^0$  resonance. The amplitude  $A_{\rho,\omega}$  takes into account  $\rho^0$  and  $\omega$  contributions, whereas the non-resonant components are modeled by  $A_{\text{nr}}(m_{\pi\pi})$ . The two components are considered to be fully coherent, and a non-interfering background is not considered. An illustration of the model and its components is given in Figure 7.11.

The combined  $\rho^0$ - $\omega$  amplitude is modeled following a parametrization given by Akhmetshin et al. [189]

$$A_{\rho,\omega}(m_{\pi\pi}) = \mathcal{BW}_\rho(m_{\pi\pi}) \left( 1 + f_\omega e^{i\phi_\omega} \frac{m_{\pi\pi}^2}{m_\omega^2} \mathcal{BW}_\omega(m_{\pi\pi}) \right), \quad (7.20)$$

where  $f_\omega$  and  $\phi_\omega$  are a normalization factor and an electromagnetic mixing phase for the  $\omega$  contribution. The  $\omega$  meson is not expected to decay into a pair of charged pions directly because of the conservation of G-parity by the strong interaction. However, electromagnetic  $\omega \rightarrow \rho^0$ -mixing with a subsequent  $\rho^0 \rightarrow \pi^+\pi^-$  decay is possible. A detailed discussion on the topic is given by O'Connell et al. [191], for example. Both resonances are modeled by a relativistic Breit-Wigner [192]:

$$\mathcal{BW}_{\text{VM}}(m_{\pi\pi}) = \frac{m_{\text{VM}}\Gamma_{\text{VM},0}}{m_{\pi\pi}^2 - m_{\text{VM}}^2 + i m_{\text{VM}}\Gamma(m_{\pi\pi})}. \quad (7.21)$$

The parameters  $m_{\text{VM}}$  and  $\Gamma_{\text{VM},0}$  are the respective vector meson's Breit-Wigner mass and width. The Breit-Wigner function is normalized to  $\mathcal{BW}_{\text{VM}}(m_{\text{VM}}) = 1$ . For the  $\rho^0$  resonance a p-wave mass-dependent width [190] is used:

$$\Gamma(m_{\pi\pi}) = \Gamma_{\text{VM},0} \frac{q^3(m_{\pi\pi})}{q^3(m_{\text{VM}})} \frac{m_{\text{VM}}}{m_{\pi\pi}}. \quad (7.22)$$

whereas for the very narrow  $\omega$  a constant width is assumed.

The unknown non-resonant amplitude is parametrized by the function:

$$A_{\text{nr}}(m_{\pi\pi}) = \frac{f_{\text{nr}}}{(m_{\pi\pi}^2 - 4m_\pi^2 + \Lambda_{\text{nr}})^{\delta_{\text{nr}}}}, \quad (7.23)$$

where the relative normalization is given by  $f_{\text{nr}}$ , and  $\Lambda_{\text{nr}}$  and  $\delta_{\text{nr}}$  are free model parameters. They can shape the amplitude and thus allow to model a possible internal structure of the non-resonant  $\gamma\pi\pi$ -coupling. In similar past analyses, typically a purely real non-resonant amplitude has been assumed. Following that assumption,  $f_{\text{nr}}$  is set to be real although it could potentially also have a complex component. For  $\delta_{\text{nr}} > \frac{3}{4}$ , the non-resonant cross-section has a local maximum at:

$$m_{\pi\pi} = \frac{\sqrt{\Lambda_{\text{nr}} + (\frac{4}{3}\delta_{\text{nr}} - 1) 4m_\pi^2}}{\sqrt{\frac{4}{3}\delta_{\text{nr}} - 1}}, \quad (7.24)$$

and falls proportional to  $(1/m_{\pi\pi}^2)^{2\delta_{\text{nr}}-3}$  in the high mass region.

The model and hence the definition of the  $\rho^0$  cross-section is by no means unique. On the contrary, it has well-known limitations. From studies in  $e^+e^- \rightarrow \pi^+\pi^-$  production, it is known that a Breit-Wigner does not sufficiently describe the  $\rho^0$  lineshape, and also that the  $\rho^0$ - $\omega$ -mixing is more complex than assumed here. For a review see Reference [193], for example. Unfortunately, these results can not be used directly for  $\pi^+\pi^-$  photoproduction. There, the presence of the non-resonant component complicates matters. The mass-dependence of the non-resonant contribution and its interference structure with the resonances are likely much more complex than parametrized here. Furthermore, a  $\rho^0$  form-factor might have to be introduced to take into account off-shell effects in the  $\rho^0$ -Pomeron interaction. This would alter the effective  $\rho^0$  resonance lineshape. Compare the discussion in [124], for example.

These effects can not be disentangled from a parametric fit to the  $m_{\pi\pi}$  distribution alone, as it is performed in this analysis.

Nonetheless, the Söding model is chosen for the extraction of the  $\rho^0$  contribution to the  $\pi^+\pi^-$  cross-section. The primary motivation is that very similar models have been widely used in past  $\rho^0$  cross-section measurements. Results can then be compared on the same basis. Furthermore, the model is practical in its application, is able to describe the measured distributions well, and is physical in the sense that is defined in terms of (interfering) amplitudes.

In principle, there are better models available to describe the  $\pi^+\pi^-$  photoproduction cross-section, e.g., the model presented in Section 2.3. These are typically too impractical for the context of this thesis. In particular, they do not allow to perform fits to the measured data easily. See also Appendix A.2.

A priori, it is also not clear how the model should be applied to multi-differential cross-sections. It was found that by allowing for some few model parameters to have kinematic dependencies, the model can describe the  $\pi^+\pi^-$  mass spectrum in many different kinematic regimes. In practice, the present data do not allow to study potential kinematic dependencies of all model parameters. When applying the model, further assumptions on these dependencies need to be made. Details are discussed only in Chapter 8, where they become relevant.

In this thesis, no model uncertainties are assigned to results obtained via the Söding model. In order to illustrate that those are potentially significant, the  $m_{\pi\pi}$  distribution is also interpreted with the Ross-Stodolsky model. This model also has been widely used in the past to describe the photoproduction  $m_{\pi\pi}$  lineshape. However, it is *physically* less well motivated. It is thus only used for reference in this thesis. No results are derived from it, and it is also not used to estimate systematic model uncertainties.

### 7.3.2 Ross-Stodolsky Model

The Ross-Stodolsky model [194] introduces an ad hoc skewing parameter  $k$  to distort the  $\rho^0$  Breit-Wigner amplitude artificially. Taking also into account the  $\omega$  contribution, here it is used in the form:

$$\frac{d\sigma_{\pi\pi}}{dm_{\pi\pi}}(m_{\pi\pi}) = N \frac{q^3(m_{\pi\pi})}{q^3(m_\rho)} \left| A_{\rho,\omega}(m_{\pi\pi}) \right|^2 \left( \frac{m_\rho}{m_{\pi\pi}} \right)^k. \quad (7.25)$$

### 7.3.3 Cross-Section Extraction

In order to extract the  $\rho^0$  contribution to the  $\pi^+\pi^-$  cross-section, the unfolded mass distributions are fitted using Equation (7.18). The  $\rho^0$  Breit-Wigner contribution is then defined by the integral:

$$\frac{d\sigma(\rho \rightarrow \pi^+\pi^-)}{dt} = \frac{N}{q^3(m_\rho)} \int_{2m_\pi}^{m_\rho+5\Gamma_\rho} |\mathcal{BW}_\rho(m)|^2 q^3(m) dm. \quad (7.26)$$

As the  $\rho^0$  resonance decays almost exclusively into two charged pions, this is assumed to be equal to the total  $\rho^0$  photoproduction cross-section without correcting for the  $\rho^0 \rightarrow \pi^+\pi^-$  branching fraction  $BR(\rho^0 \rightarrow \pi^+\pi^-) \simeq 100\%$  [1].

The non-resonant and  $\omega$  contribution to the cross-section in that mass range can be calculated analogously:

$$\frac{d\sigma(\text{non-res. } \pi^+\pi^-)}{dt} = \frac{N}{q^3(m_\rho)} \int_{2m_\pi}^{m_\rho+5\Gamma_\rho} |A_{\text{nr}}(m)|^2 q^3(m) dm, \quad (7.27)$$

$$\frac{d\sigma(\omega \rightarrow \pi^+\pi^-)}{dt} = \frac{N f_\omega^2}{m_\omega^4 q^3(m_\rho)} \int_{2m_\pi}^{m_\omega+5\Gamma_\omega} |\mathcal{BW}_\rho(m)\mathcal{BW}_\omega(m)|^2 m^4 q^3(m) dm. \quad (7.28)$$

For better comparison, the non-resonant contribution is integrated over the same mass range as the  $\rho^0$  resonance. Fit parameter uncertainties are propagated through the integrals by applying Gaussian error propagation and numerically evaluating the derivation of the integrand with respect to the parameters<sup>4</sup>.

## 7.4 Cross-Section Fits and $\chi^2$ Definition

The measured differential cross-sections are parametrized and fitted with the goal to extract more fundamental model parameters. Only one-dimensional model parametrizations are used. However, for multi-dimensional cross-sections, multiple one-dimensional distributions are fitted in parallel. This allows taking the full uncertainty correlations into account and fitting a shared set of model parameters. As the TUnfold package provides Gaussian (statistical) uncertainties, the fits are performed using a  $\chi^2$  approach, in which a  $\chi^2$  function is minimized by varying a set of model parameters  $\vec{\theta}$ . The  $\chi^2$  function is defined as

$$\chi^2(\vec{\theta}) = \sum_{i=0}^{n_{\text{dist}}} \sum_{j=0}^{n_{\text{dist}}} \left[ \vec{\sigma}_i - \vec{\mathcal{F}}_i(\vec{\theta}) \right]^T \cdot (\mathbf{U}^{-1})_{ij} \cdot \left[ \vec{\sigma}_j - \vec{\mathcal{F}}_j(\vec{\theta}) \right] \quad (7.29)$$

Here,  $n_{\text{dist}}$  cross-section distributions  $\vec{\sigma}_i$  are fitted in parallel and  $\mathbf{U}$  is the combined covariance matrix of all bins in all distributions. The cross-section dependence on some variable  $m$  is parametrized by fit functions  $f_i(m; \vec{\theta})$ . Generally, different functions can be used for each distribution, which can depend on a different subset of the fit parameters. Since binned cross-section distributions are measured, fit functions describing differential cross-sections are averaged over the bins:

$$\mathcal{F}_{ik}(\vec{\theta}) = \frac{1}{\Delta_{ik}} \int_{m_{ik} - \frac{1}{2}\Delta_{ik}}^{m_{ik} + \frac{1}{2}\Delta_{ik}} f_i(m, \vec{\theta}) dm, \quad (7.30)$$

for a bin  $[m_{ik} - \frac{1}{2}\Delta_{ik}; m_{ik} + \frac{1}{2}\Delta_{ik}]$ .

### 7.4.1 Propagation of Uncertainties Through Fits

#### Offset Method

An offset approach is taken to propagate systematic uncertainty through the fits. The minimization of Equation (7.29) then is performed with the statistical covariance matrix  $\mathbf{U}_{\text{stat}}$  only. In a first step, fitting the nominal cross-section distributions provides the nominal set of fit parameters  $\hat{\vec{\theta}}$  that minimize the nominal  $\chi^2$ . The statistical covariance matrix of these fit parameters is then calculated from the Hessian-matrix of the  $\chi^2$  function evaluated at the minimum  $\hat{\vec{\theta}}$  [182]. Subsequently, in order to propagate systematic uncertainties, the fit is repeated with the fitted cross-sections varied by the systematic uncertainties  $\vec{\sigma}_i \rightarrow \vec{\sigma}_i + \Delta\vec{\sigma}_{\text{syst},i}^{\text{up/dn}}$  (but always with the nominal statistical covariance matrix). Corresponding systematic fit parameter uncertainties are estimated from the resulting parameter shifts:

$$\hat{\vec{\theta}}_{\text{nom}} \pm \Delta\hat{\vec{\theta}}_{\text{up/dn}} = \hat{\vec{\theta}}_{\text{nom}} \begin{pmatrix} +(\hat{\vec{\theta}}_{\text{up}} - \hat{\vec{\theta}}_{\text{nom}}) \\ -(\hat{\vec{\theta}}_{\text{nom}} - \hat{\vec{\theta}}_{\text{dn}}) \end{pmatrix}. \quad (7.31)$$

The offset method is chosen because it provides stable and transparent fit results and gives conservative estimates for systematic fit parameter uncertainties, compared to other approaches. It has two big disadvantages, however. First, the minimal  $\chi^2$  values obtained in

<sup>4</sup>  $U_{ij}^\sigma = \left( \int \frac{\partial f}{\partial \theta_j} dm \right) \left( \int \frac{\partial f}{\partial \theta_j} dm \right) U_{ij}^\theta$ , with  $\mathbf{U}^\sigma$  and  $\mathbf{U}^\theta$  the cross-section and fit parameter covariance matrices, respectively.

the fits can not be used for hypothesis testing to evaluate whether a given model describes the data or not. Since only statistical uncertainties are considered in the  $\chi^2$  definition, a large  $\chi^2$  value per degree of freedom can either indicate a wrong fit model or a systematic bias in the measured distribution which might be covered by the systematic uncertainties. Secondly, such biases are then also reflected in the nominal fit parameters.

### Total Covariance Matrix

The present measurements are indeed mostly systematically dominated. Ideally, the systematic uncertainties should then be included directly in the fits. One way to achieve this is by using the total covariance matrix in the  $\chi^2$  definition. This approach has been used in similar past diffractive H1 analyses, e.g., in Reference [24]. The total covariance matrix is defined from the statistical covariance matrix and the systematic uncertainties:

$$\mathbf{U}_{\text{tot}}^{-1} = \mathbf{U}_{\text{stat}}^{-1} + \sum_{\text{syst.}} \Delta\vec{\sigma}_{\text{syst}} \cdot (\Delta\vec{\sigma}_{\text{syst}})^T. \quad (7.32)$$

This requires a symmetrization of the systematic up and down uncertainties:

$$\Delta\vec{\sigma}_{\text{syst}} = \frac{1}{2} (\Delta\vec{\sigma}_{\text{up}} - \Delta\vec{\sigma}_{\text{dn}}). \quad (7.33)$$

Since the systematic uncertainties are now directly considered in the  $\chi^2$  definition, it is implicitly assumed that they are normally distributed. Compared to the offset method, this typically results in smaller estimates for total fit parameter uncertainties. While desirable in principle, it is often technically challenging in practice to include systematic uncertainties in that way. In general, it requires much “better” estimates for the systematic uncertainties than the offset method. In particular, they need to provide correct shapes for all systematic effects that can lead to a bias of the measured distributions. Wrong shapes or features such as statistical fluctuations in the systematic uncertainties can otherwise easily bias the fit result because of the large correlations they introduce even between far away bins of a distribution. For the present analysis, the estimated uncertainties are not guaranteed to satisfy these criteria. Smooth uncertainties with correct shapes would need to be ensured in up to three dimensions and simultaneously for the elastic and proton-dissociative distributions. Within the context of this thesis, this was not feasible. One particular problem of the systematic uncertainties of the present measurement is that they often combine shape and normalization uncertainties within a single variation. An example of this is the large uncertainty associated with the trigger correction; compare Figure 5.6. Biases in the shape of a fitted distribution that are accounted for by a systematic uncertainty can then result in wrong shifts of the fitted normalization parameters. In the offset method, on the other hand, such uncertainties only increase the estimated uncertainty of the normalization parameters.

In the following analysis of the measured cross-sections, the more robust offset method is always used for the extraction of the  $\rho^0$  contributions via the Söding fits. There, many bins are fitted in parallel, making the chance to pick up some artifact of the total covariance matrix more likely. Also, most systematic variations do not have a strong  $m_{\pi\pi}$  dependence. Consequently, the offset method can be expected to provide reliable and unbiased results. For the subsequent analysis of the  $\rho^0$  cross-section distributions, standard fits are also performed via the offset method. However, the systematic uncertainties exhibit quite significant  $W_{\gamma p}$  and  $t$  dependencies. Fits with the total covariance matrix are thus used as a reference. They allow investigating potential biases in the nominal fit result and test if these are covered by systematic uncertainties. They can thus help to understand the results of the offset method better and to validate them. Such a validation is most relevant in cases of a poor fit quality of the nominal fit with statistical uncertainties only.



## 8 RESULTS

Measurements of the single-, double-, and triple-differential elastic and proton-dissociative  $\pi^+\pi^-$  photoproduction cross-sections as a function of the invariant  $\pi^+\pi^-$  mass  $m_{\pi\pi}$ , the photon-proton center-of-mass energy  $W_{\gamma p}$ , and the momentum transfer at the proton vertex  $t$  are presented. By parametrizing and fitting the  $m_{\pi\pi}$  dependence of the  $\pi^+\pi^-$  cross-sections, the  $\rho^0$  contributions can be extracted, and single- and double-differential elastic and proton-dissociative  $\rho^0$  cross-sections are measured as a function of  $W_{\gamma p}$  and  $t$ . The differential  $\rho^0$  cross-sections are interpreted with fits of parametric models and compared with previous measurements.

In Section 8.1, the fiducial elastic and proton-dissociative  $\pi^+\pi^-$  cross-section and the single-differential cross-sections as a function of  $m_{\pi\pi}$  are measured and discussed. The Söding model that is introduced in Section 7.3.1 is fitted to the  $m_{\pi\pi}$  distributions in the restricted analysis range  $0.6 \text{ GeV} \leq m_{\pi\pi} \leq 1 \text{ GeV}$ . The fit is used to illustrate the extraction of the  $\rho^0$  contributions to the  $\pi^+\pi^-$  cross-sections and to constrain model parameters for the further analysis. In Section 8.2, multi-dimensional  $\pi^+\pi^-$  cross-sections as a function of  $m_{\pi\pi}$  and the other kinematic variables are presented. By fitting the Söding model to the  $m_{\pi\pi}$  distributions, single- and double-differential  $\rho^0$  cross-sections as a function of  $W_{\gamma p}$  and  $t$  are extracted. The  $\rho^0$  cross-sections are parametrized and interpreted within the models for hadronic scattering cross-sections that are discussed in Chapter 2. In particular, the parameters of the effective leading Regge trajectory are extracted from the double-differential elastic  $\rho^0$  cross-section.

### 8.1 $\pi^+\pi^-$ Photoproduction Cross-Sections

The single-differential  $\pi^+\pi^-$  cross-section  $d\sigma(\gamma p \rightarrow \pi^+\pi^- Y)/dm_{\pi\pi}$  is measured as a function of the di-pion mass and for elastic and proton-dissociative scattering events. The result is obtained by unfolding the one-dimensional  $m_{\pi\pi}$  distributions following the procedure described in Chapter 7. The unfolded cross-sections are shown in Figure 8.1.

The differential elastic and proton-dissociative  $\pi^+\pi^-$  cross-section are dominated by the  $\rho^0$  resonance peaking at about 770 MeV and fall off steeply towards higher masses. However, a second and very broad excited  $\rho'$  resonance peak appears at around 1600 MeV. The peak, which has been previously observed in both photoproduction and electron-positron annihilation, is ascribed by the PDG [1] to the presence of two resonances: The  $\rho(1450)$  and  $\rho(1700)$  resonances. Due to their broadness of approximately 400 MeV and 250 MeV, respectively, and the limited precision and resolution provided by the present measurement, they cannot be visually separated. At the  $\rho^0$  peak, the measured proton-dissociative cross-section is about half as large as the elastic. Interestingly, the respective ratio exhibits a mass dependence and appears to grow with rising  $m_{\pi\pi}$ . The shape of the  $\rho^0$  resonance can not depend on the proton system in the final state. The difference in the  $m_{\pi\pi}$  lineshape can thus be taken as a model-independent indication for contributions to  $\pi^+\pi^-$  photoproduction beyond the  $\rho^0$  resonance. These must then contribute differently to the elastic and the proton-dissociative component. An  $\omega$  contribution directly on top of the  $\rho^0$  peak is not visible on the logarithmic scale of the plots. It is discussed in more detail in the context of the Söding fit of the mass distributions that is described further on in the text.

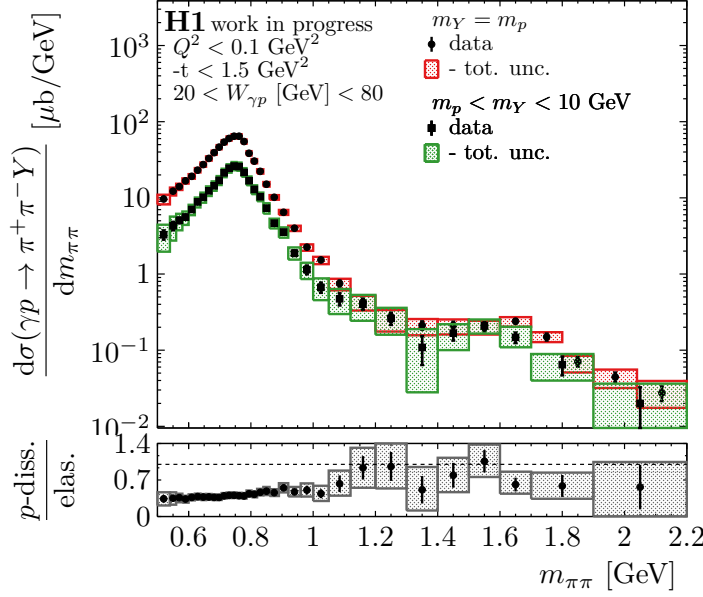


**Figure 8.1:** Unfolded elastic and proton-dissociative differential cross-section  $d\sigma(\gamma p \rightarrow \pi^+\pi^-Y)/dm_{\pi\pi}$  as a function of  $m_{\pi\pi}$ . The black points and error bars show the nominal cross-section values with statistical uncertainties from the input data and the MC unfolding factors. The data uncertainties alone are marked by the small perpendicular lines. The red and green bands show the total uncertainty of the elastic and proton-dissociative component, respectively. For the ratio plot, elastic bins are merged to match the proton-dissociative binning and uncertainty correlations are fully propagated.

### 8.1.1 Fiducial $\pi^+\pi^-$ Cross-Section

The fiducial  $\pi^+\pi^-$  cross-section in the phasespace defined in Table 7.2 is calculated from the single-differential cross-section  $d\sigma(\gamma p \rightarrow \pi^+\pi^-Y)/dm_{\pi\pi}$  by summing all bins over the considered mass range. The inclusive cross-section for elastic and proton-dissociative events is determined to be:

$$\sigma(\gamma p \rightarrow \pi^+\pi^-Y) = 17.20 \pm 0.05 \text{ (stat.) } {}_{-1.16}^{+1.13} \text{ (syst.) } \mu\text{b}, \text{ for } m_p \leq m_Y < 10 \text{ GeV}.$$

The elastic and the proton-dissociative contribution to the cross-section are separated in the unfolding. They are found to be

$$\begin{aligned} \sigma(\gamma p \rightarrow \pi^+\pi^-p) &= 12.22 \pm 0.05 \text{ (stat.) } {}_{-0.78}^{+0.77} \text{ (syst.) } \mu\text{b}, \text{ for } \text{ and} \\ \sigma(\gamma p \rightarrow \pi^+\pi^-Y) &= 4.98 \pm 0.06 \text{ (stat.) } {}_{-0.66}^{+0.65} \text{ (syst.) } \mu\text{b}, \text{ for } m_p < m_Y < 10 \text{ GeV}, \end{aligned}$$

respectively. The uncertainties of the two components are correlated with a statistical and total Pearson correlation coefficient of  $\rho_{\text{stat}} = -0.57$ , and  $\rho_{\text{tot}} = +0.27$ , respectively. Considering both statistical and systematic correlations, the ratio of the proton-dissociative to the elastic cross-section in the considered phasespace is:

$$\frac{\sigma(\gamma p \rightarrow \pi^+\pi^-Y)}{\sigma(\gamma p \rightarrow \pi^+\pi^-p)} = 0.408 \pm 0.006 \text{ (stat.) } {}_{-0.052}^{+0.053} \text{ (syst.)}, \text{ for } m_p < m_Y < 10 \text{ GeV}.$$

The present measurement is statistically very precise with uncertainties of the fiducial cross-sections on the one percent level and lower. However, it suffers from large systematic uncertainties with an estimated size of around 6% to 13% for the elastic and the proton-dissociative cross-section, respectively. The composition of the systematic uncertainties of the elastic and the proton-dissociative fiducial cross-section is illustrated in Figure 8.2.

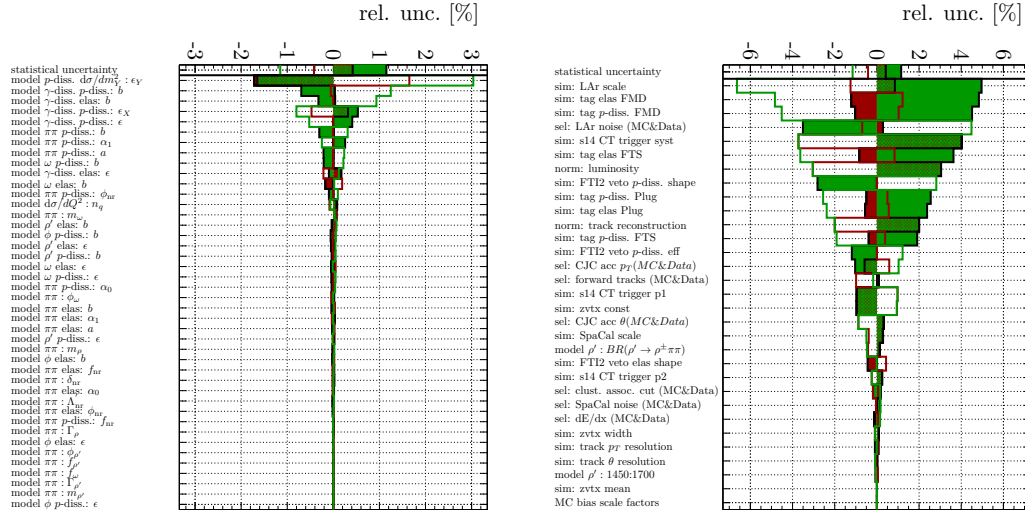


**Figure 8.2:** Contributions to the uncertainty of the elastic (red) and proton-dissociative (green) fiducial  $\pi^+\pi^-$  cross-section. The cross-sections are obtained from unfolding the one-dimensional  $m_{\pi\pi}$  distributions. Model parameters (left) and all other sources of uncertainties (right) are shown separately and ordered by size. The filled areas show the  $up$  variation and illustrate the correlation between elastic and dissociative uncertainties. For reference, the statistical uncertainty is plotted twice.

uncertainty group	relative uncertainty [%]	
	$m_Y = m_p$	$m_p < m_Y < 10 \text{ GeV}$
Sim.: forward tagging	2.1	8.9
Sim.: detector (LAr, SpaCal, tracker)	1.9	6.1
Selection	1.6	5.4
Sim.: trigger	4.0	5.1
MC model: others ( $m_Y$ , $Q^2$ , bkg.)	2.0	4.2
Normalization	3.6	3.6
Statistical	0.4	1.2
MC model: $\pi\pi w(W_{\gamma p}, t)$	0.1	0.5
MC model: $\pi\pi w(m_{\pi\pi}, t)$	0.1	0.2
Total	6.3	13.0

**Table 8.1:** Summary table of the combined impact of systematic uncertainty groups on the fiducial  $\pi^+\pi^-$  cross-sections. The numbers are obtained from unfolding the one-dimensional  $m_{\pi\pi}$  distribution and with symmetrized systematic uncertainties.

As discussed previously, model uncertainties are significantly reduced by the unfolding; in particular, those directly affecting the unfolded distributions. The dominant remaining uncertainties are then the ones related to the detector simulation. For the elastic cross-section, the trigger uncertainty has the biggest impact at roughly 4%. In contrast, the proton-dissociative cross-section is dominantly affected by calorimeter and tagging uncertainties of the order of 6% to 9%. A summary of the combined impact of selected groups of systematic uncertainties on the fiducial  $\pi^+\pi^-$  cross-sections is given in Table 8.1.

For validation, the fiducial cross-sections are also measured by unfolding other single- or multi-differential distributions of the variables  $m_{\pi\pi}$ ,  $t$ , or  $W_{\gamma p}$ . The values obtained via the different distributions are all consistent and agree within statistical uncertainties. By

construction of the unfolding, systematic model uncertainties can vary slightly between the approaches.

### 8.1.2 Söding Fit and Extraction of the $\rho^0$ Cross-Sections

The unfolded single-differential cross-sections  $d\sigma(\gamma p \rightarrow \pi^+\pi^-Y)/dm_{\pi\pi}$  can be parametrized by the Söding model defined by Equation (7.18) in Chapter 7. The model is fitted to the data in a reduced mass range  $0.6 \leq m_{\pi\pi} \leq 1$  GeV. The motivation for considering only the reduced range is two-fold: On the one hand, the model is not expected to describe the full measured  $m_{\pi\pi}$  range. In particular, the second resonance peak that can be observed in Figure 8.1 is not included in the model. Furthermore, it is not clear how reliable the modeling of the non-resonant background is in the tails of the  $\rho^0$  peak. On the other hand, the systematic uncertainties of the measured distributions are mostly flat in the reduced range. As a consequence, they can be safely propagated through the fit via the offset method and need not be included directly in the  $\chi^2$  definition; compare discussion in Section 7.4.

The fit is performed simultaneously to the elastic and the proton-dissociative distribution with all uncertainty correlations taken into account. For physical parameters, such as the masses and widths of resonance contributions, a single fit parameter is assumed. All other model parameters are allowed to differ for the elastic and proton-dissociative fit function. The  $\omega$  width is of the order of the  $m_{\pi\pi}$  resolution and can not be constrained by the present data. Instead, the PDG value  $\Gamma_\omega = 8.5$  MeV is assumed and fixed in the fit, and only the  $\omega$  normalization, mass, and phase are allowed to vary.

#### Fit Result

The fit result is compared to the measured data in Figure 8.3, and the fit parameters are summarized in Table 8.2. The physical parameters are discussed further on in the text where they are compared to reference values. For the other model parameters, there are no expectations, in particular not regarding the consistency of elastic and proton-dissociative parameters. The difference between the elastic and proton-dissociative  $m_{\pi\pi}$  lineshape suggests that the non-resonant parameters should in-fact differ. The reduced  $\chi^2$  calculated with Equation (7.29) for the fit of the nominal distributions is good at  $\chi_{\text{stat}}^2/\text{ndf} = 23.6/(38 - 14) = 0.99$  with statistical uncertainties only. Systematic uncertainties are propagated through the fit using the offset method.

Within the Söding model, the  $\pi^+\pi^-$  cross-sections obtain the dominant contribution from the  $\rho^0$  resonance. However, there is also a significant non-resonant component. At the resonance peaks, it directly contributes at around 8% and 6% to the elastic and proton-dissociative cross-section, respectively. For both processes, the non-resonant amplitude changes only very little with the invariant di-pion mass in the considered range. However, the total impact of the non-resonant contribution is greatly enhanced by a strong interference with the  $\rho^0$  amplitude. Due to the Breit-Wigner phase shift, the interference changes sign at the resonance peak and thus results in the characteristic skewing of the  $\pi^+\pi^-$  lineshape in photoproduction. For the first time at HERA, there is also evidence for an  $\omega$  component in the  $\pi^+\pi^-$  spectrum. The direct  $\omega$  contribution to the cross-sections is negligibly small. However, the  $\omega$  gives rise to much larger interference contributions that cause a steep edge on top of the  $\rho^0$  resonance peak.

Since the width of the  $\omega$  is of the size of the  $m_{\pi\pi}$  resolution, the  $\omega$  contribution is mainly contained within a single bin of the cross-section distributions. It is thus very sensitive to the unfolding. As the  $\omega$  contribution results in a steep edge of the cross-sections, it is particularly prone to be biased by the regularization of the curvature of the unfolded distributions. It is found that in order to avoid a large bias, the  $\omega$  contribution must be included in the reference distributions used for the regularization. That is why it is essential that the  $\omega$  contribution is considered in the tuning of the signal MC samples; compare Section 5.4. For validation,

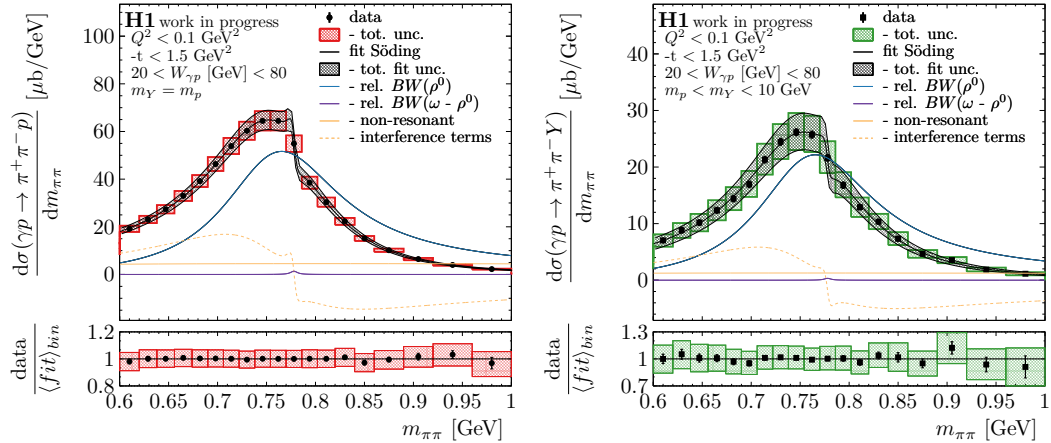


**Figure 8.3:** Elastic (left) and proton-dissociative (right) differential cross-section  $d\sigma(\gamma p \rightarrow \pi^+ \pi^- Y)/dm_{\pi\pi}$  as a function of  $m_{\pi\pi}$ . A Söding model is fitted to the cross-sections in the shown mass region  $0.6 \text{ GeV} \leq m_{\pi\pi} \leq 1 \text{ GeV}$  as described in the text. The model and its components are drawn as indicated in the legend. In the ratio panel, the data are compared to the bin-averaged fit function values as they are also considered in the  $\chi^2$  calculation for the fit. The data uncertainties are described in Figure 8.1.

parameter	value	stat.	syst.
$m_\rho$ [GeV]	0.7708	0.0012	+0.0005 -0.0009
$\Gamma_\rho$ [GeV]	0.1512	0.0021	+0.0014 -0.0023
$m_\omega$ [GeV]	0.7780	0.0016	+0.0010 -0.0008
$\Gamma_\omega$ [GeV]	0.0085	fixed	
$\delta_{nr}$	0.85	0.36	+0.07 -0.06

parameter	$m_Y = m_p$			$m_p < m_Y < 10 \text{ GeV}$		
	value	stat.	syst.	value	stat.	syst.
$A$ [ $\mu\text{b}/\text{GeV}^2$ ]	51.4	0.8	+3.3 -3.2	22.1	0.4	+2.9 -2.7
$f_\omega$	0.166	0.016	+0.017 -0.017	0.123	0.039	+0.031 -0.027
$\phi_\omega$	-0.52	0.19	+0.15 -0.11	-0.08	0.27	+0.21 -0.20
$f_{nr}$	0.191	0.034	+0.012 -0.015	0.151	0.032	+0.019 -0.013
$\Lambda_{nr}$ [ $\text{GeV}^2$ ]	0.08	0.22	+0.01 -0.01	0.06	0.23	+0.08 -0.05

**Table 8.2:** Fit parameters for the Söding fit of the single-differential elastic and proton-dissociative cross-sections  $d\sigma(\gamma p \rightarrow \pi^+ \pi^- Y)/dm_{\pi\pi}$  as a function of  $m_{\pi\pi}$ . The corresponding fit is shown in Figure 8.3.

the  $m_{\pi\pi}$  distributions are also unfolded without applying any regularization condition, and the Söding fit is repeated with the unregularized cross-sections. The fit parameters for the regularized and unregularized fit are found to differ only minimally and well within statistical uncertainties. Also, the impact of the regularization on the fit parameter uncertainties is small. It can thus be concluded that the measured  $\omega$  contribution to the  $\pi^+ \pi^-$  cross-sections is indeed a feature of the data and not an artifact of the unfolding.

### Cross-Section Contributions

The overall  $\rho^0$ ,  $\omega$ , and non-resonant contributions to the  $\pi^+ \pi^-$  cross-sections are calculated using equations (7.26 ff.). The values are summarized in Table 8.3. For reference, also the

full model is integrated over the same mass range as the  $\rho^0$  contribution and included in the table. The given values are not to be confused with the fiducial  $\pi^+\pi^-$  cross-sections that are presented in the previous section because some features of the data are not included in the model. Concerning the cross-section values, it is particularly noteworthy that the relative non-resonant contribution is indeed smaller in proton-dissociative than elastic scattering. This is consistent with a weaker skewing of the  $\rho^0$  peak in proton-dissociative scattering and explains the previously discussed difference between the elastic and proton-dissociative  $m_{\pi\pi}$  lineshapes. A potential explanation is discussed further on in the text in Section 8.2.2. The value obtained for the elastic  $\omega$  cross-section deviates from 0 by just over  $3\sigma$  considering the total uncertainty. This is taken as evidence for an  $\omega$  contribution to  $\pi^+\pi^-$  photoproduction. The corresponding proton-dissociative value, on the other hand, is roughly compatible with 0 at just over  $1\sigma$ . Simultaneously, the relative  $\omega$  to  $\rho^0$  contributions for elastic and proton-dissociative scattering are also consistent within uncertainties.

$X$	$\sigma(X)$ stat. syst.			$\frac{\sigma(X)}{\sigma(\rho)}$ stat. syst.			$\int m_{\pi\pi} \max$ [GeV ]
	[ $\mu\text{b}$ ]						
<b><math>m_Y = m_p</math></b>							
$\mathcal{BW}(\rho^0)$	11.62	0.15	$^{+0.74}_{-0.73}$			-	1.53
Söding $\pi^+\pi^-$	13.24	0.61	$^{+0.82}_{-0.82}$	1.139	0.042	$^{+0.013}_{-0.012}$	1.53
non-resonant	4.96	0.92	$^{+0.50}_{-0.50}$	0.427	0.075	$^{+0.037}_{-0.037}$	1.53
$\mathcal{BW}(\omega-\rho^0)$	1.72	0.33	$^{+0.36}_{-0.34} \times 10^{-2}$	2.56	0.51	$^{+0.54}_{-0.50} \times 10^{-3}$	0.82
<b><math>m_p &lt; m_Y &lt; 10 \text{ GeV}</math></b>							
$\mathcal{BW}(\rho^0)$	4.99	0.08	$^{+0.64}_{-0.60}$			-	1.53
Söding $\pi^+\pi^-$	5.23	0.27	$^{+0.72}_{-0.72}$	1.049	0.052	$^{+0.031}_{-0.046}$	1.53
non-resonant	1.39	0.28	$^{+0.23}_{-0.23}$	0.279	0.055	$^{+0.032}_{-0.035}$	1.53
$\mathcal{BW}(\omega-\rho^0)$	0.41	0.26	$^{+0.21}_{-0.17} \times 10^{-2}$	1.42	0.90	$^{+0.74}_{-0.59} \times 10^{-3}$	0.82

**Table 8.3:** Integrated contributions to the  $\pi^+\pi^-$  cross-sections obtained from the Söding fit.

It has to be assumed that the measured physical parameters strongly depend on the model parametrization. A corresponding uncertainty is not quantitatively evaluated. In order to estimate a potential impact, the Ross-Stodolsky parametrization (Equation (7.25)) is also fitted to the  $m_{\pi\pi}$  distributions. Overall, the description of the nominal data is worse for the Ross-Stodolsky model ( $\chi_{\text{stat}}^2/\text{ndf} = 43.7/(38 - 11) = 1.6$ ). Compared to the Söding model, the Ross-Stodolsky model leads to an increase of the extracted the  $\rho^0$  cross-sections by roughly 6% and 4% for the elastic and proton-dissociative cross-section, respectively. The  $\omega$  cross-section values, on the other hand, are decreased by about 30%, each. Furthermore, different  $\rho^0$  and  $\omega$  model parameters are obtained. They are discussed in the following section.

### Comparison With Other Measurements

The invariant  $\pi^+\pi^-$  mass spectrum has been studied extensively in both photoproduction and electron-positron annihilation. The results obtained in this analysis can be put into context by comparing them to selected reference measurements. In Table 8.4, the  $\rho^0$  and  $\omega$  mass and the  $\rho^0$  width obtained from the Söding and Ross-Stodolsky fits are compared to the world averages calculated by the PDG [1]. There exists a long-standing discrepancy between the  $\rho^0$  parameters measured in  $e^+e^-$  annihilation vs those measured in photoproduction. The values measured here are in agreement with the PDG photoproduction parameters and thus confirm this. However, the parameters vary strongly for the Ross-Stodolsky model. It

should thus be assumed that there are potentially large model uncertainties, which are not quantitatively evaluated<sup>1</sup>. The  $\omega$  mass also deviates from the PDG value. Interestingly, the shift between the values obtained with Söding fit and the from the  $e^+e^-$  analyses is of the same size for the  $\rho^0$  and  $\omega$  mass.

	this analysis		PDG [1]		$\Delta(e^+e^-, \text{Söding})$
	Söding	RS	$\gamma p$	$e^+e^-$	
$m_{\rho^0}$ [MeV]	$770.8^{+1.3}_{-1.5}$	$769.6^{+0.7}_{-0.9}$	$769.0 \pm 1.0$	$775.26 \pm 0.25$	$4.5^{+1.5}_{-1.3}$
$\Gamma_{\rho^0}$ [MeV]	$151.2^{+2.5}_{-3.1}$	$143.2^{+2.1}_{-3.1}$	$151.7 \pm 2.6$	$147.8 \pm 0.9$	
$m_\omega$ [MeV]	$778.0^{+1.9}_{-1.8}$	$780.5^{+2.9}_{-2.6}$		$782.65 \pm 0.12$	$4.7^{+1.8}_{-1.9}$

**Table 8.4:** Comparison of measured  $\rho^0$  and  $\omega$  values with the PDG. Only total uncertainties are given.

In a measurement by the ZEUS Collaboration [11], also a Söding model is used to describe the photoproduction  $m_{\pi\pi}$  lineshape. The exact parametrizations differ, so model parameters cannot be directly compared. Visually, the measured non-resonant contributions are very similar. Alternatively, using the Ross-Stodolsky model, the background induced skewing of the peak lineshape can be quantized with the skewing parameter  $k$ . For the elastic cross-section it is measured to be  $k_{\text{el}} = 5.38 \pm 0.06$  (stat.) $^{+0.09}_{-0.07}$  (syst.) and in reasonable agreement with the ZEUS measurement  $k_{\text{el,ZEUS}} = 5.13 \pm 0.13$  (tot.) considering the combined total uncertainty.

The measured  $\rho^0$  cross-sections are compared to other measurements only further on in the text in Section 8.2.1 because they depend on the fiducial analysis phasespace. The ratio of the proton-dissociative to the elastic  $\rho^0$  cross-section is measured by the ZEUS Collaboration to be  $(\sigma_{\rho,\text{el}}/\sigma_{\rho,\text{pd}})_{\text{ZEUS}} = 0.5 \pm 0.18$  (tot.), and thus is compatible with value obtained here:  $\sigma_{\rho,\text{el}}/\sigma_{\rho,\text{pd}} = 0.429 \pm 0.007$  (stat.) $^{+0.056}_{-0.052}$  (syst.)<sup>2</sup>.

The total elastic  $\omega$  photoproduction cross-section can be calculated by normalizing the contribution to  $\pi^+\pi^-$  production by the  $\omega \rightarrow \pi^+\pi^-$  branching fraction  $BR(\omega \rightarrow \pi^+\pi^-) = (1.53 \pm 0.06)\%$  [1]. This yields  $\sigma(\gamma p \rightarrow \omega p) = 1.12^{+0.32}_{-0.31}$  (tot.)  $\mu\text{b}$ . Photoproduction of  $\omega$  mesons can also directly be measured at HERA in the alternative and dominant  $\omega \rightarrow \pi^+\pi^-\gamma$  decay channel. A measurement performed by the ZEUS Collaboration in that channel has yielded a cross-section  $\sigma(\gamma p \rightarrow \omega p)_{\text{ZEUS}} = 1.21 \pm 0.26$  (tot.)  $\mu\text{b}$  [19]. The two values are in good agreement within the combined total uncertainty<sup>3</sup>.

A comparison of the  $\omega$ - $\rho^0$  mixing parameters with other measurements is difficult because they are only available from  $e^+e^- \rightarrow \pi^+\pi^-$  production. In  $e^+e^- \rightarrow \pi^+\pi^-$  production there is no non-resonant contribution and generally, slightly different parametrizations for the  $\pi^+\pi^-$  amplitude are used. Nonetheless, as one reference the CMD Collaboration measured a mixing phase  $\phi_{\omega,\text{CMD}} = 0.22 \pm 0.06$  (tot.) [189] with a very similar model for the  $\omega$ - $\rho^0$  mixing. This is significantly different from the value obtained here  $\phi_{\omega,\text{el}} = -0.52 \pm 0.19$  (stat.) $^{+0.15}_{-0.11}$  (syst.). Again, model uncertainties would need to be evaluated for a more stringent comparison. They can be expected to be significant. Using the Ross-Stodolsky model, for example, quite a different value  $\phi_{\omega,\text{el}}^{\text{RS}} = 0.01 \pm 0.21$  (stat.) $^{+0.24}_{-0.17}$  (syst.) is measured. This value would be compatible with the CMD result.

## Further Studies

Further studies on the one-dimensional  $\pi^+\pi^-$  cross-sections are presented in Appendix A.

<sup>1</sup>Model uncertainties are also not evaluated in most analyses that are considered for the PDG average value.

<sup>2</sup>The impact from phasespace differences is significantly reduced in the cross-section ratio. Remaining differences are assumed to be covered by the large ZEUS uncertainties.

<sup>3</sup>Again, there are phasespace differences between the analyses (ZEUS:  $70 \leq W_{\gamma p} \leq 90$  GeV,  $|t| < 0.6$  GeV<sup>2</sup>,  $Q^2 \leq 4$  GeV<sup>2</sup>) that should in principle be considered in a comparison. However, it is assumed that they can be neglected relative to the large experimental uncertainties.

## 8.2 $\rho^0$ Photoproduction Cross-Sections

### 8.2.1 Energy Dependence of the $\rho^0$ Cross-Sections

The energy dependence of the elastic and proton-dissociative  $\rho^0$  cross-section is extracted from the differential  $\pi^+\pi^-$  cross-sections  $d\sigma(\gamma p \rightarrow \pi^+\pi^-Y)/dm_{\pi\pi}$  measured as a function of  $m_{\pi\pi}$  and  $W_{\gamma p}$ . The  $\pi^+\pi^-$  cross-sections are measured by unfolding the two-dimensional  $m_{\pi\pi} \otimes W_{\gamma p}$  distributions, following the procedure described in Chapter 7. The elastic  $\pi^+\pi^-$  cross-section is shown in 9  $W_{\gamma p}$  bins and as a function of  $m_{\pi\pi}$  in Figure D.1, and the proton-dissociative cross-section in 6  $W_{\gamma p}$  bins in Figure D.2 in Appendix D.

In order to extract the  $\rho^0$  cross-sections, the Söding model is fitted in parallel to all mass distributions. Not all model parameters are well constrained independently in all  $W_{\gamma p}$  bins. Thus, further model assumptions are made to stabilize the fit. First, the  $\rho^0$  and  $\omega$  mass and width are fixed to the values obtained in Section 8.1.2. The other  $\omega$  parameters ( $f_\omega$  and  $\phi_\omega$ ) are also fixed to the respective elastic and proton-dissociative values obtained there. Finally, the parameters of the non-resonant background can not all be independently constrained. Assuming the shape of the non-resonant background does not change with energy,  $\Lambda_{\text{nr}}$  and  $\delta_{\text{nr}}$  are chosen to be shared in all  $W_{\gamma p}$  bins. Only its normalization  $f_{\text{nr}}$  is allowed to float independently.

The fit of the nominal distributions yields a good  $\chi^2_{\text{stat}}/\text{ndf} = 190.3/(210 - 33) = 1.1$  with statistical uncertainties alone. Systematic uncertainties are propagated through the fit using the offset method. The fit functions are plotted together with the cross-sections in figures D.1 and D.2.

The energy dependence of the elastic and proton-dissociative fit parameters  $f_{\text{nr}}$  is shown in Figure 8.4. No significant variation with  $W_{\gamma p}$  is observed. In agreement with previous observations [11], this suggests the same  $W_{\gamma p}$  dependence for the  $\rho^0$  and non-resonant components. If alternatively no  $W_{\gamma p}$  dependence of the parameter  $f_{\text{nr}}$  is assumed in the fit, this has no significant effect on any of the following results and only causes slight variations of numerical values within statistical uncertainties.

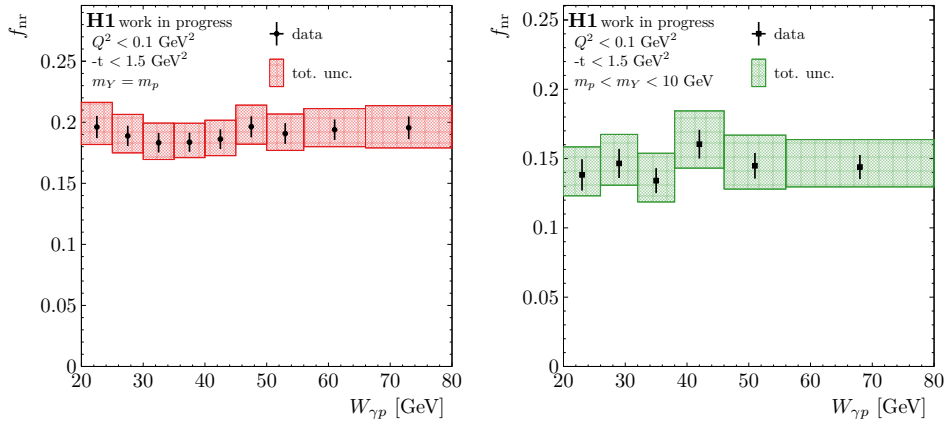


**Figure 8.4:** Fit parameters  $f_{\text{nr}}$  as a function of  $W_{\gamma p}$ . The parameters are obtained from the Söding fit to the double-differential cross-sections  $d\sigma(\gamma p \rightarrow \pi^+\pi^-Y)/dm_{\pi\pi}(m_{\pi\pi}, W_{\gamma p})$  that is described in the text. The left and right plot show the elastic and proton-dissociative parameter values, respectively.

The components of the Söding model are integrated over  $m_{\pi\pi}$  to extract their respective contributions to the  $\pi^+\pi^-$  cross-sections. Calculating the contributions in every  $W_{\gamma p}$  bin then allows measuring the  $W_{\gamma p}$  dependence of the respective cross-sections. These are shown in Figure 8.5 for the  $\rho^0$  and non-resonant components. For comparison, also the full model is integrated over  $m_{\pi\pi}$ , and the respective cross-sections are included in the plots. The

integration does not yield the actual  $\pi^+\pi^-$  cross-sections because higher mass features, such as the previously observed  $\rho'$  resonance, are not included in the model. The shown cross-sections only depend weakly on  $W_{\gamma p}$ , as is expected for diffractive processes.

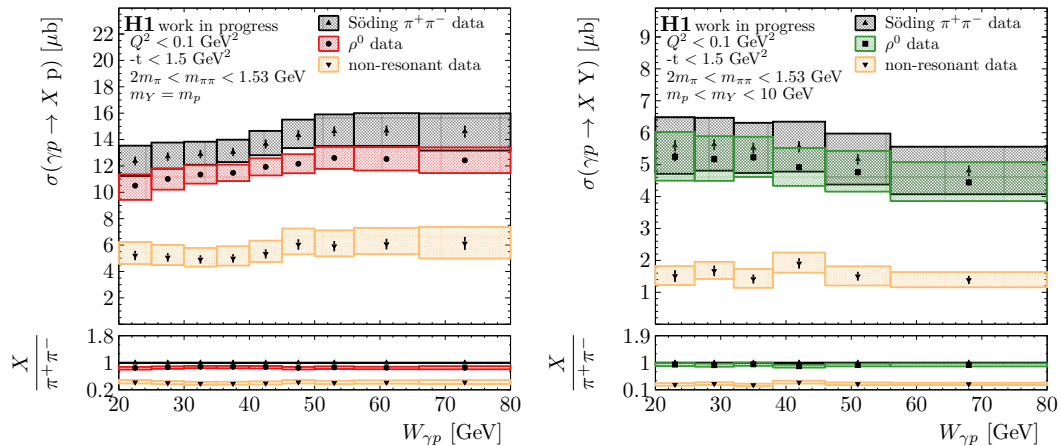


**Figure 8.5:** Contributions to the Söding model as a function of  $W_{\gamma p}$  for the elastic (left) and proton-dissociative cross-section (right). The contributions are obtained as described in the text and labeled in the legend. Uncertainty correlations are propagated to the ratio plot. The data uncertainties are described in Figure 8.1.

In order to quantify the energy dependence of the  $\rho^0$  cross-sections, a power-law

$$\sigma^{\rho p}(W_{\gamma p}) = \sigma^{\rho p}(W_0) \left( \frac{W_{\gamma p}}{W_0} \right)^\delta \quad (8.1)$$

is fitted simultaneously to the elastic and proton-dissociative  $\rho^0$  distribution. The reference energy is fixed to  $W_0 = 40$  GeV, corresponding to the average energy in the dataset. The nominal fit gives a very poor  $\chi^2_{\text{stat}}/\text{ndf} = 47.9/(15 - 4) = 4.4$  with statistical uncertainties alone. Generally, the measured  $W_{\gamma p}$  dependence is prone to systematic mismodeling because it is strongly correlated to the polar angle of the  $\pi^+\pi^-$  system and many detector effects have a strong polar dependence. The poor  $\chi^2$  value is taken as an indication for systematic biases in the measured nominal distribution. Those can be considered by performing the fit with the total covariance matrix in the  $\chi^2$  definition as is discussed in Section 7.4. This yields a more reasonable value of  $\chi^2_{\text{tot}}/\text{ndf} = 16.7/(15 - 4) = 1.5$ . The fitted model parameters are summarized in Table 8.5. Parameter uncertainties are estimated with the offset method. For reference, the parameters extracted from the fit with the total uncertainties are also given. Generally, the central values obtained in that way can be shifted with respect to the central values from the offset method. Also, the total parameter uncertainties tend to be smaller.

The value extracted for the fit parameter  $\delta_{\text{el}}$  is positive and thus indicates a slight but significant rise of the elastic cross-section with increasing energy. The negative value for  $\delta_{\text{pd}}$ , on the other hand, shows a slightly falling proton-dissociative cross-section. The central value of the elastic parameter is very robust concerning systematic uncertainties and does not change if the fit is performed with the offset method or the total covariance matrix. However, the value for the proton-dissociative parameter changes drastically. It is not clear whether this is simply an artifact of poorly defined systematic uncertainties. Alternatively, the used model might also not be suitable for the proton-dissociative cross-section. The measured distribution is strongly shaped by the fiducial phasespace restrictions. Compare the discussion in Chapter 7.1 for details and Figure 7.4, in particular. Most notably, the requirement  $m_Y < 10$  GeV severely shapes the  $W_{\gamma p}$  dependence. The precise energy dependence of the phasespace factor is not known and requires knowledge of the  $m_Y$  spectrum outside the fiducial region; compare discussion in Chapter 5. The implicit assumption in the parametrization is that a power law can describe it. This assumption might be wrong, thus

parameter	offset method			total covariance matrix	
	value	stat.	syst.	value	tot.
<b>without shrinkage</b>					
$\sigma_{\text{el}}^{\rho p}(W_0)$ [ $\mu\text{b}$ ]	11.74	0.05	$^{+0.72}_{-0.72}$	11.55	0.60
$\delta_{\text{el}}$	0.166	0.009	$^{+0.041}_{-0.023}$	0.165	0.021
$\sigma_{\text{pd}}^{\rho p}(W_0)$ [ $\mu\text{b}$ ]	4.92	0.06	$^{+0.63}_{-0.60}$	4.47	0.52
$\delta_{\text{pd}}$	-0.167	0.024	$^{+0.091}_{-0.081}$	-0.344	0.084
			$\chi_{\text{stat}}^2/\text{ndf} = 47.9/11 = 4.4$	$\chi_{\text{tot}}^2/\text{ndf} = 16.7/11 = 1.5$	
<b>with shrinkage</b>					
$\sigma_{\text{el}}^{\rho p}(W_0)$ [ $\mu\text{b}$ ]	11.72	0.05	$^{+0.73}_{-0.73}$	11.56	0.60
$\delta_{\text{el}}$	0.265	0.009	$^{+0.022}_{-0.022}$	0.267	0.022
$c$	0.1	fixed		0.1	fixed
			$\chi_{\text{stat, elas}}^2/\text{ndf} = 30.5/7 = 4.4$	$\chi_{\text{tot, elas}}^2/\text{ndf} = 9.3/7 = 1.3$	

**Table 8.5:** Fit parameters for the fits of the energy dependence of the elastic and proton-dissociative  $\rho^0$  cross-sections  $\sigma(\gamma p \rightarrow \rho^0 Y)$  ( $W_{\gamma p}$ ). The fits are described in the text. They are performed both with the offset method and total covariance matrix to propagate systematic cross-section uncertainties to the fit parameters.

rendering the model invalid. Within the context of this thesis, a more reasonable modeling of the phasespace could not be achieved. If the fit is performed to the elastic cross-section independently, it gives a reduced  $\chi_{\text{tot, elas}}^2/\text{ndf} = 9.0/(9 - 2) = 1.3$  with the total uncertainty. This reduction can be interpreted as a further indication, that the model is inapplicable for the proton-dissociative cross-section. Furthermore, without accounting for the phasespace, no conclusion about the energy dependence of the proton-dissociative *amplitude* can be drawn from the fit. In particular, the measured value for  $\delta_{\text{pd}}$  on its own does not indicate factorization breaking<sup>4</sup>.

The parametrization in Equation (8.1) has further limitations concerning also the modeling of the elastic cross-section. Most importantly, it does not take the shrinkage of the diffractive forward peak into account; compare Section 2.2. Assuming a purely exponential  $t$  dependence of the differential cross-section with exponent  $b$ , as well as a linear leading trajectory with slope  $\alpha'$ , the energy dependence of the elastic cross-section can be parametrized as:

$$\sigma^{\rho p}(W_{\gamma p}) = \sigma^{\rho p}(W_0) \frac{(W_{\gamma p}/W_0)^\delta}{1 + \frac{4\alpha'}{b} \ln(W_{\gamma p}/W_0)}. \quad (8.2)$$

For typical values of  $b \sim 10 \text{ GeV}^{-2}$  and  $\alpha' \sim 0.25 \text{ GeV}^{-2}$ ,  $4\alpha'/b \sim 0.1$  is expected. The result is an enhancement of the cross-section by 7% relative to Equation (8.1) at  $W_{\gamma p} = 20 \text{ GeV}$  in a suppression by 7% at  $W_{\gamma p} = 80 \text{ GeV}$ , respectively. Repeating the fit of the elastic cross-section with these values consistently results in an increase of  $\delta_{\text{el}}$  but not in a better  $\chi^2$  value; compare Table 8.5. If instead a free parameter  $c$  is introduced to replace  $4\alpha'/b$ , it can not be reasonably constrained by the data. The preferred value  $c \sim 0.001$  is very small, i.e., the logarithmic term is completely suppressed<sup>5</sup>.

Another limitation of both considered parametrizations is that they neglect potential Reggeon contributions that dominate diffractive cross-sections at very low  $W_{\gamma p} < 10 \text{ GeV}$ . These

<sup>4</sup>The assumption of factorization of diffractive processes predicts the same energy dependence for elastic and dissociative diffractive amplitudes; compare Section 2.2.

<sup>5</sup>The problem of parametrizing the shrinkage becomes irrelevant for the analysis of the double-differential  $\rho^0$  cross-section that is presented further on in the text in Section 8.2.3. For completeness, it should be noted that the parameters extracted from the one-dimensional elastic cross-section are consistent with the parameters extracted from the double-differential cross-section. For the fit without taking shrinkage into account,  $\delta_{\text{el}}$  corresponds to  $4(\alpha(\langle t \rangle) - 1)$  measured at the average momentum transfer  $\langle t \rangle \simeq 0.1 \text{ GeV}^2$ . The value measured with taking shrinkage into account corresponds to  $4(\alpha(0) - 1)$  measured at  $t \simeq 0 \text{ GeV}^2$ .

contributions can not be constrained with the present data alone. However, they might still play a role in the lowest energy bins of the present measurement. A more detailed discussion follows further on in the text in relation to very low energy cross-section measurements performed by other experiments.

### Comparison With Other Measurements

The energy dependence of the elastic  $\rho^0$  photoproduction cross-section has also been measured by other experiments. The rise of the cross-section observed here generally is in agreement with other results. Using a simple power law to parameterize the cross-section, such as given in Equation (8.1), the ZEUS Collaboration has measured  $\delta_{\text{el,ZEUS}} = 0.16 \pm 0.06$  (stat.)  $^{+0.11}_{-0.15}$  (syst.) [11] and the CMS Collaboration  $\delta_{\text{el,CMS}} = 0.23 \pm 0.14$  (stat.)  $\pm 0.04$  (syst.) [195].

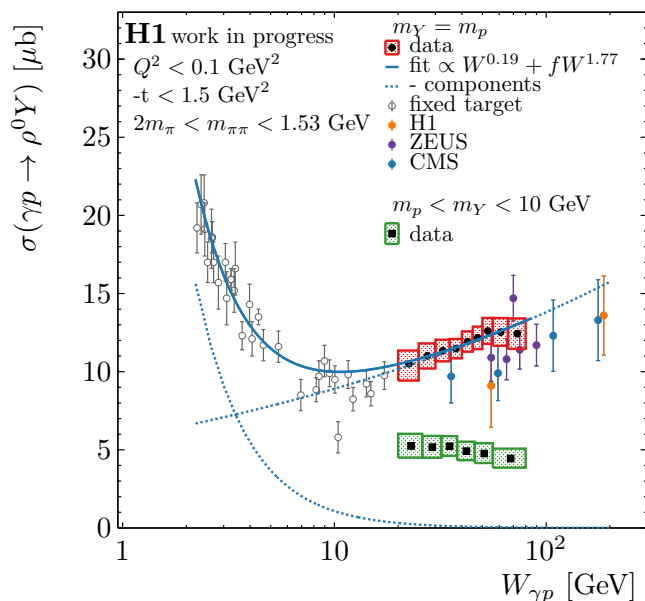


**Figure 8.6:** Elastic and proton-dissociative  $\rho^0$  photoproduction cross-section  $\sigma(\gamma p \rightarrow \rho^0 Y)$  as a function of  $W_{\gamma p}$ . The elastic cross-section is compared to measurements by fixed-target [196–202], HERA [6, 11, 13], and LHC [195] experiments. All data points are labeled in the legend. The lines show the Donnachie-Landshoff model fitted to the data as is described in the text.

The measured elastic and proton-dissociative  $\rho^0$  photoproduction cross-section as a function of the center-of-mass energy are also directly compared to other measurements. In Figure 8.6, they are shown together with elastic cross-section measurements by selected fixed-target [196–202], HERA [6, 11, 13], and LHC [195] experiments.

The comparison in Figure 8.6 is potentially problematic because the fiducial phasespaces of the various measurements do not entirely agree<sup>6</sup>. In particular, the phasespaces of the high-energy collider results cover different  $t$  and  $Q^2$  ranges. The difference in the  $t$  ranges is found to be insignificant. Reducing the maximal  $|t|$  of this measurement to  $0.5 \text{ GeV}^2$  in accord to Reference [11] changes the overall elastic  $\rho^0$  cross-section by less than 2%. The  $Q^2$  range is found to be much more critical. This analysis made an effort to correct the data for  $Q^2 > 0.1 \text{ GeV}^2$  contributions. The effective  $Q^2$  ranges vary strongly for the other measurements with a maximal  $Q^2 \leq 4 \text{ GeV}^2$  in Reference [11]. The  $Q^2$  range is crucial for

<sup>6</sup>There are also other measurements of the proton-dissociative  $\rho^0$  photoproduction cross-section, e.g., by the ZEUS Collaboration [11]. There, the phasespace differences are even more significant so that they can not be meaningfully included in the figure, at all.

calculating the integrated photon-flux that is used to transform the directly measured  $ep$  into a  $\gamma p$  cross-section. Having a large  $Q^2$  range can be problematic if it is not accounted for in the photon-flux correction appropriately. The approach that is taken by this and other HERA analyses is to normalize the  $ep$  cross-section, which is implicitly integrated over the considered  $Q^2$  range, by the integrated photon-flux; compare Section 2.4. This approach is not valid for large  $Q^2$  windows. If applied anyhow, the calculated  $\gamma p$  cross-section is shifted down systematically. The integrated  $ep$  cross-section and the photon-flux both grow as the  $Q^2$  window is opened. However, the integrated photon-flux increases more rapidly because the differential  $ep$  cross-section falls more steeply with  $Q^2$  than the flux. For this analysis, it is found that measuring the elastic “photoproduction” cross-section like this in the range  $Q^2 < 4 \text{ GeV}^2$  effectively lowers it by approximately 10% compared to the cross-section measured in the range  $Q^2 < 0.1 \text{ GeV}^2$ . Considering this effect brings the other high-energy results into much better agreement with the present measurement. The fixed-target measurements that are included in the plot are all based on experiments with a real photon source. They are thus not affected by these considerations.

The complete energy dependence of the elastic  $\rho^0$  cross-section is described by the Donnachie-Landshoff [83, 84] parametrization. It considers two power parameters  $\delta_1$  and  $\delta_2$  that describe the low and high  $W_{\gamma p}$  dependence of the cross-section, respectively:

$$\sigma^{\rho p}(W_{\gamma p}) = \sigma^{\rho p}(W_0) \left( \left( \frac{W_{\gamma p}}{W_0} \right)^{\delta_1} + f_2 \left( \frac{W_{\gamma p}}{W_0} \right)^{\delta_2} \right). \quad (8.3)$$

$f_2$  is the relative contribution from the  $\delta_2$  component with respect to the  $\delta_1$  component at  $W_0$ . Shrinkage of the forward peak is not taken into account. The model is fitted to the elastic data from this and the fixed-target measurements. Other high-energy data are not included in the fit to avoid troubles concerning the photon-flux normalization. The uncertainties of the fixed-target data are assumed to be fully uncorrelated. The nominal fit with statistical uncertainties yields  $\chi_{\text{stat, elas}}^2/\text{ndf} = 93.5/(42 - 4) = 2.4$ . The measured power parameters are  $\delta_1 = 0.190 \pm 0.012$  (stat.) $^{+0.041}_{-0.026}$  (syst.) and  $\delta_2 = -1.77 \pm 0.14$  (stat.) $^{+0.17}_{-0.16}$  (syst.), respectively. The fit parameter uncertainties are calculated with the offset method. The measured value for  $\delta_2$  is slightly increased in comparison with the previous fit of the presently measured elastic  $\rho^0$  cross-section on its own. This is a consequence of a small but seemingly relevant contribution from Reggeon exchange in the considered energy range. From the fit, its relative contribution is found to be  $f_2 = 0.8 \pm 0.3$  (stat.) $^{+0.5}_{-0.4}$  (syst.) % at  $W_0$ . Previous photoproduction analyses obtained a somewhat larger value for  $\delta_1 \sim -1$  [118]. However,  $\delta_1$  is very sensitive to the normalization of the cross-section at high  $W_{\gamma p}$ . It is thus strongly affected by the previous considerations concerning the fiducial range in  $Q^2$ . Furthermore, the value measured here is consistent with values of  $\delta_1 \sim -2$  obtained in DIS  $\rho^0$  production where there is no ambiguity about  $Q^2$  [118]. Expected values  $\delta_1$  and  $\delta_2$  can also be obtained from Regge theory via the respective Reggeon trajectories. The average  $t$  of the elastic cross-section in this analysis is  $\langle t \rangle \simeq 0.1 \text{ GeV}^2$ . Evaluating the Pomeron and Reggeon trajectories at that point provides estimated values for  $\delta \sim 4(\alpha(\langle t \rangle) - 1)$ . With the canonical trajectories (compare Section 2.2), one finds  $\delta_1 \sim -2.4$  and  $\delta_2 \sim 0.22$ , respectively.

### 8.2.2 $t$ Dependence of the $\rho^0$ Cross-Sections

The  $t$  dependence of the elastic and proton-dissociative  $\rho^0$  cross-section is extracted from the double-differential  $\pi^+\pi^-$  cross-sections  $d^2\sigma(\gamma p \rightarrow \pi^+\pi^-Y)/dm_{\pi\pi}dt$  measured as a function of  $m_{\pi\pi}$  and  $t$ . The  $\pi^+\pi^-$  cross-sections are measured by unfolding the two-dimensional  $m_{\pi\pi} \otimes t$  distributions, following the procedure described in Chapter 7. The elastic  $\pi^+\pi^-$  cross-section is shown in 12  $t$  bins and as a function of  $m_{\pi\pi}$  in Figure D.3, and proton-dissociative cross-section in 9  $t$  bins in Figure D.4 in Appendix D.

In order to extract the  $\rho^0$  cross-sections, the Söding model is fitted in parallel to all mass distributions. Not all model parameters are well constrained independently in all  $t$  bins.

Thus, further model assumptions are made to stabilize the fit. First, the  $\rho^0$  and  $\omega$  mass and width are fixed to the values obtained in Section 8.1.2. The other  $\omega$  parameters ( $f_\omega$  and  $\phi_\omega$ ) are also fixed to the respective elastic and proton-dissociative values obtained there. Furthermore, the parameters of the non-resonant background can not all be independently constrained. However, already visually the  $m_{\pi\pi}$  lineshape changes significantly with  $t$  such that the skewing becomes weaker for larger  $|t|$ . This indicates that also the non-resonant background must change with  $t$ . It is found that the variation is best described by a  $t$  dependence of the parameter  $\Lambda_{\text{nr}}$ , which is thus allowed to float freely in all  $t$  bins. A further  $t$  dependence of  $f_{\text{nr}}$  or  $\delta_{\text{nr}}$  can not be well constrained by the fit. Thus, the parameters are assumed to not change with  $t$ . This can be interpreted as the total  $\rho^0$  and non-resonant cross-sections integrated over  $m_{\pi\pi}$  having the same  $t$  dependence. If they are both dominated by Pomeron exchange, this is to be expected. A  $t$  dependence of  $\Lambda_{\text{nr}}$  then suggests that the  $m_{\pi\pi}$  distribution of the non-resonant background is dynamically created and thus changes with  $t$ .

The fit of the nominal distributions yields a  $\chi^2_{\text{stat}}/\text{ndf} = 381/(294 - 45) = 1.5$  with statistical uncertainties only. The  $\chi^2$  value is increased in comparison other mass fits performed in this analysis but still deemed to be reasonable. It is assumed that the model does not describe all aspects of the non-resonant background properly. Unfortunately, a better yet still practical model could not be found in the context of this thesis. Systematic uncertainties are propagated through the fit using the offset method. The fit functions are plotted together with the cross-sections in figures D.3 and D.4.

The  $t$  dependence of the elastic and proton-dissociative fit parameters  $\Lambda_{\text{nr}}$  is shown in Figure 8.7. The measured  $\Lambda_{\text{nr}}$  values rise with increasing  $|t|$ . The  $t$  dependence of  $\Lambda_{\text{nr}}$  appears to be consistent for the elastic and proton-dissociative cross-section, although no quantitative comparison is made. The differential non-resonant cross-section has a local maximum at

$$m_{\pi\pi} = \frac{\sqrt{\Lambda_{\text{nr}} + (\frac{4}{3}\delta_{\text{nr}} - 1)4m_\pi^2}}{\sqrt{\frac{4}{3}\delta_{\text{nr}} - 1}}. \quad (8.4)$$

In the model, the non-resonant background is thus shifted towards higher masses as  $\Lambda_{\text{nr}}$  grows with increasing  $|t|$ .

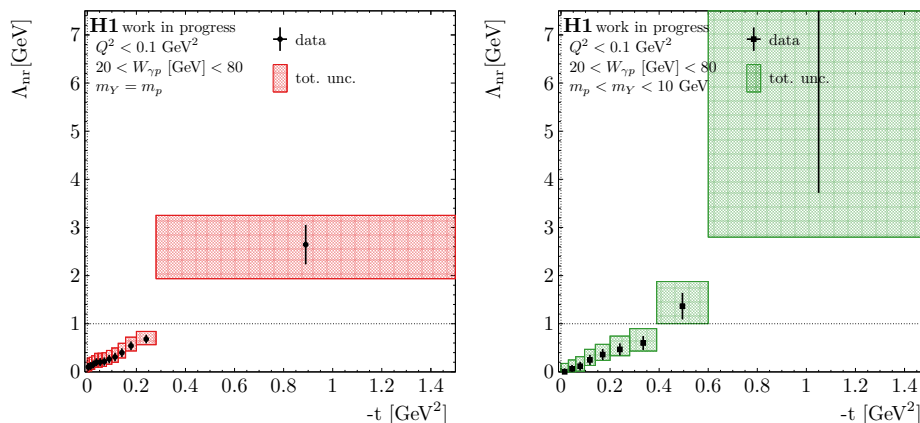


**Figure 8.7:** Fit parameters  $\Lambda_{\text{nr}}$  as a function of  $t$ . The parameters are obtained from the Söding fit to the double-differential cross-sections  $d^2\sigma(\gamma p \rightarrow \pi^+\pi^-Y)/dm_{\pi\pi}dt(m_{\pi\pi}; t)$  that is described in the text. The left and right plot show the elastic and proton-dissociative parameters, respectively.

The components of the Söding model are integrated over  $m_{\pi\pi}$  to extract their respective contributions to the  $\pi^+\pi^-$  cross-sections. Calculating the contributions in every  $t$  bin then

allows measuring the dependence of the respective differential cross-sections. The single-differential elastic and proton-dissociative  $\rho^0$  cross-section  $d\sigma(\gamma p \rightarrow \rho^0 Y)/dt$  as a function of  $t$  are compared to the respective non-resonant cross-sections and the full Söding model in Figure 8.8.

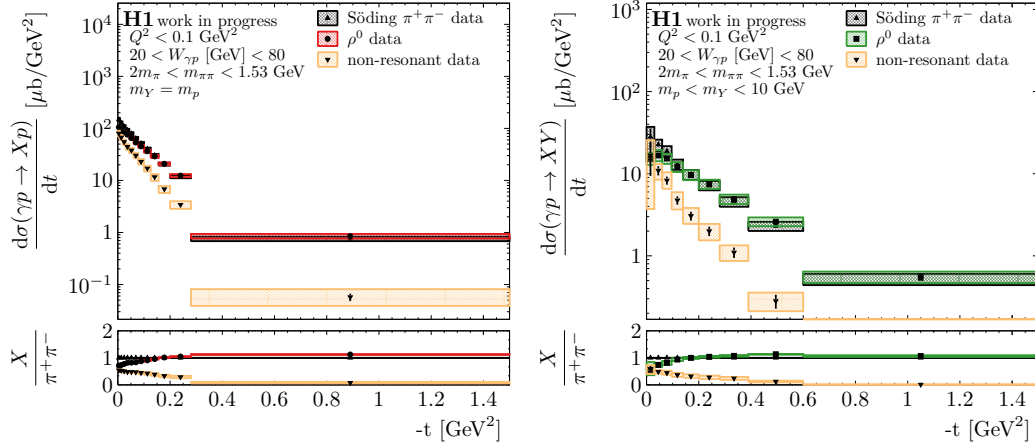


**Figure 8.8:** Contributions to the Söding model as a function of  $t$  for the elastic (left) and proton-dissociative cross-section (right). The contributions are obtained as described in the text and labeled in the legend. Uncertainty correlations are propagated to the ratio plot. The data uncertainties are described in Figure 8.1.

Both for the elastic and proton-dissociative cross-section, the considered contributions have quite different  $t$  dependencies visually. The full  $\pi^+\pi^-$  and non-resonant cross-sections fall more steeply than the  $\rho^0$  cross-sections. As the non-resonant component dies out towards high  $|t|$ , the  $\pi^+\pi^-$  and  $\rho^0$  cross-sections slowly converge. Qualitatively, this has been observed before, e.g., by the ZEUS Collaboration [11] in elastic scattering. However, with the present model and the variation of  $\Lambda_{\text{nr}}$  with  $t$ , it can be interpreted as a kinematic effect. Rather than the non-resonant amplitudes having a different  $t$  behavior than the  $\rho^0$  amplitudes, the non-resonant contributions are simply shifting out of the considered  $m_{\pi\pi}$  integration range with increasing  $|t|$ . It can also be seen that the proton-dissociative  $t$  distributions are generally harder than the elastic distributions. In combination with the  $t$  dependence of the non-resonant background, this explains the smaller overall non-resonant contribution to the proton-dissociative cross-section that is observed and discussed previously in the text in Section 8.1.2.

Diffractive cross-sections are typically observed to fall exponentially with  $t$ . However, at larger  $|t|$  perturbative effects may come into play resulting in some deviation from the exponential behavior. The following parametrization is proposed in Reference [24] to take both effects into account:

$$\frac{d\sigma^{pp}}{dt}(t) = \frac{d\sigma^{pp}}{dt}(t=0) \left(1 - \frac{bt}{a}\right)^{-a}. \quad (8.5)$$

It interpolates smoothly between an exponential  $d\sigma^{pp}/dt \propto \exp(bt + b^2 t^2/2a)$  at low  $|t|$  and a power-law  $d\sigma^{pp}/dt \propto |t|^{-a}$  at large  $|t|$ . For  $a \rightarrow \infty$ , it transforms into a simple exponential. The parametrization is fitted in parallel to the elastic and proton-dissociative differential  $\rho^0$  cross-sections  $d\sigma(\gamma p \rightarrow \rho^0 Y)/dt$ . The fit parameters are summarized in Table 8.6. Parameter uncertainties are obtained via the offset method. The fit functions are compared to the measured cross-sections in Figure 8.9.

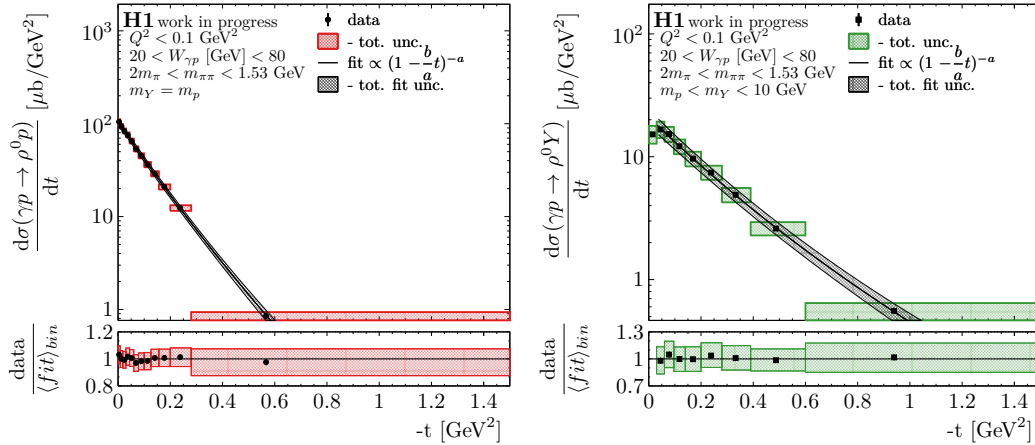


**Figure 8.9:** Elastic (left) and proton-dissociative differential cross-section  $d\sigma(\gamma p \rightarrow \rho^0 Y)/dt$  (right) as a function of  $t$ . The cross-sections are parametrized and fitted as described in the text. The fit functions are included in the plots with uncertainties obtained with the offset method. In the ratio panels, the data is compared to the bin-averaged fit function values as used in the  $\chi^2$  definition. The bin-centers in the figure are corrected so that the fit functions evaluated at the bin-centers match the average function values in the bins<sup>7</sup>. The data uncertainties are described in Figure 8.1.

The fit of the nominal distributions gives a poor  $\chi^2_{\text{stat}}/\text{ndf} = 25.3/(20-6) = 1.8$  with statistical uncertainties only. It is assumed that rather than the parametrization failing to describe the model, systematic uncertainties can not be neglected in the fit. Mismodeling of the forward tagging or the  $t$  dependences of background contributions can quite possibly introduce biases in the measured nominal distributions. Furthermore, the poor quality of the Söding fits of the double-differential  $\pi^+\pi^-$  cross-sections hints at a break-down of the model that is most likely due to poor modeling of the non-resonant amplitude. This can also reflect on the  $t$  dependence of the extracted  $\rho^0$  cross-sections. While model uncertainties are not estimated, the other effects can be taken into account by performing the fit with the total covariance matrix of the  $\rho^0$  cross-sections. This already gives a good  $\chi^2_{\text{tot}}/\text{ndf} = 15.3/(20-6)/1.1$ . The fit parameters obtained with the total covariance matrix are also summarized in Table 8.6. The nominal values between the two fit approaches slightly differ, and the offset method results in more conservative estimates for the total parameter uncertainties overall.

The measured cross-sections are again subject to shaping by the phasespace restrictions; compare Figure 7.4. The shaping applies mainly to the proton-dissociative distribution because of the restriction of  $m_Y < 10$  GeV. In particular, very low  $|t|$  can not be accessed kinematically for large  $m_Y$ ; compare Equation (7.2). The first bin of the proton-dissociative distribution is thus not included in the fits. However, also the elastic distribution is somewhat shaped by the restricted energy range. Generally, when interpreting the fit result, it has to be considered that the chosen parametrization does not model the phasespace. Under these considerations, the proton-dissociative cross-section is observed to be much harder than the elastic cross-section with about half the value for the exponential slope  $b_{\text{pd}} \sim 0.5 b_{\text{el}}$ . Also, the proton-dissociative cross-section deviates stronger from a simple exponential, as is indicated by the smaller value for  $a_{\text{pd}} \sim 0.5 a_{\text{el}}$ .

<sup>7</sup>**Bin-Center Correction:** The  $t$  dependence of the measured cross-section is very steep and bins of the measured distributions can be very wide. The geometric bin-center can then be very different from the actual average  $t$  in a bin. For parameter fits and for visualization in some plots thus a cross-section corrected bin-center is used. It is defined via  $\frac{d\sigma}{dt}(\langle t \rangle) = \frac{1}{t_{\text{max}} - t_{\text{min}}} \int_{t_{\text{min}}}^{t_{\text{max}}} \frac{d\sigma}{dt} dt$ .  $\langle t \rangle$  is calculated numerically by parametrizing  $d\sigma/dt$  with Equation (8.5) and using the nominal parameters from the fitted, single-differential  $\rho^0$  cross-sections as given in Table 8.6.

parameter	offset method			total covariance matrix	
	value	stat.	syst.	value	tot.
$\frac{d\sigma_{\text{el}}^{\rho\rho}}{dt}(0)$ [ $\mu\text{b}/\text{GeV}^2$ ]	105.8	0.7	$^{+6.5}_{-6.5}$	101, 0	6.3
$b_{\text{el}}$ [ $\text{GeV}^{-2}$ ]	9.59	0.10	$^{+0.17}_{-0.12}$	9.76	0.15
$a_{\text{el}}$	19.8	2.7	$^{+4.9}_{-4.7}$	15.9	2.8
$\frac{d\sigma_{\text{pd}}^{\rho\rho}}{dt}(0)$ [ $\mu\text{b}/\text{GeV}^2$ ]	21.0	0.6	$^{+3.2}_{-3.2}$	18.8	3.0
$b_{\text{pd}}$ [ $\text{GeV}^{-2}$ ]	4.79	0.19	$^{+0.37}_{-0.39}$	4.95	0.47
$a_{\text{pd}}$	9.1	1.5	$^{+3.1}_{-2.4}$	8.9	3.1
$\chi_{\text{stat}}^2/\text{ndf} = 25.3/14 = 1.8$				$\chi_{\text{tot}}^2/\text{ndf} = 15.2/14 = 1.1$	

**Table 8.6:** Fit parameters for the fit of the differential cross-sections  $d\sigma(\gamma p \rightarrow \rho^0 Y)/dt$  as a function of  $t$ . The fit is performed with the offset method and using the total covariance matrix to propagate systematic uncertainties to the fit parameters, as described in the text. The fit result obtained with the offset method is compared to data in Figure 8.9.

### Comparison With Other Measurements

In Figure 8.10, the measured elastic differential cross-section  $d\sigma(\gamma p \rightarrow \rho^0 Y)/dt$  as a function of  $t$  is directly compared to other measurements by the H1 [6], ZEUS [11] and CMS [195] collaborations. Only results obtained at similar center-of-mass energy are considered because of the shrinkage of the diffractive peak with increasing energy. Qualitatively, the distributions are very similar, although the logarithmic scale hides some details.

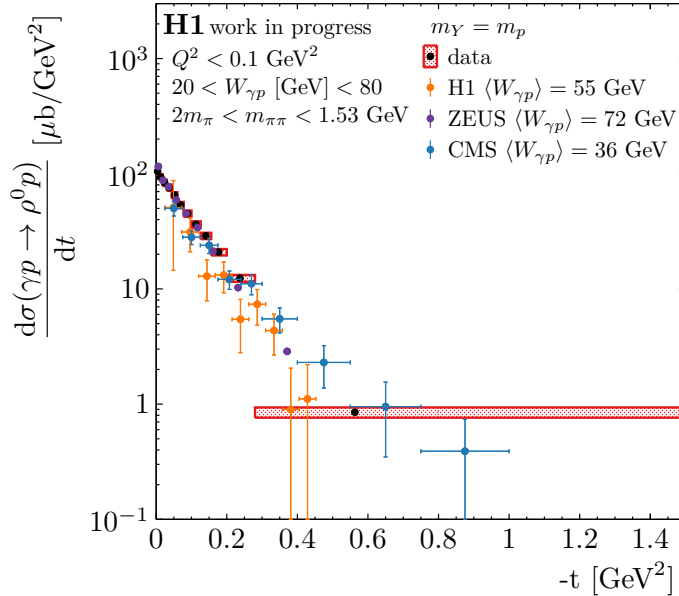


**Figure 8.10:** Differential elastic cross-section  $d\sigma(\gamma p \rightarrow \rho^0 p)/dt$  as a function of  $t$ . The measurement presented in this thesis is compared to selected measurements by the H1 [6], ZEUS [11], and CMS [195] Collaboration at comparable center-of-mass energies.

For a more quantitative comparison, the measurement by the ZEUS Collaboration [11] is used as a reference. There, the elastic cross-section is parametrized with the function  $d\sigma^{\gamma p}/dt \propto \exp(bt + c^2 t^2)$  and a fit results in  $b_{\text{el,ZEUS}} = 10.9 \pm 0.3$  (stat.) $^{+1.0}_{-0.5}$  (syst.)  $\text{GeV}^{-2}$

and  $c_{\text{el,ZEUS}} = 2.7 \pm 0.9$  (stat.) $_{-1.7}^{+1.9}$  (syst.)  $\text{GeV}^{-4}$ . The  $b$ -value is larger than what is measured here. However, it is measured at a higher average center-of-mass energy  $\langle W_{\gamma p} \rangle = 72$  GeV compared to  $\langle W_{\gamma p} \rangle = W_0 = 40$  GeV for the present dataset. An energy dependence of the form  $b(W_{\gamma p}) = b_0 + 4\alpha'_{\text{IP}} \ln(W_{\gamma p}/W_0)$  is expected from Regge theory; compare Chapter 2. Assuming  $\alpha'_{\text{IP}} \simeq 0.25$ , a difference of  $\Delta b = 0.6$   $\text{GeV}^{-2}$  is to be expected from the difference in the average energies alone. Considering such a relative shift, the measured  $b$  values agree within just around  $1\sigma$  of the combined total uncertainty (using the uncertainties from the offset method). The parameter  $c$  approximately corresponds to  $b^2/2a$  for the parametrization used here. The value measured for  $c$  by the ZEUS Collaboration then is consistent with the values measured for  $b$  and  $a$  here. In the given reference, the ZEUS Collaboration also measures the  $t$  dependence of the proton-dissociative cross-section. However, the measurement is performed in a completely different phasespace where in particular  $m_Y^2 < 0.1W_{\gamma p}^2$  is required. Due to the large shaping of the fiducial distributions by the  $m_Y$  restrictions, the ZEUS result can not be directly compared to the present measurement.

### 8.2.3 Double-Differential $\rho^0$ Cross-Sections

The double-differential elastic and proton-dissociative  $\rho^0$  cross-sections is extracted from the triple-differential  $\pi^+\pi^-$  cross-sections  $d^2\sigma(\gamma p \rightarrow \pi^+\pi^-Y)/dm_{\pi\pi}dt$  measured as a function of  $m_{\pi\pi}$ ,  $W_{\gamma p}$ , and  $t$ . The  $\pi^+\pi^-$  cross-sections are measured by unfolding the three-dimensional  $m_{\pi\pi} \otimes W_{\gamma p} \otimes t$  distributions. The elastic  $\pi^+\pi^-$  cross-section is shown as a function of  $m_{\pi\pi}$  in 4  $W_{\gamma p}$  and 7  $t$  bins in Figure D.6 and the proton-dissociative cross-section in 4  $W_{\gamma p}$  and 5  $t$  bins in Figure D.7 in Appendix D.

In order to extract the  $\rho^0$  contributions, the Söding model is fitted in parallel to all mass distributions. Again, not all model parameters can be independently constrained for every distribution. The  $\rho^0$  and  $\omega$  parameters are thus fixed to the values from the one-dimensional fit. For the non-resonant amplitude, only  $\Lambda_{\text{nr}}$  is fitted independently in every  $t$  bin. All other parameters, including now  $f_{\text{nr}}$ , are assumed to have neither a  $t$  nor  $W_{\gamma p}$  dependence to stabilize the fit. The fit yields a  $\chi^2_{\text{stat}}/\text{ndf} = 828.3/(672 - 63) = 1.4$  for the nominal distributions using only statistical uncertainties. Systematic uncertainties are propagated through the fit using the offset method.

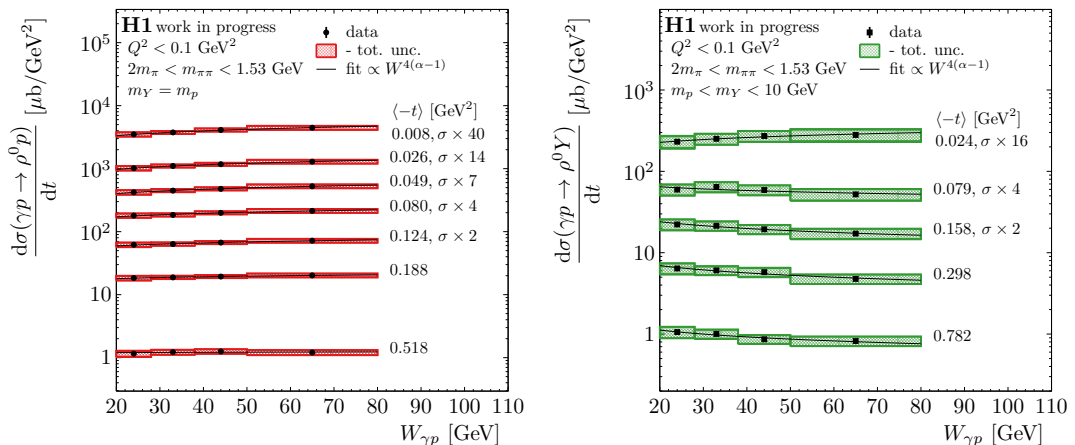


**Figure 8.11:** Elastic (left) and proton-dissociative double-differential cross-section  $d\sigma(\gamma p \rightarrow \rho^0 Y)/dt$  (right) as a function of  $W_{\gamma p}$  and in multiple bins of  $t$ . Individual distributions are scaled for visual separation, as labeled. The given bin-centers  $\langle t \rangle$  are cross-section weighted with the procedure described in the text and using the parametrizations of the single-differential  $\rho^0$  cross-sections  $d\sigma(\gamma p \rightarrow \rho^0 Y)/dt(t)$ . The cross-sections are parametrized and fitted as described in the text. The fit functions obtained via the offset method are drawn on top of the data.

Following the procedure outlined in Section 7.3, the  $W_{\gamma p}$  and  $t$  dependence of the  $\rho^0$  contribution to the  $\pi^+\pi^-$  cross-sections is calculated. The resulting elastic and proton-dissociative differential cross-section  $d\sigma(\gamma p \rightarrow \rho^0 Y)/dt$  are plotted in Figure 8.11 as a function of  $W_{\gamma p}$  and in bins of  $t$ .

From Regge theory, the  $W_{\gamma p}$  dependence of the cross-sections is expected to change with  $t$ . This change is quantified by re-parametrizing the power-law in terms of an effective leading trajectory  $\alpha(t)$ :

$$\frac{d\sigma^{\rho p}}{dt}(W_{\gamma p}; t) = \frac{d\sigma^{\rho p}}{dt}(W_0; t) \left( \frac{W_{\gamma p}}{W_0} \right)^{4(\alpha(t)-1)}. \quad (8.6)$$

Instead of assuming a  $t$  dependence for the cross-sections or the trajectory, independent parameters for the normalization and  $\alpha$  are fitted in every  $t$  bin. For the nominal distribution, the fit yields  $\chi_{\text{stat}}^2/\text{ndf} = 37.9/(48 - 24) = 1.6$  considering statistical uncertainties only. The corresponding fit functions are shown together with the cross-sections in Figure 8.11. The  $t$  dependence of the elastic and proton-dissociative fit parameter  $\alpha$  with parameter uncertainties propagated via the offset method is shown in Figure 8.12. For reference, the fit is also performed with the total uncertainty matrix. This results in  $\chi_{\text{tot}}^2/\text{ndf} = 25.0/(48 - 24) = 1.0$ . The resulting fit parameters are slightly shifted and have reduced (total) uncertainties in comparison to the parameters obtained with the offset approach. Similar to the analysis of the one-dimensional energy dependence of the  $\rho^0$  cross-section, the shifts of the elastic values for  $\alpha$  are negligible, whereas the proton-dissociative values become significantly smaller. Again, the underlying cause is not understood, but the effect might be an indication that the model can not be applied to the proton-dissociative distribution in the fiducial phase-space.

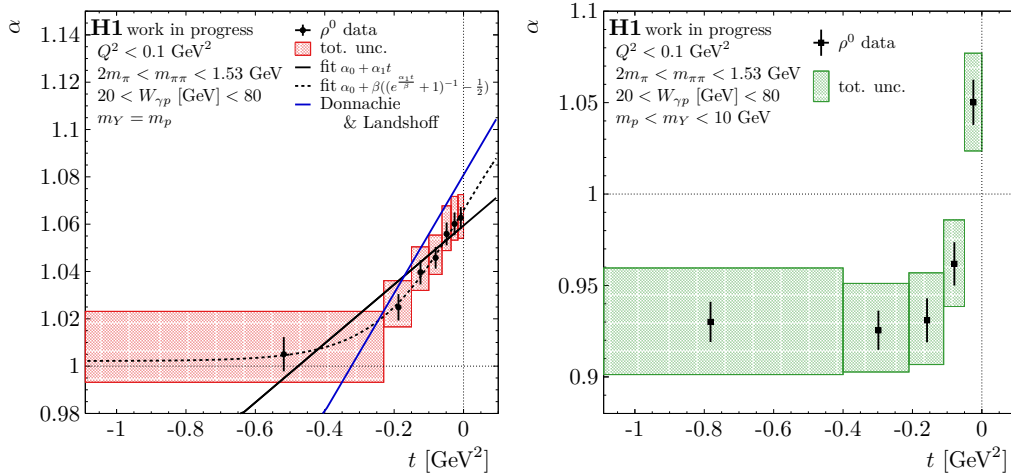


**Figure 8.12:** Fit parameters  $\alpha$  as a function of  $t$ . The parameters are obtained from the fit of the power-law to the double-differential cross-section  $d\sigma(\gamma p \rightarrow \rho^0 Y)/dt(W_{\gamma p}; t)$  as described in the text. The left and right plot show the elastic and proton-dissociative parameters, respectively. The elastic parameters are parametrized and fitted as described in the text. The fit functions are included as labeled in the legend. For reference, the Donnachie-Landshoff Pomeron trajectory is included in the plot.

The  $\alpha$  parameter values of the elastic cross-section are expected to lie on the effective Regge trajectory of the exchange. From the Regge trajectories of vector meson families, one expects a linear behavior at least for small  $|t|$ ; compare Chapter 2. Thus, the elastic parameters  $\alpha$  are parametrized by a linear function:

$$\alpha_{\text{lin}}(t) = \alpha_0 + \alpha_1 t. \quad (8.7)$$

A fit to the data is performed to test the linearity and extract the parameters of the Regge trajectory. For the fit, the function is evaluated at the cross-section corrected  $t$  bin-centers.

The bin-center correction is performed using the parametrizations of the single-differential  $\rho^0$  cross-sections  $d\sigma(\gamma p \rightarrow \rho^0 Y)/dt$  as a function of  $t$  that is measured as described above in the text.

The fit of the nominal parameter values gives  $\chi_{\text{stat}}^2/\text{ndf} = 9.1/(7 - 2) = 1.8$  using statistical uncertainties only. The corresponding function is drawn on top of the data in Figure 8.12. In addition to the poor  $\chi^2$  value, also visually the linear function does not appear to describe the data well over the complete  $t$ -range. When considering systematic uncertainties by using the total covariance matrix in the  $\chi^2$  minimization, the fit improves to give  $\chi_{\text{tot}}^2/\text{ndf} = 6.3/(7 - 2) = 1.3$ . The fit parameters obtained via both the offset method and the fit with the total covariance matrix are summarized in Table 8.7. They are discussed and compared to values obtained by other measurements further on in the text.

parameter	offset method			total covariance matrix	
	value	stat.	syst.	value	tot.
<b>fit <math>\alpha_0 + \alpha_1 t</math></b>					
$\alpha_0$	1.0594	0.0022	$+0.0093$ $-0.0056$	1.0607	0.0073
$\alpha_1$ [GeV $^{-2}$ ]	0.125	0.015	$+0.020$ $-0.027$	0.110	0.032
$\chi_{\text{stat}}^2/\text{ndf}$	9.1/5 = 1.8			6.3/5 = 1.3	
<b>fit <math>\alpha_0 + \beta \left( (e^{-4\alpha_1/\beta t} + 1)^{-1} - \frac{1}{2} \right)</math></b>					
$\alpha_0$	1.0659	0.0033	$+0.0099$ $-0.0059$	1.0674	0.0079
$\alpha_1$ [GeV $^{-2}$ ]	0.243	0.050	$+0.030$ $-0.042$	0.229	0.065
$\beta$	0.127	0.018	$+0.023$ $-0.030$	0.117	0.036
$\chi_{\text{stat}}^2/\text{ndf}$	0.5/4 = 0.1			0.5/4 = 0.1	

**Table 8.7:** Fit parameters for the trajectory fits of the elastic parameters  $\alpha(t)$  using a linear and quadratic parametrization.

The  $\chi^2$  value of the linear fit does not allow to confidently exclude linearity of the leading trajectory in the considered  $t$  range. However, the  $\alpha$  value in the bin with the largest  $|t|$  is a clear outlier and significantly lowers the fitted slope parameter. Furthermore, linearity of Regge trajectories is not a feature of Regge theory, but only an experimental observation. On the contrary, the linearity is expected to break down at large negative  $t$  once perturbative contributions become relevant. Compare also the discussion in Section 2.2.3. Where exactly this deviation is expected to occur is not known. Nonetheless, in order to account for the possibility of a non-linearity in the present  $t$  range, the measured values  $\alpha$  are alternatively parametrized by the function

$$\alpha_{\text{non-lin}}(t) = \alpha_0 + \beta \left( \left( e^{-4\alpha_1/\beta t} + 1 \right)^{-1} - \frac{1}{2} \right). \quad (8.8)$$

The parametrization approximates a linear trajectory  $\alpha_0 + \alpha_1 t$  for small  $|t|$  and approaches a constant value  $\alpha_0 - \beta/2$  for  $t \rightarrow -\infty$ . It thus meets the expectations for Regge trajectories in the respective  $t$  regions. However, it is mostly chosen on technical grounds because it allows for a rapid transition from a linear into a non-linear regime. For the present data, this allows fitting the outlier point in the highest  $|t|$  bin without affecting the parameters obtained for the linear segment. The parametrization does indeed describe the data much better. A fit of the nominal elastic parameter values gives  $\chi_{\text{stat}}^2/\text{ndf} = 0.5/(7 - 3) = 0.1$  with statistical uncertainties only. The fit is also included in the plot of the elastic  $\alpha$  parameters in Figure 8.12. The fit parameters with uncertainties obtained both with the offset method and from the fit with the total covariance matrix are summarized in Table 8.7.

Allowing for non-linearity at large  $|t|$  results in an increase of the effective slope at small  $|t|$ . The measured slope is consistent with a fit of a linear function to the data without the data

point at the highest  $|t|$  value. Since the non-linearity is then only constrained by a single data point, the fit can not be used to reliably extrapolate the trajectory to higher values of  $|t|$ .

For the  $\alpha$  parameters measured for the proton-dissociative cross-section, a linear behavior is clearly not given. Again, the proton-dissociative cross-section is strongly shaped by the fiducial phasespace cuts on  $m_Y$ . That is why the parameters  $\alpha$  can not be directly related to the underlying dissociative scattering amplitude. Consequently, no attempt is made to parametrize and fit the proton-dissociative parameters. However, the phasespace impact is expected to be small at small  $|t|$  because large  $m_Y$  are kinematically inaccessible; compare also Figure 7.4. In the lowest  $|t|$  bin, the measured proton-dissociative  $\alpha$  value does indeed agree with the corresponding elastic value within statistical uncertainties. This is in agreement with expectations from factorization of the diffractive amplitudes.

### Comparison With Other Measurements

The parameters of the leading Regge trajectory extracted in this measurement can be compared to other results. When doing so, it has to be taken into account how the analysis phasespace might affect the measurements. In the study of the one-dimensional energy dependence of the  $\rho^0$  cross-section, it is found that Reggeon exchange might still contribute in the considered energy range. Correspondingly, the Regge trajectory that is measured from the double-differential cross-section might not be the pure Pomeron trajectory but an effective trajectory with contributions also from Reggeon exchange. The study of the one-dimensional cross-section can help to quantify the size of the bias that could be expected from neglecting Reggeon contributions. In the fit of the one-dimensional cross-section, doing so lowers the effective power parameter by  $\Delta\delta = 0.166 - 0.190 = -0.024$ . On average, this would correspond to measured values for  $\alpha$  to be lowered by approximately  $\Delta\alpha \simeq -0.006$  with respect to the pure Pomeron trajectory. However, the effect can be expected to have some  $t$  dependence. With the slope of the Reggeon trajectories  $\alpha'_{R} \simeq 0.9 \text{ GeV}^{-2}$  being steeper than the Pomeron slope, the impact of the Reggeons can be expected to be larger at small  $|t|$ . Consequently, neglecting it can both lower the intercept and slope of the measured effective trajectory.

Under these considerations, the measured trajectory can be compared to the *canonical* Pomeron trajectory that has been determined by Donnachie and Landshoff (DL):

$$\alpha_{DL}(t) = 1.0808 + 0.25 \text{ GeV}^{-2} t. \quad (8.9)$$

The DL parameters are obtained from studies of high-energy elastic  $pp$  and  $p\bar{p}$  scattering cross-sections in the energy range  $10 < \sqrt{s} < 540 \text{ GeV}$  and for  $-t < 2.5 \text{ GeV}^{-2}$  [83]. Reggeon contributions at low energies, as well as non-diffractive effects at large  $|t|$  are all considered independently in the analysis and should thus not affect the Pomeron parameters. Uncertainties are not quantified.

The linear trajectory extracted here,

$$\alpha_{\text{lin}}(t) = [1.0594_{-0.0059}^{+0.0095} \text{ (tot.)}] + [0.125_{-0.031}^{+0.025} \text{ (tot.)}] t, \quad (8.10)$$

has both a lower intercept and slope than the DL trajectory. The intercept deviates from the DL value by 2.4 and the slope by 5.3 standard deviations, considering the total uncertainties estimated via the offset method and neglecting uncertainty correlations. However, if the trajectory is assumed to be non-linear at large  $|t|$ , the linearised trajectory at small  $|t|$  is found to be:

$$\alpha_{\text{non-lin}}(t) = [1.0659_{-0.0067}^{+0.0104} \text{ (tot.)}] + [0.243_{-0.065}^{+0.058} \text{ (tot.)}] t + \mathcal{O}(t^3). \quad (8.11)$$

In particular, it has a slope that is in good agreement with the DL value. The measured intercept can be brought into better agreement with the DL value if a potential bias of the order of  $\Delta\alpha_0 \sim -0.006$  from neglecting a Reggeon contribution is considered.

Alternatively, the Pomeron trajectory has also been measured by the ZEUS Collaboration in  $\rho^0$  meson photoproduction [16]:

$$\alpha_{\text{ZEUS}}(t) = [1.096 \pm 0.021 \text{ (tot.)}] + [0.125 \pm 0.038 \text{ (tot.)}] t. \quad (8.12)$$

The trajectory is obtained by an analysis and fit of the double-differential elastic  $\rho^0$  cross-section in a similar energy and  $t$  range as is considered in the present analysis. The ZEUS trajectory should thus be directly comparable to the linear trajectory measured in this analysis. Indeed, the values for the slope parameter are in good agreement. The values for the intercept deviate by roughly 1.6 standard deviations considering the combined total uncertainty<sup>8,9</sup>.

<sup>8</sup>On the ZEUS uncertainties: the ZEUS measurement is performed by combining low-energy  $\rho^0$  photoproduction cross-section measurements by the Omega Collaboration ( $\langle W_{\gamma p} \rangle = 8.2$  and  $10.1$  GeV) [202] with high-energy measurements by the H1 ( $\langle W_{\gamma p} \rangle = 55$  GeV) [6] and ZEUS Collaboration ( $\langle W_{\gamma p} \rangle = 71.2, 73,$  and  $94$  GeV) [11, 12, 16]. Despite a lower precision of the individual considered cross-section measurements, the estimated parameters on the Pomeron trajectory are competitive with the present analysis. The uncertainty of the offset parameter is presumably artificially decreased by treating normalization uncertainties as uncorrelated in the cross-section fits, even though they dominate all considered measurements. The uncertainty of the slope parameter potentially gains from a lever arm effect provided by the somewhat larger energy range, as well as more data-points at high  $|t|$ .

<sup>9</sup>A previous preliminary measurement by the H1 Collaboration [41, 203] should not be considered for comparison. From the available information about the underlying analysis, it appears that a wrong unfolding approach was taken, which strongly affected the results: It was assumed that the reconstruction efficiency is the same for elastic and proton-dissociative events and thus that detector level forward tagging information could be used to estimate the proton-dissociative contribution to the efficiency corrected event yields; compare Section 8.2 in Reference [41]. Considering Figure 7.1 of the present document, such an assumption is clearly invalid. As a consequence, what is labeled as an elastic cross-section in the references is in-fact ill-defined. While the proton-dissociative phasespaces differ for the two analyses, it was verified that the assumption about the factorization of the efficiency is wrong for either definition. Furthermore, a plausibility study was performed in the context of the present analysis, which verified that the effect size and direction could realistically explain the differences in the measured trajectories.



## 9 CONCLUSION

In this thesis, a simultaneous measurement of differential elastic and proton-dissociative  $\pi^+\pi^-$  and  $\rho^0$  photoproduction cross-sections is performed. The cross-sections are measured single-, double-, and-triple-differentially as a function of the invariant  $\pi^+\pi^-$  mass  $m_{\pi\pi}$ , the photon-proton center-of-mass energy  $W_{\gamma p}$ , and the momentum transfer at the proton-vertex  $t$ .

The measurement is performed by unfolding  $\pi^+\pi^-$  distributions under consideration of background contributions, the finite resolution of reconstructed variables, the detector efficiency, and migrations into and out of the fiducial phasespace. In particular, the data is corrected for contributions with large photon-virtuality  $Q^2$ . The information from forward detectors is used to define control regions enriched in elastic and proton-dissociative events. They enter the unfolding and thus allow to separate the respective contributions statistically. Technically, the unfolding is performed via a template fit of the detector level distributions with the TUnfold package. The fit is set up in a way to reduce the dependence of the result on the MC modeling.

The data-sample used for the measurement provides a very high statistical precision. For the integrated cross-section, it is on the sub-percent level. Simultaneously, the measurement suffers from much larger limitations of the MC modeling and detector simulation. Since the unfolding is performed with the MC simulation, these affect the final results. In the context of this thesis, not all systematic effects could be understood on a level demanded by the statistical precision. Often, corresponding uncertainties could only be estimated conservatively. Also, not all systematic effects could be corrected in the simulation so that the nominal measured distributions might suffer from systematic biases. The systematic uncertainties are propagated through the unfolding and the subsequent cross-section fits via an offset approach. Within the context of this thesis, it has not been feasible to directly include them in the unfolding fit or in subsequent fits of the differential cross-sections. Concerning the latter, some first studies are performed by considering total uncertainty matrices directly in the fits. This allows studying the aforementioned biases, which are mostly found to be small. Nonetheless, the analysis could be greatly improved by better treatment of systematic uncertainties and, in particular, by a better understanding of systematic effects and more realistic estimates of corresponding uncertainties.

The measured one-dimensional cross-section  $d\sigma(\gamma p \rightarrow \pi^+\pi^- Y)/dm_{\pi\pi}(m_{\pi\pi})$  is parametrized by and interpreted with a Söding model. Among other variables, the model allows to fit the  $\rho^0$  meson mass and width at a precision comparable to the PDG world average:

$$m_\rho = 770.8 \pm 1.2 \text{ (stat.)}_{-0.9}^{+0.5} \text{ (syst.) MeV,} \quad (9.1)$$

$$\Gamma_\rho = 151.2 \pm 2.1 \text{ (stat.)}_{-2.3}^{+1.4} \text{ (syst.) MeV.} \quad (9.2)$$

The  $m_{\pi\pi}$  spectrum also provides some evidence for an  $\omega$  contribution to  $\pi^+\pi^-$  photoproduction. By including the  $\omega$  contribution in the Söding model, the  $\omega$  mass is fitted, and the fiducial elastic  $\omega$  photoproduction cross-section is extracted. This is the first such measurement in the  $\omega \rightarrow \pi^+\pi^-$  channel at HERA:

$$m_\omega = 778.0 \pm 1.6 \text{ (stat.)}_{-0.8}^{+1.0} \text{ (syst.) MeV,} \quad (9.3)$$

$$\sigma(\gamma p \rightarrow \omega p) = 1.12 \pm_{-0.31}^{+0.32} \text{ (tot.) } \mu\text{b.} \quad (9.4)$$

The Söding model is then used to extract the  $\rho^0$  contribution to  $\pi^+\pi^-$  photoproduction. This allows to measured single- and double-differential  $\rho^0$  cross-sections as a function of  $W_{\gamma p}$

---

and  $t$ . They are parametrized and interpreted with fits. In particular precise parameters for the rise of the cross-section with energy are extracted:

$$\delta_{\text{el}} = 0.166 \pm 0.009 \text{ (stat.)}_{-0.023}^{+0.041} \text{ (syst.)}, \quad (9.5)$$

$$\delta_{\text{pd}} = -0.167 \pm 0.024 \text{ (stat.)}_{-0.081}^{+0.091} \text{ (syst.)}. \quad (9.6)$$

As well as parameters for the exponential slope describing the  $t$  distribution at small  $|t|$ :

$$b_{\text{el}} = 9.59 \pm 0.10 \text{ (stat.)}_{-0.12}^{+0.17} \text{ (syst.)}, \quad (9.7)$$

$$b_{\text{pd}} = 4.79 \pm 0.19 \text{ (stat.)}_{-0.39}^{+0.37} \text{ (syst.)}. \quad (9.8)$$

From the elastic double-differential  $\rho^0$  cross-section the leading Regge trajectory is measured. The data allows for potential non-linearities of the trajectory at large  $|t|$ . If they are parametrized, the linear section of the trajectory at small  $|t|$  is found to be described by:

$$\begin{aligned} \alpha_{\text{non-lin}}(t) = & [1.0659 \pm 0.0033 \text{ (stat.)}_{-0.0059}^{+0.0099} \text{ (syst.)}] \\ & + [0.243 \pm 0.050 \text{ (stat.)}_{-0.042}^{+0.030} \text{ (syst.)}] t + \mathcal{O}(t^3). \end{aligned} \quad (9.9)$$

The slope parameter is measured in good agreement with the canonical Donnachie and Landshoff Pomeron trajectory. The intercept is somewhat lower. A small remaining Reggeon contribution in the analyzed medium energy range is considered as a potential explanation. This can not be constrained with the present data alone.

However, the present data does not allow to completely rule out a purely linear trajectory in the considered  $t$  range  $-t < 1.5 \text{ GeV}^{-2}$ . Assuming a purely linear trajectory, its parameters are found to be:

$$\begin{aligned} \alpha_{\text{lin}}(t) = & [1.0594 \pm 0.0022 \text{ (stat.)}_{-0.0056}^{+0.0093} \text{ (syst.)}] \\ & + [0.125 \pm 0.015 \text{ (stat.)}_{-0.027}^{+0.020} \text{ (syst.)}] t \end{aligned} \quad (9.10)$$

In particular, this assumption results in a reduced value for the slope. The slope is then measured in agreement with values obtained from independent studies of vector meson photoproduction in similar  $t$  ranges. The present analysis thus offers a potential deviation from a linear trajectory already at small  $t \lesssim -0.6 \text{ GeV}^2$  as a possible explanation for the two distinct values that are regularly measured for the slope.

More than 10 years after the HERA machine was shut off, the data recorded by the H1 detector thus still provides opportunities for interesting and competitive measurements.

# A FURTHER $\pi^+\pi^-$ CROSS-SECTION STUDIES

## A.1 Interpreting the Extended Mass Range

The Söding model introduced in Section 7.3.1 breaks down in the tails of the  $\rho^0$  resonance and in particular above  $m_{\pi\pi} \gtrsim 1$  GeV. From  $e^+e^- \rightarrow \rho^0$  production it is known that the relativistic Breit-Wigner chosen here does not describe the high mass tail well. It does not include other decay modes and threshold effects [193], for example. Furthermore, higher mass  $\rho'$  resonances need to be taken into account. In  $\pi^+\pi^-$  photoproduction the situation is yet more complicated because of the non-resonant contributions. From an experimental perspective, also the measured data become less trustworthy in the tails. There, reducible non-di-pion background processes contribute significantly to the detector level distributions at a level of up to 50% below 0.6 GeV and above 1.0 GeV. They are subtracted from the data in the unfolding, but the procedure relies strongly on the predicted MC shapes. Nonetheless, an attempt is made to extend the Söding model so that it can describe the complete measured  $\pi^+\pi^-$  mass spectrum in the range  $0.5 < m_{\pi\pi} < 2.2$  GeV.

### Extended Söding Model

The Söding model defined Equation (7.18) is extended to describe the complete measured  $\pi^+\pi^-$  mass range. The central components of the model are left unchanged. In particular, the  $\rho^0$  resonance is modeled by as simple relativistic Breit-Wigner as introduced in Section 7.3 despite potential problems associated with it. The modeling of the non-resonant background on the other hand is slightly changed. The previous assumption of it being purely real is abandoned, and a global complex non-resonant phase is introduced:

$$f_{nr} \rightarrow f_{nr} e^{i\phi_{nr}}. \quad (\text{A.1})$$

The tails of the  $m_{\pi\pi}$  distributions are much more sensitive to the interference between the  $\rho^0$  and non-resonant amplitudes because it becomes of a similar size as the individual contributions. Allowing for a non-zero phase is found to be necessary for a good description of the tails. A non-zero phase could arise from final-state interactions between the pions and the scattered proton, for example, and is thus not necessarily unphysical

The model is then extended by a third amplitude to describe the mass peak observed in the data around a mass of 1.6 GeV. For the resonance, a single additional Breit-Wigner is assumed:

$$A_{\rho'}(m_{\pi\pi}) = f_{\rho'} e^{i\phi_{\rho'}} \mathcal{BW}_{\rho'}(m_{\pi\pi}). \quad (\text{A.2})$$

In particular, a global phase  $\phi_{\rho'}$  between the  $\rho'$  and  $\rho^0$  resonance contributions is considered. The  $\rho'$  width is assumed to be mass-dependent as parametrized in Equation (7.22).

The extended Söding model then has the form:

$$\frac{d\sigma_{\pi\pi}}{dm_{\pi\pi}}(m_{\pi\pi}) = N \frac{q^3(m_{\pi\pi})}{q^3(m_\rho)} \left| A_{\rho,\omega}(m_{\pi\pi}) + e^{i\phi_{nr}} A_{nr}(m_{\pi\pi}) + A_{\rho'}(m_{\pi\pi}) \right|^2. \quad (\text{A.3})$$

## Fit Result

The extended Söding model is simultaneously fitted to the elastic and proton-dissociative differential cross-section  $d\sigma(\gamma p \rightarrow \pi^+\pi^-Y)/dm_{\pi\pi}$ . The fit result is shown in Figure A.1. The nominal fit provides a good  $\chi^2$  using statistical uncertainties only  $\chi^2_{\text{stat}}/\text{ndf} = 37.8/(68-22) = 0.82$ . The fit parameters are summarized in Table A.1 with systematic uncertainties being propagated with the offset method.

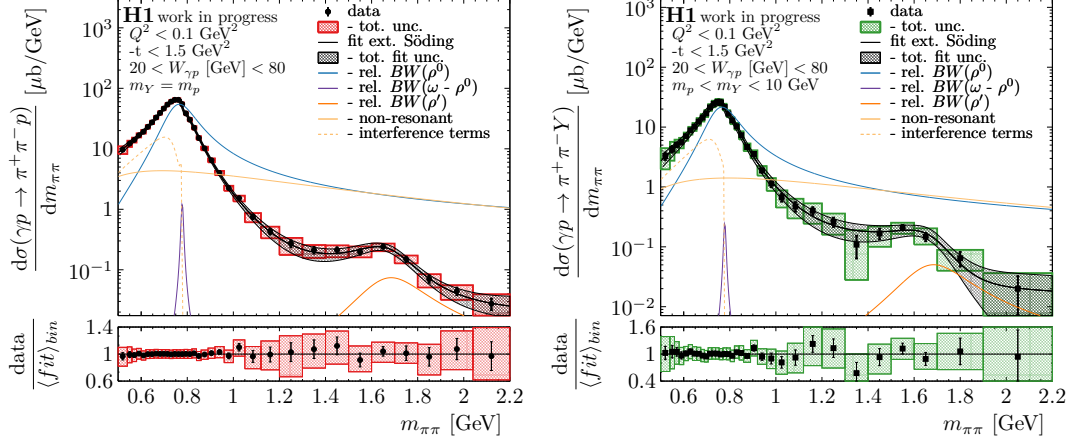


**Figure A.1:** Elastic (left) and proton-dissociative (right) differential cross-section  $d\sigma(\gamma p \rightarrow \pi^+\pi^-Y)/dm_{\pi\pi}$  as a function of  $m_{\pi\pi}$ . The extended Söding model is fitted to the data as described in the text. The model and its components are drawn as indicated in the legend. The data uncertainties are described in Figure 8.1.

The interpretation of cross-section with the model around the  $\rho^0$  resonance remains as discussed in the previous section. In the high mass tail, the fit model suggests a continued strong interference between the  $\rho^0$  and non-resonant amplitude. The interference has a negative sign so that the two contributions cancel one another out almost entirely. This allows the  $\rho'$  peak to emerge even though it is much smaller than both the  $\rho^0$  and non-resonant contributions on their own.

Extending the fit to higher  $m_{\pi\pi}$  values slightly changes the non-resonant fit parameters in comparison with the previous fit in the reduced mass range. In particular, a non-zero phase is necessary to describe the (elastic) cross-section well. It is not clear how the phase should be interpreted. It could have a physical origin, e.g., in final state interactions between the non-resonant pions and the proton, or merely compensate mismodeling of the considered amplitudes. This is not investigated further.

According to the PDG, there should be two resonances in the region of the observed peak around 1.6 GeV [1]. However, a single Breit-Wigner is sufficient for a good description of the peak with the Söding model. Moreover, two  $\rho'$  resonances can not be independently constrained in a fit. Without a proper estimate for model uncertainties, no attempt is made to test if the data would agree with the two PDG  $\rho'$  resonances.

## Relative $\rho'$ Cross-Section

For completeness, in Table A.2 individual contributions to the fit model are integrated to extract the cross-sections of the corresponding subprocesses. A model uncertainty is again not evaluated but should be expected to be large. This is even more true so for the extracted  $\rho'$  cross-section, which should be much very sensitive to the modeling of the non-resonant background.

parameter	value	stat.	syst.
$m_\rho$ [GeV]	0.7712	0.0006	$+0.0003$ $-0.0008$
$\Gamma_\rho$ [GeV]	0.1509	0.0016	$+0.0021$ $-0.0023$
$m_\omega$ [GeV]	0.7782	0.0014	$+0.0011$ $-0.0014$
$\Gamma_\omega$ [GeV]	0.0085	fixed	
$\delta_{nr}$	1.29	0.15	$+0.16$ $-0.15$
$m_{\rho'}$ [GeV]	1.692	0.021	$+0.018$ $-0.024$
$\Gamma_{\rho'}$ [GeV]	0.298	0.051	$+0.026$ $-0.054$

parameter	$m_Y = m_p$			$m_p < m_Y < 10$ GeV		
	value	stat.	syst.	value	stat.	syst.
$A$ [ $\mu\text{b}/\text{GeV}^2$ ]	54.3	1.5	$+3.7$ $-3.2$	21.5	0.6	$+2.8$ $-2.4$
$f_\omega$	0.164	0.015	$+0.016$ $-0.016$	0.117	0.038	$+0.034$ $-0.022$
$\phi_\omega$	-0.47	0.16	$+0.17$ $-0.17$	-0.06	0.26	$+0.24$ $-0.26$
$f_{nr}$	0.211	0.026	$+0.049$ $-0.034$	0.23	0.05	$+0.10$ $-0.07$
$\phi_{nr}$	-0.100	0.050	$+0.024$ $-0.061$	0.030	0.040	$+0.055$ $-0.089$
$\Lambda_{nr}$ [ $\text{GeV}^2$ ]	0.29	0.09	$+0.16$ $-0.12$	0.40	0.14	$+0.32$ $-0.22$
$f_{\rho'}$	0.0104	0.0034	$+0.0037$ $-0.0016$	0.0137	0.0033	$+0.0043$ $-0.0010$
$\phi_{\rho'}$	0.67	0.63	$+0.72$ $-0.50$	1.17	0.27	$+0.36$ $-0.36$

**Table A.1:** Fit parameters for the extended Söding fit described in the text. The corresponding fit is shown in Figure A.1.

$X$	$\sigma(X)$	stat.	syst.	$\frac{\sigma(X)}{\sigma(\rho)}$	stat.	syst.	$\int m_{\pi\pi} \max$
	[ $\mu\text{b}$ ]						[GeV]
<b><math>m_Y = m_p</math></b>							
$\mathcal{BW}(\rho^0)$	12.28	0.32	$+0.83$ $+0.74$	-	-	-	1.53
Söding $\pi^+\pi^-$	12.95	0.10	$+0.83$ $+0.85$	1.055	0.031	$+0.030$ $-0.054$	1.53
non-resonant	3.84	0.21	$+0.29$ $+0.33$	0.313	0.024	$+0.016$ $-0.026$	1.53
$\mathcal{BW}(\omega-\rho^0)$	1.77	0.32	$+0.38$ $+0.34$ $\times 10^{-2}$	2.51	0.46	$+0.51$ $-0.48$ $\times 10^{-3}$	0.82
$\mathcal{BW}(\rho'')$	3.3	2.5	$+2.8$ $+1.1$ $\times 10^{-2}$	2.4	1.7	$+1.9$ $-0.8$ $\times 10^{-3}$	3.5
<b><math>m_p &lt; m_Y &lt; 10</math> GeV</b>							
$\mathcal{BW}(\rho^0)$	4.85	0.12	$+0.61$ $+0.54$	-	-	-	1.53
Söding $\pi^+\pi^-$	5.15	0.07	$+0.70$ $+0.71$	1.062	0.032	$+0.054$ $-0.078$	1.53
non-resonant	1.31	0.11	$+0.17$ $+0.19$	0.270	0.027	$+0.014$ $-0.029$	1.53
$\mathcal{BW}(\omega-\rho^0)$	3.6	2.4	$+2.2$ $+1.3$ $\times 10^{-3}$	1.28	0.84	$+0.80$ $-0.47$ $\times 10^{-3}$	0.82
$\mathcal{BW}(\rho'')$	2.3	1.2	$+1.4$ $+0.4$ $\times 10^{-2}$	4.0	2.1	$+2.5$ $-0.7$ $\times 10^{-3}$	3.5

**Table A.2:** Integrated contributions to the  $\pi^+\pi^-$  cross-sections obtained from the extended Söding fit described in the text.

## A.2 Model Comparison

### Tensor Pomeron Model by Ewerz et al. [123]

Ewerz et al. [123] give a theoretical model for soft high-energy scattering of hadrons. It is applied to  $\pi^+\pi^-$  photoproduction in Reference [124]<sup>1</sup>. The approach taken by the authors is that of a quantum field theory with effective propagators and couplings for Reggeon and Pomeron exchange. For  $\pi^+\pi^-$  photoproduction, a set of gauge-invariant amplitudes for a large variety of resonant ( $\rho^0$ ,  $\omega(780)$ ,  $f_2(1200)$ ,  $\rho(1450)$ ) and non-resonant contributions are calculated. The model relies on a large set of externally provided parameters. In particular, to determine the various coupling strengths, form-factors, and propagators. A MC even generator for the model is available to the author of this thesis. The generator is described in more detail in Refs. [124, 149].

The model as it is presented in Reference [124] is compared to the single-differential elastic  $\pi^+\pi^-$  photoproduction cross-section as a function of  $m_{\pi\pi}$ ,  $W_{\gamma p}$ , and  $t$  in Figure A.3. A priori, it does not describe the data very well. The modeled  $W_{\gamma p}$  and  $t$  dependence appear to be reasonably described in shape, but not normalization, with potential shape differences occurring above  $|t| \gtrsim 0.1$  GeV. The measured  $m_{\pi\pi}$  lineshape, on the other hand, is not reproduced, at all. The skewing of the  $\rho^0$  resonance is significantly too weak, and the model breaks down completely above  $m_{\pi\pi} \gtrsim 1$  GeV. The high mass region is very challenging to model because the  $\rho^0$  and non-resonant contributions appear to cancel one another out perfectly in reality. They thus need to be simultaneously very well described; compare Figure 8.3. Concerning the low mass region and skewing of the  $\rho^0$  resonance, a flaw in the modeling of the non-resonant amplitude could be identified in correspondence with the authors of Reference [124].

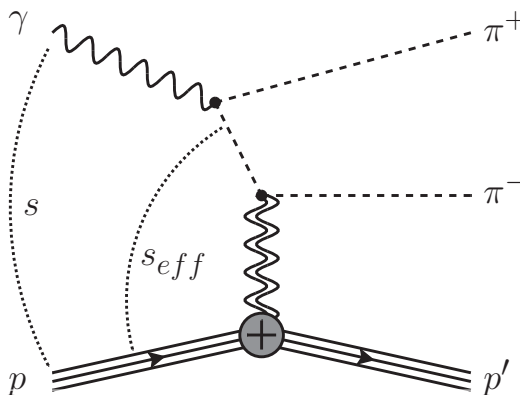


**Figure A.2:** Diagram for non-resonant  $\pi^+\pi^-$  production.

The non-resonant amplitudes included in the model have a structure as illustrated in Figure A.2. For the energy dependence of the diffractive interaction, the photon-proton center-of-mass energy  $s$  is assumed. However, the photon-momentum is split between the two pion lines. This results in a lower effective scattering energy  $s_{eff}$  between the proton and the pion undergoing the soft interaction. In consultation with Prof. Nachtmann [204], on average  $s_{eff} \simeq \frac{s}{2}$  can be expected. In order to test this hypothesis, the non-resonant amplitudes presented in Reference [124] are modified accordingly, i.e.,  $s$  is replaced by  $s \rightarrow s_{eff} = \frac{s}{2}$  in the non-resonant amplitudes  $\mathcal{M}^{(e)}(s)$  of the model (Equation (2.26) in the reference). The prediction of the modified model is also included in Figure A.3. Indeed, it results in a significant improvement of the description of the skewing of the  $\rho^0$  resonance.

<sup>1</sup>The author of this thesis contributed to the study of  $\pi^+\pi^-$  photoproduction within the model in Reference [124] but was not involved in the model building itself.

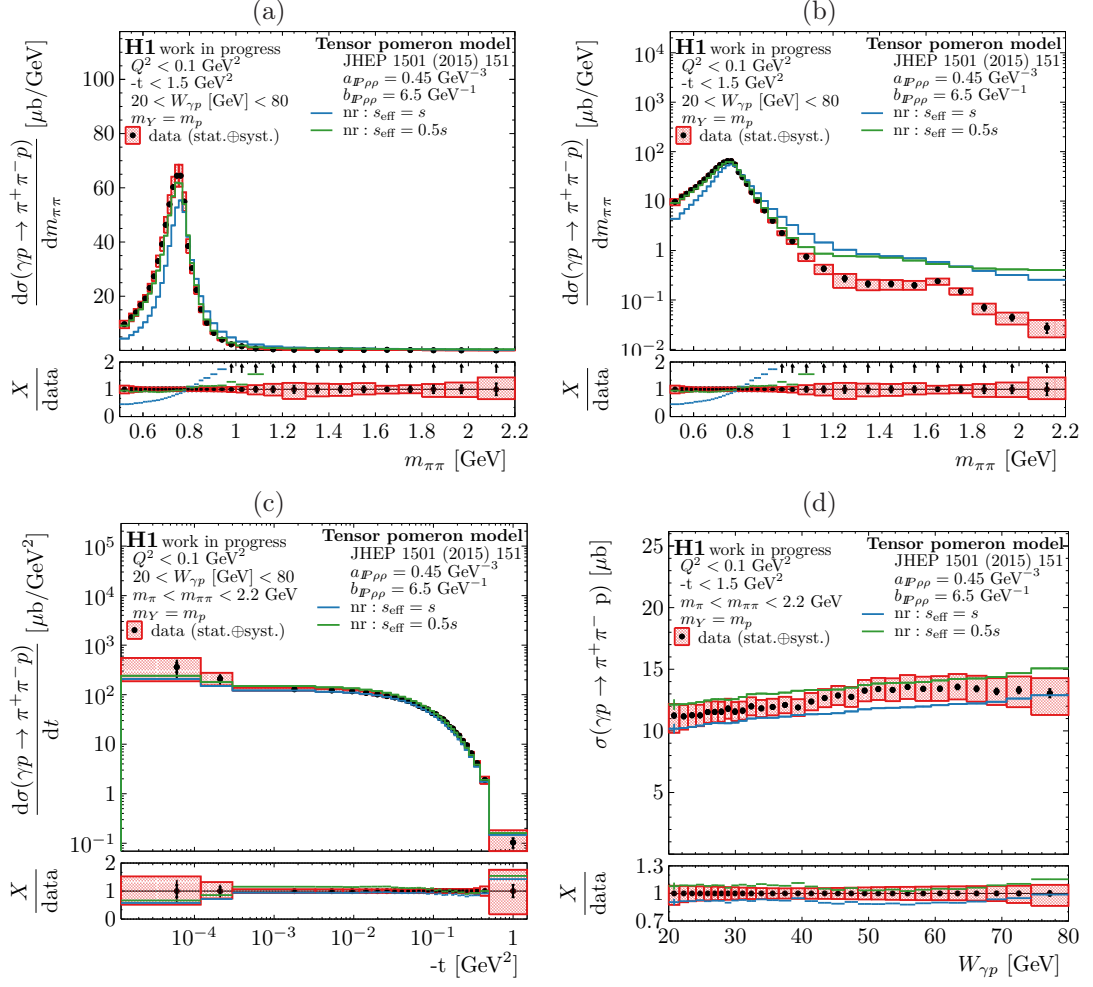


**Figure A.3:** Comparison of measured single-differential  $\pi^+\pi^-$  photoproduction cross-sections with the model by Ewerz et al. [123].  $d\sigma(\gamma p \rightarrow \pi^+\pi^- p)/dm_{\pi\pi}$  as a function of  $m_{\pi\pi}$  on a linear (a) and logarithmic  $y$ -axis scale (b),  $d\sigma(\gamma p \rightarrow \pi^+\pi^- p)/dt$  as a function of  $t$  (c), and  $\sigma(\gamma p \rightarrow \pi^+\pi^- p)$  as a function of  $W_{\gamma p}$  (d). The data is compared with the model as presented in reference [124] (blue line) and to the modified model as described in the text (green line).

Even after modifying the non-resonant amplitudes, the agreement between data and the model is not very good. In particular, the model still fails at describing the high mass region. However, the model as presented in Reference [124] depends on multiple parameters, some of which are not well known. In principle, these could be optimized to achieve a better description of the data. Unfortunately, this was not feasible for this thesis.



## B EVENT SELECTION CUTS

category	cuts
trigger	$s0 \    \ s1 \    \ s2 \    \ s3$
electron selection	$E_{SpaCal} > 17 \text{ GeV}$ fiducial SpaCal cuts [179] $R_{CT,e'} < 16 \text{ cm}$
timing	$40 < T_{0,CJC} < 52 \text{ ns}$ $ \Delta T_0(\pi^+, \pi^-)  < 30 \text{ ns}$ $ T_{0,LAr}  < 52 \text{ ns}$
#tracks	== 2 selected central tracks (“H1PartSelTrack”) opposite charges cosmic $\mu$ veto
CJC acceptance	$20^\circ < \theta < 160^\circ$ $p_T > 160 \text{ MeV}$
track quality	$dca' < 0.1 \text{ cm}$ cosmic $\mu$ veto
$z_{vtx}$	$ z_{vtx}  < 25 \text{ cm}$
track dE/dx PID	$p > 0.4 \text{ GeV} \    \ \mathcal{P}_{dE/dx}(K) < 0.1$ $p > 0.9 \text{ GeV} \    \ \mathcal{P}_{dE/dx}(P) < 0.1$ $p > 2 \text{ GeV} \    \ \mathcal{P}_{dE/dx}(D) < 0.1$ $\mathcal{P}_{dE/dx}(\pi) > 1e-9$
LRG	$E_{LAr}(\theta < 20^\circ) == 0 \text{ GeV}$ #forward tracks < 2
LAr	$E_{LAr}^{!assoc} == 0 \text{ GeV}$
phasespace	$0.6 < m_{\pi\pi} < 1 \text{ GeV}$ $ t  < 3 \text{ GeV}^2$ $20 < W_{\gamma p} < 160 \text{ GeV}$

**Table B.1:** Summary of all selection cuts for the  $\pi^+\pi^-$  DIS dataset. Compare Chapter 6

category		cuts	
trigger	<b>base selection</b>	<b>s14</b>	
electron veto		$E_{SpaCal}^{assoc} < 10 \text{ GeV}$	
timing		$40 < T_{0,CJC} < 52 \text{ ns}$ $ \Delta T_0(\pi^+, \pi^-)  < 30 \text{ ns}$ $ T_{0,LAr}  < 52 \text{ ns}$	
#tracks		== 2 selected central tracks (“H1PartSelTrack”) opposite charges cosmic $\mu$ veto	
track quality and trigger performance		$25^\circ < \theta < 155^\circ$ $p_T > 160 \text{ MeV}$ $dca' < 0.1 \text{ cm}$ $ \Delta\phi_{FTT}  > 20^\circ$ cosmic $\mu$ veto	
LRG		$E_{LAr}(\theta < 20^\circ) == 0 \text{ GeV}$ #forward tracks < 2	
phasespace		$0.4 < m_{\pi\pi} < 2.3 \text{ GeV}$ $p_{T,\pi\pi}^2 < 3 \text{ GeV}^2$ $20 < W_{\gamma p} < 90 \text{ GeV}$	
		<b>signal and control regions</b>	
$z_{vtx}$		all but beam-gas	$ z_{vtx}  < 25 \text{ cm}$
		beam-gas	$25 <  z_{vtx}  < 40 \text{ cm}$
$\rho' \rightarrow \rho^0 \pi^0 \pi^0$ veto	all but $\phi$	$ \Delta\phi_{\pi\pi}  > 50^\circ$	
track dE/dx PID	all but $\phi$	$p > 0.4 \text{ GeV} \parallel \mathcal{P}_{dE/dx}(K) < 0.1$ $p > 0.9 \text{ GeV} \parallel \mathcal{P}_{dE/dx}(P) < 0.1$ $p > 2 \text{ GeV} \parallel \mathcal{P}_{dE/dx}(D) < 0.1$ $\mathcal{P}_{dE/dx}(\pi) > 1e-9$	
	$\phi$	$\mathcal{P}_{dE/dx}(K) > 0.01$	
SpaCal (noise level 300 MeV)	$\rho', \omega, \pi\pi, \phi$	$E_{SpaCal}^{assoc} < 4 \text{ GeV}$	
	$\gamma$ -dissoc.	$E_{SpaCal}^{assoc} > 4 \text{ GeV}$	
LAr (noise level 600 MeV)	$\pi\pi, \phi$	$E_{LAr}^{assoc} < 0.8 \text{ GeV}$	
	$\rho', \omega$	$E_{LAr}^{assoc} > 0.8 \text{ GeV}$	
mass windows	$\omega$	$m_{\pi\pi} < 0.55 \text{ GeV}, m_{evt} < 1.2 \text{ GeV}$	
	$\rho'$	$m_{evt} > 1.2 \text{ GeV}$	
	$\phi$	$1.005 < m_{KK} < 1.035 \text{ GeV}$	

**Table B.2:** Summary of all selection cuts for the  $\pi^+\pi^-$  photoproduction dataset applied to the various signal  $\rho$  and background  $\omega \rightarrow 3\pi$ ,  $\rho' \rightarrow 4\pi$ ,  $\phi$ , and  $\gamma$ -dissociation control regions. Compare Chapter 4

## C DERIVATIONS

### C.1 Reconstructing $W_{\gamma p}$ from the $\pi^+\pi^-$ System

The photon-proton center-of-mass energy  $W_{\gamma p}$  is defined as

$$W_{\gamma p}^2 = |p_p + q|^2 = m_p^2 - Q^2 + 2p_p \cdot q, \quad (\text{C.1})$$

in terms of the incoming proton momentum four-vector  $p_p$ , the photon momentum  $q$ , and the photon virtuality  $Q^2 = -q^2$ . Using momentum conservation of the scattering process  $\gamma^* p \rightarrow \pi^+ \pi^- p'$ , the last term in the equation can be expressed as

$$p_p \cdot q = p_q \cdot (p_{\pi\pi} + p_{p'} - p) = (p_p \cdot p_{\pi\pi} + p_p \cdot p_{p'} - m_p^2), \quad (\text{C.2})$$

with the four-momentum of the  $\pi^+\pi^-$  system  $p_{\pi\pi}$  and the scattered proton  $p_{p'}$ . Neglecting  $m_p \ll E_p$ , the first term in the second equation becomes

$$p_p \cdot p_{\pi\pi} \simeq E_p (E_{\pi\pi} - p_{z,\pi\pi}). \quad (\text{C.3})$$

The second term can be expressed as

$$2p_p \cdot p_{p'} = m_p^2 + m_Y^2 - t \quad (\text{C.4})$$

Typically,  $|t| \ll 1 \text{ GeV}^2$  is very small and in photoproduction also  $Q^2 \ll 1 \text{ GeV}^2$  is negligible. Furthermore for elastic scattering  $m_Y = m_p$ . Then all remaining terms can be neglected relative to  $E_p (E_{\pi\pi} - p_{z,\pi\pi})$  and  $W_{\gamma p}$  approximated by

$$W_{\gamma p}^2 \simeq 2E_p (E_{\pi\pi} - p_{z,\pi\pi}) + \mathcal{O}(m_p^2, m_Y^2, Q^2, t). \quad (\text{C.5})$$

However, for proton-dissociation  $M_Y^2$  can become quite large and of the order of  $100 \text{ GeV}^2$ . The two terms then are of comparable size and the approximation of  $W_{\gamma p}$  breaks down.

### C.2 Reconstructing $t$ from the $\pi^+\pi^-$ System

The momentum transfer  $t$  at the proton-vertex is defined as

$$t = (p_p - p_{p'})^2 = (p_{\pi\pi} - q)^2 = m_{\pi\pi}^2 - Q^2 - 2p_{\pi\pi} \cdot q \quad (\text{C.6})$$

Neglecting  $Q^2 \simeq 0 \text{ GeV}^2$  the second equation can be re-written as

$$p_{\pi\pi} \cdot q \simeq E_{\pi\pi} E_\gamma + p_{z,\pi\pi} E_\gamma \quad (\text{C.7})$$

with approximately  $q = (E_\gamma, 0, 0, -E_\gamma)^T$ . Under these assumptions and neglecting  $m_p \ll E_p$ , the proton-photon center-of-mass energy becomes

$$W_{\gamma p}^2 = |p_p + q|^2 \simeq 4E_\gamma E_p. \quad (\text{C.8})$$

A comparison with Equation (C.5) then yields  $E_\gamma \simeq \frac{1}{2}(E_{\pi\pi} - p_{z,\pi\pi})$ . Inserting into Equation (C.7) gives

$$p_{\pi\pi} \cdot q \simeq (E_{\pi\pi}^2 - p_{z,\pi\pi}^2) = m_{\pi\pi}^2 - p_{T,\pi\pi}^2. \quad (\text{C.9})$$

Inserting into Equation (C.7) then results in

$$t \simeq -p_{T,\pi\pi}^2 + \mathcal{O}(Q^2, \Delta W_{\gamma p}^2). \quad (\text{C.10})$$

### C.3 Splitting The Total Covariance Matrix

The goal is to split a covariance matrix  $\mathbf{U}_\sigma$  of a distribution  $\vec{\sigma}$  into a pure normalization uncertainty and a remaining covariance matrix  $\mathbf{U}_{\text{rest}}$ :

$$\mathbf{U}_\sigma = \Delta_{\text{norm}} \vec{\sigma} \cdot \vec{\sigma}^T + \mathbf{U}_{\text{rest}}. \quad (\text{C.11})$$

The minimum requirement is that  $\mathbf{U}_{\text{rest}}$  remains positive definite with full rank and the goal is to minimize its off-diagonal elements while maximising  $\Delta_{\text{norm}}$ . The goal is achieved by scanning  $\Delta_{\text{norm}}$  in order to minimize the maximum global correlation coefficient of  $\mathbf{U}_{\text{rest}}$

$$\max \rho_{\text{rest}} = \max_i \left\{ 1 - \frac{1}{(\mathbf{U}_{\text{rest}})_{ii} (\mathbf{U}_{\text{rest}}^{-1})_{ii}} \right\} \quad (\text{C.12})$$

while simultaneously ensuring that  $\mathbf{U}_{\text{rest}}$  remains positive and has full rank.

# D MASS FIT PLOTS FOR $\rho^0$ EXTRACTION

## D.1 Fit $\sigma(\gamma p \rightarrow \pi^+ \pi^- Y)(W_{\gamma p}; m_{\pi\pi})$ (Section 8.2.1)

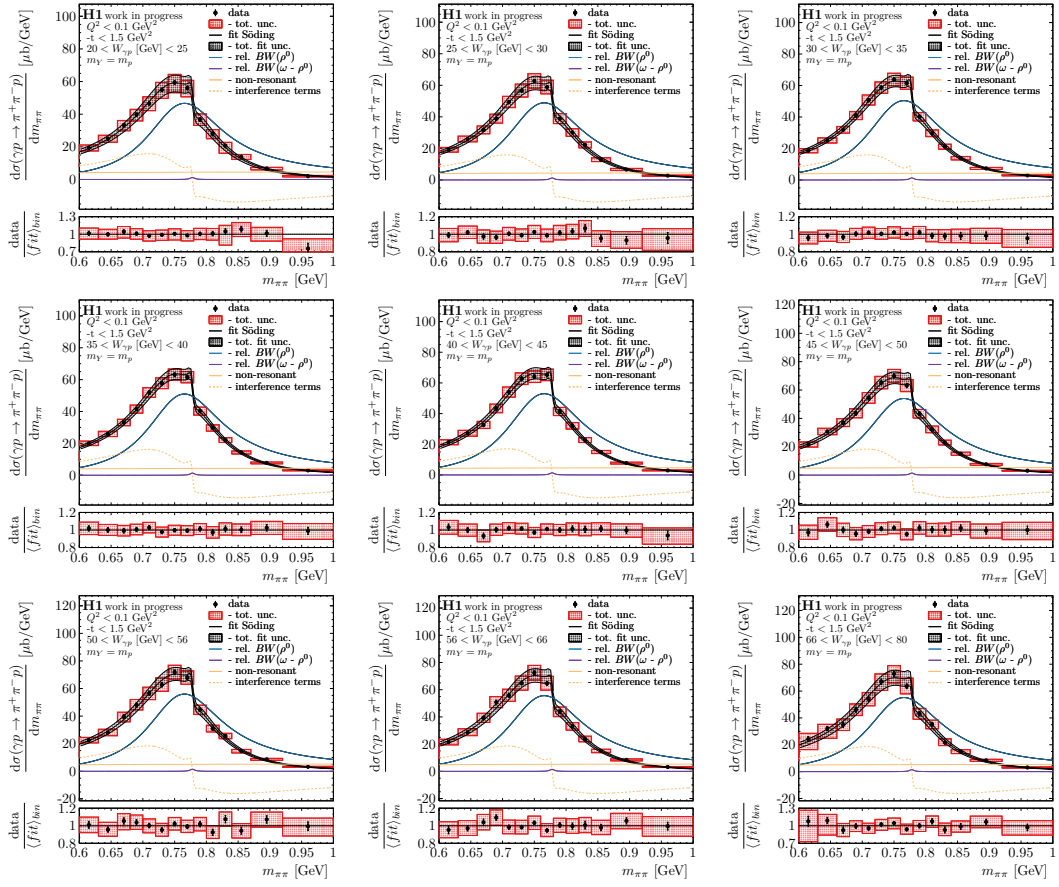


**Figure D.1:** Elastic double-differential cross-section  $d\sigma(\gamma p \rightarrow \pi^+ \pi^- p)/dm_{\pi\pi}$  as a function of  $m_{\pi\pi}$  shown in 9 bins of rising  $W_{\gamma p}$  (from left to right, top to bottom). The Söding model defined in Equation (7.18) is fitted simultaneously to the elastic and proton-dissociative distributions that are shown Figure D.2. Further model assumptions are applied as described in the text in Chapter 8. The fit function for the respective bins is shown together with a subset of contributing components. The composition of the data errors is explained in Figure 8.1.

D.1. FIT  $\sigma(\gamma p \rightarrow \pi^+\pi^-Y)(W_{\gamma p}; m_{\pi\pi})$   
(SECTION 8.2.1)

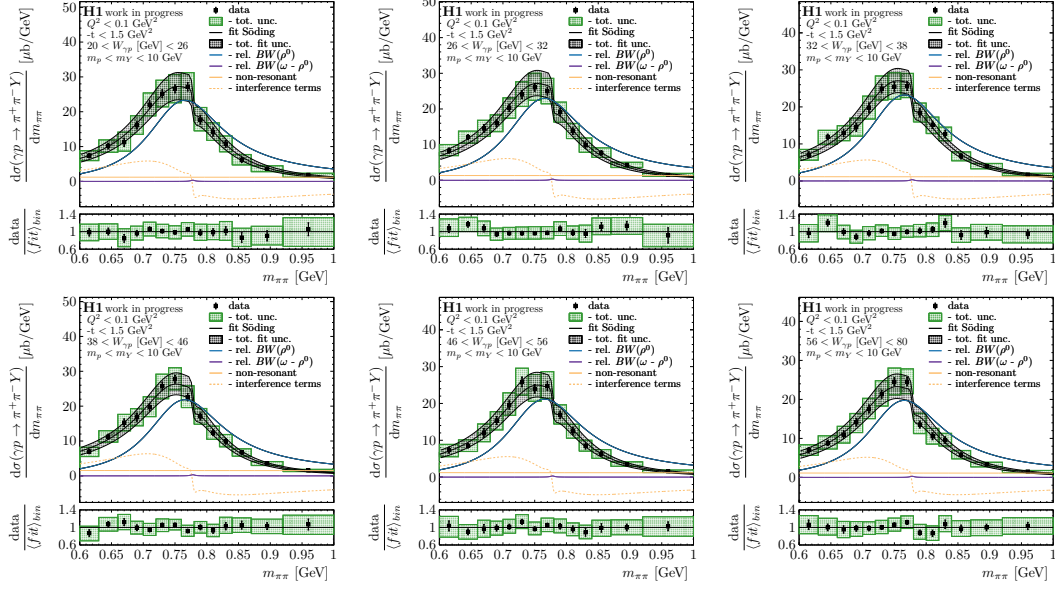


**Figure D.2:** proton-dissociative double-differential cross-section  $d\sigma(\gamma p \rightarrow \pi^+\pi^-Y)/dm_{\pi\pi}$  as a function of  $m_{\pi\pi}$  shown in 6 bins of rising  $W_{\gamma p}$  (from left to right, top to bottom). The Söding model defined in Equation (7.18) is fitted simultaneously to the proton-dissociative and elastic distributions that are shown in Figure D.1. Further model assumptions are applied as described in the text in Chapter 8. The fit function for the respective bins is shown together with a subset of contributing components. The composition of the data errors is explained in Figure 8.1.

## D.2 Fit $d^2\sigma(\gamma p \rightarrow \pi^+\pi^-Y)/dm_{\pi\pi}dt(t; m_{\pi\pi})$ (Section 8.2.2)

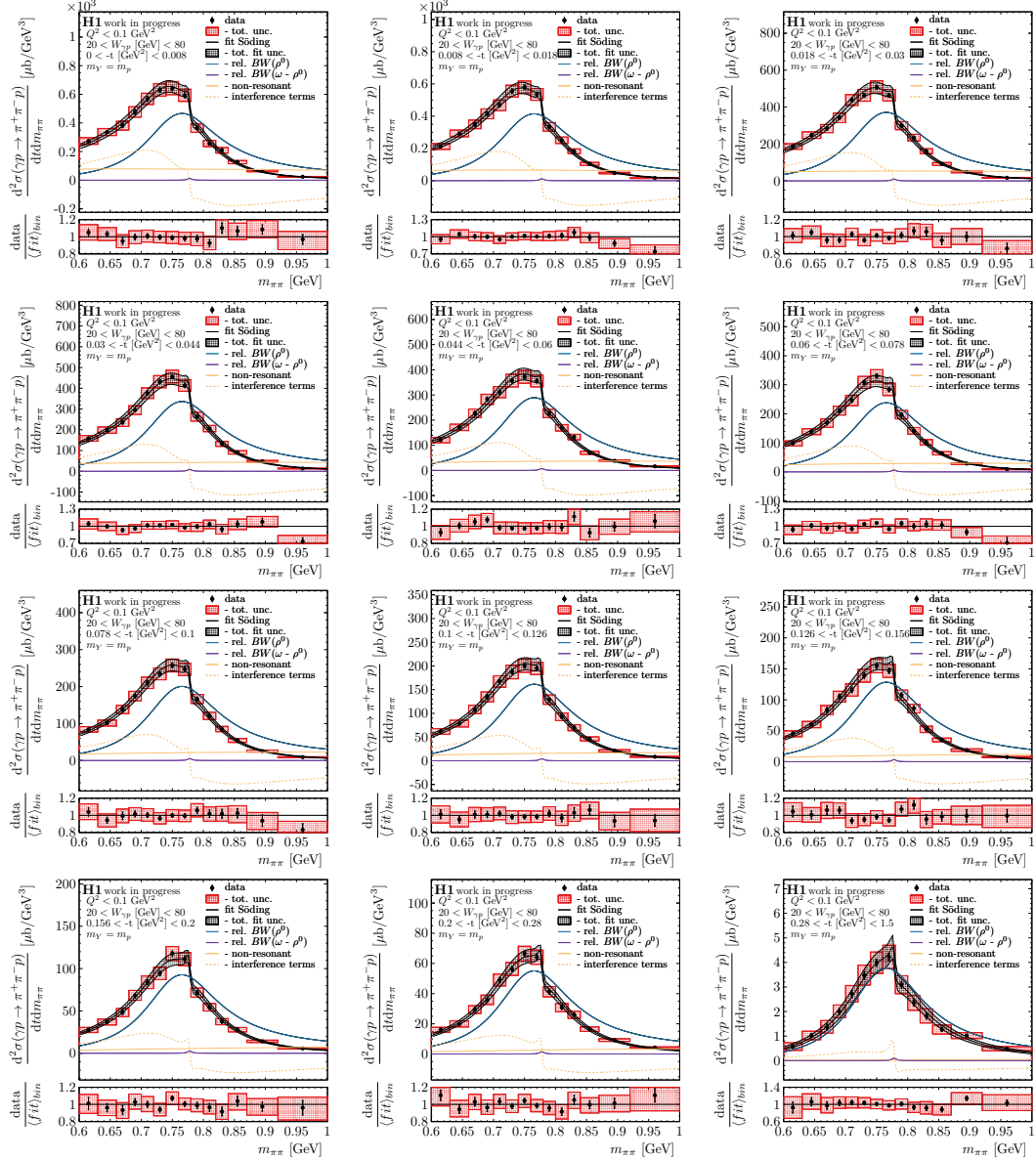


**Figure D.3:** Elastic double-differential cross-section  $d^2\sigma(\gamma p \rightarrow \pi^+\pi^-p)/dm_{\pi\pi}dt$  as a function of  $m_{\pi\pi}$  shown in 12 bins of increasing  $|t|$  (from left to right, top to bottom). The Söding model defined in Equation (7.18) is simultaneously fitted to the elastic and proton-dissociative distributions that are shown in Figure D.4. Further model assumptions are applied as described in the text in Chapter 8. The fit function for the respective bins is shown together with a subset of contributing components. The composition of the data errors is explained in Figure 8.1.

D.2. FIT  $D^2\sigma(\gamma p \rightarrow \pi^+\pi^-Y)/Dm_{\pi\pi}Dt(t; m_{\pi\pi})$   
(SECTION 8.2.2)

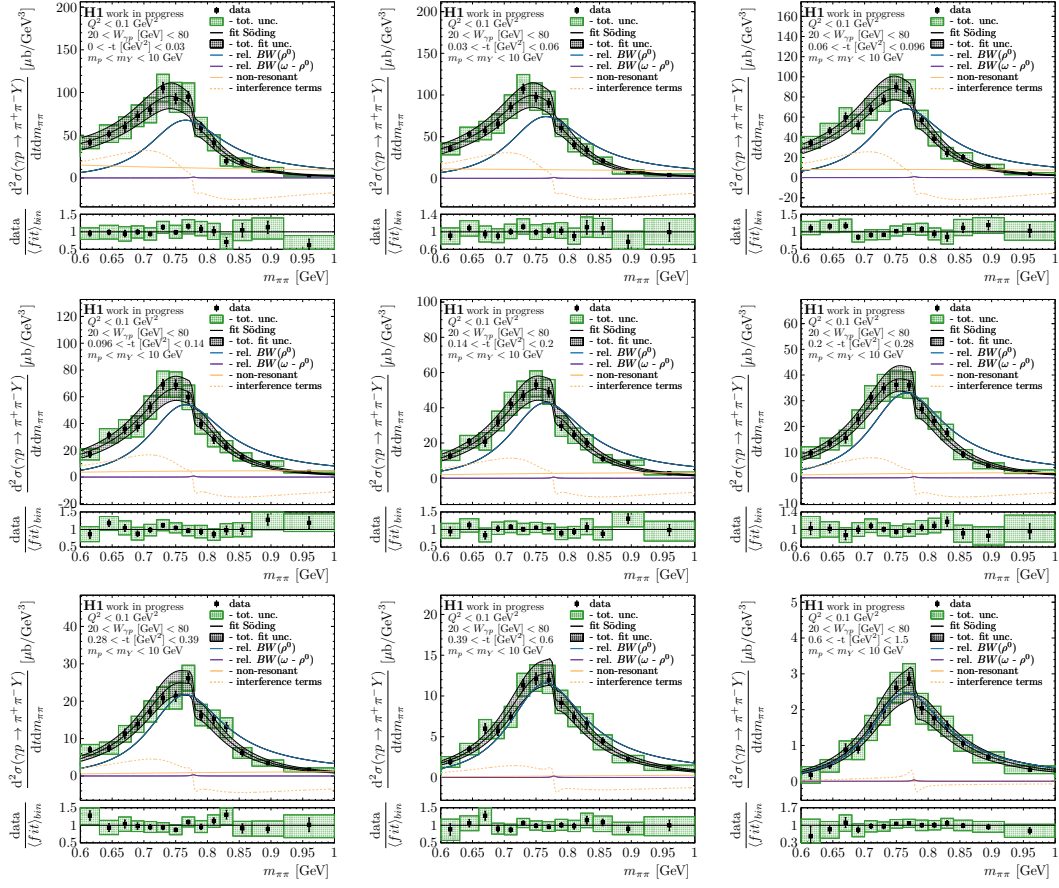


**Figure D.4:** Proton-dissociative double-differential cross-section  $d\sigma(\gamma p \rightarrow \pi^+\pi^-Y)/dm_{\pi\pi}$  as a function of  $m_{\pi\pi}$  shown in 8 bins of rising  $W_{\gamma p}$  (from left to right, top to bottom). The Söding model defined in Equation (7.18) is simultaneously fitted to the proton-dissociative and elastic distributions that are shown in Figure D.3. Further model assumptions are applied as described in the text in Chapter 8. The fit function for the respective bins is shown together with a subset of contributing components. The composition of the data errors is explained in Figure 8.1.

### D.3 Fit $d^2\sigma(\gamma p \rightarrow \pi^+\pi^-Y)/dm_{\pi\pi}dt(W_{\gamma p}, t; m_{\pi\pi})$ (Section 8.2.3)

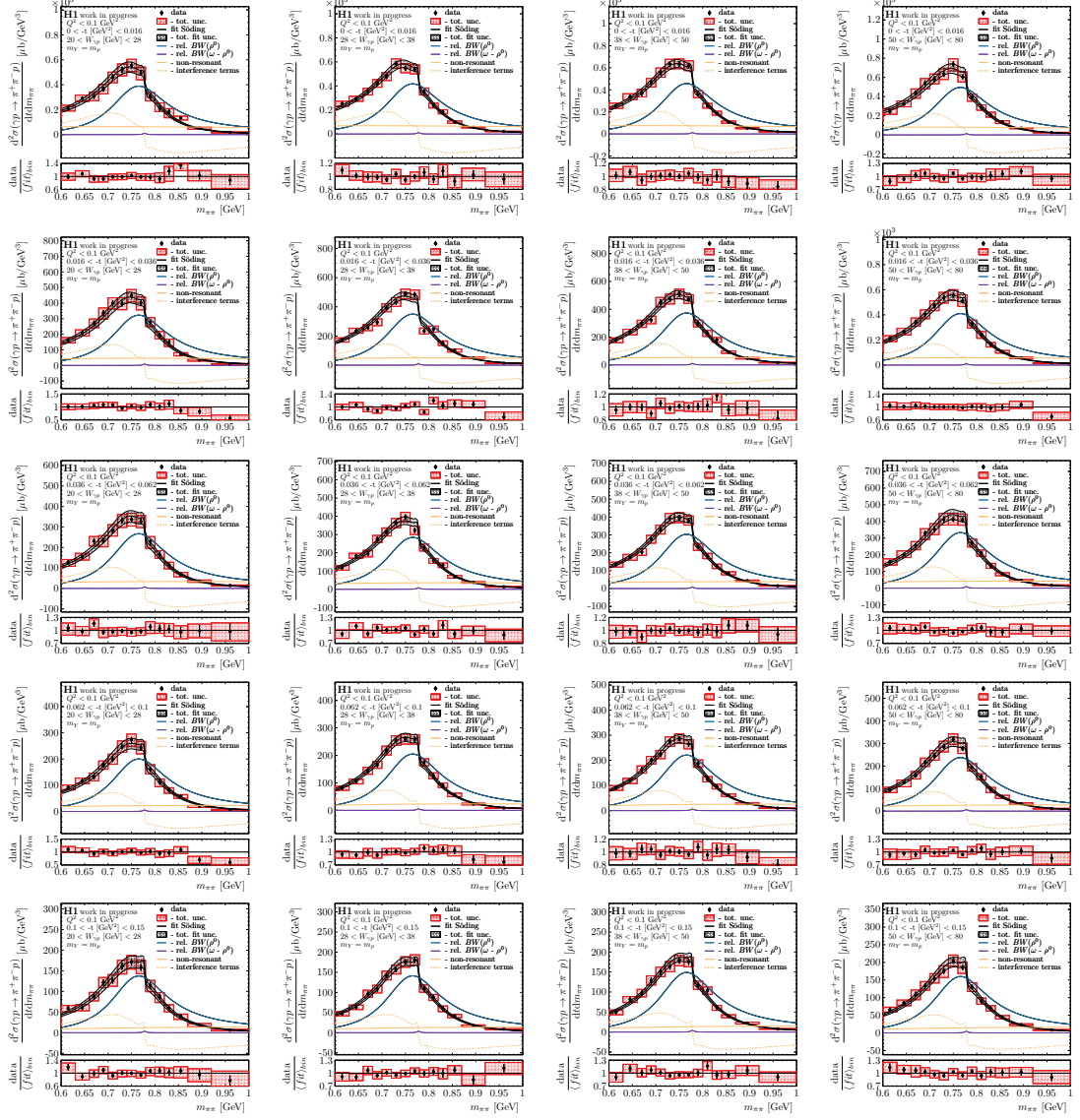
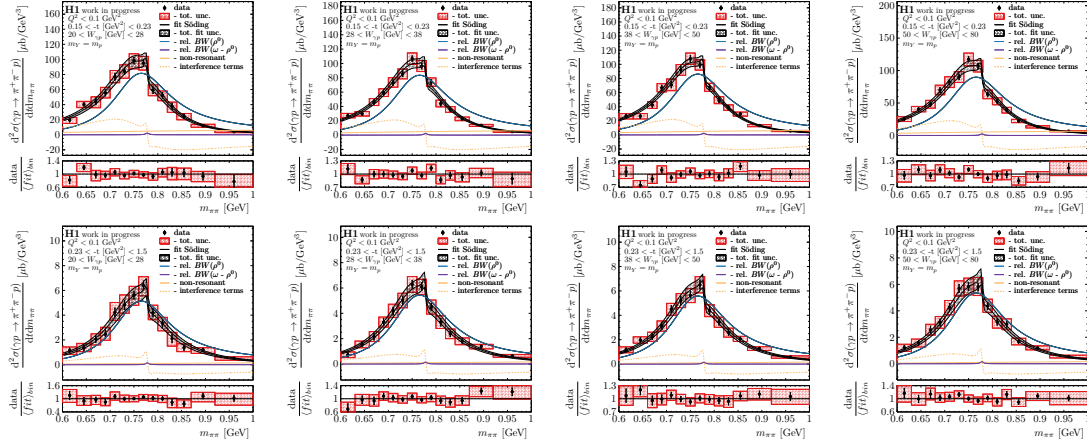
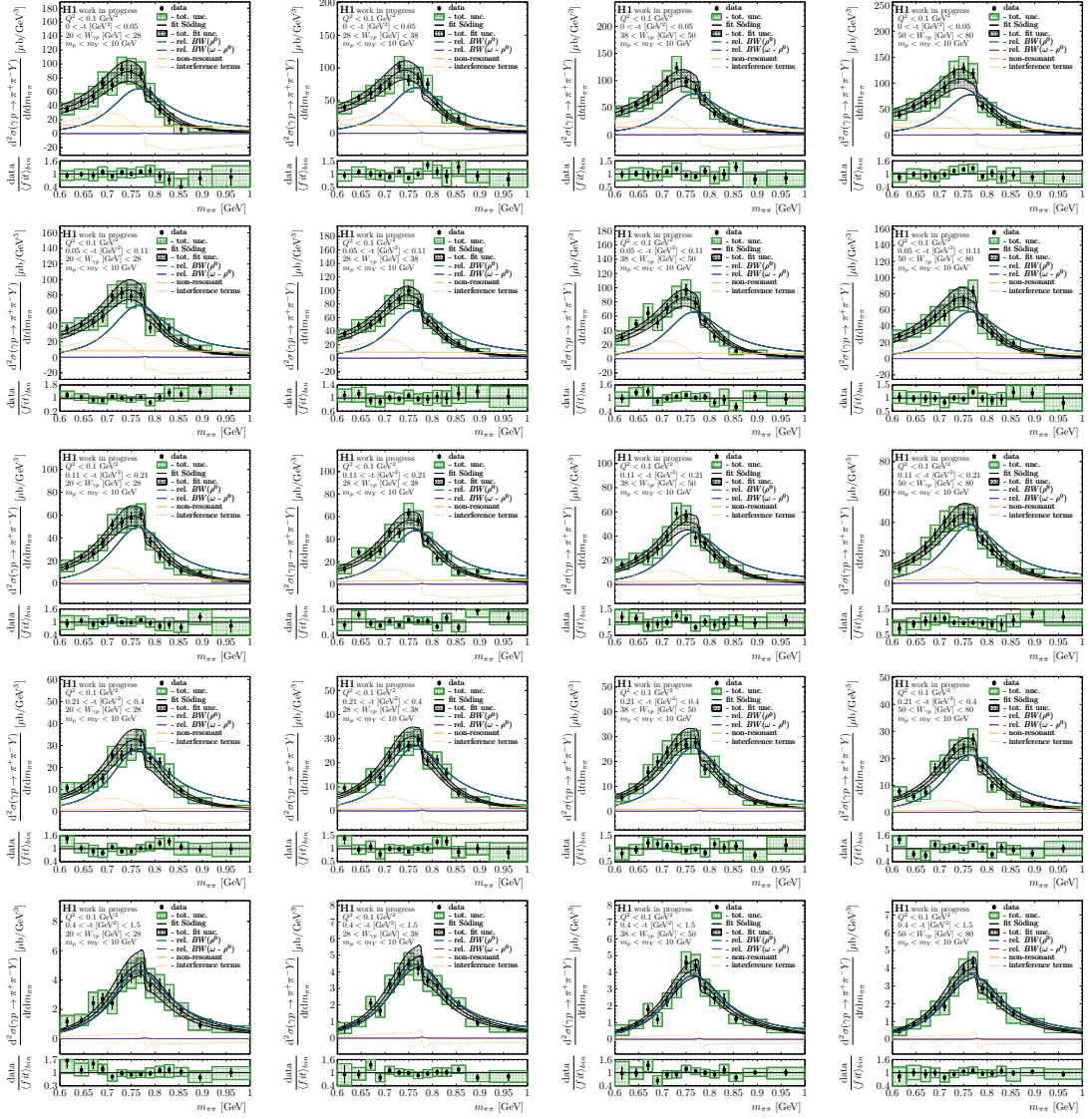


Figure D.5: Multipage figure. Caption in Figure D.6

D.3. FIT  $D^2\sigma(\gamma p \rightarrow \pi^+\pi^-Y)/Dm_{\pi\pi}Dt(W_{\gamma p}, t; m_{\pi\pi})$   
(SECTION 8.2.3)



**Figure D.6:** Elastic triple-differential cross-section  $d^2\sigma(\gamma p \rightarrow \pi^+\pi^-p)/dm_{\pi\pi}dt$  as a function of  $m_{\pi\pi}$  shown in 4 bins of increasing  $W_{\gamma p}$  (from left to right) and in 7 bins of increasing  $|t|$  (from top to bottom). The Söding model defined in Equation (7.18) is simultaneously fitted to the elastic and proton-dissociative distributions that are shown in Figure D.7. Further model assumptions are applied as described in the text in Chapter 8. The fit function for the respective bins is shown together with a subset of contributing components. The composition of the data errors is explained in Figure 8.1.



**Figure D.7:** Proton-dissociative triple-differential cross-section  $d^2\sigma(\gamma p \rightarrow \pi^+\pi^-Y)/dm_{\pi\pi}dt$  as a function of  $m_{\pi\pi}$  shown in 4 bins of increasing  $W_{\gamma p}$  (from left to right) and in 5 bins of increasing  $|t|$  (from top to bottom). The Söding model defined in Equation (7.18) is simultaneously fitted to the proton-dissociative and elastic distributions that are shown in Figure D.6. Further model assumptions are applied as described in the text in Chapter 8. The fit function for the respective bins is shown together with a subset of contributing components. The composition of the data errors is explained in Figure 8.1.



# E UNFOLDING FACTORS

## E.1 1D $\pi^+\pi^-$ Distributions

gen. lvl. regs.	det. lvl. regs.	axis	binning
$\pi^+\pi^-$ elas.	zero-tag	$m_{\pi\pi}$ [GeV]	0.500, 0.540, 0.560, 0.580, 0.600, 0.620, 0.638, 0.656, 0.674, 0.690, 0.706, 0.722, 0.738, 0.754, 0.770, 0.786, 0.802, 0.820, 0.840, 0.860, 0.890, 0.920, 0.960, 1.000, 1.050, 1.120, 1.200, 1.300, 1.400, 1.500, 1.600, 1.700, 1.800, 1.900, 2.040, 2.200
$\pi^+\pi^-$ pdis.	single-tag multi-tag		0.500, 0.540, 0.560, 0.580, 0.600, 0.620, 0.638, 0.656, 0.674, 0.690, 0.706, 0.722, 0.738, 0.754, 0.770, 0.786, 0.802, 0.820, 0.840, 0.860, 0.890, 0.920, 0.960, 1.000, 1.050, 1.120, 1.200, 1.300, 1.400, 1.500, 1.600, 1.700, 1.900, 2.200
$\omega$ , $\phi$ , $\gamma$ -diss. elas. & pdis.			0.30, 2.30
$\rho'$ elas. & pdis.			0.30, 0.65, 0.90, 2.30

**Table E.1:** Binning scheme for unfolding the 1D  $m_{\pi\pi}$  distributions. Not listed are the  $\pi^+\pi^-$  signal bins for not reconstructed or selected events and the overflow bins for events out of the fiducial phasepace.

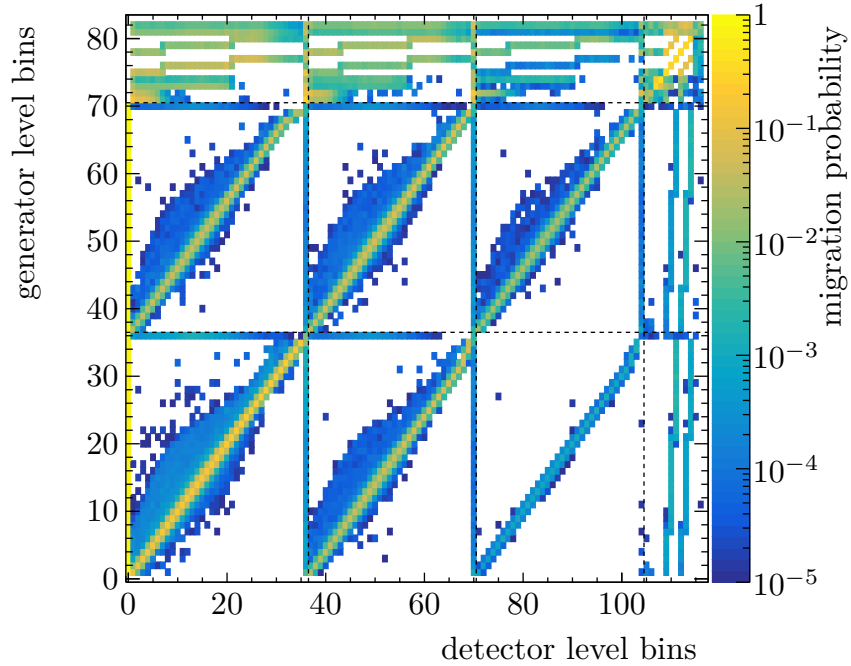


**Figure E.1:** Response matrix  $A$ .

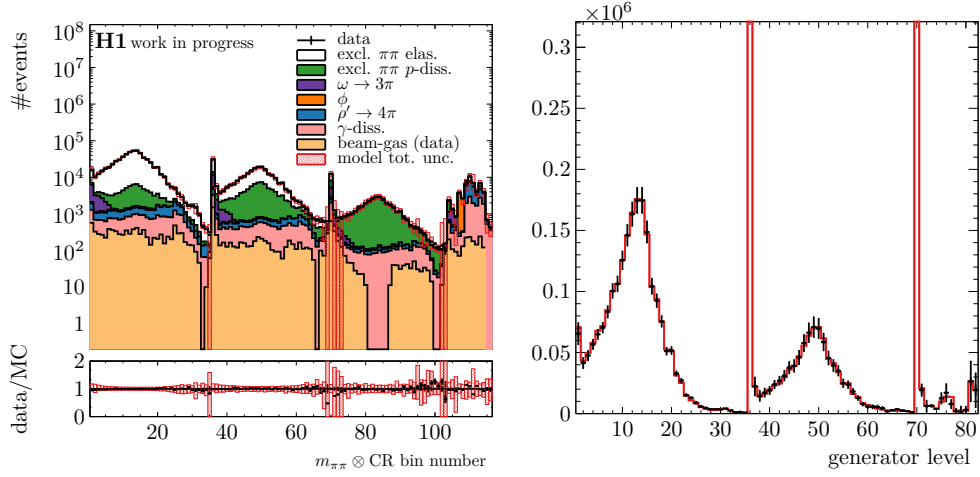


Figure E.2: Unfolding input (left) and output distribution (right).

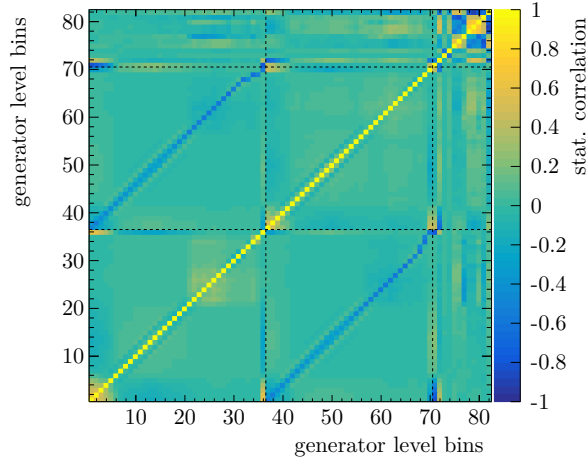


Figure E.3: Statistical covariance matrix.

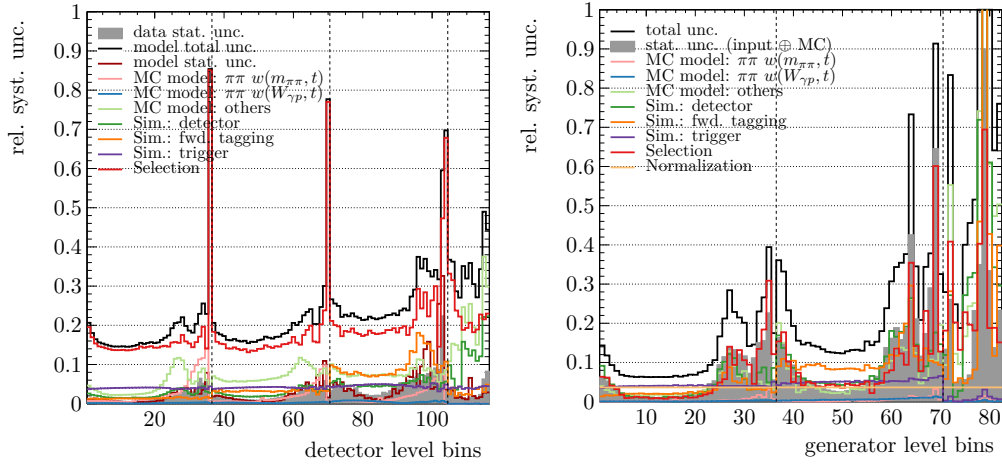


Figure E.4: Uncertainty on detector level (left) and after unfolding (right).

## E.2 2D $\pi^+\pi^-$ Distributions

### E.2.1 $t \otimes m_{\pi\pi}$

gen. lvl. regs.	det. lvl. regs.	axis	binning
$\pi^+\pi^-$ elas.	zero-tag	$m_{\pi\pi}$ [GeV]	0.500, 0.560, 0.600, 0.630, 0.660, 0.680, 0.700, 0.720,
$\pi^+\pi^-$ pdis.	single-tag		0.740, 0.760, 0.780, 0.800, 0.820, 0.840, 0.870, 0.920,
	multi-tag		1.000, 1.200, 2.200
$\pi^+\pi^-$ elas.	zero-tag	$t$ [GeV <sup>2</sup> ]	0.000, 0.008, 0.018, 0.030, 0.044, 0.060, 0.078, 0.100,
			0.126, 0.156, 0.200, 0.280, 1.500
$\pi^+\pi^-$ pdis.	single-tag		0.000, 0.030, 0.060, 0.096, 0.140, 0.200, 0.280, 0.390,
	multi-tag		0.600, 1.500,
$\omega, \phi, \rho', \gamma$ -diss. elas. & pdis.		$m_{\pi\pi}$ [GeV]	0.3, 2.3
		$t$ [GeV <sup>2</sup> ]	0.0, 3.0

**Table E.2:** Binning scheme for unfolding the 2D  $t \otimes m_{\pi\pi}$  distributions. Not listed are the  $\pi^+\pi^-$  signal bins for not reconstructed or selected events and the overflow bins for events out of the fiducial phasepace.

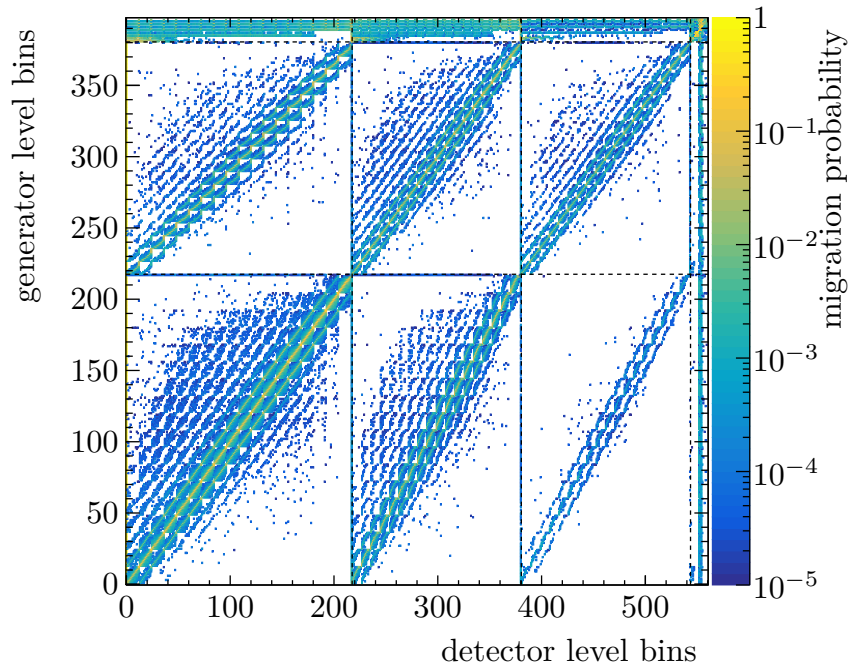


**Figure E.5:** Response matrix  $A$ .

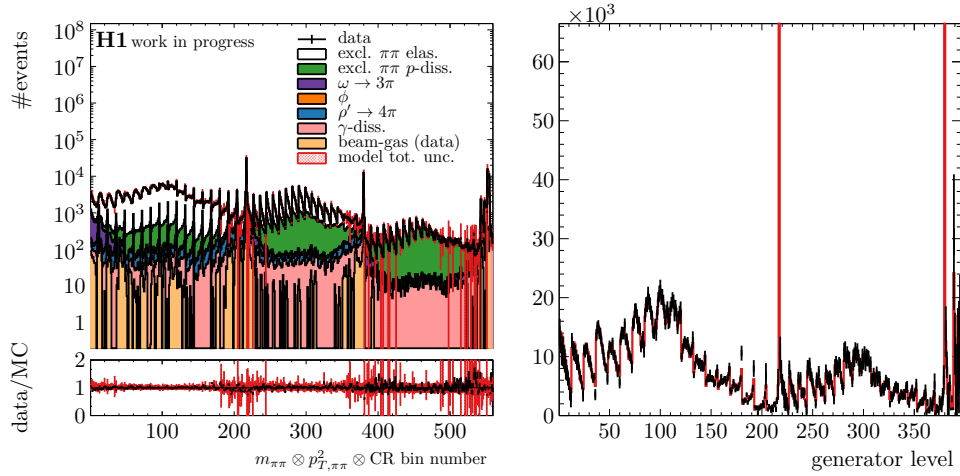


Figure E.6: Unfolding input (left) and output distribution (right).

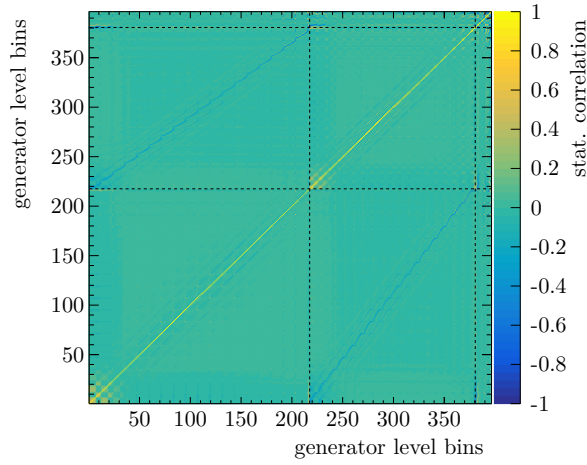


Figure E.7: Statistical covariance matrix.

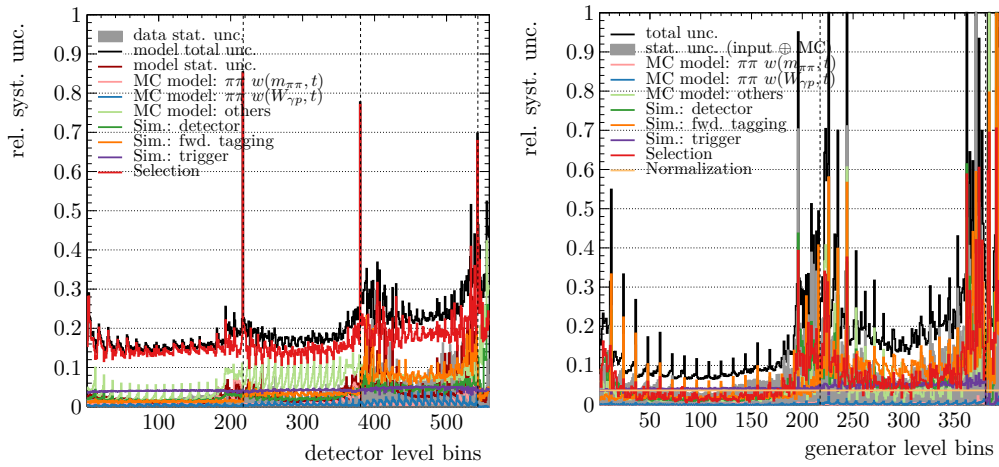
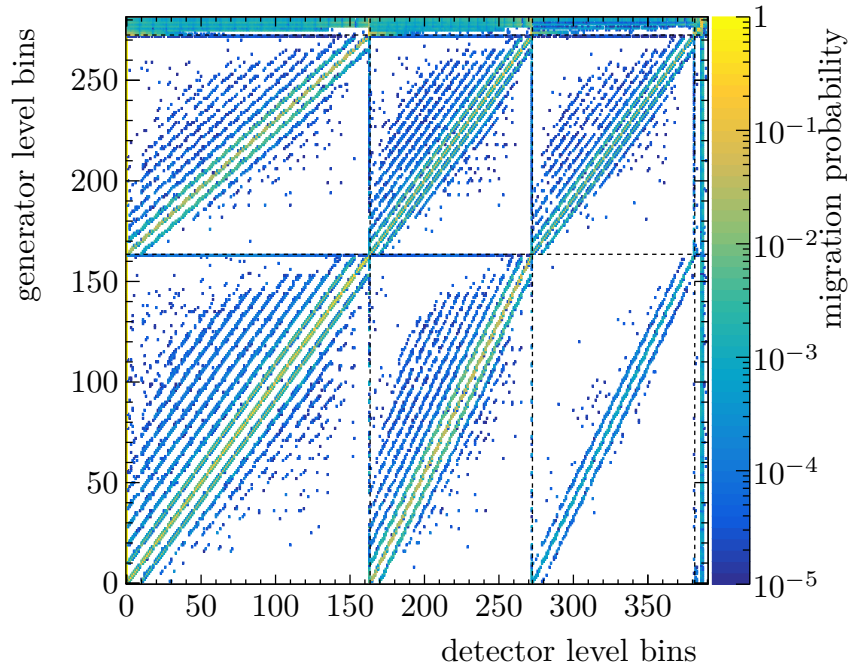


Figure E.8: Uncertainty on detector level (left) and after unfolding (right).

E.2.2  $m_{\pi\pi} \otimes W_{\gamma p}$ 

gen. lvl. regs.	det. lvl. regs.	axis	binning
$\pi^+\pi^-$ elas. pdis.	zero-tag	$m_{\pi\pi}$ [GeV]	0.500, 0.560, 0.600, 0.630, 0.660, 0.680, 0.700, 0.720,
$\pi^+\pi^-$ pdis.	single-tag		0.740, 0.760, 0.780, 0.800, 0.820, 0.840, 0.870, 0.920,
	multi-tag		1.000, 1.200, 2.200
$\pi^+\pi^-$ elas.	zero-tag	$W_{\gamma p}$ [GeV]	20, 25, 30, 35, 40, 45, 50, 56, 66, 80
$\pi^+\pi^-$ pdis.	single-tag		20, 26, 32, 38, 46, 56, 80
	multi-tag		
$\omega, \phi, \rho', \gamma$ -diss. elas. & pdis.		$m_{\pi\pi}$ [GeV]	0.3, 2.3
		$W_{\gamma p}$ [GeV]	15, 90

**Table E.3:** Binning scheme for unfolding the 2D  $m_{\pi\pi} \otimes W_{\gamma p}$  distributions. Not listed are the  $\pi^+\pi^-$  signal bins for not reconstructed or selected events and the overflow bins for events out of the fiducial phasespace.



**Figure E.9:** Response matrix  $A$ .

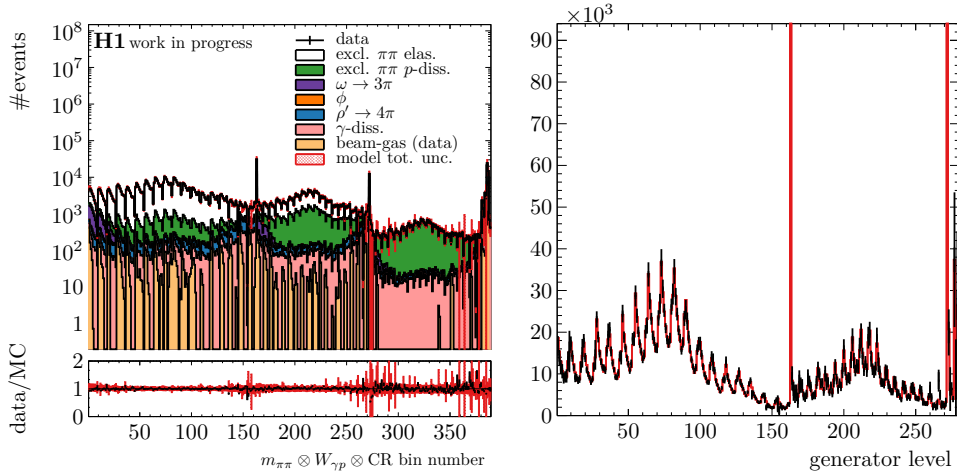


Figure E.10: Unfolding input (left) and output distribution (right).

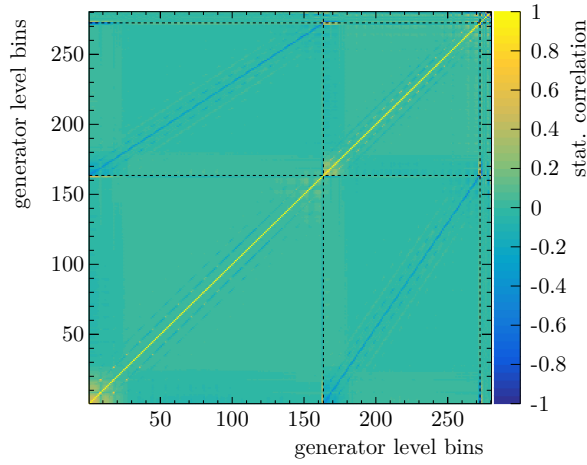


Figure E.11: Statistical covariance matrix.

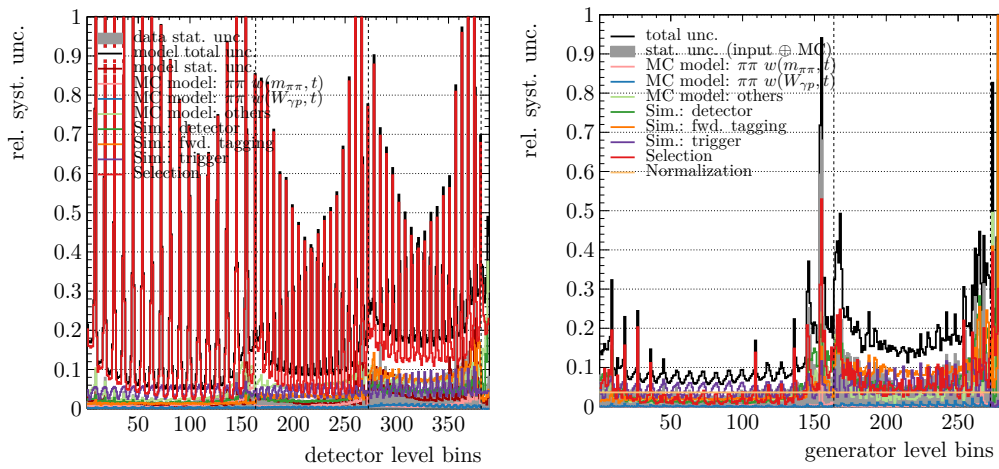


Figure E.12: Uncertainty on detector level (left) and after unfolding (right).

### E.3 3D $\pi^+\pi^-$ Distributions

#### E.3.1 $m_{\pi\pi} \otimes W_{\gamma p} \otimes t$

gen. lvl. regs.	det. lvl. regs.	axis	binning
$\pi^+\pi^-$ elas. pdis.	zero-tag	$m_{\pi\pi}$ [GeV]	0.500, 0.560, 0.600, 0.630, 0.660, 0.680, 0.700, 0.720,
$\pi^+\pi^-$ pdis.	single-tag		0.740, 0.760, 0.780, 0.800, 0.820, 0.840, 0.870, 0.920,
	multi-tag		1.000, 1.200, 2.200
		$W_{\gamma p}$ [GeV]	20, 28, 38, 50, 80
$\pi^+\pi^-$ elas.	zero-tag	$t$ [GeV <sup>2</sup> ]	0.000, 0.016, 0.036, 0.062, 0.100, 0.150, 0.230, 1.500
$\pi^+\pi^-$ pdis.	single-tag		
	multi-tag		0.000, 0.050, 0.110, 0.210, 0.400, 1.500
$\omega, \phi, \rho', \gamma$ -diss. elas. & pdis.		$m_{\pi\pi}$ [GeV]	0.3, 2.3
		$W_{\gamma p}$ [GeV]	15, 90
		$t$ [GeV <sup>2</sup> ]	0.0, 3.0

**Table E.4:** Binning scheme for unfolding the 3D  $m_{\pi\pi} \otimes W_{\gamma p} \otimes t$  distributions. Not listed are the  $\pi^+\pi^-$  signal bins for not reconstructed or selected events and the overflow bins for events out of the fiducial phasespace.

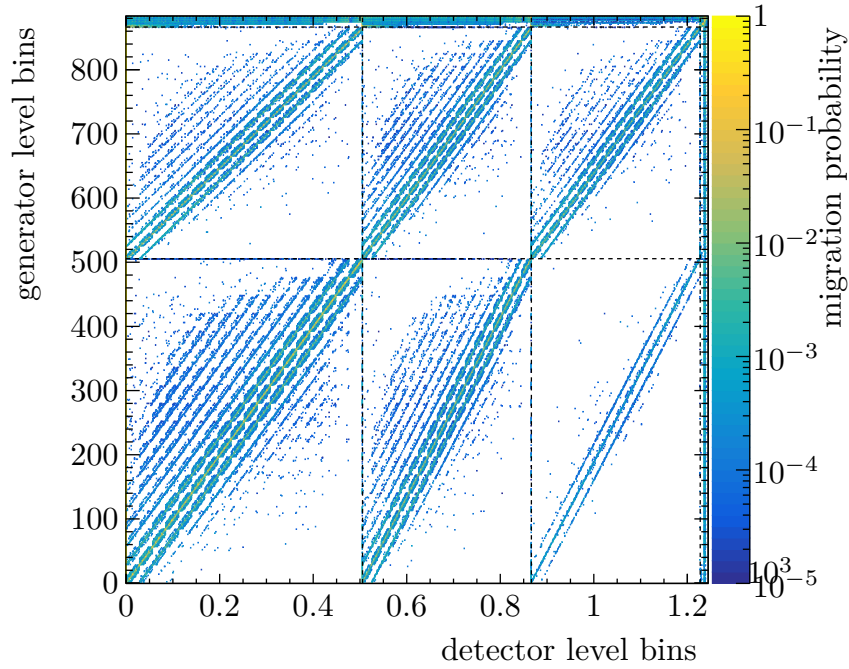


**Figure E.13:** Response matrix **A**.

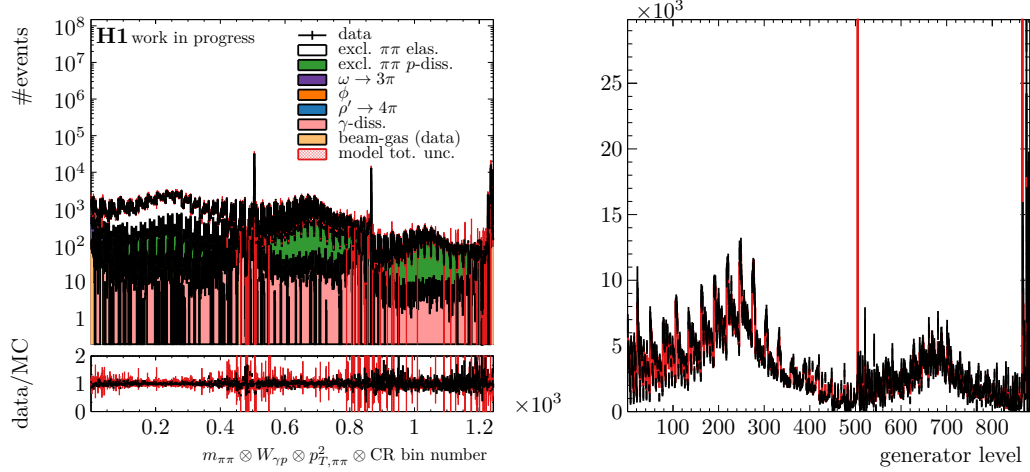


Figure E.14: Unfolding input (left) and output distribution (right).

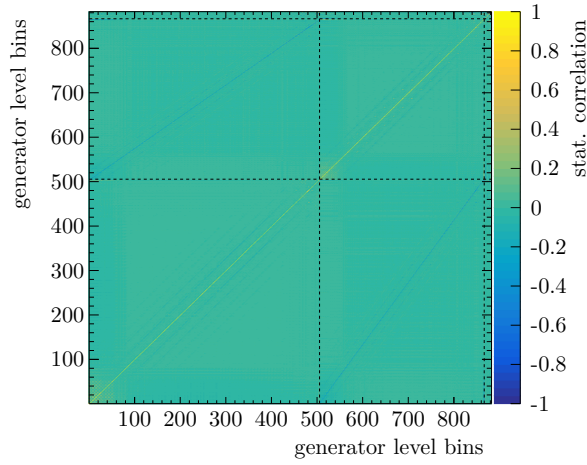


Figure E.15: Statistical covariance matrix.

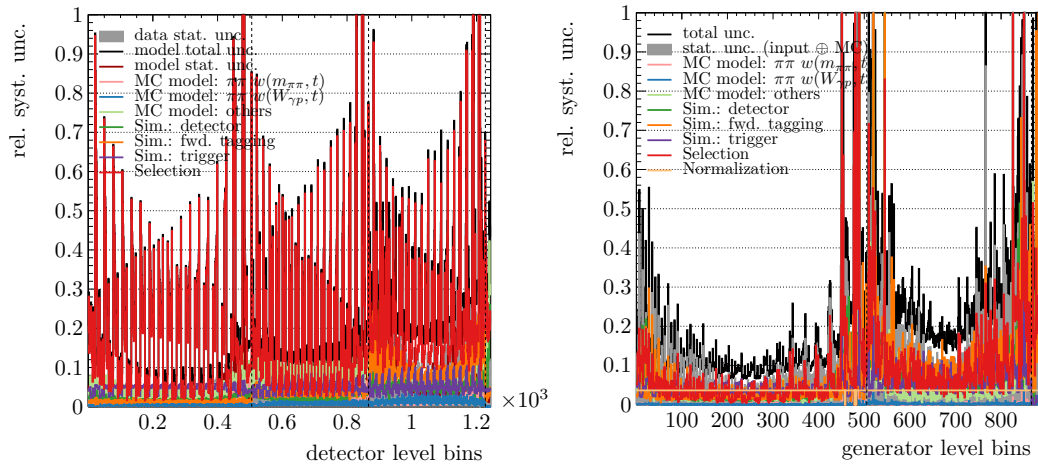


Figure E.16: Uncertainty on detector level (left) and after unfolding (right).

# F CROSS-SECTION AND RELATED TABLES

## F.1 $\pi^+\pi^-$ Cross-Sections

### F.1.1 $d\sigma(\gamma p \rightarrow \pi^+\pi^-Y)/dm_{\pi\pi}(m_{\pi\pi})$

$m_Y = m_p$		$\Phi_{\gamma/e} : 0.1271$			$m_p < m_Y < 10 \text{ GeV}$		$\Phi_{\gamma/e} : 0.1271$		
$m_{\pi\pi}$		$\frac{d\sigma_{\pi\pi}}{dm_{\pi\pi}}$	stat.	syst.	$m_{\pi\pi}$		$\frac{d\sigma_{\pi\pi}}{dm_{\pi\pi}}$	stat.	syst.
[GeV]			$[\frac{\mu\text{b}}{\text{GeV}}]$		[GeV]			$[\frac{\mu\text{b}}{\text{GeV}}]$	
0.5	0.54	9.68	0.59	+1.14 -1.34	0.5	0.54	3.29	0.53	+1.03 -1.21
0.54	0.56	11.93	0.62	+1.20 -1.29	0.54	0.56	4.38	0.64	+1.23 -1.43
0.56	0.58	14.09	0.53	+1.11 -1.20	0.56	0.58	5.09	0.52	+0.98 -1.22
0.58	0.6	16.67	0.45	+1.19 -1.25	0.58	0.6	5.62	0.52	+0.89 -1.07
0.6	0.62	19.08	0.39	+1.26 -1.24	0.6	0.62	7.06	0.43	+0.98 -1.02
0.62	0.638	23.00	0.43	+1.45 -1.45	0.62	0.638	8.86	0.52	+1.15 -1.25
0.638	0.656	27.36	0.44	+1.73 -1.68	0.638	0.656	10.18	0.51	+1.45 -1.46
0.656	0.674	32.92	0.44	+2.01 -2.07	0.656	0.674	12.37	0.54	+1.69 -1.69
0.674	0.69	39.18	0.51	+2.44 -2.46	0.674	0.69	14.41	0.58	+1.96 -1.93
0.69	0.706	46.46	0.53	+2.88 -2.90	0.69	0.706	16.92	0.60	+2.30 -2.13
0.706	0.722	53.86	0.55	+3.36 -3.32	0.706	0.722	21.29	0.61	+2.75 -2.56
0.722	0.738	60.36	0.56	+3.79 -3.76	0.722	0.738	24.44	0.64	+3.06 -2.97
0.738	0.754	64.47	0.56	+4.04 -4.00	0.738	0.754	26.16	0.63	+3.33 -3.09
0.754	0.77	64.26	0.55	+4.06 -3.98	0.754	0.77	25.76	0.63	+3.27 -3.01
0.77	0.786	54.87	0.52	+3.41 -3.44	0.77	0.786	21.66	0.58	+2.88 -2.63
0.786	0.802	38.45	0.47	+2.50 -2.53	0.786	0.802	16.79	0.56	+2.22 -2.06
0.802	0.82	30.44	0.39	+1.91 -1.93	0.802	0.82	12.90	0.47	+1.64 -1.66
0.82	0.84	22.34	0.31	+1.43 -1.45	0.82	0.84	10.31	0.40	+1.33 -1.26
0.84	0.86	15.06	0.28	+1.00 -1.03	0.84	0.86	7.34	0.39	+1.09 -1.05
0.86	0.89	10.15	0.18	+0.66 -0.70	0.86	0.89	4.67	0.25	+0.62 -0.64
0.89	0.92	6.47	0.16	+0.44 -0.47	0.89	0.92	3.56	0.23	+0.48 -0.50
0.92	0.96	4.00	0.11	+0.29 -0.30	0.92	0.96	1.88	0.17	+0.30 -0.29
0.96	1	2.279	0.099	+0.171 -0.206	0.96	1	1.13	0.16	+0.21 -0.23
1	1.05	1.467	0.077	+0.150 -0.160	1	1.05	0.70	0.11	+0.17 -0.19
1.05	1.12	0.751	0.066	+0.090 -0.130	1.05	1.12	0.477	0.088	+0.135 -0.146
1.12	1.2	0.421	0.046	+0.074 -0.089	1.12	1.2	0.405	0.063	+0.113 -0.140
1.2	1.3	0.272	0.038	+0.052 -0.087	1.2	1.3	0.263	0.049	+0.084 -0.087
1.3	1.4	0.210	0.028	+0.035 -0.047	1.3	1.4	0.110	0.046	+0.064 -0.065
1.4	1.5	0.211	0.025	+0.033 -0.044	1.4	1.5	0.168	0.035	+0.038 -0.056
1.5	1.6	0.197	0.023	+0.039 -0.030	1.5	1.6	0.211	0.024	+0.035 -0.037
1.6	1.7	0.240	0.017	+0.027 -0.033	1.6	1.7	0.148	0.025	+0.050 -0.028
1.7	1.8	0.149	0.017	+0.016 -0.014	1.7	1.9	0.065	0.019	+0.016 -0.016
1.8	1.9	0.070	0.011	+0.009 -0.017	1.9	2.2	0.020	0.013	+0.009 -0.016
1.9	2.04	0.0442	0.0069	+0.0089 -0.0105					
2.04	2.2	0.0273	0.0062	+0.0103 -0.0077					

**Table F.1:** Unfolded differential cross-section  $d\sigma(\gamma p \rightarrow \pi^+\pi^-Y)/dm_{\pi\pi}$  in bins of  $m_{\pi\pi}$ .  $ep$  cross-sections are scaled by a photon flux factor as given in the table. Splitting a normalization uncertainty from the (symmetrized) total covariance matrix according to Appendix C.3 yields  $\Delta_{\text{norm}} = 5.6\%$ . Further correlations are not provided.

F.1.2  $\sigma(\gamma p \rightarrow \pi^+\pi^-Y)(W_{\gamma p})$ 

$m_Y = m_p$						$m_p < m_Y < 10 \text{ GeV}$					
$W_{\gamma p}$		$\Phi_{\gamma/e}$	$\sigma_{\pi\pi}$	stat.	syst.	$W_{\gamma p}$		$\Phi_{\gamma/e}$	$\sigma_{\pi\pi}$	stat.	syst.
[GeV]				[ $\mu\text{b}$ ]		[GeV]				[ $\mu\text{b}$ ]	
20	21.6	0.0081	11.24	0.20	+0.92 -1.38	20	22.9	0.0142	5.15	0.20	+0.81 -0.78
21.6	22.9	0.0060	11.18	0.18	+0.90 -1.06	22.9	25.3	0.0101	5.14	0.15	+0.78 -0.78
22.9	24.1	0.0052	11.27	0.18	+0.88 -0.94	25.3	27.4	0.0080	5.34	0.16	+0.72 -0.72
24.1	25.3	0.0049	11.26	0.18	+0.84 -0.86	27.4	29.4	0.0070	5.17	0.18	+0.72 -0.72
25.3	26.4	0.0043	11.53	0.18	+0.84 -0.85	29.4	31.7	0.0074	5.26	0.16	+0.67 -0.69
26.4	27.4	0.0037	11.54	0.20	+0.83 -0.82	31.7	34.7	0.0086	5.36	0.15	+0.65 -0.69
27.4	28.4	0.0035	11.55	0.21	+0.78 -0.79	34.7	38.4	0.0095	4.91	0.13	+0.65 -0.64
28.4	29.4	0.0034	11.80	0.21	+0.78 -0.78	38.4	42.4	0.0091	5.18	0.12	+0.65 -0.64
29.4	30.5	0.0036	11.56	0.21	+0.75 -0.73	42.4	46.4	0.0081	4.96	0.12	+0.64 -0.66
30.5	31.7	0.0038	11.64	0.19	+0.71 -0.70	46.4	50.4	0.0073	4.89	0.14	+0.66 -0.66
31.7	33.1	0.0041	11.99	0.18	+0.71 -0.71	50.4	54.7	0.0070	4.71	0.14	+0.66 -0.65
33.1	34.7	0.0045	11.82	0.16	+0.67 -0.69	54.7	59.4	0.0069	4.63	0.14	+0.66 -0.65
34.7	36.5	0.0048	11.94	0.16	+0.65 -0.66	59.4	64.7	0.0070	4.42	0.15	+0.65 -0.65
36.5	38.4	0.0047	12.10	0.14	+0.65 -0.66	64.7	70.7	0.0071	4.57	0.18	+0.69 -0.71
38.4	40.4	0.0047	11.90	0.14	+0.65 -0.68	70.7	80	0.0095	4.41	0.22	+0.64 -0.65
40.4	42.4	0.0044	12.38	0.14	+0.68 -0.70						
42.4	44.4	0.0041	12.66	0.15	+0.71 -0.73						
44.4	46.4	0.0039	12.87	0.16	+0.76 -0.76						
46.4	48.4	0.0037	12.76	0.17	+0.79 -0.80						
48.4	50.4	0.0035	13.27	0.17	+0.85 -0.85						
50.4	52.5	0.0035	13.39	0.18	+0.89 -0.87						
52.5	54.7	0.0035	13.33	0.18	+0.92 -0.90						
54.7	57	0.0035	13.56	0.19	+0.95 -0.95						
57	59.4	0.0034	13.41	0.19	+0.97 -0.97						
59.4	62	0.0035	13.42	0.21	+1.00 -0.96						
62	64.7	0.0035	13.57	0.22	+1.03 -0.99						
64.7	67.7	0.0036	13.41	0.23	+1.03 -1.02						
67.7	70.7	0.0034	13.20	0.26	+1.04 -1.07						
70.7	74.4	0.0040	13.30	0.28	+1.08 -1.35						
74.4	80	0.0055	13.06	0.37	+1.17 -1.73						

**Table F.2:** Unfolded differential cross-section  $\sigma(\gamma p \rightarrow \pi^+\pi^-Y)$  in bins of  $W_{\gamma p}$ .  $ep$  cross-sections are scaled by photon flux factors as given in the table. Splitting a normalization uncertainty from the (symmetrized) total covariance matrix according to Appendix C.3 yields  $\Delta_{\text{norm}} = 4.8\%$ . Further correlations are not provided.

F.1.3  $d\sigma(\gamma p \rightarrow \pi^+\pi^-Y)/dt(t)$ 

$m_Y = m_p$		$\Phi_{\gamma/e} : 0.1271$			$m_p < m_Y < 10 \text{ GeV}$		$\Phi_{\gamma/e} : 0.1271$		
$ t $ [GeV <sup>2</sup> ]		$\frac{d\sigma_{\pi\pi}}{dt}$	stat.	syst.	$ t $ [GeV <sup>2</sup> ]		$\frac{d\sigma_{\pi\pi}}{dt}$	stat.	syst.
			$\left[\frac{\mu\text{b}}{\text{GeV}^2}\right]$					$\left[\frac{\mu\text{b}}{\text{GeV}^2}\right]$	
0	0.00012	361.8	145.3	+121.4 -98.7	0	0.0003	65.7	86.6	+35.8 -59.1
0.00012	0.0003	209.5	48.0	+46.8 -28.0	0.0003	0.0073	15.7	1.3	+2.9 -3.0
0.0003	0.0033	129.0	2.5	+8.1 -8.5	0.0073	0.0168	20.7	1.0	+3.3 -3.4
0.0033	0.0073	122.3	2.1	+7.6 -7.6	0.0168	0.0293	22.56	0.86	+3.25 -3.46
0.0073	0.0118	117.5	1.9	+7.2 -7.2	0.0293	0.0443	20.69	0.74	+3.02 -2.92
0.0118	0.0168	109.0	1.7	+6.6 -6.9	0.0443	0.0613	18.95	0.65	+2.77 -2.57
0.0168	0.0228	101.7	1.5	+6.1 -6.3	0.0613	0.0803	18.50	0.58	+2.42 -2.34
0.0228	0.0293	93.9	1.4	+5.8 -5.8	0.0803	0.1018	15.22	0.53	+2.10 -2.08
0.0293	0.0363	88.2	1.3	+5.4 -5.4	0.1018	0.1263	12.78	0.48	+1.80 -1.83
0.0363	0.0443	81.5	1.2	+4.9 -5.0	0.1263	0.1533	10.59	0.41	+1.56 -1.44
0.0443	0.0523	74.5	1.1	+4.6 -4.6	0.1533	0.1828	9.95	0.38	+1.29 -1.40
0.0523	0.0613	67.10	1.00	+4.10 -4.29	0.1828	0.2213	7.89	0.33	+1.11 -1.14
0.0613	0.0703	59.60	0.98	+3.72 -3.74	0.2213	0.2788	6.35	0.22	+0.87 -0.86
0.0703	0.0803	53.87	0.86	+3.38 -3.46	0.2788	0.3853	4.57	0.15	+0.65 -0.64
0.0803	0.0908	50.15	0.82	+3.06 -3.04	0.3853	1.5	0.926	0.033	+0.112 -0.119
0.0908	0.1018	42.62	0.77	+2.69 -2.91					
0.1018	0.1138	40.08	0.70	+2.46 -2.61					
0.1138	0.1263	34.13	0.67	+2.17 -2.17					
0.1263	0.1393	31.73	0.62	+1.96 -2.05					
0.1393	0.1533	27.29	0.57	+1.71 -1.82					
0.1533	0.1673	22.26	0.55	+1.49 -1.47					
0.1673	0.1828	20.66	0.49	+1.33 -1.33					
0.1828	0.2003	17.01	0.44	+1.20 -1.16					
0.2003	0.2213	14.84	0.36	+1.00 -1.03					
0.2213	0.2468	11.67	0.30	+0.81 -0.89					
0.2468	0.2788	9.48	0.24	+0.64 -0.69					
0.2788	0.3223	6.52	0.17	+0.47 -0.48					
0.3223	0.3853	4.15	0.15	+0.41 -0.42					
0.3853	0.4998	1.90	0.11	+0.30 -0.30					
0.4998	1.5	0.104	0.024	+0.075 -0.083					

**Table F.3:** Unfolded differential cross-section  $d\sigma(\gamma p \rightarrow \pi^+\pi^-Y)/dt$  in bins of  $t$ .  $ep$  cross-sections are scaled by a photon flux factor as given in the table. Splitting a normalization uncertainty from the (symmetrized) total covariance matrix according to Appendix C.3 yields  $\Delta_{\text{norm}} = 5.4\%$ . Further correlations are not provided.

F.1.4  $d\sigma(\gamma p \rightarrow \pi^+\pi^-Y)/dm_{\pi\pi}(m_{\pi\pi}, W_{\gamma p})$ 

multipage set of tables; common caption Table F.4

$m_Y = m_p$ $\Phi_{\gamma/e} : 0.0231$				$m_Y = m_p$ $\Phi_{\gamma/e} : 0.0182$					
$20 < W_{\gamma p} [\text{GeV}] < 25$				$25 < W_{\gamma p} [\text{GeV}] < 30$					
$m_{\pi\pi}$ [GeV]	$\frac{d\sigma_{\pi\pi}}{dm_{\pi\pi}}$	stat. [ $\frac{\mu\text{b}}{\text{GeV}}$ ]	syst.	$m_{\pi\pi}$ [GeV]	$\frac{d\sigma_{\pi\pi}}{dm_{\pi\pi}}$	stat. [ $\frac{\mu\text{b}}{\text{GeV}}$ ]	syst.		
0.5	0.56	9.04	0.73	+0.98 -1.18	0.5	0.56	9.54	0.66	+1.01 -1.21
0.56	0.6	14.02	0.66	+1.18 -1.34	0.56	0.6	14.72	0.67	+1.21 -1.29
0.6	0.63	19.38	0.80	+1.55 -1.74	0.6	0.63	19.13	0.67	+1.32 -1.31
0.63	0.66	24.95	0.83	+1.97 -1.92	0.63	0.66	25.93	0.69	+1.71 -1.63
0.66	0.68	33.3	1.1	+2.6 -3.3	0.66	0.68	31.7	1.1	+2.2 -2.2
0.68	0.7	39.7	1.2	+3.1 -3.6	0.68	0.7	38.8	1.1	+2.7 -2.6
0.7	0.72	46.5	1.2	+3.9 -4.2	0.7	0.72	49.4	1.1	+3.4 -3.4
0.72	0.74	54.9	1.2	+4.4 -5.1	0.72	0.74	56.6	1.2	+3.9 -3.9
0.74	0.76	59.4	1.2	+4.8 -6.2	0.74	0.76	62.7	1.2	+4.4 -4.4
0.76	0.78	56.1	1.2	+4.5 -5.3	0.76	0.78	58.9	1.1	+4.2 -4.1
0.78	0.8	36.7	1.2	+3.3 -3.4	0.78	0.8	38.9	1.0	+3.1 -3.0
0.8	0.82	28.0	1.1	+2.2 -2.9	0.8	0.82	30.11	0.94	+2.16 -2.29
0.82	0.84	20.7	1.0	+1.8 -4.5	0.82	0.84	22.23	0.90	+1.64 -1.69
0.84	0.87	13.86	0.66	+1.31 -1.47	0.84	0.87	12.89	0.56	+1.04 -1.10
0.87	0.92	6.75	0.36	+0.58 -0.82	0.87	0.92	6.61	0.32	+0.63 -0.56
0.92	1	2.02	0.25	+0.37 -0.39	0.92	1	2.76	0.18	+0.25 -0.36
1	1.2	0.69	0.11	+0.12 -0.23	1	1.2	0.40	0.10	+0.10 -0.12
1.2	2.2	0.092	0.054	+0.025 -0.045	1.2	2.2	0.048	0.033	+0.025 -0.040

$m_Y = m_p$ $\Phi_{\gamma/e} : 0.0149$				$m_Y = m_p$ $\Phi_{\gamma/e} : 0.0125$					
$30 < W_{\gamma p} [\text{GeV}] < 35$				$35 < W_{\gamma p} [\text{GeV}] < 40$					
$m_{\pi\pi}$ [GeV]	$\frac{d\sigma_{\pi\pi}}{dm_{\pi\pi}}$	stat. [ $\frac{\mu\text{b}}{\text{GeV}}$ ]	syst.	$m_{\pi\pi}$ [GeV]	$\frac{d\sigma_{\pi\pi}}{dm_{\pi\pi}}$	stat. [ $\frac{\mu\text{b}}{\text{GeV}}$ ]	syst.		
0.5	0.56	9.82	0.74	+1.14 -1.33	0.5	0.56	10.68	0.80	+1.46 -1.60
0.56	0.6	14.60	0.64	+0.94 -1.04	0.56	0.6	13.77	0.84	+1.47 -1.52
0.6	0.63	18.57	0.71	+1.08 -1.12	0.6	0.63	20.01	0.74	+1.20 -1.18
0.63	0.66	25.10	0.73	+1.46 -1.44	0.63	0.66	25.91	0.82	+1.42 -1.42
0.66	0.68	31.9	1.0	+1.8 -1.8	0.66	0.68	33.1	1.1	+1.7 -1.7
0.68	0.7	40.9	1.1	+2.3 -2.3	0.68	0.7	41.5	1.2	+2.2 -2.2
0.7	0.72	50.8	1.2	+3.0 -2.9	0.7	0.72	52.0	1.3	+2.7 -2.8
0.72	0.74	58.7	1.3	+3.4 -3.4	0.72	0.74	57.8	1.3	+3.0 -3.1
0.74	0.76	63.8	1.2	+3.8 -3.8	0.74	0.76	63.1	1.3	+3.3 -3.4
0.76	0.78	61.5	1.2	+3.6 -3.7	0.76	0.78	61.5	1.4	+3.3 -3.3
0.78	0.8	40.2	1.1	+2.5 -2.4	0.78	0.8	40.3	1.1	+2.2 -2.3
0.8	0.82	29.62	0.96	+1.89 -1.85	0.8	0.82	29.6	1.0	+1.7 -1.7
0.82	0.84	21.11	0.80	+1.41 -1.37	0.82	0.84	22.11	0.81	+1.26 -1.33
0.84	0.87	13.83	0.60	+0.90 -0.93	0.84	0.87	14.28	0.51	+0.79 -0.82
0.87	0.92	7.33	0.33	+0.54 -0.56	0.87	0.92	7.72	0.30	+0.46 -0.49
0.92	1	2.91	0.18	+0.25 -0.26	0.92	1	3.05	0.13	+0.22 -0.27
1	1.2	0.61	0.11	+0.09 -0.16	1	1.2	0.673	0.080	+0.096 -0.146
1.2	2.2	0.121	0.028	+0.022 -0.033	1.2	2.2	0.111	0.023	+0.023 -0.036

## F. CROSS-SECTION AND RELATED TABLES

$m_Y = m_p$ $\Phi_{\gamma/e} : 0.0107$				$m_Y = m_p$ $\Phi_{\gamma/e} : 0.0093$			
$40 < W_{\gamma p} [\text{GeV}] < 45$				$45 < W_{\gamma p} [\text{GeV}] < 50$			
$m_{\pi\pi}$ [GeV]	$\frac{d\sigma_{\pi\pi}}{dm_{\pi\pi}}$	stat. [ $\frac{\mu\text{b}}{\text{GeV}}$ ]	syst.	$m_{\pi\pi}$ [GeV]	$\frac{d\sigma_{\pi\pi}}{dm_{\pi\pi}}$	stat. [ $\frac{\mu\text{b}}{\text{GeV}}$ ]	syst.
0.5 0.56	10.57	0.82	+1.24 -1.45	0.5 0.56	12.48	0.95	+1.43 -1.77
0.56 0.6	15.95	0.84	+1.28 -1.38	0.56 0.6	16.98	0.96	+1.35 -1.53
0.6 0.63	21.35	0.89	+1.33 -1.39	0.6 0.63	21.5	1.0	+1.5 -1.4
0.63 0.66	27.20	0.95	+1.61 -1.66	0.63 0.66	30.8	1.1	+2.0 -2.0
0.66 0.68	32.6	1.3	+1.9 -1.9	0.66 0.68	37.0	1.5	+2.5 -2.3
0.68 0.7	43.4	1.3	+2.4 -2.5	0.68 0.7	43.6	1.6	+2.8 -2.7
0.7 0.72	54.0	1.4	+3.0 -3.0	0.7 0.72	54.5	1.6	+3.4 -3.5
0.72 0.74	62.7	1.6	+3.5 -3.5	0.72 0.74	65.2	1.7	+4.1 -4.0
0.74 0.76	64.1	1.5	+3.5 -3.5	0.74 0.76	69.9	1.7	+4.2 -4.2
0.76 0.78	65.3	1.4	+3.4 -3.5	0.76 0.78	63.2	1.7	+3.8 -3.9
0.78 0.8	41.4	1.3	+2.3 -2.3	0.78 0.8	43.2	1.5	+2.6 -2.6
0.8 0.82	32.1	1.2	+1.8 -1.8	0.8 0.82	32.3	1.2	+2.0 -2.0
0.82 0.84	22.80	0.90	+1.28 -1.40	0.82 0.84	22.93	1.00	+1.38 -1.35
0.84 0.87	14.96	0.54	+0.83 -0.85	0.84 0.87	15.07	0.59	+0.90 -0.91
0.87 0.92	7.73	0.32	+0.47 -0.52	0.87 0.92	7.63	0.33	+0.48 -0.56
0.92 1	2.97	0.17	+0.21 -0.27	0.92 1	3.10	0.15	+0.23 -0.31
1 1.2	0.705	0.060	+0.100 -0.137	1 1.2	0.754	0.080	+0.120 -0.164
1.2 2.2	0.142	0.012	+0.023 -0.030	1.2 2.2	0.133	0.013	+0.026 -0.030

$m_Y = m_p$ $\Phi_{\gamma/e} : 0.0097$				$m_Y = m_p$ $\Phi_{\gamma/e} : 0.0135$			
$50 < W_{\gamma p} [\text{GeV}] < 56$				$56 < W_{\gamma p} [\text{GeV}] < 66$			
$m_{\pi\pi}$ [GeV]	$\frac{d\sigma_{\pi\pi}}{dm_{\pi\pi}}$	stat. [ $\frac{\mu\text{b}}{\text{GeV}}$ ]	syst.	$m_{\pi\pi}$ [GeV]	$\frac{d\sigma_{\pi\pi}}{dm_{\pi\pi}}$	stat. [ $\frac{\mu\text{b}}{\text{GeV}}$ ]	syst.
0.5 0.56	12.25	0.96	+1.76 -1.90	0.5 0.56	12.1	1.0	+1.7 -2.2
0.56 0.6	16.90	0.97	+1.48 -1.47	0.56 0.6	16.2	1.0	+1.5 -1.7
0.6 0.63	22.6	1.1	+1.7 -1.7	0.6 0.63	21.5	1.1	+1.8 -1.7
0.63 0.66	28.0	1.0	+2.2 -2.0	0.63 0.66	28.7	1.1	+2.4 -2.2
0.66 0.68	39.7	1.6	+2.7 -3.4	0.66 0.68	39.3	1.6	+3.0 -2.9
0.68 0.7	48.1	1.8	+3.5 -3.2	0.68 0.7	50.8	1.6	+3.8 -3.7
0.7 0.72	56.7	1.7	+3.9 -4.3	0.7 0.72	55.7	1.6	+4.3 -4.0
0.72 0.74	62.7	1.9	+4.6 -4.4	0.72 0.74	64.9	1.6	+4.9 -4.9
0.74 0.76	71.8	1.9	+4.8 -4.6	0.74 0.76	72.4	1.7	+5.2 -5.0
0.76 0.78	67.8	1.7	+4.6 -4.4	0.76 0.78	64.6	1.5	+5.0 -4.6
0.78 0.8	44.6	1.5	+3.0 -3.1	0.78 0.8	43.8	1.4	+3.1 -3.4
0.8 0.82	30.9	1.3	+2.1 -2.0	0.8 0.82	33.0	1.2	+2.5 -2.4
0.82 0.84	25.6	1.1	+1.6 -1.7	0.82 0.84	23.8	1.1	+1.8 -1.7
0.84 0.87	14.57	0.67	+1.07 -1.11	0.84 0.87	14.96	0.60	+1.11 -1.09
0.87 0.92	8.67	0.36	+0.58 -0.61	0.87 0.92	8.41	0.30	+0.62 -0.65
0.92 1	3.26	0.17	+0.25 -0.32	0.92 1	3.21	0.15	+0.31 -0.34
1 1.2	0.765	0.066	+0.130 -0.162	1 1.2	0.905	0.053	+0.134 -0.151
1.2 2.2	0.155	0.013	+0.027 -0.031	1.2 2.2	0.1493	0.0097	+0.0267 -0.0294

F.1.  $\pi^+\pi^-$  CROSS-SECTIONS

$m_Y = m_p$ $\Phi_{\gamma/e} : 0.0150$				$m_p < m_Y < 10 \text{ GeV}$ $\Phi_{\gamma/e} : 0.0271$					
$66 < W_{\gamma p} [\text{GeV}] < 80$				$20 < W_{\gamma p} [\text{GeV}] < 26$					
$m_{\pi\pi}$ [GeV]		$\frac{d\sigma_{\pi\pi}}{dm_{\pi\pi}}$	stat. [ $\frac{\mu\text{b}}{\text{GeV}}$ ]	syst.	$m_{\pi\pi}$ [GeV]		$\frac{d\sigma_{\pi\pi}}{dm_{\pi\pi}}$	stat. [ $\frac{\mu\text{b}}{\text{GeV}}$ ]	syst.
0.5	0.56	12.8	2.0	+2.4 -4.6	0.5	0.56	4.12	0.70	+1.13 -1.20
0.56	0.6	18.7	1.9	+2.3 -6.0	0.56	0.6	5.06	0.73	+1.06 -1.04
0.6	0.63	24.3	2.2	+3.6 -7.6	0.6	0.63	7.41	0.77	+1.18 -1.23
0.63	0.66	32.1	1.8	+2.5 -7.1	0.63	0.66	10.15	0.90	+1.53 -1.55
0.66	0.68	34.9	2.4	+3.5 -3.5	0.66	0.68	11.2	1.3	+2.6 -2.2
0.68	0.7	46.1	2.2	+3.6 -3.7	0.68	0.7	16.1	1.2	+2.5 -2.3
0.7	0.72	54.0	2.2	+4.4 -4.4	0.7	0.72	22.1	1.3	+3.1 -3.0
0.72	0.74	67.0	2.2	+5.3 -6.1	0.72	0.74	25.2	1.3	+3.6 -3.6
0.74	0.76	72.9	2.1	+5.7 -6.5	0.74	0.76	26.6	1.3	+3.9 -3.8
0.76	0.78	63.6	2.0	+5.7 -5.3	0.76	0.78	27.2	1.3	+3.8 -3.7
0.78	0.8	43.1	1.8	+3.5 -3.8	0.78	0.8	17.7	1.3	+3.2 -2.9
0.8	0.82	35.3	1.6	+2.6 -3.1	0.8	0.82	14.2	1.2	+2.3 -2.1
0.82	0.84	21.7	1.3	+2.4 -1.9	0.82	0.84	10.8	1.1	+2.0 -2.0
0.84	0.87	14.91	0.80	+1.17 -1.24	0.84	0.87	6.20	0.82	+1.28 -1.23
0.87	0.92	8.39	0.37	+0.68 -0.70	0.87	0.92	3.62	0.49	+0.73 -0.67
0.92	1	3.08	0.19	+0.31 -0.37	0.92	1	1.88	0.28	+0.38 -0.64
1	1.2	0.937	0.058	+0.119 -0.175	1	1.2	0.86	0.15	+0.17 -0.28
1.2	2.2	0.1346	0.0100	+0.0262 -0.0330	1.2	2.2	0.232	0.056	+0.043 -0.052

$m_p < m_Y < 10 \text{ GeV}$ $\Phi_{\gamma/e} : 0.0205$				$m_p < m_Y < 10 \text{ GeV}$ $\Phi_{\gamma/e} : 0.0163$					
$26 < W_{\gamma p} [\text{GeV}] < 32$				$32 < W_{\gamma p} [\text{GeV}] < 38$					
$m_{\pi\pi}$ [GeV]		$\frac{d\sigma_{\pi\pi}}{dm_{\pi\pi}}$	stat. [ $\frac{\mu\text{b}}{\text{GeV}}$ ]	syst.	$m_{\pi\pi}$ [GeV]		$\frac{d\sigma_{\pi\pi}}{dm_{\pi\pi}}$	stat. [ $\frac{\mu\text{b}}{\text{GeV}}$ ]	syst.
0.5	0.56	3.56	0.70	+1.21 -1.28	0.5	0.56	4.01	0.82	+1.29 -1.83
0.56	0.6	6.51	0.76	+1.19 -1.41	0.56	0.6	5.43	0.70	+0.96 -1.20
0.6	0.63	8.35	0.80	+1.49 -1.18	0.6	0.63	7.11	0.89	+1.09 -1.22
0.63	0.66	12.12	0.79	+1.48 -1.51	0.63	0.66	11.89	0.88	+1.56 -1.79
0.66	0.68	14.6	1.2	+1.9 -1.9	0.66	0.68	12.9	1.1	+1.7 -1.7
0.68	0.7	16.0	1.1	+2.1 -2.1	0.68	0.7	14.5	1.2	+2.1 -2.0
0.7	0.72	20.3	1.2	+2.6 -2.6	0.7	0.72	19.8	1.4	+2.8 -2.7
0.72	0.74	24.1	1.3	+3.3 -3.1	0.72	0.74	24.9	1.3	+3.1 -2.8
0.74	0.76	26.0	1.2	+3.8 -3.4	0.74	0.76	25.4	1.3	+3.5 -3.1
0.76	0.78	24.9	1.2	+3.4 -3.3	0.76	0.78	25.6	1.3	+3.2 -2.8
0.78	0.8	19.1	1.1	+2.6 -2.5	0.78	0.8	18.4	1.3	+2.3 -2.2
0.8	0.82	13.80	0.99	+1.91 -1.84	0.8	0.82	15.1	1.1	+1.9 -2.1
0.82	0.84	9.88	1.00	+1.72 -1.77	0.82	0.84	12.7	1.1	+1.5 -1.5
0.84	0.87	7.72	0.67	+1.20 -1.09	0.84	0.87	6.65	0.74	+0.93 -0.96
0.87	0.92	4.34	0.39	+0.60 -0.65	0.87	0.92	4.00	0.46	+0.56 -0.56
0.92	1	1.52	0.30	+0.31 -0.32	0.92	1	1.72	0.19	+0.29 -0.32
1	1.2	0.79	0.11	+0.15 -0.19	1	1.2	0.49	0.14	+0.15 -0.15
1.2	2.2	0.182	0.024	+0.032 -0.042	1.2	2.2	0.118	0.037	+0.032 -0.039

## F. CROSS-SECTION AND RELATED TABLES

$m_p < m_Y < 10 \text{ GeV}$				$m_p < m_Y < 10 \text{ GeV}$					
$\Phi_{\gamma/e} : 0.0174$				$\Phi_{\gamma/e} : 0.0171$					
$38 < W_{\gamma p} [\text{GeV}] < 46$				$46 < W_{\gamma p} [\text{GeV}] < 56$					
$m_{\pi\pi}$		$\frac{d\sigma_{\pi\pi}}{dm_{\pi\pi}}$	stat.	syst.	$m_{\pi\pi}$		$\frac{d\sigma_{\pi\pi}}{dm_{\pi\pi}}$	stat.	syst.
[GeV]			$[\frac{\mu\text{b}}{\text{GeV}}]$		[GeV]			$[\frac{\mu\text{b}}{\text{GeV}}]$	
0.5	0.56	3.92	0.73	+1.23 -1.37	0.5	0.56	2.68	0.64	+1.13 -1.23
0.56	0.6	4.74	0.65	+0.92 -1.22	0.56	0.6	5.58	0.75	+1.01 -1.03
0.6	0.63	6.96	0.73	+1.01 -1.22	0.6	0.63	7.34	0.92	+1.25 -1.57
0.63	0.66	11.29	0.79	+1.45 -1.43	0.63	0.66	8.52	0.75	+1.39 -1.37
0.66	0.68	15.3	1.3	+2.0 -2.0	0.66	0.68	12.0	1.3	+2.0 -2.0
0.68	0.7	16.8	1.3	+2.2 -2.1	0.68	0.7	15.4	1.3	+2.0 -2.2
0.7	0.72	19.7	1.2	+2.7 -2.4	0.7	0.72	19.6	1.3	+3.0 -2.5
0.72	0.74	25.8	1.3	+3.2 -3.4	0.72	0.74	25.9	1.5	+3.4 -3.3
0.74	0.76	27.7	1.3	+3.1 -2.8	0.74	0.76	24.0	1.3	+3.6 -3.1
0.76	0.78	22.6	1.2	+3.0 -2.8	0.76	0.78	24.8	1.3	+3.7 -3.1
0.78	0.8	17.0	1.1	+2.0 -2.0	0.78	0.8	16.9	1.1	+2.5 -2.2
0.8	0.82	12.39	0.94	+1.63 -1.64	0.8	0.82	12.5	1.0	+1.5 -1.7
0.82	0.84	9.89	0.86	+1.78 -1.31	0.82	0.84	8.45	0.89	+1.29 -1.08
0.84	0.87	6.71	0.62	+0.86 -0.88	0.84	0.87	6.32	0.65	+0.93 -1.05
0.87	0.92	3.55	0.29	+0.47 -0.52	0.87	0.92	3.54	0.29	+0.54 -0.51
0.92	1	1.56	0.19	+0.24 -0.27	0.92	1	1.59	0.17	+0.29 -0.31
1	1.2	0.547	0.072	+0.110 -0.147	1	1.2	0.438	0.064	+0.154 -0.164
1.2	2.2	0.116	0.018	+0.032 -0.032	1.2	2.2	0.101	0.014	+0.033 -0.036

$m_p < m_Y < 10 \text{ GeV}$				
$\Phi_{\gamma/e} : 0.0286$				
$56 < W_{\gamma p} [\text{GeV}] < 80$				
$m_{\pi\pi}$		$\frac{d\sigma_{\pi\pi}}{dm_{\pi\pi}}$	stat.	syst.
[GeV]			$[\frac{\mu\text{b}}{\text{GeV}}]$	
0.5	0.56	3.52	0.78	+0.87 -1.08
0.56	0.6	5.94	0.75	+0.98 -1.32
0.6	0.63	6.99	0.81	+1.12 -1.08
0.63	0.66	8.81	0.77	+1.68 -1.33
0.66	0.68	11.0	1.1	+1.8 -1.9
0.68	0.7	14.2	1.1	+1.9 -2.4
0.7	0.72	17.6	1.1	+2.5 -2.2
0.72	0.74	21.3	1.1	+3.3 -2.8
0.74	0.76	24.5	1.2	+3.3 -3.2
0.76	0.78	24.5	1.2	+3.1 -2.9
0.78	0.8	13.55	0.96	+2.73 -2.11
0.8	0.82	10.53	0.94	+1.82 -1.76
0.82	0.84	9.55	0.90	+1.49 -1.22
0.84	0.87	5.82	0.51	+0.95 -0.94
0.87	0.92	3.31	0.27	+0.51 -0.56
0.92	1	1.50	0.13	+0.24 -0.24
1	1.2	0.346	0.050	+0.136 -0.160
1.2	2.2	0.084	0.012	+0.025 -0.027

**Table F.4:** Unfolded differential cross-section  $d\sigma(\gamma p \rightarrow \pi^+ \pi^- Y)/dm_{\pi\pi}$  in bins of  $m_{\pi\pi}$  and  $W_{\gamma p}$ .  $ep$  cross-sections are scaled by a  $W_{\gamma p}$  dependent photon flux factor as given in the tables. Splitting a normalization uncertainty from the (symmetrized) total covariance matrix according to Appendix C.3 yields  $\Delta_{\text{norm}} = 4.3\%$ . Further correlations are not provided.

F.1.5  $d^2\sigma(\gamma p \rightarrow \pi^+\pi^-Y)/dm_{\pi\pi}dt(m_{\pi\pi}, t)$ 

multipage set of tables; common caption Table F.5

$m_Y = m_p$ $\Phi_{\gamma/e} : 0.1271$				$m_Y = m_p$ $\Phi_{\gamma/e} : 0.1271$					
$0 <  t  [\text{GeV}^2] < 0.008$				$0.008 <  t  [\text{GeV}^2] < 0.018$					
$m_{\pi\pi}$ [GeV]		$\frac{d^2\sigma_{\pi\pi}}{dt dm_{\pi\pi}}$ [ $\frac{\mu\text{b}}{\text{GeV}^3}$ ]	stat.	syst.	$m_{\pi\pi}$ [GeV]		$\frac{d^2\sigma_{\pi\pi}}{dt dm_{\pi\pi}}$ [ $\frac{\mu\text{b}}{\text{GeV}^3}$ ]	stat.	syst.
0.5	0.56	173.3	13.2	+26.0 -25.5	0.5	0.56	123.0	10.5	+13.8 -18.3
0.56	0.6	235.1	12.0	+19.2 -21.6	0.56	0.6	168.3	10.4	+15.1 -15.8
0.6	0.63	273.3	12.8	+20.1 -19.2	0.6	0.63	211.5	11.1	+14.5 -13.8
0.63	0.66	336.7	12.6	+21.0 -21.0	0.63	0.66	292.9	10.5	+18.5 -17.8
0.66	0.68	381.8	18.4	+23.6 -25.6	0.66	0.68	348.9	15.3	+22.3 -21.5
0.68	0.7	477.0	20.0	+29.8 -30.8	0.68	0.7	415.1	15.4	+25.9 -26.9
0.7	0.72	568.6	19.7	+33.7 -34.7	0.7	0.72	468.4	15.9	+28.4 -30.1
0.72	0.74	630.0	20.4	+39.3 -37.3	0.72	0.74	555.4	16.3	+33.4 -32.7
0.74	0.76	641.3	19.9	+43.6 -38.8	0.74	0.76	579.4	16.3	+35.3 -34.4
0.76	0.78	591.8	18.9	+39.2 -36.8	0.76	0.78	535.5	14.8	+33.1 -33.8
0.78	0.8	364.7	16.1	+23.0 -26.2	0.78	0.8	335.0	13.4	+22.0 -24.3
0.8	0.82	255.6	13.0	+17.9 -17.1	0.8	0.82	250.6	12.3	+15.9 -15.9
0.82	0.84	209.4	12.8	+13.8 -15.6	0.82	0.84	182.0	10.2	+11.1 -11.0
0.84	0.87	126.6	7.3	+8.3 -9.1	0.84	0.87	104.4	6.4	+6.6 -7.4
0.87	0.92	64.8	3.6	+5.1 -4.7	0.87	0.92	47.2	3.1	+3.3 -3.7
0.92	1	24.1	1.6	+1.7 -2.5	0.92	1	16.3	2.0	+1.7 -1.8
1	1.2	5.53	0.67	+0.76 -1.10	1	1.2	3.87	0.64	+0.51 -1.02
1.2	2.2	1.63	0.16	+0.24 -0.33	1.2	2.2	0.61	0.14	+0.18 -0.13

$m_Y = m_p$ $\Phi_{\gamma/e} : 0.1271$				$m_Y = m_p$ $\Phi_{\gamma/e} : 0.1271$					
$0.018 <  t  [\text{GeV}^2] < 0.03$				$0.03 <  t  [\text{GeV}^2] < 0.044$					
$m_{\pi\pi}$ [GeV]		$\frac{d^2\sigma_{\pi\pi}}{dt dm_{\pi\pi}}$ [ $\frac{\mu\text{b}}{\text{GeV}^3}$ ]	stat.	syst.	$m_{\pi\pi}$ [GeV]		$\frac{d^2\sigma_{\pi\pi}}{dt dm_{\pi\pi}}$ [ $\frac{\mu\text{b}}{\text{GeV}^3}$ ]	stat.	syst.
0.5	0.56	86.4	8.4	+13.1 -16.0	0.5	0.56	76.6	7.5	+15.2 -17.6
0.56	0.6	133.1	8.5	+15.8 -16.0	0.56	0.6	111.7	7.3	+12.8 -13.8
0.6	0.63	186.6	9.1	+11.8 -12.1	0.6	0.63	158.7	7.6	+10.8 -11.7
0.63	0.66	248.0	8.9	+15.2 -15.2	0.63	0.66	197.9	7.6	+13.4 -12.1
0.66	0.68	283.8	12.6	+17.8 -18.0	0.66	0.68	235.1	10.3	+15.1 -16.4
0.68	0.7	342.9	13.0	+20.8 -23.7	0.68	0.7	294.9	10.9	+18.0 -18.4
0.7	0.72	438.3	13.3	+26.3 -26.4	0.7	0.72	376.3	11.5	+22.8 -22.7
0.72	0.74	463.5	13.3	+29.5 -28.8	0.72	0.74	432.2	11.5	+26.6 -27.5
0.74	0.76	508.5	13.2	+31.5 -30.2	0.74	0.76	455.5	11.3	+29.5 -27.5
0.76	0.78	464.1	12.7	+28.6 -28.5	0.76	0.78	413.4	11.0	+25.7 -26.0
0.78	0.8	299.3	11.3	+18.9 -19.0	0.78	0.8	263.9	9.9	+17.1 -20.1
0.8	0.82	234.2	10.2	+15.4 -14.6	0.8	0.82	205.7	8.7	+12.3 -12.4
0.82	0.84	161.0	8.7	+10.0 -10.5	0.82	0.84	131.8	8.1	+8.9 -8.5
0.84	0.87	91.7	5.3	+6.0 -6.0	0.84	0.87	91.4	5.3	+5.7 -6.7
0.87	0.92	48.3	2.8	+3.5 -3.4	0.87	0.92	48.2	2.9	+3.0 -3.0
0.92	1	17.0	1.4	+1.2 -1.8	0.92	1	13.2	1.3	+1.4 -1.4
1	1.2	3.26	0.77	+0.59 -0.75	1	1.2	0.98	0.69	+0.61 -0.71
1.2	2.2	0.817	0.098	+0.103 -0.148	1.2	2.2	0.570	0.093	+0.106 -0.087

F. CROSS-SECTION AND RELATED TABLES

$m_Y = m_p$				$\Phi_{\gamma/e} : 0.1271$			
$0.044 <  t  \text{ [GeV}^2\text{]} < 0.06$							
$m_{\pi\pi}$ [GeV]		$\frac{d^2\sigma_{\pi\pi}}{dt dm_{\pi\pi}}$	stat. [ $\frac{\mu\text{b}}{\text{GeV}^3}$ ]	syst.			
0.5	0.56	61.3	6.1	+10.5 -12.0			
0.56	0.6	91.8	6.0	+8.8 -10.3			
0.6	0.63	120.9	6.5	+8.5 -8.5			
0.63	0.66	170.9	6.7	+11.0 -10.4			
0.66	0.68	227.5	9.5	+13.3 -14.7			
0.68	0.7	283.5	9.9	+16.6 -19.1			
0.7	0.72	311.6	9.9	+19.0 -20.0			
0.72	0.74	356.3	10.2	+23.6 -22.3			
0.74	0.76	371.9	9.9	+23.3 -23.3			
0.76	0.78	355.5	9.8	+21.2 -21.4			
0.78	0.8	226.8	8.7	+14.3 -14.9			
0.8	0.82	169.3	7.8	+10.5 -10.1			
0.82	0.84	133.1	6.8	+8.0 -9.1			
0.84	0.87	70.1	4.1	+4.4 -4.8			
0.87	0.92	38.4	2.1	+2.6 -2.7			
0.92	1	16.4	1.3	+1.1 -1.5			
1	1.2	2.24	0.44	+0.45 -0.78			
1.2	2.2	0.36	0.14	+0.09 -0.16			

$m_Y = m_p$				$\Phi_{\gamma/e} : 0.1271$			
$0.06 <  t  \text{ [GeV}^2\text{]} < 0.078$							
$m_{\pi\pi}$ [GeV]		$\frac{d^2\sigma_{\pi\pi}}{dt dm_{\pi\pi}}$	stat. [ $\frac{\mu\text{b}}{\text{GeV}^3}$ ]	syst.			
0.5	0.56	50.9	5.0	+9.1 -10.1			
0.56	0.6	71.5	5.0	+6.0 -6.9			
0.6	0.63	98.3	5.4	+6.6 -7.3			
0.63	0.66	138.4	5.8	+8.6 -8.5			
0.66	0.68	168.8	8.3	+11.2 -13.0			
0.68	0.7	210.9	8.4	+12.9 -12.7			
0.7	0.72	246.0	8.5	+15.6 -15.6			
0.72	0.74	308.1	8.6	+18.8 -18.8			
0.74	0.76	330.3	8.8	+19.6 -20.2			
0.76	0.78	283.2	8.3	+20.7 -18.8			
0.78	0.8	197.2	7.6	+12.2 -12.5			
0.8	0.82	141.0	7.1	+9.4 -8.6			
0.82	0.84	102.5	6.2	+6.6 -7.7			
0.84	0.87	64.0	3.8	+4.2 -4.2			
0.87	0.92	28.6	1.7	+2.0 -2.6			
0.92	1	9.1	1.3	+0.9 -1.2			
1	1.2	2.17	0.45	+0.42 -0.65			
1.2	2.2	0.47	0.11	+0.08 -0.10			

$m_Y = m_p$				$\Phi_{\gamma/e} : 0.1271$			
$0.078 <  t  \text{ [GeV}^2\text{]} < 0.1$							
$m_{\pi\pi}$ [GeV]		$\frac{d^2\sigma_{\pi\pi}}{dt dm_{\pi\pi}}$	stat. [ $\frac{\mu\text{b}}{\text{GeV}^3}$ ]	syst.			
0.5	0.56	34.9	3.6	+6.1 -7.5			
0.56	0.6	63.1	4.1	+4.9 -5.5			
0.6	0.63	84.3	4.6	+6.1 -5.7			
0.63	0.66	101.6	4.5	+6.5 -7.2			
0.66	0.68	138.1	6.8	+8.9 -8.7			
0.68	0.7	174.6	6.9	+10.6 -11.1			
0.7	0.72	209.8	7.0	+14.2 -13.0			
0.72	0.74	234.4	7.1	+14.4 -14.2			
0.74	0.76	257.2	7.1	+15.8 -15.9			
0.76	0.78	246.6	6.8	+15.2 -15.1			
0.78	0.8	166.4	6.2	+10.6 -10.4			
0.8	0.82	121.2	5.7	+7.3 -8.8			
0.82	0.84	85.3	4.8	+5.2 -5.4			
0.84	0.87	54.9	3.2	+3.5 -5.1			
0.87	0.92	25.7	2.0	+1.8 -2.1			
0.92	1	9.15	0.82	+0.71 -1.04			
1	1.2	2.15	0.30	+0.42 -0.53			
1.2	2.2	0.272	0.097	+0.068 -0.077			

$m_Y = m_p$				$\Phi_{\gamma/e} : 0.1271$			
$0.1 <  t  \text{ [GeV}^2\text{]} < 0.126$							
$m_{\pi\pi}$ [GeV]		$\frac{d^2\sigma_{\pi\pi}}{dt dm_{\pi\pi}}$	stat. [ $\frac{\mu\text{b}}{\text{GeV}^3}$ ]	syst.			
0.5	0.56	27.4	3.3	+3.9 -4.0			
0.56	0.6	44.6	3.4	+3.3 -4.3			
0.6	0.63	61.9	3.7	+4.8 -4.9			
0.63	0.66	78.3	3.8	+6.0 -6.0			
0.66	0.68	108.2	5.4	+7.1 -7.0			
0.68	0.7	134.6	5.6	+8.9 -8.5			
0.7	0.72	166.9	5.7	+10.9 -10.4			
0.72	0.74	187.7	5.9	+12.3 -13.6			
0.74	0.76	200.4	5.9	+12.8 -12.6			
0.76	0.78	194.9	5.6	+11.8 -11.9			
0.78	0.8	129.0	5.2	+8.4 -8.5			
0.8	0.82	93.0	4.7	+6.0 -6.9			
0.82	0.84	70.0	4.3	+4.4 -5.2			
0.84	0.87	46.5	2.6	+2.9 -3.8			
0.87	0.92	21.1	1.6	+1.6 -1.7			
0.92	1	8.48	0.65	+1.02 -0.96			
1	1.2	1.78	0.31	+0.40 -0.47			
1.2	2.2	0.446	0.054	+0.059 -0.092			

F.1.  $\pi^+\pi^-$  CROSS-SECTIONS

$m_Y = m_p$		$\Phi_{\gamma/e} : 0.1271$		$m_Y = m_p$		$\Phi_{\gamma/e} : 0.1271$		
$0.126 <  t  \text{ [GeV}^2\text{]} < 0.156$				$0.156 <  t  \text{ [GeV}^2\text{]} < 0.2$				
$m_{\pi\pi}$ [GeV]		$\frac{d^2\sigma_{\pi\pi}}{dt dm_{\pi\pi}}$	stat. [ $\frac{\mu\text{b}}{\text{GeV}^3}$ ]	syst.	$m_{\pi\pi}$ [GeV]	$\frac{d^2\sigma_{\pi\pi}}{dt dm_{\pi\pi}}$	stat. [ $\frac{\mu\text{b}}{\text{GeV}^3}$ ]	syst.
0.5	0.56	20.8	2.8	+3.0 -3.0	0.5	12.1	1.6	+2.0 -1.7
0.56	0.6	33.4	2.9	+2.4 -3.3	0.56	20.7	1.6	+1.8 -2.0
0.6	0.63	45.4	3.1	+3.2 -4.0	0.6	27.6	2.1	+1.9 -2.3
0.63	0.66	60.0	3.2	+4.0 -3.9	0.63	36.9	2.1	+2.7 -2.9
0.66	0.68	83.7	4.6	+5.4 -6.2	0.66	48.4	3.0	+3.3 -4.2
0.68	0.7	105.3	4.7	+7.1 -7.7	0.68	68.1	3.0	+5.4 -4.6
0.7	0.72	115.6	4.8	+9.0 -8.3	0.7	83.7	3.3	+6.9 -6.4
0.72	0.74	139.0	4.9	+8.8 -9.2	0.72	94.4	3.3	+6.5 -6.7
0.74	0.76	154.9	4.9	+10.2 -10.3	0.74	118.0	3.3	+7.4 -7.5
0.76	0.78	146.7	4.8	+9.5 -9.3	0.76	111.2	3.3	+7.0 -6.9
0.78	0.8	107.5	4.4	+6.8 -7.1	0.78	71.5	2.9	+4.7 -4.5
0.8	0.82	86.2	4.1	+5.2 -6.2	0.8	54.2	2.7	+3.7 -3.4
0.82	0.84	52.5	3.4	+3.7 -4.2	0.82	37.4	2.3	+2.6 -2.9
0.84	0.87	35.2	2.0	+2.2 -2.3	0.84	28.0	1.7	+1.7 -2.3
0.87	0.92	18.7	1.4	+1.6 -1.3	0.87	14.10	0.83	+1.08 -1.17
0.92	1	7.53	0.59	+0.70 -0.86	0.92	5.74	0.53	+0.51 -0.68
1	1.2	2.16	0.26	+0.35 -0.35	1	1.16	0.22	+0.27 -0.25
1.2	2.2	0.373	0.072	+0.058 -0.097	1.2	0.144	0.049	+0.037 -0.047

$m_Y = m_p$		$\Phi_{\gamma/e} : 0.1271$		$m_Y = m_p$		$\Phi_{\gamma/e} : 0.1271$		
$0.2 <  t  \text{ [GeV}^2\text{]} < 0.28$				$0.28 <  t  \text{ [GeV}^2\text{]} < 1.5$				
$m_{\pi\pi}$ [GeV]		$\frac{d^2\sigma_{\pi\pi}}{dt dm_{\pi\pi}}$	stat. [ $\frac{\mu\text{b}}{\text{GeV}^3}$ ]	syst.	$m_{\pi\pi}$ [GeV]	$\frac{d^2\sigma_{\pi\pi}}{dt dm_{\pi\pi}}$	stat. [ $\frac{\mu\text{b}}{\text{GeV}^3}$ ]	syst.
0.5	0.56	4.61	0.92	+1.22 -1.12	0.5	0.250	0.063	+0.123 -0.124
0.56	0.6	9.43	0.86	+0.77 -1.05	0.56	0.432	0.077	+0.122 -0.123
0.6	0.63	16.2	1.0	+1.1 -1.5	0.6	0.573	0.087	+0.130 -0.130
0.63	0.66	19.8	1.2	+1.9 -1.5	0.63	1.021	0.099	+0.149 -0.138
0.66	0.68	29.6	1.6	+1.9 -2.1	0.66	1.37	0.14	+0.22 -0.20
0.68	0.7	35.7	1.8	+2.8 -2.4	0.68	2.00	0.14	+0.22 -0.21
0.7	0.72	49.0	1.9	+3.4 -3.4	0.7	2.72	0.15	+0.31 -0.30
0.72	0.74	56.4	1.9	+3.8 -3.9	0.72	3.48	0.17	+0.38 -0.36
0.74	0.76	66.6	1.9	+4.3 -4.8	0.74	3.99	0.16	+0.41 -0.41
0.76	0.78	64.1	1.9	+4.3 -4.3	0.76	4.22	0.17	+0.45 -0.43
0.78	0.8	41.3	1.7	+2.9 -2.9	0.78	3.10	0.15	+0.33 -0.34
0.8	0.82	30.9	1.5	+2.2 -2.5	0.8	2.36	0.14	+0.27 -0.27
0.82	0.84	26.1	1.4	+1.8 -2.0	0.82	1.81	0.13	+0.27 -0.25
0.84	0.87	16.58	0.83	+1.10 -1.38	0.84	1.269	0.089	+0.155 -0.164
0.87	0.92	9.24	0.55	+0.66 -0.73	0.87	1.025	0.051	+0.108 -0.117
0.92	1	4.26	0.31	+0.37 -0.63	0.92	0.484	0.034	+0.082 -0.076
1	1.2	1.28	0.13	+0.15 -0.25	1	0.162	0.019	+0.051 -0.050
1.2	2.2	0.189	0.034	+0.027 -0.039	1.2	0.0257	0.0044	+0.0122 -0.0119

## F. CROSS-SECTION AND RELATED TABLES

$m_p < m_Y < 10 \text{ GeV}$				$m_p < m_Y < 10 \text{ GeV}$					
$0 <  t  [\text{GeV}^2] < 0.03$				$0.03 <  t  [\text{GeV}^2] < 0.06$					
$\Phi_{\gamma/e} : 0.1271$				$\Phi_{\gamma/e} : 0.1271$					
$m_{\pi\pi}$ [GeV]		$\frac{d^2\sigma_{\pi\pi}}{dt dm_{\pi\pi}}$	stat. $\left[\frac{\mu\text{b}}{\text{GeV}^3}\right]$	syst.	$m_{\pi\pi}$ [GeV]		$\frac{d^2\sigma_{\pi\pi}}{dt dm_{\pi\pi}}$	stat. $\left[\frac{\mu\text{b}}{\text{GeV}^3}\right]$	syst.
0.5	0.56	34.5	5.5	+7.2 -8.4	0.5	0.56	24.5	4.3	+5.2 -4.5
0.56	0.6	38.4	4.3	+5.2 -7.5	0.56	0.6	31.5	4.0	+4.8 -5.1
0.6	0.63	41.7	4.3	+5.4 -6.0	0.6	0.63	35.8	4.4	+5.2 -6.2
0.63	0.66	51.6	4.6	+9.5 -8.9	0.63	0.66	53.0	4.2	+7.2 -7.8
0.66	0.68	59.5	6.7	+10.1 -11.6	0.66	0.68	56.9	6.1	+9.7 -8.7
0.68	0.7	72.6	6.3	+11.1 -10.9	0.68	0.7	65.3	6.1	+10.1 -9.4
0.7	0.72	79.8	6.5	+12.9 -13.8	0.7	0.72	85.5	6.2	+13.3 -12.1
0.72	0.74	105.6	7.0	+14.1 -15.0	0.72	0.74	107.4	6.4	+16.0 -15.2
0.74	0.76	92.7	6.7	+18.0 -14.5	0.74	0.76	97.4	6.3	+15.9 -14.6
0.76	0.78	95.3	6.5	+14.5 -16.5	0.76	0.78	90.3	5.9	+12.9 -12.1
0.78	0.8	59.0	6.0	+10.1 -8.8	0.78	0.8	60.5	5.4	+9.4 -8.9
0.8	0.82	41.3	5.5	+7.4 -7.8	0.8	0.82	40.1	4.8	+6.5 -6.7
0.82	0.84	19.7	4.0	+5.0 -4.2	0.82	0.84	34.0	5.2	+5.1 -4.7
0.84	0.87	18.2	3.6	+3.6 -3.8	0.84	0.87	21.1	2.8	+3.4 -3.0
0.87	0.92	9.9	1.6	+1.7 -2.4	0.87	0.92	7.6	1.6	+1.8 -1.9
0.92	1	2.24	0.66	+0.73 -0.64	0.92	1	3.99	0.90	+0.86 -0.71
1	1.2	0.48	0.27	+0.49 -0.53	1	1.2	2.14	0.45	+0.37 -0.56
1.2	2.2	0.075	0.085	+0.073 -0.068	1.2	2.2	0.290	0.077	+0.072 -0.070

$m_p < m_Y < 10 \text{ GeV}$				$m_p < m_Y < 10 \text{ GeV}$					
$0.06 <  t  [\text{GeV}^2] < 0.096$				$0.096 <  t  [\text{GeV}^2] < 0.14$					
$\Phi_{\gamma/e} : 0.1271$				$\Phi_{\gamma/e} : 0.1271$					
$m_{\pi\pi}$ [GeV]		$\frac{d^2\sigma_{\pi\pi}}{dt dm_{\pi\pi}}$	stat. $\left[\frac{\mu\text{b}}{\text{GeV}^3}\right]$	syst.	$m_{\pi\pi}$ [GeV]		$\frac{d^2\sigma_{\pi\pi}}{dt dm_{\pi\pi}}$	stat. $\left[\frac{\mu\text{b}}{\text{GeV}^3}\right]$	syst.
0.5	0.56	14.6	3.2	+3.2 -3.7	0.5	0.56	10.6	2.3	+1.8 -2.7
0.56	0.6	19.8	3.2	+3.0 -4.2	0.56	0.6	14.2	2.5	+3.5 -2.9
0.6	0.63	34.4	3.5	+5.3 -4.3	0.6	0.63	17.0	2.7	+3.3 -3.2
0.63	0.66	46.6	3.5	+6.3 -6.2	0.63	0.66	31.1	2.8	+4.2 -4.7
0.66	0.68	59.7	4.9	+8.3 -7.5	0.66	0.68	35.9	3.9	+5.8 -5.6
0.68	0.7	52.0	4.9	+9.2 -6.9	0.68	0.7	37.7	3.8	+7.0 -6.7
0.7	0.72	67.2	4.9	+10.1 -9.1	0.7	0.72	52.2	4.2	+7.4 -7.9
0.72	0.74	77.4	5.1	+11.5 -10.6	0.72	0.74	69.2	4.0	+9.1 -8.6
0.74	0.76	89.4	5.0	+12.1 -11.0	0.74	0.76	68.9	4.1	+8.8 -8.4
0.76	0.78	84.9	4.8	+11.2 -10.2	0.76	0.78	59.6	3.9	+8.2 -8.4
0.78	0.8	57.4	4.5	+8.2 -7.7	0.78	0.8	39.4	3.7	+6.9 -6.3
0.8	0.82	38.5	4.1	+5.3 -5.8	0.8	0.82	28.1	3.3	+4.3 -4.5
0.82	0.84	24.4	3.8	+4.0 -4.4	0.82	0.84	22.8	3.1	+3.3 -3.4
0.84	0.87	20.3	2.6	+3.6 -3.1	0.84	0.87	15.1	2.1	+2.1 -2.2
0.87	0.92	11.1	1.3	+1.5 -1.8	0.87	0.92	10.3	1.3	+1.5 -1.9
0.92	1	3.89	0.73	+0.68 -0.73	0.92	1	3.89	0.60	+0.58 -0.54
1	1.2	0.77	0.31	+0.31 -0.32	1	1.2	0.67	0.25	+0.42 -0.34
1.2	2.2	0.184	0.088	+0.073 -0.065	1.2	2.2	0.114	0.059	+0.076 -0.110

# F.1. $\pi^+\pi^-$ CROSS-SECTIONS

$m_p < m_Y < 10 \text{ GeV}$		$\Phi_{\gamma/e} : 0.1271$		$m_p < m_Y < 10 \text{ GeV}$		$\Phi_{\gamma/e} : 0.1271$		
$0.14 <  t  [\text{GeV}^2] < 0.2$				$0.2 <  t  [\text{GeV}^2] < 0.28$				
$m_{\pi\pi}$ [GeV]		$\frac{d^2\sigma_{\pi\pi}}{dt dm_{\pi\pi}}$	stat. $\left[\frac{\mu\text{b}}{\text{GeV}^3}\right]$	syst.	$m_{\pi\pi}$ [GeV]	$\frac{d^2\sigma_{\pi\pi}}{dt dm_{\pi\pi}}$	stat. $\left[\frac{\mu\text{b}}{\text{GeV}^3}\right]$	syst.
0.5	0.56	5.8	1.5	+3.5 -3.5	0.5	3.28	0.96	+2.08 -2.32
0.56	0.6	9.8	1.7	+2.8 -2.5	0.56	5.0	1.2	+2.0 -1.7
0.6	0.63	12.7	1.9	+2.5 -1.8	0.6	9.5	1.4	+2.1 -1.4
0.63	0.66	20.9	1.9	+2.9 -3.2	0.63	13.4	1.3	+1.7 -2.1
0.66	0.68	20.7	3.0	+4.2 -3.7	0.66	15.5	2.0	+2.2 -2.2
0.68	0.7	32.2	2.9	+5.1 -4.4	0.68	22.8	2.1	+2.9 -2.8
0.7	0.72	42.3	3.0	+5.8 -5.8	0.7	31.3	2.1	+4.1 -3.8
0.72	0.74	46.9	3.0	+7.7 -6.3	0.72	34.9	2.1	+4.9 -4.6
0.74	0.76	53.1	2.9	+7.3 -6.2	0.74	36.2	2.1	+5.0 -4.3
0.76	0.78	48.8	2.9	+6.7 -6.2	0.76	35.9	2.1	+4.9 -4.5
0.78	0.8	29.7	2.7	+5.1 -5.3	0.78	26.8	2.0	+3.6 -3.2
0.8	0.82	24.7	2.4	+3.0 -4.3	0.8	22.1	1.8	+3.0 -2.8
0.82	0.84	20.1	2.5	+3.9 -3.1	0.82	17.6	1.7	+2.8 -2.2
0.84	0.87	11.0	1.4	+2.0 -1.7	0.84	9.1	1.2	+1.5 -1.6
0.87	0.92	8.85	0.97	+1.10 -1.26	0.87	4.70	0.71	+0.86 -0.92
0.92	1	2.77	0.48	+0.53 -0.74	0.92	2.24	0.42	+0.75 -0.39
1	1.2	1.17	0.22	+0.27 -0.32	1	0.54	0.14	+0.22 -0.21
1.2	2.2	0.251	0.048	+0.068 -0.075	1.2	0.139	0.042	+0.060 -0.058

$m_p < m_Y < 10 \text{ GeV}$		$\Phi_{\gamma/e} : 0.1271$		$m_p < m_Y < 10 \text{ GeV}$		$\Phi_{\gamma/e} : 0.1271$		
$0.28 <  t  [\text{GeV}^2] < 0.39$				$0.39 <  t  [\text{GeV}^2] < 0.6$				
$m_{\pi\pi}$ [GeV]		$\frac{d^2\sigma_{\pi\pi}}{dt dm_{\pi\pi}}$	stat. $\left[\frac{\mu\text{b}}{\text{GeV}^3}\right]$	syst.	$m_{\pi\pi}$ [GeV]	$\frac{d^2\sigma_{\pi\pi}}{dt dm_{\pi\pi}}$	stat. $\left[\frac{\mu\text{b}}{\text{GeV}^3}\right]$	syst.
0.5	0.56	2.20	0.73	+1.07 -1.06	0.5	0.90	0.29	+0.49 -0.48
0.56	0.6	3.87	0.75	+0.90 -0.88	0.56	1.26	0.36	+0.39 -0.45
0.6	0.63	7.08	0.82	+1.08 -1.22	0.6	1.91	0.39	+0.52 -0.55
0.63	0.66	7.44	0.96	+1.33 -1.31	0.63	3.49	0.39	+0.56 -0.60
0.66	0.68	11.3	1.3	+1.7 -1.8	0.66	6.01	0.65	+0.89 -1.13
0.68	0.7	13.8	1.4	+1.6 -1.7	0.68	5.75	0.64	+0.76 -0.76
0.7	0.72	17.2	1.4	+2.5 -2.4	0.7	7.38	0.67	+1.17 -1.05
0.72	0.74	20.8	1.5	+2.7 -2.5	0.72	11.33	0.73	+1.25 -1.15
0.74	0.76	21.3	1.5	+3.4 -3.1	0.74	12.12	0.75	+1.53 -1.35
0.76	0.78	26.1	1.5	+3.2 -3.0	0.76	11.99	0.75	+1.62 -1.51
0.78	0.8	16.2	1.4	+2.7 -2.4	0.78	9.18	0.68	+1.37 -1.16
0.8	0.82	15.2	1.3	+2.0 -2.1	0.8	7.39	0.68	+1.07 -0.96
0.82	0.84	13.1	1.3	+2.1 -2.5	0.82	6.67	0.66	+0.97 -1.06
0.84	0.87	6.20	0.91	+1.04 -1.16	0.84	4.47	0.41	+0.64 -1.00
0.87	0.92	3.42	0.44	+0.74 -0.65	0.87	2.24	0.26	+0.39 -0.33
0.92	1	1.69	0.34	+0.33 -0.51	0.92	1.22	0.19	+0.24 -0.30
1	1.2	0.48	0.14	+0.25 -0.30	1	0.425	0.076	+0.155 -0.177
1.2	2.2	0.103	0.030	+0.069 -0.064	1.2	0.090	0.019	+0.036 -0.039

$m_p < m_Y < 10 \text{ GeV}$        $\Phi_{\gamma/e} : 0.1271$

$0.6 < |t| [\text{GeV}^2] < 1.5$

$m_{\pi\pi}$ [GeV]		$\frac{d^2\sigma_{\pi\pi}}{dt dm_{\pi\pi}}$	stat.	syst.
			$\left[ \frac{\mu\text{b}}{\text{GeV}^3} \right]$	
0.5	0.56	0.099	0.057	+0.081 -0.104
0.56	0.6	0.225	0.063	+0.129 -0.162
0.6	0.63	0.18	0.13	+0.18 -0.19
0.63	0.66	0.441	0.089	+0.141 -0.164
0.66	0.68	0.88	0.17	+0.18 -0.22
0.68	0.7	0.92	0.14	+0.24 -0.28
0.7	0.72	1.50	0.15	+0.30 -0.33
0.72	0.74	1.96	0.19	+0.32 -0.33
0.74	0.76	2.61	0.17	+0.39 -0.39
0.76	0.78	2.86	0.19	+0.38 -0.39
0.78	0.8	2.04	0.17	+0.38 -0.41
0.8	0.82	1.76	0.18	+0.28 -0.28
0.82	0.84	1.53	0.15	+0.23 -0.24
0.84	0.87	1.062	0.097	+0.208 -0.201
0.87	0.92	0.669	0.074	+0.134 -0.136
0.92	1	0.324	0.054	+0.095 -0.096
1	1.2	0.169	0.022	+0.057 -0.067
1.2	2.2	0.0398	0.0053	+0.0148 -0.0163

**Table F.5:** Unfolded differential cross-section  $d^2\sigma(\gamma p \rightarrow \pi^+\pi^-Y)/dm_{\pi\pi}dt$  in bins of  $m_{\pi\pi}$  and  $t$ .  $ep$  cross-sections are scaled by a photon flux factor as given in the table. Splitting a normalization uncertainty from the (symmetrized) total covariance matrix according to Appendix C.3 yields  $\Delta_{\text{norm}} = 5.10 \%$ . Further correlations are not provided.

F.1.6  $d^2\sigma(\gamma p \rightarrow \pi^+\pi^-Y)/dm_{\pi\pi}dt(m_{\pi\pi}, W_{\gamma p}, t)$ 

multipage set of tables; common caption Table F.6

$m_Y = m_p$		$\Phi_{\gamma/e} : 0.0346$		$m_Y = m_p$		$\Phi_{\gamma/e} : 0.0294$			
$0 <  t  [\text{GeV}^2] < 0.016$		$0 <  t  [\text{GeV}^2] < 0.016$		$0 <  t  [\text{GeV}^2] < 0.016$		$0 <  t  [\text{GeV}^2] < 0.016$			
$20 < W_{\gamma p} [\text{GeV}] < 28$		$28 < W_{\gamma p} [\text{GeV}] < 38$		$28 < W_{\gamma p} [\text{GeV}] < 38$		$28 < W_{\gamma p} [\text{GeV}] < 38$			
$m_{\pi\pi}$ [GeV]		$\frac{d^2\sigma_{\pi\pi}}{dt dm_{\pi\pi}}$	stat. [ $\frac{\mu\text{b}}{\text{GeV}^3}$ ]	syst.	$m_{\pi\pi}$ [GeV]		$\frac{d^2\sigma_{\pi\pi}}{dt dm_{\pi\pi}}$	stat. [ $\frac{\mu\text{b}}{\text{GeV}^3}$ ]	syst.
0.5	0.56	147.7	12.3	+15.0 -17.2	0.5	0.56	134.5	12.2	+15.2 -16.9
0.56	0.6	175.3	12.0	+15.5 -17.2	0.56	0.6	200.9	11.9	+14.6 -15.9
0.6	0.63	211.7	16.0	+17.9 -16.2	0.6	0.63	251.9	14.5	+14.5 -14.1
0.63	0.66	291.4	14.9	+20.7 -21.3	0.63	0.66	292.5	14.0	+16.0 -15.4
0.66	0.68	307.7	22.8	+23.2 -27.8	0.66	0.68	353.4	20.1	+18.7 -20.5
0.68	0.7	365.7	22.5	+28.7 -31.6	0.68	0.7	420.4	20.7	+25.1 -23.5
0.7	0.72	460.8	24.1	+32.5 -37.3	0.7	0.72	478.3	22.0	+26.8 -25.4
0.72	0.74	518.8	26.2	+40.2 -39.8	0.72	0.74	585.6	23.8	+31.8 -30.1
0.74	0.76	554.3	26.4	+42.4 -41.9	0.74	0.76	546.9	22.7	+30.7 -29.9
0.76	0.78	494.4	23.5	+41.3 -49.3	0.76	0.78	536.5	21.1	+32.1 -29.3
0.78	0.8	303.0	22.3	+26.3 -24.3	0.78	0.8	353.6	20.2	+21.4 -21.7
0.8	0.82	211.7	21.4	+37.4 -15.9	0.8	0.82	236.7	15.1	+13.6 -14.2
0.82	0.84	184.6	19.3	+13.9 -45.8	0.82	0.84	185.0	13.0	+10.9 -11.9
0.84	0.87	133.1	11.7	+10.2 -10.9	0.84	0.87	98.7	8.3	+6.1 -6.9
0.87	0.92	51.3	5.9	+5.3 -5.7	0.87	0.92	55.1	3.7	+3.9 -3.5
0.92	1	18.3	3.2	+1.6 -4.3	0.92	1	21.3	1.8	+1.5 -2.0
1	1.2	5.04	0.88	+2.72 -0.87	1	1.2	3.45	0.91	+0.69 -0.93
1.2	2.2	0.87	0.50	+0.69 -0.42	1.2	2.2	0.97	0.32	+0.13 -0.43

$m_Y = m_p$		$\Phi_{\gamma/e} : 0.0248$		$m_Y = m_p$		$\Phi_{\gamma/e} : 0.0383$			
$0 <  t  [\text{GeV}^2] < 0.016$		$0 <  t  [\text{GeV}^2] < 0.016$		$0 <  t  [\text{GeV}^2] < 0.016$		$0 <  t  [\text{GeV}^2] < 0.016$			
$38 < W_{\gamma p} [\text{GeV}] < 50$		$50 < W_{\gamma p} [\text{GeV}] < 80$		$50 < W_{\gamma p} [\text{GeV}] < 80$		$50 < W_{\gamma p} [\text{GeV}] < 80$			
$m_{\pi\pi}$ [GeV]		$\frac{d^2\sigma_{\pi\pi}}{dt dm_{\pi\pi}}$	stat. [ $\frac{\mu\text{b}}{\text{GeV}^3}$ ]	syst.	$m_{\pi\pi}$ [GeV]		$\frac{d^2\sigma_{\pi\pi}}{dt dm_{\pi\pi}}$	stat. [ $\frac{\mu\text{b}}{\text{GeV}^3}$ ]	syst.
0.5	0.56	166.4	15.0	+18.5 -19.4	0.5	0.56	180.2	21.0	+51.0 -30.7
0.56	0.6	232.7	15.3	+18.9 -21.2	0.56	0.6	215.3	19.6	+24.5 -22.2
0.6	0.63	255.8	15.5	+17.7 -18.6	0.6	0.63	242.8	21.5	+25.3 -18.2
0.63	0.66	337.9	16.8	+20.9 -22.6	0.63	0.66	322.8	19.9	+24.9 -22.3
0.66	0.68	368.1	24.7	+25.2 -21.4	0.66	0.68	437.2	28.9	+31.7 -46.4
0.68	0.7	464.9	25.8	+28.3 -29.0	0.68	0.7	540.5	29.8	+37.1 -52.8
0.7	0.72	555.7	26.8	+32.1 -31.7	0.7	0.72	582.6	29.5	+43.5 -40.2
0.72	0.74	632.7	26.4	+35.5 -35.0	0.72	0.74	634.0	28.7	+47.0 -48.5
0.74	0.76	634.8	26.2	+36.2 -35.1	0.74	0.76	737.4	28.0	+49.7 -63.3
0.76	0.78	617.3	25.9	+37.2 -35.3	0.76	0.78	605.6	25.7	+44.2 -47.3
0.78	0.8	360.8	20.6	+21.8 -25.4	0.78	0.8	389.4	22.0	+26.6 -32.1
0.8	0.82	255.8	16.3	+13.8 -15.4	0.8	0.82	285.6	18.3	+21.0 -22.6
0.82	0.84	188.5	14.2	+10.4 -12.3	0.82	0.84	207.0	17.7	+24.6 -13.7
0.84	0.87	107.2	7.9	+6.0 -6.6	0.84	0.87	134.1	10.0	+9.6 -12.4
0.87	0.92	52.3	4.8	+3.0 -3.4	0.87	0.92	71.3	4.5	+5.1 -5.5
0.92	1	20.4	2.0	+1.6 -1.7	0.92	1	24.9	1.9	+2.0 -3.5
1	1.2	3.2	1.0	+1.1 -1.0	1	1.2	5.91	0.75	+0.81 -1.08
1.2	2.2	1.16	0.14	+0.26 -0.28	1.2	2.2	1.25	0.11	+0.33 -0.22

F. CROSS-SECTION AND RELATED TABLES

$m_Y = m_p$		$\Phi_{\gamma/e} : 0.0346$		$m_Y = m_p$		$\Phi_{\gamma/e} : 0.0294$			
$0.016 <  t  \text{ [GeV}^2\text{]} < 0.036$		$20 < W_{\gamma p} \text{ [GeV]} < 28$		$0.016 <  t  \text{ [GeV}^2\text{]} < 0.036$		$28 < W_{\gamma p} \text{ [GeV]} < 38$			
$m_{\pi\pi}$ [GeV]		$\frac{d^2\sigma_{\pi\pi}}{dt dm_{\pi\pi}}$	stat. [ $\frac{\mu\text{b}}{\text{GeV}^3}$ ]	syst.	$m_{\pi\pi}$ [GeV]		$\frac{d^2\sigma_{\pi\pi}}{dt dm_{\pi\pi}}$	stat. [ $\frac{\mu\text{b}}{\text{GeV}^3}$ ]	syst.
0.5	0.56	84.3	10.1	+8.3 -11.1	0.5	0.56	74.2	9.7	+11.6 -13.5
0.56	0.6	136.2	10.9	+14.6 -14.5	0.56	0.6	114.8	12.3	+16.1 -16.3
0.6	0.63	161.2	12.8	+12.1 -12.6	0.6	0.63	172.5	11.1	+9.8 -9.6
0.63	0.66	207.7	12.4	+16.6 -15.5	0.63	0.66	236.1	12.1	+12.8 -12.7
0.66	0.68	270.1	18.5	+20.3 -21.5	0.66	0.68	259.2	15.6	+14.3 -15.9
0.68	0.7	336.1	20.2	+25.9 -31.8	0.68	0.7	293.9	17.0	+16.1 -16.0
0.7	0.72	399.0	20.0	+28.8 -30.5	0.7	0.72	393.0	17.9	+20.7 -20.1
0.72	0.74	396.8	20.0	+31.2 -34.0	0.72	0.74	432.3	18.7	+23.8 -23.3
0.74	0.76	448.4	20.0	+32.9 -34.6	0.74	0.76	488.4	18.8	+27.6 -27.1
0.76	0.78	401.7	20.0	+31.2 -41.1	0.76	0.78	483.2	18.4	+26.2 -29.0
0.78	0.8	279.1	18.2	+20.8 -24.0	0.78	0.8	233.9	14.1	+15.6 -15.0
0.8	0.82	192.5	15.5	+20.7 -14.9	0.8	0.82	247.7	14.4	+14.1 -15.3
0.82	0.84	148.0	15.5	+11.6 -21.4	0.82	0.84	150.5	12.4	+10.3 -10.4
0.84	0.87	71.8	7.7	+6.4 -7.7	0.84	0.87	100.4	7.7	+6.0 -7.3
0.87	0.92	34.7	3.9	+5.3 -6.1	0.87	0.92	49.4	3.7	+3.2 -3.3
0.92	1	9.6	1.9	+1.1 -1.9	0.92	1	12.7	2.6	+1.4 -1.7
1	1.2	1.4	1.9	+0.8 -0.9	1	1.2	3.5	1.2	+1.3 -1.3
1.2	2.2	0.66	0.43	+0.80 -0.19	1.2	2.2	0.64	0.16	+0.11 -0.29

$m_Y = m_p$		$\Phi_{\gamma/e} : 0.0248$		$m_Y = m_p$		$\Phi_{\gamma/e} : 0.0383$			
$0.016 <  t  \text{ [GeV}^2\text{]} < 0.036$		$38 < W_{\gamma p} \text{ [GeV]} < 50$		$0.016 <  t  \text{ [GeV}^2\text{]} < 0.036$		$50 < W_{\gamma p} \text{ [GeV]} < 80$			
$m_{\pi\pi}$ [GeV]		$\frac{d^2\sigma_{\pi\pi}}{dt dm_{\pi\pi}}$	stat. [ $\frac{\mu\text{b}}{\text{GeV}^3}$ ]	syst.	$m_{\pi\pi}$ [GeV]		$\frac{d^2\sigma_{\pi\pi}}{dt dm_{\pi\pi}}$	stat. [ $\frac{\mu\text{b}}{\text{GeV}^3}$ ]	syst.
0.5	0.56	111.9	11.7	+18.0 -18.6	0.5	0.56	128.1	13.5	+22.5 -21.5
0.56	0.6	126.9	12.8	+14.2 -14.5	0.56	0.6	155.0	13.9	+14.4 -14.2
0.6	0.63	176.1	13.1	+12.2 -11.4	0.6	0.63	212.0	15.5	+15.7 -19.2
0.63	0.66	236.6	13.6	+14.3 -15.3	0.63	0.66	264.2	15.0	+24.4 -18.4
0.66	0.68	295.1	18.6	+18.4 -17.6	0.66	0.68	341.5	21.6	+25.5 -24.6
0.68	0.7	321.7	18.8	+21.4 -18.4	0.68	0.7	404.7	21.1	+28.3 -28.9
0.7	0.72	451.2	21.6	+25.7 -27.3	0.7	0.72	472.2	21.4	+33.8 -32.4
0.72	0.74	473.1	22.3	+28.0 -27.7	0.72	0.74	535.4	20.9	+38.3 -35.9
0.74	0.76	509.2	20.5	+28.0 -27.8	0.74	0.76	555.5	20.5	+40.3 -36.9
0.76	0.78	473.0	19.5	+25.1 -24.9	0.76	0.78	510.6	19.2	+45.8 -39.6
0.78	0.8	297.1	17.0	+17.4 -16.6	0.78	0.8	328.8	17.4	+23.7 -28.7
0.8	0.82	225.9	16.5	+14.9 -13.9	0.8	0.82	243.5	16.1	+17.4 -26.0
0.82	0.84	180.4	13.1	+9.4 -11.1	0.82	0.84	162.2	12.9	+11.8 -13.5
0.84	0.87	92.0	7.2	+5.6 -5.4	0.84	0.87	105.4	7.6	+7.6 -7.1
0.87	0.92	48.0	4.6	+2.7 -3.0	0.87	0.92	57.3	3.9	+4.4 -4.6
0.92	1	16.3	2.3	+1.1 -1.6	0.92	1	15.2	1.8	+2.4 -2.0
1	1.2	2.63	0.76	+0.64 -0.72	1	1.2	3.66	0.54	+0.59 -0.82
1.2	2.2	0.63	0.11	+0.16 -0.15	1.2	2.2	0.834	0.094	+0.083 -0.104

## F.1. $\pi^+\pi^-$ CROSS-SECTIONS

$m_Y = m_p$   $\Phi_{\gamma/e} : 0.0346$   
 $0.036 < |t| [\text{GeV}^2] < 0.062$   
 $20 < W_{\gamma p} [\text{GeV}] < 28$

$m_{\pi\pi}$ [GeV]	$\frac{d^2\sigma_{\pi\pi}}{dt dm_{\pi\pi}}$	stat. [ $\frac{\mu\text{b}}{\text{GeV}^3}$ ]	syst.
0.5 0.56	57.2	7.5	+9.4 -10.7
0.56 0.6	93.2	7.9	+10.2 -10.7
0.6 0.63	127.1	10.4	+9.8 -16.5
0.63 0.66	153.8	10.4	+14.2 -11.4
0.66 0.68	231.4	14.5	+16.3 -20.3
0.68 0.7	234.0	14.8	+18.6 -27.5
0.7 0.72	284.0	15.3	+22.9 -24.1
0.72 0.74	331.4	15.5	+25.2 -29.8
0.74 0.76	337.0	15.0	+25.6 -29.0
0.76 0.78	327.6	15.1	+24.3 -26.7
0.78 0.8	228.2	13.9	+20.6 -29.6
0.8 0.82	165.6	13.3	+13.2 -12.7
0.82 0.84	114.2	10.6	+8.8 -15.7
0.84 0.87	67.4	8.3	+6.1 -6.8
0.87 0.92	35.2	4.7	+3.2 -3.1
0.92 1	14.0	2.6	+1.2 -1.7
1 1.2	0.4	1.3	+1.0 -0.7
1.2 2.2	-0.26	0.44	+0.28 -0.11

$m_Y = m_p$   $\Phi_{\gamma/e} : 0.0294$   
 $0.036 < |t| [\text{GeV}^2] < 0.062$   
 $28 < W_{\gamma p} [\text{GeV}] < 38$

$m_{\pi\pi}$ [GeV]	$\frac{d^2\sigma_{\pi\pi}}{dt dm_{\pi\pi}}$	stat. [ $\frac{\mu\text{b}}{\text{GeV}^3}$ ]	syst.
0.5 0.56	73.3	7.6	+10.9 -12.0
0.56 0.6	86.7	7.6	+7.9 -8.7
0.6 0.63	117.2	8.0	+9.8 -9.8
0.63 0.66	183.8	9.2	+10.2 -10.0
0.66 0.68	195.6	12.2	+13.3 -13.5
0.68 0.7	275.1	14.2	+14.4 -14.6
0.7 0.72	314.4	14.7	+16.5 -16.6
0.72 0.74	363.2	14.6	+19.9 -20.6
0.74 0.76	395.9	14.9	+21.7 -21.2
0.76 0.78	323.4	14.4	+18.7 -19.0
0.78 0.8	229.2	13.0	+13.7 -15.1
0.8 0.82	154.9	9.7	+9.4 -9.4
0.82 0.84	131.7	10.0	+7.7 -8.4
0.84 0.87	68.4	6.3	+5.0 -4.7
0.87 0.92	37.7	3.1	+2.5 -2.9
0.92 1	13.7	1.7	+1.2 -1.8
1 1.2	-0.04	0.98	+0.84 -0.62
1.2 2.2	0.32	0.25	+0.13 -0.24

$m_Y = m_p$   $\Phi_{\gamma/e} : 0.0248$   
 $0.036 < |t| [\text{GeV}^2] < 0.062$   
 $38 < W_{\gamma p} [\text{GeV}] < 50$

$m_{\pi\pi}$ [GeV]	$\frac{d^2\sigma_{\pi\pi}}{dt dm_{\pi\pi}}$	stat. [ $\frac{\mu\text{b}}{\text{GeV}^3}$ ]	syst.
0.5 0.56	75.2	8.8	+12.5 -13.6
0.56 0.6	97.0	9.7	+10.5 -11.1
0.6 0.63	134.6	10.1	+8.5 -10.1
0.63 0.66	174.6	10.6	+12.6 -12.4
0.66 0.68	204.0	13.8	+13.5 -13.0
0.68 0.7	275.8	15.2	+16.0 -16.1
0.7 0.72	329.5	15.9	+19.7 -18.7
0.72 0.74	392.2	16.9	+22.2 -20.9
0.74 0.76	396.4	16.6	+22.5 -22.1
0.76 0.78	380.0	16.0	+20.9 -19.8
0.78 0.8	232.4	13.4	+14.5 -13.5
0.8 0.82	181.9	11.9	+9.5 -9.2
0.82 0.84	123.8	10.0	+8.4 -7.3
0.84 0.87	85.8	6.5	+4.9 -6.7
0.87 0.92	43.5	2.9	+2.6 -2.8
0.92 1	15.3	1.7	+0.9 -1.2
1 1.2	2.55	0.45	+0.52 -0.78
1.2 2.2	0.55	0.15	+0.08 -0.20

$m_Y = m_p$   $\Phi_{\gamma/e} : 0.0383$   
 $0.036 < |t| [\text{GeV}^2] < 0.062$   
 $50 < W_{\gamma p} [\text{GeV}] < 80$

$m_{\pi\pi}$ [GeV]	$\frac{d^2\sigma_{\pi\pi}}{dt dm_{\pi\pi}}$	stat. [ $\frac{\mu\text{b}}{\text{GeV}^3}$ ]	syst.
0.5 0.56	71.6	9.3	+11.1 -11.3
0.56 0.6	116.1	9.9	+9.9 -14.3
0.6 0.63	158.6	11.3	+12.9 -17.2
0.63 0.66	201.0	10.9	+19.8 -14.0
0.66 0.68	254.6	16.1	+18.9 -18.7
0.68 0.7	329.5	15.5	+22.1 -34.5
0.7 0.72	352.4	15.7	+30.1 -27.3
0.72 0.74	411.6	15.4	+33.0 -29.2
0.74 0.76	412.7	15.2	+32.1 -30.0
0.76 0.78	408.2	14.5	+32.5 -27.4
0.78 0.8	270.7	13.5	+19.8 -19.9
0.8 0.82	209.9	11.9	+14.6 -14.9
0.82 0.84	132.7	10.9	+11.9 -9.3
0.84 0.87	83.6	6.4	+5.9 -6.7
0.87 0.92	46.3	3.4	+3.1 -4.1
0.92 1	17.7	1.4	+1.5 -1.8
1 1.2	3.39	0.43	+0.52 -0.64
1.2 2.2	0.533	0.077	+0.125 -0.149

F. CROSS-SECTION AND RELATED TABLES

$m_Y = m_p$ $\Phi_{\gamma/e} : 0.0346$				$m_Y = m_p$ $\Phi_{\gamma/e} : 0.0294$					
$0.062 <  t  \text{ [GeV}^2\text{]} < 0.1$				$0.062 <  t  \text{ [GeV}^2\text{]} < 0.1$					
$20 < W_{\gamma p} \text{ [GeV]} < 28$				$28 < W_{\gamma p} \text{ [GeV]} < 38$					
$m_{\pi\pi}$ [GeV]		$\frac{d^2\sigma_{\pi\pi}}{dt dm_{\pi\pi}}$	stat. [ $\frac{\mu\text{b}}{\text{GeV}^3}$ ]	syst.	$m_{\pi\pi}$ [GeV]		$\frac{d^2\sigma_{\pi\pi}}{dt dm_{\pi\pi}}$	stat. [ $\frac{\mu\text{b}}{\text{GeV}^3}$ ]	syst.
0.5	0.56	35.6	4.5	+6.1 -7.0	0.5	0.56	40.1	4.3	+5.6 -6.2
0.56	0.6	62.8	5.5	+5.2 -6.4	0.56	0.6	66.4	5.0	+4.9 -5.4
0.6	0.63	92.0	6.2	+6.7 -7.9	0.6	0.63	80.4	5.6	+4.7 -4.9
0.63	0.66	116.9	6.8	+8.4 -8.1	0.63	0.66	104.5	5.8	+6.4 -6.3
0.66	0.68	131.9	10.1	+10.3 -11.9	0.66	0.68	143.9	9.4	+8.8 -8.7
0.68	0.7	176.8	10.0	+12.2 -12.3	0.68	0.7	165.8	9.0	+9.3 -9.4
0.7	0.72	198.9	10.2	+16.8 -15.9	0.7	0.72	217.7	9.8	+12.6 -12.8
0.72	0.74	248.0	10.3	+18.2 -20.1	0.72	0.74	254.1	9.9	+14.0 -14.3
0.74	0.76	273.2	10.7	+19.3 -21.9	0.74	0.76	259.0	9.8	+15.2 -15.1
0.76	0.78	242.3	10.1	+22.7 -20.3	0.76	0.78	258.2	9.5	+14.5 -14.4
0.78	0.8	161.3	9.6	+14.4 -15.5	0.78	0.8	174.9	8.4	+9.8 -9.6
0.8	0.82	111.4	9.1	+8.9 -14.4	0.8	0.82	125.8	8.0	+7.3 -7.7
0.82	0.84	80.4	7.7	+6.8 -8.2	0.82	0.84	90.7	6.3	+6.0 -5.4
0.84	0.87	57.7	4.9	+4.5 -5.9	0.84	0.87	56.5	4.2	+4.1 -5.5
0.87	0.92	19.0	2.8	+2.5 -2.4	0.87	0.92	23.0	2.5	+1.9 -2.1
0.92	1	6.5	1.8	+0.8 -1.1	0.92	1	8.6	1.3	+0.9 -0.9
1	1.2	2.86	0.55	+0.42 -0.99	1	1.2	1.72	0.64	+0.47 -0.59
1.2	2.2	0.12	0.29	+0.25 -0.14	1.2	2.2	0.36	0.17	+0.10 -0.14

$m_Y = m_p$ $\Phi_{\gamma/e} : 0.0248$				$m_Y = m_p$ $\Phi_{\gamma/e} : 0.0383$					
$0.062 <  t  \text{ [GeV}^2\text{]} < 0.1$				$0.062 <  t  \text{ [GeV}^2\text{]} < 0.1$					
$38 < W_{\gamma p} \text{ [GeV]} < 50$				$50 < W_{\gamma p} \text{ [GeV]} < 80$					
$m_{\pi\pi}$ [GeV]		$\frac{d^2\sigma_{\pi\pi}}{dt dm_{\pi\pi}}$	stat. [ $\frac{\mu\text{b}}{\text{GeV}^3}$ ]	syst.	$m_{\pi\pi}$ [GeV]		$\frac{d^2\sigma_{\pi\pi}}{dt dm_{\pi\pi}}$	stat. [ $\frac{\mu\text{b}}{\text{GeV}^3}$ ]	syst.
0.5	0.56	51.5	5.3	+7.2 -9.2	0.5	0.56	44.2	5.7	+5.8 -8.1
0.56	0.6	65.9	6.0	+5.2 -5.5	0.56	0.6	69.8	6.2	+6.8 -7.3
0.6	0.63	89.9	7.2	+6.4 -5.9	0.6	0.63	92.5	7.3	+11.0 -7.6
0.63	0.66	118.4	7.4	+6.8 -8.1	0.63	0.66	126.4	7.0	+9.3 -17.5
0.66	0.68	163.5	10.7	+10.0 -9.8	0.66	0.68	158.3	10.0	+14.2 -12.6
0.68	0.7	200.7	10.8	+11.0 -11.6	0.68	0.7	216.6	10.4	+15.2 -15.3
0.7	0.72	223.1	10.5	+12.8 -12.9	0.7	0.72	246.2	10.4	+19.9 -17.8
0.72	0.74	274.3	11.3	+15.6 -14.5	0.72	0.74	286.4	10.3	+21.1 -21.8
0.74	0.76	286.1	10.8	+15.6 -15.7	0.74	0.76	318.0	10.1	+21.6 -20.7
0.76	0.78	264.4	10.9	+14.2 -15.1	0.76	0.78	277.1	9.6	+22.1 -19.2
0.78	0.8	186.9	10.3	+10.6 -10.4	0.78	0.8	193.5	8.6	+14.3 -13.8
0.8	0.82	124.7	8.2	+6.8 -6.6	0.8	0.82	152.9	8.3	+10.0 -10.9
0.82	0.84	96.2	7.0	+5.4 -7.4	0.82	0.84	94.6	7.4	+7.7 -10.1
0.84	0.87	61.0	4.1	+3.2 -3.4	0.84	0.87	63.6	4.8	+4.6 -5.3
0.87	0.92	27.7	2.3	+2.3 -1.9	0.87	0.92	33.3	2.3	+2.8 -2.6
0.92	1	9.7	1.0	+0.8 -1.3	0.92	1	11.1	1.3	+1.1 -1.3
1	1.2	1.65	0.33	+0.37 -0.64	1	1.2	2.44	0.33	+0.42 -0.69
1.2	2.2	0.35	0.12	+0.06 -0.13	1.2	2.2	0.424	0.066	+0.078 -0.076

F.1.  $\pi^+\pi^-$  CROSS-SECTIONS

$m_Y = m_p$   $\Phi_{\gamma/e} : 0.0346$   
 $0.1 < |t| [\text{GeV}^2] < 0.15$   
 $20 < W_{\gamma p} [\text{GeV}] < 28$

$m_{\pi\pi}$ [GeV]	$\frac{d^2\sigma_{\pi\pi}}{dt dm_{\pi\pi}}$	stat. [ $\frac{\mu\text{b}}{\text{GeV}^3}$ ]	syst.
0.5 0.56	19.3	3.4	+3.7 -2.9
0.56 0.6	32.1	4.2	+3.0 -4.4
0.6 0.63	59.3	4.8	+4.5 -7.9
0.63 0.66	60.5	5.2	+5.2 -5.1
0.66 0.68	87.7	7.1	+7.2 -7.8
0.68 0.7	121.6	7.6	+9.6 -9.8
0.7 0.72	126.5	7.5	+12.5 -11.6
0.72 0.74	161.0	8.0	+11.8 -16.9
0.74 0.76	171.6	7.9	+13.5 -15.7
0.76 0.78	157.9	7.8	+15.5 -13.0
0.78 0.8	114.6	7.2	+9.9 -13.5
0.8 0.82	87.9	6.8	+6.8 -13.2
0.82 0.84	59.8	6.0	+5.2 -7.3
0.84 0.87	40.4	3.6	+3.3 -7.4
0.87 0.92	18.6	2.7	+2.6 -3.2
0.92 1	6.1	1.2	+2.0 -0.7
1 1.2	1.87	0.42	+0.52 -0.46
1.2 2.2	0.29	0.17	+0.22 -0.27

$m_Y = m_p$   $\Phi_{\gamma/e} : 0.0294$   
 $0.1 < |t| [\text{GeV}^2] < 0.15$   
 $28 < W_{\gamma p} [\text{GeV}] < 38$

$m_{\pi\pi}$ [GeV]	$\frac{d^2\sigma_{\pi\pi}}{dt dm_{\pi\pi}}$	stat. [ $\frac{\mu\text{b}}{\text{GeV}^3}$ ]	syst.
0.5 0.56	25.2	3.6	+3.5 -3.2
0.56 0.6	38.3	4.1	+2.8 -3.1
0.6 0.63	47.4	4.1	+3.0 -3.7
0.63 0.66	63.2	4.3	+3.7 -3.7
0.66 0.68	96.8	6.6	+6.1 -5.7
0.68 0.7	108.2	6.5	+7.3 -6.9
0.7 0.72	141.9	6.8	+8.7 -8.4
0.72 0.74	157.1	7.0	+8.8 -8.9
0.74 0.76	175.3	6.9	+11.5 -10.7
0.76 0.78	180.9	7.2	+10.4 -10.5
0.78 0.8	109.7	6.2	+6.7 -6.9
0.8 0.82	87.5	5.6	+5.3 -5.1
0.82 0.84	59.6	5.5	+4.2 -5.0
0.84 0.87	41.5	3.0	+2.6 -2.9
0.87 0.92	17.0	2.0	+1.6 -1.4
0.92 1	9.04	0.74	+0.78 -0.95
1 1.2	2.07	0.51	+0.25 -0.49
1.2 2.2	0.17	0.12	+0.14 -0.12

$m_Y = m_p$   $\Phi_{\gamma/e} : 0.0248$   
 $0.1 < |t| [\text{GeV}^2] < 0.15$   
 $38 < W_{\gamma p} [\text{GeV}] < 50$

$m_{\pi\pi}$ [GeV]	$\frac{d^2\sigma_{\pi\pi}}{dt dm_{\pi\pi}}$	stat. [ $\frac{\mu\text{b}}{\text{GeV}^3}$ ]	syst.
0.5 0.56	24.4	4.0	+4.4 -3.9
0.56 0.6	45.1	4.1	+3.6 -3.6
0.6 0.63	49.2	4.5	+3.9 -4.2
0.63 0.66	81.2	5.6	+4.7 -5.0
0.66 0.68	97.1	7.1	+6.4 -5.9
0.68 0.7	129.0	7.8	+8.2 -8.8
0.7 0.72	150.0	7.7	+9.4 -8.6
0.72 0.74	163.7	7.9	+9.7 -10.3
0.74 0.76	178.9	7.9	+10.5 -10.3
0.76 0.78	175.2	7.4	+9.2 -9.7
0.78 0.8	117.0	7.2	+7.1 -7.8
0.8 0.82	103.6	7.0	+5.8 -6.2
0.82 0.84	60.4	5.0	+3.7 -3.8
0.84 0.87	39.5	2.9	+2.2 -2.1
0.87 0.92	22.5	2.0	+1.3 -1.3
0.92 1	7.78	0.77	+0.63 -0.73
1 1.2	2.18	0.28	+0.37 -0.49
1.2 2.2	0.437	0.055	+0.058 -0.057

$m_Y = m_p$   $\Phi_{\gamma/e} : 0.0383$   
 $0.1 < |t| [\text{GeV}^2] < 0.15$   
 $50 < W_{\gamma p} [\text{GeV}] < 80$

$m_{\pi\pi}$ [GeV]	$\frac{d^2\sigma_{\pi\pi}}{dt dm_{\pi\pi}}$	stat. [ $\frac{\mu\text{b}}{\text{GeV}^3}$ ]	syst.
0.5 0.56	28.9	3.9	+3.7 -6.4
0.56 0.6	45.5	4.4	+4.0 -5.1
0.6 0.63	65.9	5.3	+4.7 -5.0
0.63 0.66	85.2	5.1	+6.1 -6.5
0.66 0.68	109.6	7.4	+9.7 -13.8
0.68 0.7	133.1	7.4	+10.0 -9.4
0.7 0.72	154.1	7.4	+11.9 -10.5
0.72 0.74	175.2	7.3	+13.5 -16.6
0.74 0.76	204.6	7.5	+14.5 -13.6
0.76 0.78	185.0	7.0	+14.3 -15.0
0.78 0.8	130.1	6.6	+10.5 -10.7
0.8 0.82	89.8	5.8	+7.2 -6.2
0.82 0.84	69.5	5.2	+5.4 -5.3
0.84 0.87	44.4	3.3	+3.3 -3.8
0.87 0.92	23.3	1.8	+1.8 -1.9
0.92 1	8.28	0.74	+1.20 -1.12
1 1.2	2.17	0.26	+0.35 -0.46
1.2 2.2	0.462	0.061	+0.063 -0.117

F. CROSS-SECTION AND RELATED TABLES

$m_Y = m_p$		$\Phi_{\gamma/e} : 0.0346$		$m_Y = m_p$		$\Phi_{\gamma/e} : 0.0294$			
$0.15 <  t  \text{ [GeV}^2\text{]} < 0.23$		$20 < W_{\gamma p} \text{ [GeV]} < 28$		$0.15 <  t  \text{ [GeV}^2\text{]} < 0.23$		$28 < W_{\gamma p} \text{ [GeV]} < 38$			
$m_{\pi\pi}$ [GeV]		$\frac{d^2\sigma_{\pi\pi}}{dt dm_{\pi\pi}}$	stat. [ $\frac{\mu\text{b}}{\text{GeV}^3}$ ]	syst.	$m_{\pi\pi}$ [GeV]		$\frac{d^2\sigma_{\pi\pi}}{dt dm_{\pi\pi}}$	stat. [ $\frac{\mu\text{b}}{\text{GeV}^3}$ ]	syst.
0.5	0.56	9.2	2.0	+1.3 -1.8	0.5	0.56	11.6	1.9	+2.2 -1.5
0.56	0.6	17.6	2.1	+1.6 -2.1	0.56	0.6	16.3	1.8	+1.4 -1.6
0.6	0.63	19.4	2.8	+1.9 -3.5	0.6	0.63	27.2	2.6	+1.6 -1.8
0.63	0.66	40.2	2.7	+3.1 -3.3	0.63	0.66	29.8	2.3	+2.2 -2.1
0.66	0.68	44.3	4.7	+3.7 -7.0	0.66	0.68	46.2	3.6	+3.3 -3.4
0.68	0.7	55.6	4.5	+5.6 -5.0	0.68	0.7	59.3	4.0	+3.6 -3.6
0.7	0.72	77.1	4.9	+6.5 -6.4	0.7	0.72	73.2	4.1	+5.4 -4.9
0.72	0.74	84.1	4.8	+7.2 -7.7	0.72	0.74	85.3	4.2	+5.5 -5.4
0.74	0.76	98.2	4.9	+7.8 -9.7	0.74	0.76	106.8	4.3	+6.6 -7.0
0.76	0.78	94.8	4.9	+7.7 -7.6	0.76	0.78	96.3	4.4	+6.3 -6.2
0.78	0.8	59.0	4.6	+5.6 -5.5	0.78	0.8	74.0	3.7	+4.5 -4.5
0.8	0.82	52.4	4.1	+4.0 -6.0	0.8	0.82	43.9	3.6	+3.3 -2.9
0.82	0.84	37.9	4.4	+3.3 -6.9	0.82	0.84	35.8	2.9	+2.7 -2.8
0.84	0.87	24.7	2.9	+1.9 -3.9	0.84	0.87	22.8	2.0	+1.4 -1.9
0.87	0.92	12.0	1.6	+1.1 -1.4	0.87	0.92	13.53	0.95	+1.02 -1.08
0.92	1	4.1	1.1	+0.4 -0.7	0.92	1	4.90	0.69	+0.43 -0.72
1	1.2	0.72	0.42	+0.68 -0.36	1	1.2	0.98	0.36	+0.34 -0.27
1.2	2.2	-0.00	0.14	+0.39 -0.10	1.2	2.2	0.01	0.11	+0.08 -0.07

$m_Y = m_p$		$\Phi_{\gamma/e} : 0.0248$		$m_Y = m_p$		$\Phi_{\gamma/e} : 0.0383$			
$0.15 <  t  \text{ [GeV}^2\text{]} < 0.23$		$38 < W_{\gamma p} \text{ [GeV]} < 50$		$0.15 <  t  \text{ [GeV}^2\text{]} < 0.23$		$50 < W_{\gamma p} \text{ [GeV]} < 80$			
$m_{\pi\pi}$ [GeV]		$\frac{d^2\sigma_{\pi\pi}}{dt dm_{\pi\pi}}$	stat. [ $\frac{\mu\text{b}}{\text{GeV}^3}$ ]	syst.	$m_{\pi\pi}$ [GeV]		$\frac{d^2\sigma_{\pi\pi}}{dt dm_{\pi\pi}}$	stat. [ $\frac{\mu\text{b}}{\text{GeV}^3}$ ]	syst.
0.5	0.56	9.5	2.0	+2.1 -2.1	0.5	0.56	13.4	2.2	+2.2 -2.1
0.56	0.6	17.0	2.0	+1.5 -1.9	0.56	0.6	19.6	2.3	+2.1 -2.2
0.6	0.63	26.5	3.0	+2.1 -2.5	0.6	0.63	25.5	2.7	+2.2 -3.1
0.63	0.66	26.4	3.2	+2.1 -2.1	0.63	0.66	40.6	2.8	+3.0 -3.2
0.66	0.68	42.5	4.0	+2.6 -2.9	0.66	0.68	48.1	4.0	+4.5 -4.4
0.68	0.7	66.7	4.4	+4.0 -3.8	0.68	0.7	69.9	4.4	+6.1 -5.7
0.7	0.72	70.9	4.8	+6.8 -6.8	0.7	0.72	82.1	4.6	+6.9 -6.9
0.72	0.74	92.1	5.0	+5.7 -5.7	0.72	0.74	90.0	4.6	+7.2 -6.9
0.74	0.76	108.1	5.1	+6.1 -6.3	0.74	0.76	117.4	4.5	+8.5 -9.1
0.76	0.78	99.2	4.8	+5.3 -5.8	0.76	0.78	107.0	4.3	+7.6 -8.1
0.78	0.8	67.6	4.0	+3.9 -4.3	0.78	0.8	63.2	4.0	+5.3 -5.3
0.8	0.82	48.9	3.6	+3.8 -3.0	0.8	0.82	52.5	3.8	+4.1 -3.7
0.82	0.84	38.7	3.2	+2.3 -2.4	0.82	0.84	39.1	3.1	+2.8 -3.3
0.84	0.87	29.7	2.0	+1.9 -2.3	0.84	0.87	22.3	1.8	+1.7 -1.8
0.87	0.92	13.2	1.2	+0.8 -1.1	0.87	0.92	13.3	1.2	+1.2 -1.4
0.92	1	5.61	0.54	+0.49 -0.75	0.92	1	6.69	0.66	+0.62 -0.77
1	1.2	1.30	0.18	+0.22 -0.26	1	1.2	1.74	0.20	+0.25 -0.37
1.2	2.2	0.199	0.044	+0.055 -0.049	1.2	2.2	0.268	0.033	+0.050 -0.048

F.1.  $\pi^+\pi^-$  CROSS-SECTIONS

$m_Y = m_p$   $\Phi_{\gamma/e} : 0.0346$   
 $0.23 < |t| [\text{GeV}^2] < 1.5$   
 $20 < W_{\gamma p} [\text{GeV}] < 28$

$m_{\pi\pi}$ [GeV]	$\frac{d^2\sigma_{\pi\pi}}{dt dm_{\pi\pi}}$	stat. [ $\frac{\mu\text{b}}{\text{GeV}^3}$ ]	syst.
0.5 0.56	0.32	0.14	+0.10 -0.12
0.56 0.6	0.60	0.17	+0.20 -0.17
0.6 0.63	1.16	0.20	+0.18 -0.25
0.63 0.66	1.35	0.25	+0.26 -0.17
0.66 0.68	2.06	0.29	+0.32 -0.37
0.68 0.7	2.46	0.37	+0.43 -0.32
0.7 0.72	4.22	0.38	+0.70 -0.51
0.72 0.74	4.84	0.39	+0.69 -0.57
0.74 0.76	5.63	0.35	+0.61 -0.75
0.76 0.78	6.40	0.38	+0.59 -0.75
0.78 0.8	4.19	0.35	+0.50 -0.44
0.8 0.82	3.34	0.33	+0.36 -0.51
0.82 0.84	2.11	0.36	+0.34 -0.51
0.84 0.87	1.38	0.23	+0.22 -0.23
0.87 0.92	1.19	0.14	+0.11 -0.24
0.92 1	0.520	0.073	+0.090 -0.144
1 1.2	0.136	0.039	+0.041 -0.037
1.2 2.2	0.016	0.016	+0.012 -0.020

$m_Y = m_p$   $\Phi_{\gamma/e} : 0.0294$   
 $0.23 < |t| [\text{GeV}^2] < 1.5$   
 $28 < W_{\gamma p} [\text{GeV}] < 38$

$m_{\pi\pi}$ [GeV]	$\frac{d^2\sigma_{\pi\pi}}{dt dm_{\pi\pi}}$	stat. [ $\frac{\mu\text{b}}{\text{GeV}^3}$ ]	syst.
0.5 0.56	0.38	0.13	+0.13 -0.14
0.56 0.6	0.63	0.15	+0.13 -0.14
0.6 0.63	0.73	0.18	+0.13 -0.13
0.63 0.66	1.55	0.20	+0.16 -0.19
0.66 0.68	2.15	0.27	+0.31 -0.25
0.68 0.7	3.31	0.30	+0.26 -0.26
0.7 0.72	4.18	0.32	+0.43 -0.40
0.72 0.74	5.02	0.32	+0.47 -0.48
0.74 0.76	6.30	0.32	+0.52 -0.54
0.76 0.78	6.10	0.33	+0.49 -0.51
0.78 0.8	4.49	0.31	+0.46 -0.45
0.8 0.82	3.30	0.32	+0.38 -0.38
0.82 0.84	2.40	0.25	+0.27 -0.31
0.84 0.87	1.78	0.19	+0.20 -0.18
0.87 0.92	1.39	0.11	+0.12 -0.16
0.92 1	0.653	0.065	+0.076 -0.102
1 1.2	0.157	0.037	+0.041 -0.053
1.2 2.2	0.0305	0.0093	+0.0084 -0.0126

$m_Y = m_p$   $\Phi_{\gamma/e} : 0.0248$   
 $0.23 < |t| [\text{GeV}^2] < 1.5$   
 $38 < W_{\gamma p} [\text{GeV}] < 50$

$m_{\pi\pi}$ [GeV]	$\frac{d^2\sigma_{\pi\pi}}{dt dm_{\pi\pi}}$	stat. [ $\frac{\mu\text{b}}{\text{GeV}^3}$ ]	syst.
0.5 0.56	0.47	0.11	+0.16 -0.16
0.56 0.6	0.64	0.15	+0.15 -0.16
0.6 0.63	1.17	0.18	+0.17 -0.16
0.63 0.66	1.98	0.20	+0.16 -0.17
0.66 0.68	2.25	0.27	+0.25 -0.28
0.68 0.7	3.12	0.32	+0.26 -0.27
0.7 0.72	4.50	0.32	+0.36 -0.37
0.72 0.74	5.21	0.35	+0.45 -0.46
0.74 0.76	5.63	0.35	+0.45 -0.47
0.76 0.78	6.52	0.38	+0.54 -0.56
0.78 0.8	4.39	0.32	+0.37 -0.38
0.8 0.82	3.45	0.27	+0.29 -0.34
0.82 0.84	2.59	0.24	+0.27 -0.29
0.84 0.87	2.07	0.15	+0.14 -0.15
0.87 0.92	1.274	0.088	+0.121 -0.126
0.92 1	0.580	0.052	+0.075 -0.083
1 1.2	0.227	0.027	+0.049 -0.060
1.2 2.2	0.0300	0.0052	+0.0124 -0.0129

$m_Y = m_p$   $\Phi_{\gamma/e} : 0.0383$   
 $0.23 < |t| [\text{GeV}^2] < 1.5$   
 $50 < W_{\gamma p} [\text{GeV}] < 80$

$m_{\pi\pi}$ [GeV]	$\frac{d^2\sigma_{\pi\pi}}{dt dm_{\pi\pi}}$	stat. [ $\frac{\mu\text{b}}{\text{GeV}^3}$ ]	syst.
0.5 0.56	0.40	0.11	+0.19 -0.20
0.56 0.6	0.96	0.14	+0.14 -0.17
0.6 0.63	1.22	0.17	+0.18 -0.23
0.63 0.66	1.57	0.19	+0.23 -0.24
0.66 0.68	2.57	0.30	+0.28 -0.26
0.68 0.7	3.11	0.29	+0.35 -0.32
0.7 0.72	4.26	0.31	+0.42 -0.46
0.72 0.74	5.70	0.32	+0.46 -0.49
0.74 0.76	5.83	0.32	+0.56 -0.54
0.76 0.78	5.79	0.31	+0.65 -0.55
0.78 0.8	4.37	0.28	+0.42 -0.40
0.8 0.82	3.16	0.26	+0.35 -0.39
0.82 0.84	2.99	0.25	+0.31 -0.34
0.84 0.87	1.67	0.14	+0.21 -0.20
0.87 0.92	1.198	0.081	+0.127 -0.128
0.92 1	0.540	0.047	+0.094 -0.096
1 1.2	0.223	0.021	+0.058 -0.060
1.2 2.2	0.0315	0.0042	+0.0112 -0.0121

F. CROSS-SECTION AND RELATED TABLES

$m_p < m_Y < 10 \text{ GeV}$   $\Phi_{\gamma/e} : 0.0346$   
 $0 < |t| [\text{GeV}^2] < 0.05$   
 $20 < W_{\gamma p} [\text{GeV}] < 28$

$m_{\pi\pi}$ [GeV]	$\frac{d^2\sigma_{\pi\pi}}{dt dm_{\pi\pi}}$	stat. [ $\frac{\mu\text{b}}{\text{GeV}^3}$ ]	syst.
0.5 0.56	24.6	5.5	+6.1 -7.2
0.56 0.6	25.5	4.8	+4.5 -5.3
0.6 0.63	35.4	5.8	+6.0 -6.1
0.63 0.66	45.9	6.4	+9.3 -8.8
0.66 0.68	53.0	10.1	+11.1 -10.1
0.68 0.7	72.3	9.4	+13.3 -12.1
0.7 0.72	69.8	9.5	+14.4 -11.0
0.72 0.74	92.5	10.4	+13.7 -16.4
0.74 0.76	88.8	10.1	+16.2 -14.4
0.76 0.78	85.3	9.7	+14.7 -15.6
0.78 0.8	58.2	8.8	+10.7 -8.5
0.8 0.82	35.0	8.0	+8.5 -8.2
0.82 0.84	19.7	6.3	+6.5 -5.8
0.84 0.87	6.7	5.8	+3.2 -4.5
0.87 0.92	6.8	2.8	+2.2 -4.3
0.92 1	3.0	1.4	+1.1 -0.8
1 1.2	0.38	0.59	+0.55 -0.56
1.2 2.2	0.29	0.18	+0.11 -0.26

$m_p < m_Y < 10 \text{ GeV}$   $\Phi_{\gamma/e} : 0.0294$   
 $0 < |t| [\text{GeV}^2] < 0.05$   
 $28 < W_{\gamma p} [\text{GeV}] < 38$

$m_{\pi\pi}$ [GeV]	$\frac{d^2\sigma_{\pi\pi}}{dt dm_{\pi\pi}}$	stat. [ $\frac{\mu\text{b}}{\text{GeV}^3}$ ]	syst.
0.5 0.56	29.8	6.5	+6.5 -8.4
0.56 0.6	33.5	5.4	+5.1 -7.1
0.6 0.63	39.2	5.7	+6.1 -7.2
0.63 0.66	54.5	6.1	+7.7 -7.4
0.66 0.68	61.4	8.2	+8.5 -9.1
0.68 0.7	69.5	8.3	+9.6 -9.4
0.7 0.72	74.9	9.0	+10.6 -10.8
0.72 0.74	101.9	9.3	+12.8 -13.9
0.74 0.76	81.2	8.9	+16.2 -15.6
0.76 0.78	84.6	8.5	+14.5 -13.1
0.78 0.8	75.4	8.8	+10.1 -10.2
0.8 0.82	46.0	6.9	+7.5 -8.2
0.82 0.84	26.3	7.5	+5.5 -7.7
0.84 0.87	22.8	5.0	+5.5 -3.8
0.87 0.92	8.4	1.8	+1.6 -1.5
0.92 1	2.98	0.98	+1.02 -0.69
1 1.2	1.50	0.41	+0.61 -0.40
1.2 2.2	0.23	0.18	+0.17 -0.11

$m_p < m_Y < 10 \text{ GeV}$   $\Phi_{\gamma/e} : 0.0248$   
 $0 < |t| [\text{GeV}^2] < 0.05$   
 $38 < W_{\gamma p} [\text{GeV}] < 50$

$m_{\pi\pi}$ [GeV]	$\frac{d^2\sigma_{\pi\pi}}{dt dm_{\pi\pi}}$	stat. [ $\frac{\mu\text{b}}{\text{GeV}^3}$ ]	syst.
0.5 0.56	32.6	7.3	+7.2 -9.3
0.56 0.6	38.1	7.1	+6.4 -8.8
0.6 0.63	44.0	7.2	+5.7 -7.5
0.63 0.66	55.6	6.9	+10.3 -10.2
0.66 0.68	64.5	10.5	+11.0 -12.1
0.68 0.7	74.7	10.4	+11.3 -11.7
0.7 0.72	99.3	10.6	+15.6 -13.4
0.72 0.74	123.2	11.3	+18.4 -16.4
0.74 0.76	98.1	10.5	+14.4 -15.8
0.76 0.78	82.6	9.5	+12.1 -12.0
0.78 0.8	67.2	8.3	+7.8 -7.9
0.8 0.82	39.1	6.9	+7.3 -7.7
0.82 0.84	31.0	6.2	+6.0 -4.4
0.84 0.87	24.9	3.8	+3.5 -3.7
0.87 0.92	7.9	2.0	+1.8 -2.0
0.92 1	3.40	0.92	+0.82 -0.90
1 1.2	1.07	0.42	+0.34 -0.68
1.2 2.2	0.210	0.069	+0.051 -0.045

$m_p < m_Y < 10 \text{ GeV}$   $\Phi_{\gamma/e} : 0.0383$   
 $0 < |t| [\text{GeV}^2] < 0.05$   
 $50 < W_{\gamma p} [\text{GeV}] < 80$

$m_{\pi\pi}$ [GeV]	$\frac{d^2\sigma_{\pi\pi}}{dt dm_{\pi\pi}}$	stat. [ $\frac{\mu\text{b}}{\text{GeV}^3}$ ]	syst.
0.5 0.56	37.2	8.6	+8.4 -15.2
0.56 0.6	45.8	7.5	+11.4 -9.3
0.6 0.63	38.9	7.8	+5.7 -6.8
0.63 0.66	55.7	7.2	+12.1 -8.7
0.66 0.68	62.5	10.4	+15.6 -12.6
0.68 0.7	68.4	9.9	+14.6 -12.1
0.7 0.72	91.6	10.6	+17.8 -14.5
0.72 0.74	120.0	10.5	+19.6 -17.5
0.74 0.76	128.6	10.7	+20.2 -17.7
0.76 0.78	118.3	9.8	+16.4 -15.3
0.78 0.8	55.4	8.0	+13.4 -8.9
0.8 0.82	48.3	8.4	+11.4 -10.0
0.82 0.84	26.8	6.5	+6.3 -5.1
0.84 0.87	19.4	3.8	+5.3 -4.0
0.87 0.92	8.7	1.9	+1.8 -2.1
0.92 1	3.46	0.89	+0.97 -0.85
1 1.2	0.73	0.31	+0.45 -0.61
1.2 2.2	0.136	0.052	+0.062 -0.037

## F.1. $\pi^+\pi^-$ CROSS-SECTIONS

$m_p < m_Y < 10$  GeV  $\Phi_{\gamma/e} : 0.0346$

$0.05 < |t|$  [GeV<sup>2</sup>] < 0.11

$20 < W_{\gamma p}$  [GeV] < 28

$m_{\pi\pi}$ [GeV]	$\frac{d^2\sigma_{\pi\pi}}{dt dm_{\pi\pi}}$	stat. [ $\frac{\mu\text{b}}{\text{GeV}^3}$ ]	syst.
0.5 0.56	18.8	4.1	+3.8 -5.3
0.56 0.6	27.8	4.6	+5.3 -5.0
0.6 0.63	37.0	5.3	+5.1 -4.9
0.63 0.66	42.3	5.4	+6.1 -6.1
0.66 0.68	44.9	7.0	+8.8 -6.9
0.68 0.7	52.1	7.9	+9.8 -9.4
0.7 0.72	78.8	7.7	+12.0 -11.1
0.72 0.74	82.5	8.0	+12.8 -11.0
0.74 0.76	78.4	7.9	+12.1 -12.7
0.76 0.78	81.6	7.5	+11.0 -12.1
0.78 0.8	38.2	7.0	+14.5 -7.6
0.8 0.82	41.3	6.6	+6.6 -5.2
0.82 0.84	37.1	6.5	+10.3 -8.5
0.84 0.87	21.8	4.0	+5.2 -6.5
0.87 0.92	12.2	2.5	+2.1 -2.8
0.92 1	5.7	1.3	+0.8 -1.5
1 1.2	1.69	0.52	+0.35 -1.27
1.2 2.2	0.22	0.20	+0.13 -0.08

$m_p < m_Y < 10$  GeV  $\Phi_{\gamma/e} : 0.0294$

$0.05 < |t|$  [GeV<sup>2</sup>] < 0.11

$28 < W_{\gamma p}$  [GeV] < 38

$m_{\pi\pi}$ [GeV]	$\frac{d^2\sigma_{\pi\pi}}{dt dm_{\pi\pi}}$	stat. [ $\frac{\mu\text{b}}{\text{GeV}^3}$ ]	syst.
0.5 0.56	13.8	3.8	+3.3 -4.7
0.56 0.6	19.4	4.8	+5.9 -6.2
0.6 0.63	36.3	4.9	+4.1 -4.5
0.63 0.66	48.4	5.4	+6.8 -9.0
0.66 0.68	49.7	6.9	+8.4 -7.2
0.68 0.7	57.9	6.9	+9.5 -8.2
0.7 0.72	78.6	7.8	+11.8 -10.7
0.72 0.74	86.9	7.6	+13.8 -11.6
0.74 0.76	99.6	7.7	+13.5 -12.3
0.76 0.78	81.3	7.3	+11.0 -9.7
0.78 0.8	54.6	7.2	+8.6 -8.0
0.8 0.82	44.4	6.4	+5.6 -5.7
0.82 0.84	29.7	5.3	+4.3 -4.5
0.84 0.87	21.7	4.1	+4.4 -4.0
0.87 0.92	11.7	2.1	+1.6 -2.2
0.92 1	4.11	0.99	+0.71 -0.85
1 1.2	1.70	0.63	+0.54 -0.76
1.2 2.2	0.16	0.17	+0.06 -0.09

$m_p < m_Y < 10$  GeV  $\Phi_{\gamma/e} : 0.0248$

$0.05 < |t|$  [GeV<sup>2</sup>] < 0.11

$38 < W_{\gamma p}$  [GeV] < 50

$m_{\pi\pi}$ [GeV]	$\frac{d^2\sigma_{\pi\pi}}{dt dm_{\pi\pi}}$	stat. [ $\frac{\mu\text{b}}{\text{GeV}^3}$ ]	syst.
0.5 0.56	6.0	3.8	+3.0 -4.9
0.56 0.6	20.5	4.7	+3.4 -5.0
0.6 0.63	30.2	6.5	+6.3 -8.7
0.63 0.66	49.2	5.9	+6.7 -6.0
0.66 0.68	64.1	9.3	+9.6 -9.2
0.68 0.7	50.3	7.8	+7.7 -7.2
0.7 0.72	70.6	8.0	+8.6 -8.8
0.72 0.74	87.4	8.9	+11.9 -13.7
0.74 0.76	96.8	8.5	+11.6 -10.8
0.76 0.78	78.4	7.8	+12.9 -9.9
0.78 0.8	54.2	7.1	+7.7 -7.5
0.8 0.82	31.3	6.1	+4.1 -4.6
0.82 0.84	25.5	6.1	+11.7 -4.1
0.84 0.87	10.4	3.4	+3.8 -3.4
0.87 0.92	9.6	1.8	+1.5 -1.7
0.92 1	3.48	0.96	+0.74 -0.60
1 1.2	0.72	0.32	+0.41 -0.33
1.2 2.2	0.160	0.087	+0.081 -0.097

$m_p < m_Y < 10$  GeV  $\Phi_{\gamma/e} : 0.0383$

$0.05 < |t|$  [GeV<sup>2</sup>] < 0.11

$50 < W_{\gamma p}$  [GeV] < 80

$m_{\pi\pi}$ [GeV]	$\frac{d^2\sigma_{\pi\pi}}{dt dm_{\pi\pi}}$	stat. [ $\frac{\mu\text{b}}{\text{GeV}^3}$ ]	syst.
0.5 0.56	13.5	4.2	+3.9 -8.3
0.56 0.6	20.1	4.4	+3.5 -6.4
0.6 0.63	27.9	5.0	+5.1 -3.6
0.63 0.66	34.1	4.8	+7.7 -5.7
0.66 0.68	42.6	7.0	+9.4 -9.3
0.68 0.7	52.4	7.0	+9.7 -10.4
0.7 0.72	53.3	7.2	+10.5 -11.0
0.72 0.74	72.1	7.1	+10.6 -10.4
0.74 0.76	72.0	7.1	+14.9 -11.0
0.76 0.78	83.3	6.8	+11.8 -12.2
0.78 0.8	44.6	6.0	+7.9 -12.0
0.8 0.82	31.4	5.6	+5.9 -5.2
0.82 0.84	23.1	4.7	+4.0 -4.4
0.84 0.87	18.9	3.2	+3.7 -3.0
0.87 0.92	9.4	1.7	+2.0 -2.0
0.92 1	2.62	0.81	+0.76 -0.73
1 1.2	0.65	0.28	+0.36 -0.35
1.2 2.2	0.180	0.056	+0.059 -0.057

F. CROSS-SECTION AND RELATED TABLES

$m_p < m_Y < 10 \text{ GeV}$   $\Phi_{\gamma/e} : 0.0346$   
 $0.11 < |t| [\text{GeV}^2] < 0.21$   
 $20 < W_{\gamma p} [\text{GeV}] < 28$

$m_{\pi\pi}$ [GeV]	$\frac{d^2\sigma_{\pi\pi}}{dt dm_{\pi\pi}}$	stat. $\left[\frac{\mu\text{b}}{\text{GeV}^3}\right]$	syst.
0.5 0.56	11.5	2.3	+2.8 -3.8
0.56 0.6	13.5	2.5	+3.0 -3.2
0.6 0.63	15.0	3.3	+4.6 -3.1
0.63 0.66	23.3	3.1	+3.7 -3.3
0.66 0.68	26.2	4.5	+5.4 -4.4
0.68 0.7	35.8	4.5	+5.1 -5.4
0.7 0.72	51.6	4.8	+7.4 -7.2
0.72 0.74	53.5	4.6	+11.1 -7.8
0.74 0.76	57.6	4.7	+8.0 -8.3
0.76 0.78	60.4	4.6	+8.2 -8.3
0.78 0.8	36.7	4.3	+6.4 -5.8
0.8 0.82	24.7	4.1	+4.9 -4.5
0.82 0.84	19.3	3.9	+5.5 -4.8
0.84 0.87	10.9	2.5	+3.1 -2.2
0.87 0.92	9.5	1.5	+2.1 -2.2
0.92 1	2.64	0.96	+0.75 -0.93
1 1.2	1.08	0.37	+0.38 -0.43
1.2 2.2	0.35	0.12	+0.09 -0.12

$m_p < m_Y < 10 \text{ GeV}$   $\Phi_{\gamma/e} : 0.0294$   
 $0.11 < |t| [\text{GeV}^2] < 0.21$   
 $28 < W_{\gamma p} [\text{GeV}] < 38$

$m_{\pi\pi}$ [GeV]	$\frac{d^2\sigma_{\pi\pi}}{dt dm_{\pi\pi}}$	stat. $\left[\frac{\mu\text{b}}{\text{GeV}^3}\right]$	syst.
0.5 0.56	3.9	2.1	+2.5 -3.6
0.56 0.6	12.6	2.4	+2.5 -3.3
0.6 0.63	13.3	3.0	+3.1 -2.5
0.63 0.66	28.3	2.9	+2.8 -3.2
0.66 0.68	26.4	4.0	+3.8 -3.8
0.68 0.7	29.8	4.0	+5.6 -4.9
0.7 0.72	45.9	4.5	+5.7 -5.9
0.72 0.74	45.5	4.6	+7.8 -6.3
0.74 0.76	62.6	4.4	+8.1 -7.3
0.76 0.78	56.1	4.4	+8.0 -6.8
0.78 0.8	39.1	4.0	+5.5 -4.3
0.8 0.82	23.0	3.4	+3.6 -4.5
0.82 0.84	24.7	3.5	+3.1 -3.4
0.84 0.87	10.5	2.1	+3.9 -2.0
0.87 0.92	11.4	1.5	+1.5 -1.7
0.92 1	3.70	0.73	+0.54 -0.68
1 1.2	0.92	0.36	+0.32 -0.36
1.2 2.2	0.360	0.088	+0.098 -0.109

$m_p < m_Y < 10 \text{ GeV}$   $\Phi_{\gamma/e} : 0.0248$   
 $0.11 < |t| [\text{GeV}^2] < 0.21$   
 $38 < W_{\gamma p} [\text{GeV}] < 50$

$m_{\pi\pi}$ [GeV]	$\frac{d^2\sigma_{\pi\pi}}{dt dm_{\pi\pi}}$	stat. $\left[\frac{\mu\text{b}}{\text{GeV}^3}\right]$	syst.
0.5 0.56	6.2	2.2	+3.3 -3.6
0.56 0.6	7.4	2.3	+2.2 -2.1
0.6 0.63	16.4	3.0	+3.1 -2.6
0.63 0.66	21.8	3.1	+2.6 -2.8
0.66 0.68	22.2	4.5	+3.7 -3.8
0.68 0.7	29.6	5.3	+5.9 -5.7
0.7 0.72	39.8	4.9	+6.4 -5.7
0.72 0.74	58.9	5.1	+6.7 -8.2
0.74 0.76	56.8	4.9	+6.7 -5.8
0.76 0.78	38.8	4.6	+7.5 -5.3
0.78 0.8	34.2	4.2	+6.3 -4.2
0.8 0.82	23.7	3.9	+3.3 -4.3
0.82 0.84	18.0	3.4	+2.9 -2.5
0.84 0.87	13.3	2.2	+1.6 -1.6
0.87 0.92	6.5	1.2	+0.9 -0.8
0.92 1	2.98	0.62	+0.48 -0.57
1 1.2	0.53	0.24	+0.26 -0.36
1.2 2.2	0.271	0.057	+0.055 -0.139

$m_p < m_Y < 10 \text{ GeV}$   $\Phi_{\gamma/e} : 0.0383$   
 $0.11 < |t| [\text{GeV}^2] < 0.21$   
 $50 < W_{\gamma p} [\text{GeV}] < 80$

$m_{\pi\pi}$ [GeV]	$\frac{d^2\sigma_{\pi\pi}}{dt dm_{\pi\pi}}$	stat. $\left[\frac{\mu\text{b}}{\text{GeV}^3}\right]$	syst.
0.5 0.56	5.7	1.9	+1.7 -2.7
0.56 0.6	8.9	2.1	+2.6 -2.8
0.6 0.63	9.3	2.6	+2.8 -2.3
0.63 0.66	15.7	2.6	+2.9 -2.6
0.66 0.68	23.4	4.2	+5.2 -6.5
0.68 0.7	32.0	4.1	+4.5 -5.4
0.7 0.72	40.5	4.0	+5.8 -5.2
0.72 0.74	41.1	4.0	+8.3 -5.2
0.74 0.76	43.9	3.9	+6.8 -5.8
0.76 0.78	42.2	3.9	+6.8 -6.3
0.78 0.8	28.2	3.5	+4.7 -4.4
0.8 0.82	21.4	3.2	+2.9 -3.5
0.82 0.84	15.3	3.5	+4.3 -2.7
0.84 0.87	11.8	2.2	+1.7 -1.6
0.87 0.92	7.9	1.1	+1.0 -1.2
0.92 1	2.97	0.54	+0.53 -0.60
1 1.2	0.87	0.21	+0.22 -0.23
1.2 2.2	0.093	0.036	+0.040 -0.052

## F.1. $\pi^+\pi^-$ CROSS-SECTIONS

$m_p < m_Y < 10 \text{ GeV}$		$\Phi_{\gamma/e} : 0.0346$		$m_p < m_Y < 10 \text{ GeV}$		$\Phi_{\gamma/e} : 0.0294$		
$0.21 <  t  [\text{GeV}^2] < 0.4$				$0.21 <  t  [\text{GeV}^2] < 0.4$				
$20 < W_{\gamma p} [\text{GeV}] < 28$				$28 < W_{\gamma p} [\text{GeV}] < 38$				
$m_{\pi\pi}$ [GeV]		$\frac{d^2\sigma_{\pi\pi}}{dt dm_{\pi\pi}}$	stat. $\left[\frac{\mu\text{b}}{\text{GeV}^3}\right]$	syst.	$m_{\pi\pi}$ [GeV]	$\frac{d^2\sigma_{\pi\pi}}{dt dm_{\pi\pi}}$	stat. $\left[\frac{\mu\text{b}}{\text{GeV}^3}\right]$	syst.
0.5	0.56	2.7	1.1	+1.7 -1.5	0.5	2.70	0.93	+1.10 -1.61
0.56	0.6	6.7	1.2	+1.4 -1.6	0.56	4.9	1.3	+1.1 -1.4
0.6	0.63	10.7	1.7	+1.8 -2.0	0.6	9.5	1.4	+1.3 -1.2
0.63	0.66	10.7	1.6	+1.8 -1.6	0.63	9.5	1.3	+1.3 -1.2
0.66	0.68	12.6	2.4	+3.3 -2.4	0.66	14.7	2.1	+1.9 -2.0
0.68	0.7	15.0	2.3	+2.7 -3.2	0.68	13.9	2.3	+2.1 -2.3
0.7	0.72	25.6	2.4	+3.2 -4.2	0.7	22.5	2.3	+2.9 -3.1
0.72	0.74	25.4	2.6	+4.4 -4.6	0.72	27.0	2.2	+3.4 -3.2
0.74	0.76	28.1	2.5	+4.3 -4.2	0.74	27.0	2.2	+5.2 -3.2
0.76	0.78	32.0	2.5	+4.5 -4.2	0.76	29.4	2.2	+3.7 -3.2
0.78	0.8	24.3	2.4	+3.9 -3.4	0.78	20.8	2.1	+3.3 -2.7
0.8	0.82	22.2	2.3	+3.2 -3.4	0.8	21.1	2.0	+2.6 -2.9
0.82	0.84	17.4	2.2	+3.6 -4.2	0.82	15.8	2.0	+3.0 -2.1
0.84	0.87	9.6	1.4	+1.4 -2.9	0.84	7.4	1.4	+1.2 -1.3
0.87	0.92	4.80	0.83	+1.08 -0.92	0.87	4.74	0.79	+0.78 -0.82
0.92	1	2.14	0.53	+0.38 -0.53	0.92	1.74	0.49	+0.60 -0.50
1	1.2	0.89	0.21	+0.18 -0.37	1	0.62	0.23	+0.20 -0.21
1.2	2.2	0.142	0.073	+0.074 -0.061	1.2	0.241	0.051	+0.181 -0.122

$m_p < m_Y < 10 \text{ GeV}$		$\Phi_{\gamma/e} : 0.0248$		$m_p < m_Y < 10 \text{ GeV}$		$\Phi_{\gamma/e} : 0.0383$		
$0.21 <  t  [\text{GeV}^2] < 0.4$				$0.21 <  t  [\text{GeV}^2] < 0.4$				
$38 < W_{\gamma p} [\text{GeV}] < 50$				$50 < W_{\gamma p} [\text{GeV}] < 80$				
$m_{\pi\pi}$ [GeV]		$\frac{d^2\sigma_{\pi\pi}}{dt dm_{\pi\pi}}$	stat. $\left[\frac{\mu\text{b}}{\text{GeV}^3}\right]$	syst.	$m_{\pi\pi}$ [GeV]	$\frac{d^2\sigma_{\pi\pi}}{dt dm_{\pi\pi}}$	stat. $\left[\frac{\mu\text{b}}{\text{GeV}^3}\right]$	syst.
0.5	0.56	1.34	0.95	+1.55 -1.73	0.5	1.65	0.86	+1.17 -1.60
0.56	0.6	4.7	1.1	+1.0 -1.1	0.56	3.7	1.1	+2.0 -1.2
0.6	0.63	5.4	1.2	+1.0 -1.0	0.6	7.8	1.2	+1.3 -1.4
0.63	0.66	9.0	1.3	+1.4 -1.4	0.63	5.9	1.2	+1.5 -1.4
0.66	0.68	15.7	2.3	+1.9 -2.2	0.66	7.4	1.7	+1.5 -2.0
0.68	0.7	19.8	2.5	+2.0 -2.3	0.68	16.4	1.9	+1.8 -1.8
0.7	0.72	23.7	2.5	+3.9 -3.7	0.7	18.0	2.0	+2.5 -2.6
0.72	0.74	26.6	2.5	+3.5 -3.4	0.72	23.4	2.0	+2.9 -2.6
0.74	0.76	26.7	2.5	+4.2 -2.8	0.74	23.7	2.0	+3.5 -3.9
0.76	0.78	27.6	2.5	+4.2 -3.8	0.76	27.2	2.0	+3.2 -3.4
0.78	0.8	16.8	2.2	+2.6 -2.2	0.78	17.0	1.9	+2.7 -2.3
0.8	0.82	18.8	2.0	+2.6 -2.2	0.8	9.8	1.6	+2.6 -1.6
0.82	0.84	12.3	1.7	+2.1 -1.8	0.82	10.3	1.5	+1.6 -1.4
0.84	0.87	8.7	1.3	+1.1 -1.5	0.84	6.24	0.96	+0.94 -1.08
0.87	0.92	3.35	0.62	+0.72 -0.77	0.87	2.90	0.54	+0.74 -0.61
0.92	1	2.20	0.49	+0.38 -0.44	0.92	1.63	0.29	+0.45 -0.43
1	1.2	0.55	0.13	+0.24 -0.25	1	0.29	0.11	+0.24 -0.26
1.2	2.2	0.112	0.032	+0.053 -0.052	1.2	0.090	0.020	+0.048 -0.046

## F. CROSS-SECTION AND RELATED TABLES

$m_p < m_Y < 10 \text{ GeV}$				$m_p < m_Y < 10 \text{ GeV}$					
$\Phi_{\gamma/e} : 0.0346$				$\Phi_{\gamma/e} : 0.0294$					
$0.4 <  t  [\text{GeV}^2] < 1.5$				$0.4 <  t  [\text{GeV}^2] < 1.5$					
$20 < W_{\gamma p} [\text{GeV}] < 28$				$28 < W_{\gamma p} [\text{GeV}] < 38$					
$m_{\pi\pi}$ [GeV]		$\frac{d^2\sigma_{\pi\pi}}{dt dm_{\pi\pi}}$	stat. $\left[\frac{\mu\text{b}}{\text{GeV}^3}\right]$	syst.	$m_{\pi\pi}$ [GeV]		$\frac{d^2\sigma_{\pi\pi}}{dt dm_{\pi\pi}}$	stat. $\left[\frac{\mu\text{b}}{\text{GeV}^3}\right]$	syst.
0.5	0.56	0.22	0.18	+0.32 -0.17	0.5	0.56	0.37	0.12	+0.13 -0.17
0.56	0.6	0.53	0.16	+0.20 -0.28	0.56	0.6	0.56	0.13	+0.14 -0.16
0.6	0.63	1.16	0.29	+0.32 -0.38	0.6	0.63	0.61	0.27	+0.18 -0.19
0.63	0.66	1.26	0.24	+0.33 -0.24	0.63	0.66	0.97	0.20	+0.26 -0.20
0.66	0.68	2.42	0.46	+0.59 -0.41	0.66	0.68	2.11	0.27	+0.29 -0.28
0.68	0.7	2.71	0.41	+0.44 -0.46	0.68	0.7	1.66	0.31	+0.28 -0.26
0.7	0.72	2.42	0.43	+0.55 -0.58	0.7	0.72	3.27	0.33	+0.42 -0.41
0.72	0.74	3.94	0.48	+0.58 -0.54	0.72	0.74	3.85	0.39	+0.53 -0.50
0.74	0.76	4.30	0.47	+0.76 -0.73	0.74	0.76	4.46	0.36	+0.59 -0.54
0.76	0.78	4.62	0.46	+0.73 -0.70	0.76	0.78	4.20	0.40	+0.60 -0.57
0.78	0.8	3.66	0.46	+1.02 -0.76	0.78	0.8	3.46	0.36	+0.54 -0.52
0.8	0.82	3.64	0.46	+0.57 -1.04	0.8	0.82	3.18	0.38	+0.45 -0.47
0.82	0.84	2.94	0.44	+0.60 -0.90	0.82	0.84	2.48	0.29	+0.41 -0.34
0.84	0.87	2.00	0.30	+0.33 -0.34	0.84	0.87	2.08	0.19	+0.29 -0.25
0.87	0.92	0.91	0.22	+0.36 -0.25	0.87	0.92	0.90	0.16	+0.23 -0.14
0.92	1	0.69	0.15	+0.14 -0.22	0.92	1	0.53	0.12	+0.12 -0.12
1	1.2	0.280	0.064	+0.069 -0.100	1	1.2	0.283	0.045	+0.082 -0.116
1.2	2.2	0.023	0.022	+0.030 -0.017	1.2	2.2	0.049	0.012	+0.017 -0.016

$m_p < m_Y < 10 \text{ GeV}$				$m_p < m_Y < 10 \text{ GeV}$					
$\Phi_{\gamma/e} : 0.0248$				$\Phi_{\gamma/e} : 0.0383$					
$0.4 <  t  [\text{GeV}^2] < 1.5$				$0.4 <  t  [\text{GeV}^2] < 1.5$					
$38 < W_{\gamma p} [\text{GeV}] < 50$				$50 < W_{\gamma p} [\text{GeV}] < 80$					
$m_{\pi\pi}$ [GeV]		$\frac{d^2\sigma_{\pi\pi}}{dt dm_{\pi\pi}}$	stat. $\left[\frac{\mu\text{b}}{\text{GeV}^3}\right]$	syst.	$m_{\pi\pi}$ [GeV]		$\frac{d^2\sigma_{\pi\pi}}{dt dm_{\pi\pi}}$	stat. $\left[\frac{\mu\text{b}}{\text{GeV}^3}\right]$	syst.
0.5	0.56	0.08	0.10	+0.15 -0.17	0.5	0.56	0.252	0.098	+0.131 -0.170
0.56	0.6	0.45	0.17	+0.16 -0.19	0.56	0.6	0.07	0.11	+0.14 -0.14
0.6	0.63	0.56	0.17	+0.26 -0.27	0.6	0.63	0.46	0.14	+0.18 -0.20
0.63	0.66	0.89	0.18	+0.16 -0.18	0.63	0.66	0.86	0.15	+0.23 -0.24
0.66	0.68	1.78	0.27	+0.23 -0.25	0.66	0.68	1.20	0.23	+0.33 -0.40
0.68	0.7	1.18	0.29	+0.29 -0.28	0.68	0.7	1.74	0.27	+0.29 -0.27
0.7	0.72	2.29	0.33	+0.34 -0.32	0.7	0.72	1.86	0.27	+0.43 -0.40
0.72	0.74	3.01	0.40	+0.38 -0.34	0.72	0.74	2.92	0.31	+0.47 -0.39
0.74	0.76	4.57	0.42	+0.50 -0.39	0.74	0.76	3.91	0.31	+0.52 -0.55
0.76	0.78	4.41	0.38	+0.54 -0.51	0.76	0.78	4.32	0.34	+0.51 -0.49
0.78	0.8	3.07	0.34	+0.39 -0.37	0.78	0.8	2.83	0.29	+0.42 -0.49
0.8	0.82	2.43	0.32	+0.34 -0.29	0.8	0.82	2.43	0.27	+0.29 -0.27
0.82	0.84	2.36	0.37	+0.40 -0.33	0.82	0.84	2.17	0.27	+0.31 -0.38
0.84	0.87	1.20	0.20	+0.21 -0.18	0.84	0.87	1.46	0.17	+0.24 -0.53
0.87	0.92	1.02	0.10	+0.14 -0.16	0.87	0.92	0.993	0.087	+0.149 -0.144
0.92	1	0.554	0.083	+0.100 -0.143	0.92	1	0.489	0.055	+0.106 -0.108
1	1.2	0.208	0.029	+0.054 -0.057	1	1.2	0.170	0.023	+0.068 -0.073
1.2	2.2	0.0557	0.0065	+0.0152 -0.0160	1.2	2.2	0.0357	0.0054	+0.0149 -0.0152

**Table F.6:** Unfolded differential cross-section  $d^2\sigma(\gamma p \rightarrow \pi^+\pi^-Y)/dm_{\pi\pi}dt$  in bins of  $m_{\pi\pi}$ ,  $W_{\gamma p}$ , and  $t$ .  $ep$  cross-sections are scaled by a  $W_{\gamma p}$ -dependent photon flux factor as given in the tables. Splitting a normalization uncertainty from the (symmetrized) total covariance matrix according to Appendix C.3 yields  $\Delta_{\text{norm}} = 4.2\%$ . Further correlations are not provided.

## F.2 $\rho^0$ Cross-Sections

### F.2.1 $\sigma(\gamma p \rightarrow \rho^0 Y)(W_{\gamma p})$

$m_Y = m_p$				$m_p < m_Y < 10 \text{ GeV}$					
$W_{\gamma p}$		$\sigma_\rho$	stat.	syst.	$W_{\gamma p}$		$\sigma_\rho$	stat.	syst.
[GeV]			[ $\mu\text{b}$ ]		[GeV]			[ $\mu\text{b}$ ]	
20	25	10.50	0.11	+0.84 -1.07	20	26	5.25	0.14	+0.77 -0.73
25	30	11.009	0.093	+0.795 -0.801	26	32	5.17	0.11	+0.71 -0.67
30	35	11.348	0.092	+0.693 -0.682	32	38	5.23	0.11	+0.64 -0.61
35	40	11.476	0.092	+0.614 -0.618	38	46	4.918	0.099	+0.596 -0.574
40	45	11.93	0.10	+0.64 -0.64	46	56	4.76	0.10	+0.66 -0.60
45	50	12.16	0.11	+0.71 -0.71	56	80	4.45	0.10	+0.62 -0.58
50	56	12.60	0.12	+0.83 -0.82					
56	66	12.53	0.11	+0.89 -0.87					
66	80	12.42	0.15	+0.97 -0.95					

**Table F.7:** Differential cross-section  $\sigma(\gamma p \rightarrow \rho^0 Y)$  in bins of  $W_{\gamma p}$ . The cross-section is obtained from a Söding fit of the unfolded differential cross-section  $d\sigma(\gamma p \rightarrow \pi^+ \pi^- Y)/dm_{\pi\pi}(m_{\pi\pi}; W_{\gamma p})$  and integration of the  $\rho^0$  amplitude in the range  $2m_\pi < m_{\pi\pi} < 1.53 \text{ GeV}$ . Splitting a normalization uncertainty from the (symmetrized) total covariance matrix according to Appendix C.3 yields  $\Delta_{\text{norm}} = 4.7\%$ . Further correlations are not provided.

### F.2.2 $d\sigma(\gamma p \rightarrow \rho^0 Y)/dt(t)$

$m_Y = m_p$				$m_p < m_Y < 10 \text{ GeV}$					
$ t $		$\frac{d\sigma_\rho}{dt}$	stat.	syst.	$ t $		$\frac{d\sigma_\rho}{dt}$	stat.	syst.
[GeV $^2$ ]			[ $\frac{\mu\text{b}}{\text{GeV}^2}$ ]		[GeV $^2$ ]			[ $\frac{\mu\text{b}}{\text{GeV}^2}$ ]	
0	0.008	105.0	1.5	+6.5 -6.6	0	0.03	15.21	0.60	+2.55 -2.35
0.008	0.018	93.4	1.3	+5.6 -5.7	0.03	0.06	16.68	0.61	+2.57 -2.43
0.018	0.03	83.6	1.1	+5.1 -5.1	0.06	0.096	15.31	0.52	+2.11 -2.05
0.03	0.044	75.7	1.0	+4.6 -4.6	0.096	0.14	12.17	0.41	+1.59 -1.64
0.044	0.06	65.12	0.85	+3.95 -3.95	0.14	0.2	9.65	0.30	+1.31 -1.28
0.06	0.078	53.58	0.73	+3.29 -3.37	0.2	0.28	7.44	0.22	+1.00 -0.92
0.078	0.1	45.14	0.60	+2.74 -2.82	0.28	0.39	4.90	0.15	+0.65 -0.63
0.1	0.126	36.34	0.50	+2.25 -2.34	0.39	0.6	2.604	0.068	+0.324 -0.310
0.126	0.156	28.90	0.39	+1.79 -1.80	0.6	1.5	0.557	0.019	+0.085 -0.089
0.156	0.2	20.87	0.27	+1.31 -1.31					
0.2	0.28	12.40	0.16	+0.82 -0.84					
0.28	1.5	0.850	0.021	+0.083 -0.085					

**Table F.8:** Differential cross-section  $d\sigma(\gamma p \rightarrow \rho^0 Y)/dt$  in bins of  $t$ . The cross-section is obtained from a Söding fit of the unfolded differential cross-section  $d^2\sigma(\gamma p \rightarrow \pi^+ \pi^- Y)/dm_{\pi\pi} dt(m_{\pi\pi}; t)$  and integration of the  $\rho^0$  amplitude in the range  $2m_\pi < m_{\pi\pi} < 1.53 \text{ GeV}$ . Splitting a normalization uncertainty from the (symmetrized) total covariance matrix according to Appendix C.3 yields  $\Delta_{\text{norm}} = 5.6\%$ . Further correlations are not provided.

F.2.3  $d\sigma(\gamma p \rightarrow \rho^0 Y)/dt(W_{\gamma p}, t)$ 

$m_Y = m_p$					$m_Y = m_p$				
$20 < W_{\gamma p} [\text{GeV}] < 28$					$28 < W_{\gamma p} [\text{GeV}] < 38$				
$ t $ [GeV <sup>2</sup> ]		$\frac{d\sigma_\rho}{dt}$	stat.	syst.	$ t $ [GeV <sup>2</sup> ]		$\frac{d\sigma_\rho}{dt}$	stat.	syst.
			$\left[\frac{\mu\text{b}}{\text{GeV}^2}\right]$					$\left[\frac{\mu\text{b}}{\text{GeV}^2}\right]$	
0	0.016	87.5	1.4	+6.4 -6.9	0	0.016	94.0	1.3	+5.1 -5.1
0.016	0.036	72.6	1.2	+5.3 -6.1	0.016	0.036	78.8	1.1	+4.2 -4.3
0.036	0.062	60.1	1.0	+4.4 -5.1	0.036	0.062	64.00	0.93	+3.45 -3.53
0.062	0.1	45.06	0.71	+3.30 -3.61	0.062	0.1	46.11	0.65	+2.57 -2.57
0.1	0.15	30.98	0.55	+2.37 -2.67	0.1	0.15	31.81	0.47	+1.85 -1.85
0.15	0.23	18.36	0.36	+1.43 -1.60	0.15	0.23	18.80	0.28	+1.14 -1.14
0.23	1.5	1.157	0.032	+0.117 -0.133	0.23	1.5	1.224	0.028	+0.105 -0.109

$m_Y = m_p$					$m_Y = m_p$				
$38 < W_{\gamma p} [\text{GeV}] < 50$					$50 < W_{\gamma p} [\text{GeV}] < 80$				
$ t $ [GeV <sup>2</sup> ]		$\frac{d\sigma_\rho}{dt}$	stat.	syst.	$ t $ [GeV <sup>2</sup> ]		$\frac{d\sigma_\rho}{dt}$	stat.	syst.
			$\left[\frac{\mu\text{b}}{\text{GeV}^2}\right]$					$\left[\frac{\mu\text{b}}{\text{GeV}^2}\right]$	
0	0.016	102.8	1.4	+5.7 -5.7	0	0.016	111.6	1.6	+7.8 -8.1
0.016	0.036	83.9	1.2	+4.5 -4.5	0.016	0.036	92.4	1.3	+6.4 -6.2
0.036	0.062	68.31	0.98	+3.71 -3.68	0.036	0.062	75.0	1.1	+5.2 -5.0
0.062	0.1	49.75	0.69	+2.64 -2.65	0.062	0.1	53.48	0.73	+3.70 -3.59
0.1	0.15	33.53	0.50	+1.81 -1.83	0.1	0.15	35.98	0.52	+2.49 -2.42
0.15	0.23	19.38	0.31	+1.05 -1.07	0.15	0.23	20.22	0.32	+1.41 -1.38
0.23	1.5	1.257	0.029	+0.094 -0.101	0.23	1.5	1.206	0.030	+0.109 -0.107

$m_p < m_Y < 10 \text{ GeV}$					$m_p < m_Y < 10 \text{ GeV}$				
$20 < W_{\gamma p} [\text{GeV}] < 28$					$28 < W_{\gamma p} [\text{GeV}] < 38$				
$ t $ [GeV <sup>2</sup> ]		$\frac{d\sigma_\rho}{dt}$	stat.	syst.	$ t $ [GeV <sup>2</sup> ]		$\frac{d\sigma_\rho}{dt}$	stat.	syst.
			$\left[\frac{\mu\text{b}}{\text{GeV}^2}\right]$					$\left[\frac{\mu\text{b}}{\text{GeV}^2}\right]$	
0	0.05	14.47	0.64	+2.56 -2.28	0	0.05	15.70	0.61	+2.38 -2.32
0.05	0.11	14.92	0.62	+2.30 -2.16	0.05	0.11	16.08	0.60	+2.25 -2.15
0.11	0.21	11.12	0.43	+1.69 -1.61	0.11	0.21	10.72	0.36	+1.39 -1.32
0.21	0.4	6.40	0.23	+0.93 -0.99	0.21	0.4	6.06	0.19	+0.76 -0.69
0.4	1.5	1.058	0.044	+0.165 -0.164	0.4	1.5	1.004	0.031	+0.132 -0.121

$m_p < m_Y < 10 \text{ GeV}$					$m_p < m_Y < 10 \text{ GeV}$				
$38 < W_{\gamma p} [\text{GeV}] < 50$					$50 < W_{\gamma p} [\text{GeV}] < 80$				
$ t $ [GeV <sup>2</sup> ]		$\frac{d\sigma_\rho}{dt}$	stat.	syst.	$ t $ [GeV <sup>2</sup> ]		$\frac{d\sigma_\rho}{dt}$	stat.	syst.
			$\left[\frac{\mu\text{b}}{\text{GeV}^2}\right]$					$\left[\frac{\mu\text{b}}{\text{GeV}^2}\right]$	
0	0.05	17.02	0.62	+2.54 -2.51	0	0.05	17.51	0.71	+3.12 -2.73
0.05	0.11	14.74	0.55	+2.00 -1.97	0.05	0.11	13.03	0.53	+2.12 -1.99
0.11	0.21	9.70	0.35	+1.25 -1.17	0.11	0.21	8.59	0.33	+1.26 -1.17
0.21	0.4	5.77	0.19	+0.76 -0.69	0.21	0.4	4.76	0.16	+0.62 -0.60
0.4	1.5	0.863	0.029	+0.105 -0.096	0.4	1.5	0.821	0.027	+0.108 -0.108

**Table F.9:** Differential cross-section  $d\sigma(\gamma p \rightarrow \rho^0 Y)/dt$  in bins of  $W_{\gamma p}$  and  $t$ . The cross-section is obtained from a Söding fit of the unfolded differential cross-section  $d^2\sigma(\gamma p \rightarrow \pi^+\pi^- Y)/dm_{\pi\pi}dt(m_{\pi\pi}; W_{\gamma p}, t)$  and integration of the  $\rho^0$  amplitude in the range  $2m_\pi < m_{\pi\pi} < 1.53 \text{ GeV}$ . Splitting a normalization uncertainty from the (symmetrized) total covariance matrix according to Appendix C.3 yields  $\Delta_{\text{norm}} = 4.3\%$ . Further correlations are not provided.

### F.3 Misc. Parameter Tables

$m_Y = m_p$						$m_p < m_Y < 10 \text{ GeV}$					
$-t_{\text{max}}$	$-\langle t \rangle$	$-t_{\text{min}}$	$\alpha$	stat.	syst.	$-t_{\text{max}}$	$-\langle t \rangle$	$-t_{\text{min}}$	$\alpha$	stat.	syst.
[GeV <sup>2</sup> ]											
0.000	0.008	0.016	1.063	0.005	$^{+0.009}_{-0.007}$	0.000	0.024	0.050	1.050	0.012	$^{+0.024}_{-0.024}$
0.016	0.026	0.036	1.060	0.005	$^{+0.011}_{-0.005}$	0.050	0.079	0.110	0.962	0.012	$^{+0.021}_{-0.020}$
0.036	0.049	0.062	1.056	0.005	$^{+0.011}_{-0.005}$	0.110	0.158	0.210	0.931	0.012	$^{+0.023}_{-0.021}$
0.062	0.080	0.100	1.046	0.005	$^{+0.008}_{-0.005}$	0.210	0.298	0.400	0.925	0.011	$^{+0.023}_{-0.020}$
0.100	0.124	0.150	1.040	0.005	$^{+0.009}_{-0.006}$	0.400	0.782	1.500	0.930	0.011	$^{+0.027}_{-0.027}$
0.150	0.188	0.230	1.025	0.006	$^{+0.010}_{-0.006}$						
0.230	0.518	1.500	1.005	0.007	$^{+0.017}_{-0.009}$						

**Table F.10:** Fit parameters  $\alpha(t)$  for the fit of  $d\sigma(\gamma p \rightarrow \rho^0 Y)/dt(W_{\gamma p}, t)$  shown in Figure 8.11.

## G DATA SAMPLES

MC sample	elas ID	pdis ID
rho PP	9291	9292
rho DIS	9265	9267
omega	7663	7664
phi	7665	7666
rho(1450)	9335	9336
rho(1700)	9337	9338
gamma-dissoc	9350	9354

**Table G.1:** DiffVM Samples used in the analysis.

```

H1SteerOolumi(){
  //run range HE 06/07
  fFirstRun = 468531;    fLastRun  = 500611;

  // selected sub triggers
  fSubTrigs   = "14";    // "0, 1, 2, 3"; // for DIS selection

  // excluded runs: FTT L1 not working 475320-476029,
  fExcludedRuns =
    "475440,475441,475442,475443,475445,475446,475447,
    ...,
    476023,476024,476025,476026,476027,476028,476029";

  fPoorRuns = 0;          // don't include poor runs in runselection
  fMinRunLumi = 0.1;      // minimal lumi required per run in nb^(-1)

  fDZ = 35;              // vertex range    (used e.g. for satellite corr)

  // required subdetectors
  fCJC1 = 1;    fCJC2 = 1;    fLAR   = 1;    fVETO  = 1;    fLUMI  = 1;
  fCIP  = 1;    fTOF  = 1;    fFTT   = 1;    fSPAC  = 1;

  // for tagging FTS FMD123, EPlug
  fFTS  = 1;    fPLUG = 1;    fFmd   = 1;

  fComptonCorrection = 1;
}

```

**Table G.2:** Data samples used in the analysis. Oolumi steering.



## BIBLIOGRAPHY

- [1] **Particle Data Group**, M. Tanabashi, *et al.*, “Review of particle physics”, *Phys. Rev. D* **98** Aug (2018) 030001.
- [2] **H1 Collaboration**, F. D. Aaron *et al.*, “Diffractive Electroproduction of  $\rho^0$  and  $\varphi$  Mesons at HERA”, *JHEP* **05** (2010) 032, [arXiv:0910.5831](#).
- [3] **H1 Collaboration**, C. Adloff *et al.*, “Proton dissociative  $\rho^0$  and elastic  $\varphi$  electroproduction at HERA”, *Z. Phys.* **C75** (1997) 607–618, [arXiv:hep-ex/9705014](#).
- [4] **H1 Collaboration**, A. Aktas *et al.*, “Diffractive photoproduction of  $\rho^0$  mesons with large momentum transfer at HERA”, *Phys. Lett.* **B638** (2006) 422–431, [arXiv:hep-ex/0603038](#).
- [5] **H1 Collaboration**, C. Adloff *et al.*, “Elastic electroproduction of  $\rho^0$  mesons at HERA”, *Eur. Phys. J.* **C13** (2000) 371–396, [arXiv:hep-ex/9902019](#).
- [6] **H1 Collaboration**, S. Aid *et al.*, “Elastic photoproduction of  $\rho^0$  mesons at HERA”, *Nucl. Phys.* **B463** (1996) 3–32, [arXiv:hep-ex/9601004](#).
- [7] **H1 Collaboration**, S. Aid *et al.*, “Elastic electroproduction of  $\rho^0$  and  $J/\psi$  mesons at large  $Q^2$  at HERA”, *Nucl. Phys.* **B468** (1996) 3–36, [arXiv:hep-ex/9602007](#), [Erratum: *Nucl. Phys.*B548,639(1999)].
- [8] **ZEUS Collaboration**, H. Abramowicz *et al.*, “Exclusive electroproduction of two pions at HERA”, *Eur. Phys. J.* **C72** (2012) 1869, [arXiv:1111.4905](#).
- [9] **ZEUS Collaboration**, S. Chekanov *et al.*, “Exclusive production in deep inelastic scattering at HERA”, *PMC Phys.* **A1** (2007) 6, [arXiv:0708.1478](#).
- [10] **ZEUS Collaboration**, J. Breitweg *et al.*, “Measurement of the spin density matrix elements in exclusive electroproduction of  $\rho^0$  mesons at HERA”, *Eur. Phys. J.* **C12** (2000) 393–410, [arXiv:hep-ex/9908026](#).
- [11] **ZEUS Collaboration**, J. Breitweg *et al.*, “Elastic and proton dissociative  $\rho^0$  photoproduction at HERA”, *Eur. Phys. J.* **C2** (1998) 247–267, [arXiv:hep-ex/9712020](#).
- [12] **ZEUS Collaboration**, M. Derrick *et al.*, “Study of elastic  $\rho^0$  photoproduction at HERA using the ZEUS leading proton spectrometer”, *Z. Phys.* **C73** (1997) 253–268, [arXiv:hep-ex/9609003](#).
- [13] **ZEUS Collaboration**, M. Derrick *et al.*, “Measurement of elastic  $\rho^0$  photoproduction at HERA”, *Z. Phys.* **C69** (1995) 39–54, [arXiv:hep-ex/9507011](#).
- [14] **ZEUS Collaboration**, M. Derrick *et al.*, “Exclusive  $\rho^0$  production in deep inelastic electron-proton scattering at HERA”, *Phys. Lett.* **B356** (1995) 601–616, [arXiv:hep-ex/9507001](#).
- [15] **ZEUS Collaboration**, S. Chekanov *et al.*, “Measurement of proton dissociative diffractive photoproduction of vector mesons at large momentum transfer at HERA”, *Eur. Phys. J.* **C26** (2003) 389–409, [arXiv:hep-ex/0205081](#).

- [16] **ZEUS** Collaboration, J. Breitweg *et al.*, “Measurement of diffractive photoproduction of vector mesons at large momentum transfer at HERA”, *Eur. Phys. J.* **C14** (2000) 213–238, [arXiv:hep-ex/9910038](#).
- [17] **ZEUS** Collaboration, J. Breitweg *et al.*, “Exclusive electroproduction of  $\rho^0$  and  $J/\psi$  mesons at HERA”, *Eur. Phys. J.* **C6** (1999) 603–627, [arXiv:hep-ex/9808020](#).
- [18] **ZEUS** Collaboration, J. Breitweg *et al.*, “Measurement of exclusive  $\omega$  electroproduction at HERA”, *Phys. Lett.* **B487** (2000) 273–288, [arXiv:hep-ex/0006013](#).
- [19] **ZEUS** Collaboration, M. Derrick *et al.*, “Measurement of elastic  $\omega$  photoproduction at HERA”, *Z. Phys.* **C73** (1996) 73–84, [arXiv:hep-ex/9608010](#).
- [20] **H1** Collaboration, C. Adloff *et al.*, “Measurement of elastic electroproduction of  $\varphi$  mesons at HERA”, *Phys. Lett.* **B483** (2000) 360–372, [arXiv:hep-ex/0005010](#).
- [21] **ZEUS** Collaboration, S. Chekanov *et al.*, “Exclusive electroproduction of  $\varphi$  mesons at HERA”, *Nucl. Phys.* **B718** (2005) 3–31, [arXiv:hep-ex/0504010](#).
- [22] **ZEUS** Collaboration, M. Derrick *et al.*, “Measurement of the reaction  $\gamma^* p \rightarrow \varphi p$  in deep inelastic  $e^+p$  scattering at HERA”, *Phys. Lett.* **B380** (1996) 220–234, [arXiv:hep-ex/9604008](#).
- [23] **ZEUS** Collaboration, M. Derrick *et al.*, “Measurement of elastic  $\varphi$  photoproduction at HERA”, *Phys. Lett.* **B377** (1996) 259–272, [arXiv:hep-ex/9601009](#).
- [24] **H1** Collaboration, C. Alexa *et al.*, “Elastic and Proton-Dissociative Photoproduction of  $J/\psi$  Mesons at HERA”, *Eur. Phys. J.* **C73** (2013), no. 6, 2466, [arXiv:1304.5162](#).
- [25] **H1** Collaboration, A. Aktas *et al.*, “Elastic  $J/\psi$  production at HERA”, *Eur. Phys. J.* **C46** (2006) 585–603, [arXiv:hep-ex/0510016](#).
- [26] **H1** Collaboration, A. Aktas *et al.*, “Diffractive photoproduction of  $J/\psi$  mesons with large momentum transfer at HERA”, *Phys. Lett.* **B568** (2003) 205–218, [arXiv:hep-ex/0306013](#).
- [27] **H1** Collaboration, S. Aid *et al.*, “Elastic and inelastic photoproduction of  $J/\psi$  mesons at HERA”, *Nucl. Phys.* **B472** (1996) 3–31, [arXiv:hep-ex/9603005](#).
- [28] **H1** Collaboration, T. Ahmed *et al.*, “Photoproduction of  $J/\psi$  mesons at HERA”, *Phys. Lett.* **B338** (1994) 507–518.
- [29] **H1** Collaboration, C. Adloff *et al.*, “Elastic photoproduction of  $J/\psi$  and  $\Upsilon$  mesons at HERA”, *Phys. Lett.* **B483** (2000) 23–35, [arXiv:hep-ex/0003020](#).
- [30] **ZEUS** Collaboration, S. Chekanov *et al.*, “Measurement of  $J/\psi$  photoproduction at large momentum transfer at HERA”, *JHEP* **05** (2010) 085, [arXiv:0910.1235](#).
- [31] **ZEUS** Collaboration, S. Chekanov *et al.*, “Exclusive electroproduction of  $J/\psi$  mesons at HERA”, *Nucl. Phys.* **B695** (2004) 3–37, [arXiv:hep-ex/0404008](#).
- [32] **H1** Collaboration, C. Adloff *et al.*, “Charmonium production in deep inelastic scattering at HERA”, *Eur. Phys. J.* **C10** (1999) 373–393, [arXiv:hep-ex/9903008](#).
- [33] **ZEUS** Collaboration, S. Chekanov *et al.*, “Exclusive photoproduction of  $J/\psi$  mesons at HERA”, *Eur. Phys. J.* **C24** (2002) 345–360, [arXiv:hep-ex/0201043](#).
- [34] **ZEUS** Collaboration, J. Breitweg *et al.*, “Measurement of elastic  $J/\psi$  photoproduction at HERA”, *Z. Phys.* **C75** (1997) 215–228, [arXiv:hep-ex/9704013](#).

- [35] ZEUS Collaboration, M. Derrick *et al.*, “Measurement of the cross-section for the reaction  $\gamma p \rightarrow J/\psi p$  with the ZEUS detector at HERA”, *Phys. Lett.* **B350** (1995) 120–134, [arXiv:hep-ex/9503015](#).
- [36] H1 Collaboration, C. Adloff *et al.*, “Diffractive photoproduction of  $\psi(2S)$  mesons at HERA”, *Phys. Lett.* **B541** (2002) 251–264, [arXiv:hep-ex/0205107](#).
- [37] H1 Collaboration, C. Adloff *et al.*, “Photoproduction of  $\psi(2S)$  mesons at HERA”, *Phys. Lett.* **B421** (1998) 385–394, [arXiv:hep-ex/9711012](#).
- [38] ZEUS Collaboration, H. Abramowicz *et al.*, “Measurement of the  $t$  dependence in exclusive photoproduction of  $\Upsilon(1S)$  mesons at HERA”, *Phys. Lett.* **B708** (2012) 14–20, [arXiv:1111.2133](#).
- [39] ZEUS Collaboration, S. Chekanov *et al.*, “Exclusive photoproduction of  $\Upsilon$  mesons at HERA”, *Phys. Lett.* **B680** (2009) 4–12, [arXiv:0903.4205](#).
- [40] ZEUS Collaboration, J. Breitweg *et al.*, “Measurement of elastic  $\Upsilon$  photoproduction at HERA”, *Phys. Lett.* **B437** (1998) 432–444, [arXiv:hep-ex/9807020](#).
- [41] R. Weber, “Diffractive  $\rho^0$  photoproduction at HERA”, PhD thesis, ETH Zürich, 2006. URL <https://www-h1.desy.de/psfiles/theses/h1th-440.pdf>.
- [42] N. Berger, “Measurement of Diffractive  $\varphi$  Meson Photoproduction at HERA with the H1 Fast Track Trigger”, PhD thesis, ETH Zürich, 2007. URL <https://www-h1.desy.de/psfiles/theses/h1th-459.pdf>.
- [43] F. Huber, “Elastic and Proton Dissociative  $J/\psi$  Photoproduction at low  $W_{\gamma p}$  with the H1 Detector at HERA”, PhD thesis, Ruperto-Carola Universität Heidelberg, 2012. URL <http://www-h1.desy.de/psfiles/theses/h1th-796.pdf>.
- [44] D. J. Griffiths, “Introduction to elementary particles; 2nd rev. version”, Wiley, New York, NY, 2008.
- [45] M. E. Peskin and D. V. Schroeder, “An introduction to quantum field theory”, Westview, Boulder, CO, 1995.
- [46] S. L. Glashow, “Partial Symmetries of Weak Interactions”, *Nucl. Phys.* **22** (1961) 579–588.
- [47] S. Weinberg, “A Model of Leptons”, *Phys. Rev. Lett.* **19** (1967) 1264–1266.
- [48] A. Salam and J. C. Ward, “Electromagnetic and weak interactions”, *Phys. Lett.* **13** (1964) 168–171.
- [49] F. Englert and R. Brout, “Broken Symmetry and the Mass of Gauge Vector Mesons”, *Phys. Rev. Lett.* **13** (1964) 321–323, [157(1964)].
- [50] P. W. Higgs, “Broken symmetries, massless particles and gauge fields”, *Phys. Lett.* **12** (1964) 132–133.
- [51] P. W. Higgs, “Broken Symmetries and the Masses of Gauge Bosons”, *Phys. Rev. Lett.* **13** (1964) 508–509, [160(1964)].
- [52] N. Cabibbo, “Unitary Symmetry and Leptonic Decays”, *Phys. Rev. Lett.* **10** (1963) 531–533, [648(1963)].
- [53] M. Kobayashi and T. Maskawa, “CP Violation in the Renormalizable Theory of Weak Interaction”, *Prog. Theor. Phys.* **49** (1973) 652–657.
- [54] B. Pontecorvo, “Mesonium and anti-mesonium”, *Sov. Phys. JETP* **6** (1957) 429, [Zh. Eksp. Teor. Fiz.33,549(1957)].

- [55] B. Pontecorvo, “Inverse beta processes and nonconservation of lepton charge”, *Sov. Phys. JETP* **7** (1958) 172–173, [Zh. Eksp. Teor. Fiz.34,247(1957)].
- [56] B. Pontecorvo, “Neutrino Experiments and the Problem of Conservation of Leptonic Charge”, *Sov. Phys. JETP* **26** (1968) 984–988, [Zh. Eksp. Teor. Fiz.53,1717(1967)].
- [57] Z. Maki, M. Nakagawa, and S. Sakata, “Remarks on the unified model of elementary particles”, *Prog. Theor. Phys.* **28** (1962) 870–880, [34(1962)].
- [58] H. Fritzsch, M. Gell-Mann, and H. Leutwyler, “Advantages of the Color Octet Gluon Picture”, *Phys. Lett.* **47B** (1973) 365–368.
- [59] G. Zweig, “An SU(3) model for strong interaction symmetry and its breaking. Version 1”, 1964.
- [60] D. J. Gross and F. Wilczek, “Ultraviolet Behavior of Nonabelian Gauge Theories”, *Phys. Rev. Lett.* **30** (1973) 1343–1346, [271(1973)].
- [61] H. D. Politzer, “Reliable Perturbative Results for Strong Interactions?”, *Phys. Rev. Lett.* **30** (1973) 1346–1349, [274(1973)].
- [62] R. P. Feynman, “Very high-energy collisions of hadrons”, *Phys. Rev. Lett.* **23** (1969) 1415–1417, [494(1969)].
- [63] J. D. Bjorken, “Asymptotic Sum Rules at Infinite Momentum”, *Phys. Rev.* **179** (1969) 1547–1553.
- [64] K. G. Wilson, “Confinement of Quarks”, *Phys. Rev.* **D10** (1974) 2445–2459, [319(1974)].
- [65] H. Yukawa, “On the Interaction of Elementary Particles I”, *Proc. Phys. Math. Soc. Jap.* **17** (1935) 48–57, [Prog. Theor. Phys. Suppl.1,1(1935)].
- [66] **ATLAS** Collaboration, “Standard Model Summary Plots Spring 2019”, Tech. Rep. ATL-PHYS-PUB-2019-010, CERN, Geneva, Mar 2019.
- [67] G. Alberi and G. Goggi, “Diffraction of Subnuclear Waves”, *Phys. Rept.* **74** (1981) 1–207.
- [68] E. Predazzi, “Diffraction: Past, present and future”, in “Hadron physics 98: Topics on the structure and interaction of hadronic systems. Proceedings, Workshop, Florianopolis, Brazil, March 16-21, 1998”, pp. 80–175. 1998. [arXiv:hep-ph/9809454](#).
- [69] G. Pancheri and Y. N. Srivastava, “Introduction to the physics of the total cross-section at LHC”, *Eur. Phys. J.* **C77** (2017), no. 3, 150, [arXiv:1610.10038](#).
- [70] S. Mandelstam, “Determination of the pion - nucleon scattering amplitude from dispersion relations and unitarity. General theory”, *Phys. Rev.* **112** (1958) 1344–1360.
- [71] **TOTEM** Collaboration, G. Antchev *et al.*, “Proton-proton elastic scattering at the LHC energy of  $\sqrt{s} = 7$  TeV”, *EPL* **95** (2011), no. 4, 41001, [arXiv:1110.1385](#).
- [72] **TOTEM** Collaboration, G. Antchev *et al.*, “Measurement of proton-proton elastic scattering and total cross-section at  $\sqrt{s} = 7$  TeV ”, *EPL* **101** (2013), no. 2, 21002.
- [73] L. V. P. R. de Broglie, “Recherches sur la théorie des quanta”, *Annals Phys.* **2** (1925) 22–128.
- [74] T. Regge, “Introduction to complex orbital momenta”, *Nuovo Cim.* **14** (1959) 951.
- [75] T. Regge, “Bound states, shadow states and Mandelstam representation”, *Nuovo Cim.* **18** (1960) 947–956.

- [76] P. D. B. Collins, “An introduction to regge theory and high energy physics”, Cambridge University Press, 1977.
- [77] J. R. Forshaw and D. A. Ross, “Quantum chromodynamics and the pomeron”, *Cambridge Lect. Notes Phys.* **9** (1997) 1–248.
- [78] S. Donnachie, H. G. Dosch, O. Nachtmann, and P. Landshoff, “Pomeron physics and QCD”, *Camb. Monogr. Part. Phys. Nucl. Phys. Cosmol.* **19** (2002) 1–347.
- [79] G. F. Chew and S. C. Frautschi, “Regge trajectories and the principle of maximum strength for strong interactions”, *Physical Review Letters* **8** (1962), no. 1, 41–44.
- [80] V. Gribov, “Partial waves with complex orbital angular momenta and the asymptotic behavior of the scattering amplitude”, *Sov. Phys. JETP* **14** (1962) 1395.
- [81] G. S. Sharov, “String Models, Stability and Regge Trajectories for Hadron States”, [arXiv:1305.3985](https://arxiv.org/abs/1305.3985).
- [82] L. B. Okun, “The life and legacy of Pomeranchuk”, in “International Conference: I.Ya. Pomeranchuk and Physics at the Turn of Centuries Moscow, Russia, January 24-28, 2003”, pp. 3–20. 2003. [arXiv:physics/0307123](https://arxiv.org/abs/physics/0307123).
- [83] A. Donnachie and P. V. Landshoff, “p p and anti-p p Elastic Scattering”, *Nucl. Phys.* **B231** (1984) 189–204.
- [84] A. Donnachie and P. V. Landshoff, “Total cross-sections”, *Phys. Lett.* **B296** (1992) 227–232, [arXiv:hep-ph/9209205](https://arxiv.org/abs/hep-ph/9209205).
- [85] M. Froissart, “Asymptotic behavior and subtractions in the Mandelstam representation”, *Phys. Rev.* **123** (1961) 1053–1057.
- [86] A. Martin, “Unitarity and high-energy behavior of scattering amplitudes”, *Phys. Rev.* **129** (1963) 1432–1436.
- [87] A. B. Kaidalov, L. A. Ponomarev, and K. A. Ter-Martirosian, “Total Cross-sections and Diffractive Scattering in a Theory of Interacting Pomerons With  $\alpha_{\mathcal{P}}(0) > 1$ ”, *Yad. Fiz.* **44** (1986) 722–728, [Sov. J. Nucl. Phys.44,468(1986)].
- [88] V. A. Khoze, A. D. Martin, and M. G. Ryskin, “Soft diffraction and the elastic slope at Tevatron and LHC energies: A MultiPomeron approach”, *Eur. Phys. J.* **C18** (2000) 167–179, [arXiv:hep-ph/0007359](https://arxiv.org/abs/hep-ph/0007359).
- [89] L. Lukaszuk and B. Nicolescu, “A Possible interpretation of p p rising total cross-sections”, *Lett. Nuovo Cim.* **8** (1973) 405–413.
- [90] C. Amsler and N. A. Tornqvist, “Mesons beyond the naive quark model”, *Phys. Rept.* **389** (2004) 61–117.
- [91] H. B. Meyer and M. J. Teper, “Glueball Regge trajectories and the pomeron: A Lattice study”, *Phys. Lett.* **B605** (2005) 344–354, [arXiv:hep-ph/0409183](https://arxiv.org/abs/hep-ph/0409183).
- [92] F. J. Llanes-Estrada, S. R. Cotanch, P. J. de A. Bicudo, J. E. F. T. Ribeiro, and A. P. Szczepaniak, “QCD glueball Regge trajectories and the Pomeron”, *Nucl. Phys.* **A710** (2002) 45–54, [arXiv:hep-ph/0008212](https://arxiv.org/abs/hep-ph/0008212).
- [93] M. N. Sergeenko, “Glueballs and the Pomeron”, *EPL* **89** (2010), no. 1, 11001, [arXiv:1107.1671](https://arxiv.org/abs/1107.1671).
- [94] F. E. Low, “A Model of the Bare Pomeron”, *Phys. Rev.* **D12** (1975) 163–173.
- [95] S. Nussinov, “Colored Quark Version of Some Hadronic Puzzles”, *Phys. Rev. Lett.* **34** (1975) 1286–1289.

- [96] E. A. Kuraev, L. N. Lipatov, and V. S. Fadin, “Multi - Reggeon Processes in the Yang-Mills Theory”, *Sov. Phys. JETP* **44** (1976) 443–450, [*Zh. Eksp. Teor. Fiz.*71,840(1976)].
- [97] E. A. Kuraev, L. N. Lipatov, and V. S. Fadin, “The Pomeron Singularity in Nonabelian Gauge Theories”, *Sov. Phys. JETP* **45** (1977) 199–204, [*Zh. Eksp. Teor. Fiz.*72,377(1977)].
- [98] L. N. Lipatov, “Reggeization of the Vector Meson and the Vacuum Singularity in Nonabelian Gauge Theories”, *Sov. J. Nucl. Phys.* **23** (1976) 338–345, [*Yad. Fiz.*23,642(1976)].
- [99] I. I. Balitsky and L. N. Lipatov, “The Pomeron Singularity in Quantum Chromodynamics”, *Sov. J. Nucl. Phys.* **28** (1978) 822–829, [*Yad. Fiz.*28,1597(1978)].
- [100] M. McGuigan and C. B. Thorn, “Quark - anti-quark Regge trajectories in large N(c) QCD”, *Phys. Rev. Lett.* **69** (1992) 1312–1315, [arXiv:hep-ph/9205211](#).
- [101] S. J. Brodsky, W.-K. Tang, and C. B. Thorn, “The reggeon trajectory in exclusive and inclusive large momentum transfer reactions”, *Phys. Lett.* **B318** (1993) 203–211.
- [102] V. A. Petrov and A. P. Samokhin, “Regge Trajectories in QCD: Can They Keep on Rising?”, *Phys. Lett.* **B237** (1990) 500–502.
- [103] R. Blankenbecler, S. J. Brodsky, J. F. Gunion, and R. Savit, “The Connection Between Regge Behavior and Fixed Angle Scattering”, *Phys. Rev.* **D8** (1973) 4117.
- [104] R. Fiore, L. L. Jenkovszky, F. Paccanoni, and A. Prokudin, “The Pomeron in exclusive vector meson production”, *Phys. Rev.* **D68** (2003) 014005, [arXiv:hep-ph/0302195](#).
- [105] A. Ballon-Bayona, R. Carcassés Quevedo, and M. S. Costa, “Unity of pomerons from gauge/string duality”, *JHEP* **08** (2017) 085, [arXiv:1704.08280](#).
- [106] J. M. Maldacena, “The Large N limit of superconformal field theories and supergravity”, *Int. J. Theor. Phys.* **38** (1999) 1113–1133, [arXiv:hep-th/9711200](#), [*Adv. Theor. Math. Phys.*2,231(1998)].
- [107] E. Witten, “Anti-de Sitter space and holography”, *Adv. Theor. Math. Phys.* **2** (1998) 253–291, [arXiv:hep-th/9802150](#).
- [108] S. S. Gubser, I. R. Klebanov, and A. M. Polyakov, “Gauge theory correlators from noncritical string theory”, *Phys. Lett.* **B428** (1998) 105–114, [arXiv:hep-th/9802109](#).
- [109] R. C. Brower, J. Polchinski, M. J. Strassler, and C.-I. Tan, “The Pomeron and gauge/string duality”, *JHEP* **12** (2007) 005, [arXiv:hep-th/0603115](#).
- [110] S. K. Domokos, J. A. Harvey, and N. Mann, “The Pomeron contribution to p p and anti-p scattering in AdS/QCD”, *Phys. Rev.* **D80** (2009) 126015, [arXiv:0907.1084](#).
- [111] E. L. Feinberg and I. Pomerančuk, “High energy inelastic diffraction phenomena”, *Il Nuovo Cimento (1955-1965)* **3** Apr (1956) 652–671.
- [112] M. L. Good and W. D. Walker, “Diffraction dissociation of beam particles”, *Phys. Rev.* **120** (1960) 1857–1860.
- [113] Y. Akimov *et al.*, “Diffraction Dissociation of High-Energy Protons in p d Interactions”, *Phys. Rev. Lett.* **35** (1975) 766.
- [114] N. P. Zotov and V. A. Tsarev, “Diffraction dissociation: 35 years on”, *Soviet Physics Uspekhi* **31** February (1988) 119–139.
- [115] A. B. Kaidalov, “Diffractive Production Mechanisms”, *Phys. Rept.* **50** (1979) 157–226.

- 
- [116] B. L. Ioffe, “Space-time picture of photon and neutrino scattering and electroproduction cross-section asymptotics”, *Phys. Lett.* **30B** (1969) 123–125.
- [117] J. J. Sakurai, “Vector meson dominance and high-energy electron proton inelastic scattering”, *Phys. Rev. Lett.* **22** (1969) 981–984.
- [118] L. Favart, M. Guidal, T. Horn, and P. Kroll, “Deeply Virtual Meson Production on the nucleon”, *Eur. Phys. J.* **A52** (2016), no. 6, 158, [arXiv:1511.04535](https://arxiv.org/abs/1511.04535).
- [119] T. H. Bauer, R. D. Spital, D. R. Yennie, and F. M. Pipkin, “The Hadronic Properties of the Photon in High-Energy Interactions”, *Rev. Mod. Phys.* **50** (1978) 261, [Erratum: *Rev. Mod. Phys.* 51, 407 (1979)].
- [120] A. Donnachie and P. V. Landshoff, “Small  $x$ : Two pomerons!”, *Phys. Lett.* **B437** (1998) 408–416, [arXiv:hep-ph/9806344](https://arxiv.org/abs/hep-ph/9806344).
- [121] A. Donnachie and P. V. Landshoff, “Exclusive vector meson production at HERA”, *Phys. Lett.* **B348** (1995) 213–218, [arXiv:hep-ph/9411368](https://arxiv.org/abs/hep-ph/9411368).
- [122] P. Söding, “On the apparent shift of the rho meson mass in photoproduction”, *Phys. Lett.* **19** (1966) 702–704.
- [123] C. Ewerz, M. Maniatis, and O. Nachtmann, “A Model for Soft High-Energy Scattering: Tensor Pomeron and Vector Odderon”, *Annals Phys.* **342** (2014) 31–77, [arXiv:1309.3478](https://arxiv.org/abs/1309.3478).
- [124] A. Bolz, C. Ewerz, M. Maniatis, O. Nachtmann, M. Sauter, and A. Schöning, “Photoproduction of  $\pi^+ \pi^-$  pairs in a model with tensor-pomeron and vector-odderon exchange”, *JHEP* **1501** (2015) 151, [arXiv:1409.8483](https://arxiv.org/abs/1409.8483).
- [125] F. Huber, “Elastic  $J/\psi$  Production at low  $Q^2$  at HERA”, Master’s thesis, ETH Zürich, 2009. URL <https://www-h1.desy.de/psfiles/theses/h1th-522.pdf>.
- [126] E. Fermi, “On the Theory of the impact between atoms and electrically charged particles”, *Z. Phys.* **29** (1924) 315–327.
- [127] E. J. Williams, “Nature of the high-energy particles of penetrating radiation and status of ionization and radiation formulae”, *Phys. Rev.* **45** (1934) 729–730.
- [128] C. F. von Weizsacker, “Radiation emitted in collisions of very fast electrons”, *Z. Phys.* **88** (1934) 612–625.
- [129] V. M. Budnev, I. F. Ginzburg, G. V. Meledin, and V. G. Serbo, “The Two photon particle production mechanism. Physical problems. Applications. Equivalent photon approximation”, *Phys. Rept.* **15** (1975) 181–281.
- [130] “Deutsches Elektronen-Synchrotron (DESY)”. <http://www.desy.de/>, April 2019.
- [131] H1 Collaboration, “Luminosity summary tables”. [http://www-h1.desy.de/h1/www/h1det/lumi/summary\\_tables/](http://www-h1.desy.de/h1/www/h1det/lumi/summary_tables/), April 2019.
- [132] H1 Collaboration, “ $ep$  Physics beyond 1999”. H1 internal report, October 1997. H1-IN-531(10/1997).
- [133] H1 and ZEUS Collaboration, H. Abramowicz *et al.*, “Combination of measurements of inclusive deep inelastic  $e^\pm p$  scattering cross sections and QCD analysis of HERA data”, *Eur. Phys. J.* **C75** (2015), no. 12, 580, [arXiv:1506.06042](https://arxiv.org/abs/1506.06042).
- [134] H1 Collaboration, V. Andreev *et al.*, “Determination of the strong coupling constant  $\alpha_s(m_Z)$  in next-to-next-to-leading order QCD using H1 jet cross section measurements”, *Eur. Phys. J.* **C77** (2017), no. 11, 791, [arXiv:1709.07251](https://arxiv.org/abs/1709.07251).

- [135] **ZEUS** Collaboration, M. Derrick *et al.*, “Measurement of charged and neutral current  $e$ - $p$  deep inelastic scattering cross-sections at high  $Q^2$ ”, *Phys. Rev. Lett.* **75** (1995) 1006–1011, [arXiv:hep-ex/9503016](#).
- [136] **H1** Collaboration, S. Aid *et al.*, “Measurement of the  $Q^2$  dependence of the charged and neutral current cross-sections in  $e \pm p$  scattering at HERA”, *Phys. Lett.* **B379** (1996) 319–329, [arXiv:hep-ex/9603009](#).
- [137] **H1 and ZEUS** Collaboration - HERA Combined Results.  
[https://www.desy.de/h1zeus/combined\\_results/index.php](https://www.desy.de/h1zeus/combined_results/index.php).
- [138] **H1** Collaboration - Publications.  
[https://www-h1.desy.de/publications/H1publication.short\\_list.html](https://www-h1.desy.de/publications/H1publication.short_list.html).
- [139] **ZEUS** Collaboration - Publications.  
[https://www-zeus.desy.de/zeus\\_papers/zeus\\_papers.html](https://www-zeus.desy.de/zeus_papers/zeus_papers.html).
- [140] **HERA-B** - Public webpage. <http://www-hera-b.desy.de/>.
- [141] **HERMES** - Public webpage. <http://www-hermes.desy.de/>.
- [142] **H1** Collaboration, I. Abt *et al.*, “The H1 detector at HERA”, *Nucl. Instrum. Meth.* **A386** (1997) 310–347.
- [143] **H1** Collaboration, I. Abt *et al.*, “The tracking, calorimeter and muon detectors of the H1 experiment at HERA”, *Nucl. Instrum. Meth.* **A386** (1997) 348–396.
- [144] D. Pitzl *et al.*, “The H1 silicon vertex detector”, *Nucl. Instrum. Meth.* **A454** (2000) 334–349, [arXiv:hep-ex/0002044](#).
- [145] B. List, “The H1 silicon tracker”, *Nucl. Instrum. Meth.* **A549** (2005) 33–36.
- [146] J. Becker, K. Bosiger, L. Lindfeld, K. Muller, P. Robmann, *et al.*, “A vertex trigger based on cylindrical multiwire proportional chambers”, *Nucl. Instrum. Meth.* **A586** (2008) 190–203, [arXiv:physics/0701002](#).
- [147] M. C. Urban, “The new CIP2k z-Vertex Trigger for the H1 Experiment at HERA”, PhD thesis, Universität Zürich, 2004. URL  
<https://www-h1.desy.de/psfiles/theses/h1th-366.pdf>.
- [148] J. Burger *et al.*, “The central jet chamber of the H1 experiment”, *Nucl. Instrum. Meth.* **A279** (1989) 217–222.
- [149] A. Bolz, “Charge Asymmetries in  $\pi^+\pi^-$  Photoproduction in a Model for Soft High Energy Scattering and Detector Asymmetry Measurements at the H1 Experiment”, Master’s thesis, Universität Heidelberg, 2015. URL  
<https://www-h1.desy.de/psfiles/theses/h1th-880.pdf>.
- [150] V. Blobel, “A new fast track-fit algorithm based on broken lines”, *Nucl. Instrum. Meth.* **A566** (2006) 14–17.
- [151] **H1** Tracking Group.  
<https://www-h1.desy.de/idet/itracker/TrackingGroup/home.html>,  
V. Blobel, “Central Track Reconstruction”, <https://www-h1.desy.de/idet/itracker/TrackingGroup/NotesAndFigs/VolkerJCTrec.pdf>.
- [152] **H1 Calorimeter Group**, B. Andrieu, *et al.*, “The H1 liquid argon calorimeter system”, *Nucl. Instrum. Meth.* **A336** (1993) 460–498.
- [153] L. Goerlich and H. P. Wellisch, “Documentation of the LAr clustering”. H1 internal report, December 1991. H1-IN-204 (12/1991).

- [154] H. P. Wellisch, J. P. Kubenka, H. Oberlack, and P. Schacht, “Hadronic calibration of the H1 LAr calorimeter using software weighting techniques”. H1 internal report, February 1994. H1-IN-346 (02/1994).
- [155] **H1 SpaCal Group**, R. D. Appuhn, *et al.*, “The H1 lead / scintillating fiber calorimeter”, *Nucl. Instrum. Meth.* **A386** (1997) 397–408.
- [156] A. Astvatsatourov, K. Cerny, J. Delvax, L. Favart, T. Hreus, X. Janssen, R. Roosen, T. Sykora, and P. Van Mechelen, “The H1 Very Forward Proton Spectrometer at HERA”. H1 internal report, January 2013. H1-IN-637(01/2013).
- [157] M. Dirkmann, “Messung der diffraktiven Strukturfunktion  $F_2^{D(3)}(Q^2, \beta, x_{\mathbb{P}})$  des Protons bei kleinen Impulsüberträgen mit dem H1-Detektor”, PhD thesis, Universität Dortmund, 1998. URL [/afs/desy.de/group/h1/psfiles/theses/h1th-136.pdf](http://afs.desy.de/group/h1/psfiles/theses/h1th-136.pdf).
- [158] F. Sefkow, E. Elsen, H. Krehbiel, U. Straumann, and J. Coughlan, “Experience with the first level trigger of H1”, *IEEE Transactions on Nuclear Science* **42** aug (1995) 900–904.
- [159] H.-C. Schultz-Coulon, J. Coughlan, E. Elsen, T. Nicholls, and H. Rick, “A general scheme for optimization of trigger rates in an experiment with limited bandwidth”, in “1998 IEEE Nuclear Science Symposium, 1998. Conference Record”, vol. 2, pp. 956–961 vol.2. 1998.
- [160] T. Nicholls, M. Charlet, J. Coughlan, E. Elsen, D. Hoffmann, H. Krehbiel, H.-C. Schultz-Coulon, J. Schutt, and F. Sefkow, “Concept, design and performance of the second level triggers of the H1 detector”, *IEEE Transactions on Nuclear Science* **45** June (1998) 810–816.
- [161] J. Naumann, “Entwicklung und Test der dritten H1-Triggerstufe”, PhD thesis, Universität Dortmund, 2012. URL <http://www-h1.desy.de/psfiles/theses/h1th-305.pdf>.
- [162] A. Baird *et al.*, “A Fast high resolution track trigger for the H1 experiment”, *IEEE Trans. Nucl. Sci.* **48** (2001) 1276–1285, [arXiv:hep-ex/0104010](https://arxiv.org/abs/hep-ex/0104010).
- [163] D. Meer, D. Muller, J. Muller, A. Schoning, and C. Wissing, “A Multifunctional processing board for the fast track trigger of the H1 experiment”, *IEEE Trans. Nucl. Sci.* **49** (2002) 357–361, [arXiv:hep-ex/0107010](https://arxiv.org/abs/hep-ex/0107010).
- [164] H. Bethe and W. Heitler, “On the Stopping of fast particles and on the creation of positive electrons”, *Proc. Roy. Soc. Lond.* **A146** (1934) 83–112.
- [165] **H1 Collaboration**, F. D. Aaron *et al.*, “Determination of the Integrated Luminosity at HERA using Elastic QED Compton Events”, *Eur. Phys. J.* **C72** (2012) 2163, [arXiv:1205.2448](https://arxiv.org/abs/1205.2448), [Erratum: *Eur. Phys. J.* C74, 2733 (2012)].
- [166] B. List and A. Mastroberardino, “DIFFVM - A Monte Carlo generator for diffractive processes in ep scattering”, *DESY-PROC.* **02** (1999) 396–404.
- [167] J. J. Sakurai and D. Schildknecht, “Generalized vector dominance and inelastic electron - proton scattering”, *Phys. Lett.* **40B** (1972) 121–126.
- [168] J. J. Sakurai and D. Schildknecht, “Generalized vector dominance and inelastic electron-nucleon scattering. the neutron-to-proton ratios”, *Phys. Lett.* **41B** (1972) 489–494.
- [169] J. J. Sakurai and D. Schildknecht, “Generalized vector dominance and inelastic electron nucleon scattering - the small  $\omega'$  region”, *Phys. Lett.* **42B** (1972) 216–220.
- [170] Y. Akimov *et al.*, “Analysis of Diffractive  $pd \rightarrow Xd$  and  $pp \rightarrow Xp$  Interactions and Test of the Finite Mass Sum Rule”, *Phys. Rev.* **D14** (1976) 3148.

- [171] K. A. Goulianos, “Diffractive Interactions of Hadrons at High-Energies”, *Phys. Rept.* **101** (1983) 169.
- [172] T. Sjostrand and M. Bengtsson, “The Lund Monte Carlo for Jet Fragmentation and  $e^+e^-$  Physics. Jetset Version 6.3: An Update”, *Comput. Phys. Commun.* **43** (1987) 367.
- [173] **H1** Collaboration, “Guide for the H1 simulation program H1SIM”. H1 Internal Software-Note <https://www-h1.desy.de/ipublications/inotes1/sw003.txt>, 1989. 03-11/89.
- [174] R. Brun, F. Bruyant, M. Maire, A. C. McPherson, and P. Zancarini, “GEANT3”, 1987.
- [175] H. Fesefeldt, “The  $e/H$  Ratio and Energy Resolution of Hadron Calorimeters”, *Nucl. Instrum. Meth.* **A263** (1988) 114–135.
- [176] K. Daum. Personal communication, [karin.daum@desy.de](mailto:karin.daum@desy.de).
- [177] **H1** Collaboration, V. Andreev *et al.*, “Exclusive  $\rho^0$  meson photoproduction with a leading neutron at HERA”, *Eur. Phys. J.* **C76** (2016), no. 1, 41, [arXiv:1508.03176](https://arxiv.org/abs/1508.03176).
- [178] M. D. Sauter, “Measurement of Beauty Photoproduction at Threshold Using Di-Electron Events With the H1 Detector at HERA”, PhD thesis, Swiss Federal Institute of Technology Zurich, 2009. URL <https://bib-pubdb1.desy.de/record/91126/files/h1th-518.pdf>.
- [179] A. W. Jung, “Measurement of the  $D^{*\pm}$  Meson Cross Section and Extraction of the Charm Contribution,  $F_2^c(x; Q^2)$ , to the Proton Structure in Deep Inelastic  $ep$  Scattering with the H1 Detector at HERA”, PhD thesis, Ruprecht-Karls-Universität Heidelberg, 2009. URL <https://www-h1.desy.de/psfiles/theses/h1th-504.pdf>.
- [180] B. Clerbaux, “Electroproduction élastique de mésons  $\rho$  à HERA”, PhD thesis, Université Libre de Bruxelles, 1999. URL <http://www-h1.desy.de/psfiles/theses/h1th-142.pdf>.
- [181] H. Abramowicz, “Diffraction and the Pomeron”, *Int. J. Mod. Phys.* **A15S1** (2000) 495–520, [arXiv:hep-ph/0001054](https://arxiv.org/abs/hep-ph/0001054).
- [182] V. Blobel and E. Lohrmann, “Statistische und numerische methoden der datenanalyse”, Vieweg+Teubner Verlag, 1998.
- [183] S. Schmitt, “TUnfold: an algorithm for correcting migration effects in high energy physics”, *JINST* **7** (2012) T10003, [arXiv:1205.6201](https://arxiv.org/abs/1205.6201).
- [184] S. Schmitt, “Data Unfolding Methods in High Energy Physics”, *EPJ Web Conf.* **137** (2017) 11008, [arXiv:1611.01927](https://arxiv.org/abs/1611.01927).
- [185] A. N. Tikonov, “Regularization of incorrectly posed problems”, *Doklady Akademii Nauk SSSR* **151** (1963) 1624–1627.
- [186] D. L. Phillips, “A Technique for the Numerical Solution of Certain Integral Equations of the First Kind”, *J. Assoc. Comput. Machinery* **9** (1962), no. 1, 84–97.
- [187] F. James, “Statistical methods in experimental physics”, Hackensack, USA: World Scientific (2006) 345 p, 2006.
- [188] V. Blobel, “Unfolding - Linear Inverse Problems”, in “Terascale Workshop”. DESY Hamburg, 2010.
- [189] **CMD-2** Collaboration, R. R. Akhmetshin *et al.*, “Measurement of  $e^+e^- \rightarrow \pi^+\pi^-$  cross-section with CMD-2 around  $\rho$ -meson”, *Phys. Lett.* **B527** (2002) 161–172, [arXiv:hep-ex/0112031](https://arxiv.org/abs/hep-ex/0112031).

- 
- [190] J. D. Jackson, “Remarks on the phenomenological analysis of resonances”, *Il Nuovo Cimento (1955-1965)* **34** Dec (1964) 1644–1666.
- [191] H. B. O’Connell, B. C. Pearce, A. W. Thomas, and A. G. Williams, “ $\rho - \omega$  mixing, vector meson dominance and the pion form-factor”, *Prog. Part. Nucl. Phys.* **39** (1997) 201–252, [arXiv:hep-ph/9501251](#).
- [192] G. Breit and E. Wigner, “Capture of slow neutrons”, *Phys. Rev.* **49** Apr (1936) 519–531.
- [193] D. Melikhov, O. Nachtmann, V. Nikonov, and T. Paulus, “Masses and couplings of vector mesons from the pion electromagnetic, weak, and pi gamma transition form-factors”, *Eur. Phys. J. C* **34** (2004) 345–360, [arXiv:hep-ph/0311213](#).
- [194] M. H. Ross and L. Stodolsky, “Photon dissociation model for vector meson photoproduction”, *Phys. Rev.* **149** (1966) 1172–1181.
- [195] CMS Collaboration, A. M. Sirunyan *et al.*, “Measurement of exclusive  $\rho(770)^0$  photoproduction in ultraperipheral pPb collisions at  $\sqrt{s_{NN}} = 5.02$  TeV”, [arXiv:1902.01339](#).
- [196] J. Ballam *et al.*, “Study of high-energy photoproduction with positron annihilation radiation: I three prong events”, *Phys. Rev.* **D5** (1972) 15.
- [197] J. Park *et al.*, “The reaction  $\gamma p \rightarrow \rho^0 p$  at 5.5-GeV to 18-GeV”, *Nucl. Phys.* **B36** (1972) 404.
- [198] J. Ballam *et al.*, “Bubble Chamber Study of Photoproduction by 2.8-GeV and 4.7-GeV Polarized Photons. 1. Cross-Section Determinations and Production of  $\rho^0$  and  $\Delta^{++}$  in the Reaction  $\gamma p \rightarrow p\pi^+\pi^-$ ”, *Phys. Rev.* **D5** (1972) 545.
- [199] J. Ballam *et al.*, “Vector Meson Production by Polarized Photons at 2.8-GeV, 4.7-GeV, and 9.3-GeV”, *Phys. Rev.* **D7** (1973) 3150.
- [200] G. Alexander *et al.*, “A Comparative Study of  $\rho^0$  Photoproduced on D, N and P at 7.5-GeV”, *Nucl. Phys.* **B104** (1976) 397–412.
- [201] R. M. Egloff *et al.*, “Measurements of Elastic Rho and Phi Meson Photoproduction Cross-Sections on Protons from 30 GeV to 180 GeV”, *Phys. Rev. Lett.* **43** (1979) 657.
- [202] D. Aston *et al.*, “Photoproduction of  $\rho^0$  and  $\omega$  on Hydrogen at Photon Energies of 20-GeV to 70-GeV”, *Nucl. Phys.* **B209** (1982) 56–76.
- [203] H1 Collaboration, “A Measurement of the Pomeron Trajectory based on Elastic  $\rho^0$  Photoproduction”. Preliminary, April 2009. H1prelim-09-016, H1prelim-06-011.
- [204] O. Nachtmann. Personal communication, O.Nachtmann@thphys.uni-heidelberg.de.



## DANKSAGUNG

Abschließend möchte ich mich bei allen bedanken, die diese Arbeit persönlich möglich gemacht und mir über die letzten Jahre geholfen haben, sie zu vollenden.

Zuallererst gilt mein Dank meinem Betreuer André Schöning. In den letzten Jahren hat er mich mit seiner Begeisterung für Physik immer wieder motiviert, mich bei Problemen unterstützt und nicht zuletzt immer wieder Geld für eine Anstellung organisiert. Nur aufgrund seines festen Glaubens an die Freiheit der Forschung konnte ich diese Analyse auch über zehn Jahre nach dem Ende von HERA noch durchführen.

Ferner gilt mein Dank meiner Familie, die mich in den nunmehr über zehn Jahren meines Studiums finanziell und emotional großzügig unterstützt hat. Insbesondere im letzten Jahr wurde noch einmal besonders deutlich, wie groß und wertvoll unser Zusammenhalt ist.

Meinen Kollegen und Kommilitonen, insbesondere Danilo, Loreen, Julian und Rima danke ich für ihre Freundschaft, fachliche Betreuung, anregende Gespräche und ganz allgemein für ihre Begleitung durch die letzten Jahre.

Der H1 Kollaboration, insbesondere Stefan Schmitt, bin ich für ihre reichliche Unterstützung und ihr Interesse an meiner Arbeit dankbar. Möge es nicht die letzte Dissertation sein, die über eine H1 Analyse geschrieben wird!

Prof. Ulrich Uwer danke ich dafür, dass er sich zur Begutachtung meiner Arbeit bereit erklärt hat.